ADVANCES IN MODELING MIXING AND MOLECULAR TRANSPORT IN PROBABILITY DENSITY FUNCTION METHODS OF TURBULENT REACTING FLOWS

A Dissertation

Presented to the Faculty of the Graduate School

of Cornell University

in Partial Fulfillment of the Requirements for the Degree of

Doctor of Philosophy

by

Sharadha Viswanathan

January 2011

ADVANCES IN MODELING MIXING AND MOLECULAR TRANSPORT IN PROBABILITY DENSITY FUNCTION METHODS OF TURBULENT REACTING FLOWS

Sharadha Viswanathan, Ph.D.

Cornell University 2011

Modeling of turbulent reacting flow problems using Probability Density Function (PDF) methods yields transport and reaction in closed form while the processes related to the conditional dissipation of species compositions need to be closed using mixing models.

First, we study the dispersion from line sources in decaying grid turbulence using a modified form of the Interaction by Exchange with the Conditional Mean (IECM) mixing model. These flows pose a significant challenge to statistical models, because the scalar length scale (of the initial plume) is much smaller than the turbulence integral scale. Consequently, this necessitates incorporating the effects of molecular diffusion in order to model laboratory experiments. The effects of molecular diffusion are modeled by adding a conditional mean scalar drift term and a laminar wake model is used to obtain an analytic expression for the mixing timescale at small times which is subsequently used as part of a general specification of the mixing timescale. Based on this modeling, PDF calculations are performed, and comparison is made primarily with existing experimental and numerical data on single and multiple line sources. A heated mandoline is also considered. This establishes the validity of the proposed model and the significant effect of molecular diffusion on the decay of scalar fluctuations.

Next, various numerical implementations of mixing and molecular transport in LES/PDF studies of turbulent reacting flows are evaluated for accuracy

using the Method of Manufactured Solutions (MMS). Mixing is modeled using the Interaction by Exchange with the Mean (IEM) model and the effects of molecular transport are incorporated as a mean drift term in the mixing step. This methodology avoids spurious production of scalar variance and also allows direct incorporation of differential diffusion effects. The implementation of the mixing model is shown to be successful in capturing the effects of differential diffusion accurately with the additional property of satisfying detailed conservation and realizability of species mass fractions.

Additionally, we present a new variance reduction technique by way of an implicit smoothing methodology. This smoothing scheme is shown to satisfy conservation, boundedness and regularity criteria. Moreover, for an appropriate choice of the smoothing length scale, significant improvements in accuracy can be achieved for an incremental increase in computational cost. Also, it is shown that with smoothing, the bias and statistical errors due to finite number of particles in the Lagrangian Monte Carlo simulations now scale as N_{tot}^{-1} and $N_{tot}^{-1/2}$ respectively, where N_{tot} is the total number of particles in the computational domain.

Finally, the numerical implementations described are applied to the study of a turbulent reacting jet flame (Sandia Flame D). It is shown that this implementation yields a consistent formulation between the LES and the PDF methods. Further, cross-validation is presented as a numerical technique to assist in the automatic choice of the smoothing length scale and the application of cross-validation to smoothing of PDF fields is shown to improve the consistency between the LES and PDF fields.

BIOGRAPHICAL SKETCH

Sharadha Viswanathan was born on the third of October, 1983 in Madurai, India. After her initial schooling, she went on to pursue her undergraduate studies in the Indian Institute of Technology (IIT), Madras, India where she received her Bachelor of Technology degree in Mechanical Engineering in 2005. Subsequently, she enrolled in the doctoral program at Cornell University's Sibley School of Mechanical and Aerospace Engineering in the fall of 2005, to pursue her study in the field of turbulent combustion.

To my family, for everything.

ACKNOWLEDGEMENTS

I would like to take this opportunity to express my humblest appreciation and gratitude towards my advisor and mentor, Professor Stephen B. Pope for teaching me the importance of doing research in a meticulous and rigorous fashion. Through these past few years, I have not only gained knowledge in fluid mechanics, turbulence, combustion and many related disciplines, but have begun to appreciate that even the most complex phenomena are inherently simple. If one is unable to explain something, it is highly possible that we are not asking the right questions. I have also learnt that true greatness comes with humility. I am indebted to Professor Pope for his understanding and support on many an occasion and for giving me this enriching learning opportunity. I would also like to thank Professors David Caughey and John Guckenheimer for their support and inputs through the period of my study here at Cornell and for suggestions on this dissertation.

This work benefits from the work of many of my colleagues here at Cornell. I thank the members of my group – Zhuyin Ren, Liuyan Lu, Steve Lantz, Pavel Popov, David Rowinski, Varun Hiremath and Parvez Sukheswalla – for many insightful conversations. Special thanks to Haifeng Wang for his friendship and innumerable inputs during the course of this work. I would also like to thank the faculty, staff and fellow students at Sibley School for providing me with an amicable environment to pursue my study.

I would like to express my gratitude to my undergraduate mentor, Dr. V. Babu, for his kind words of encouragement. To Baski, for being there always. To my friends – Sowmya, Pavithra, Janani, Awantika and Mekala – for countless cherished memories. I am especially indebted to Pavithra and Venkat

Narayanaswamy for supporting me through tough times.

Finally, I am very grateful to my parents and my brother for their limitless love, support and understanding through this journey and Prasad for his unending love and supreme sacrifice.

TABLE OF CONTENTS

LIST OF TABLES

LIST OF FIGURES

CHAPTER 1

INTRODUCTION

Energy forms the primary lifeline of the economic health of any society. Today, a dominant share of the world's demands for energy comes from liquid fuels, followed by coal and natural gas – for instance, in transportation, power generation, industrial growth, to name a few. With the increase in population around the world accompanied by economic growth, these demands are only expected to increase in the future. The U.S. Government's Energy Information Agency projects that up to 80% of the future energy needs are going to continue to be fueled by non-renewable resources. A sharp increase in the use of renewable resources is expected, albeit from a smaller base.

Given the limited supply of these carbon-based fuels, it is estimated that improving the efficiency of existing systems can curb the energy demand through the next twenty years by around 65%. This means that efficiency is in itself a potential source of energy. In order to build improved and more efficient systems, we require an understanding of the inherent physical processes involved in these systems such as turbulent combustion.

Over the past few decades, significant efforts have been invested in improving our understanding of turbulent combustion. Some of the books [8, 44, 48] are useful powerhouses of information on the subject. Turbulent combustion involves several different species interacting with one another via multiple chemical pathways and with the underlying turbulent flow. Typically, the processes involved in turbulent combustion span across a large range of length scales and time scales, adding further complexity.

Many numerical methods developed based on computational fluid dynamics (CFD) [5] provide varied levels of description to address the turbulent closure problem [8]. The most detailed level of description is provided by a Direct Numerical Simulation (DNS) in which all the scales involved are fully resolved [68] but is computationally prohibitive for high Reynolds numbers turbulent flow calculations. Reynolds Averaged Navier Stokes (RANS) based solvers, on the other hand, resolve the flow on length scales on the order of the integral length scale and provides only a limited description of the flow. A way to enhance the predictive capabilities of these models is to use Large Eddy Simulations (LES) to resolve the large scales and model only the effects of the small scales [47, 59, 67]. With the advancement in high performance computing facilities, LES is becoming more commonplace.

The complexity involved in modeling a turbulent reacting flow is magnified multi-fold due to the large variations in density and non-linear reaction rates. Probability Density Function (PDF) methods [59, 52] have been proven to be effective in addressing most of the closure problems. In a composition-PDF method, the reaction terms appear closed in the PDF transport equation and hence, need no modeling. But the effects due to turbulent transport and molecular diffusion need to be modeled. Typically, a gradient diffusion hypothesis is used to model turbulent transport and mixing models are developed to account for scalar dissipation due to molecular diffusion. And the PDF transport equation is solved using Lagrangian Monte Carlo particle methods [49, 52, 13], in which the turbulent flow is represented by a statistically independent set of notional particles evolving in time governed by modeled Stochastic Differential Equations (SDEs).

Molecular diffusion has a two-fold effect: molecular transport in physical space and mixing in composition space. In most previous studies, molecular transport is modeled as a random walk term in the particle position equation [1]. This modeling strategy has the following drawbacks. First, since the random walk model is based on a single specification of the molecular diffusivity, differential diffusion effects can not be directly incorporated. Secondly, this model gives rise to a spurious production of scalar variance.

In Chapter 2, we study the dispersion from line sources in decaying grid turbulence. These flows pose a significant challenge to statistical models, because the scalar length scale (of the initial plume) is much smaller than the turbulence integral scale. Consequently, this necessitates incorporating the effects of molecular diffusion correctly in order to model laboratory experiments. For this study, we use the Interaction by Exchange with the Conditional Mean (IECM) model for mixing and include the effects of molecular diffusion by adding a conditional mean scalar drift term to the IECM mixing model. This modeling technique is shown to avoid the spurious production of variance by comparing the data from PDF calculations with existing experimental and numerical data on single and multiple line sources. A heated mandoline is also considered. This establishes the validity of the proposed model and the significant effect of molecular diffusion on the decay of scalar fluctuations.

As mentioned previously, with the improvement in computing facilities, LES of turbulent reacting flows are becoming feasible. It is essential to develop models for LES/PDF methods that portray the correct behavior in the DNS limit. McDermott and Pope [37] show that modeling molecular transport as a random walk violates this requirement in the resulting modeled scalar variance

transport equation. Moreover, in a LES study of a laboratory-scale turbulent jet flame (Sandia Flame D), Kemenov and Pope [31] show that molecular diffusivity is dominant in comparison to the subgrid turbulent diffusivity close to the jet exit plane on all reasonably resolved grids. This indicates that the treatment of molecular transport is very significant in LES/PDF modeling of turbulent reacting flows.

Next, Chapter 3 describes various numerical implementations of mixing and molecular transport developed in the context of LES/PDF studies of turbulent reacting flows. These numerical schemes are evaluated for accuracy using the Method of Manufactured Solutions (MMS) and are shown to satisfy conservation and realizability, second-order accuracy and unconditional stability requirements. Mixing is modeled using the Interaction by Exchange with the Mean (IEM) model and the effects of molecular transport are incorporated as a mean drift term in the mixing step. As mentioned in [37], this methodology avoids spurious production of scalar variance and also allows direct incorporation of differential diffusion effects. The algorithm is further tested using a three-species (each with different molecular diffusivity) mixing problem. The implementation of molecular transport and mixing is shown to be successful in capturing the effects of differential diffusion accurately with the additional property of satisfying detailed conservation and realizability of species mass fractions.

In a hybrid particle/mesh method, typically, a small number of particles per cell N_{pc} are used. This gives rise to a deterministic bias error that scales as N_{pc}^{-1} and a random statistical error which scales as $N_{pc}^{-1/2}$. In LES/PDF studies, the various quantities of interest are instantaneous fields and hence, time-averaging

methods [91, 29, 40, 85] are not suitable for variance reduction. Consequently, we present a new variance reduction technique by way of an implicit smoothing methodology. This smoothing scheme is shown to satisfy conservation, boundedness and regularity criteria. Moreover, it is shown that for an appropriate choice of the smoothing length scale, significant improvements in accuracy can be achieved for an incremental increase in computational cost. With smoothing, the bias and statistical errors due to finite number of particles in the Lagrangian Monte Carlo simulations now scale as N_{tot}^{-1} and $N_{tot}^{-1/2}$ respectively, where N_{tot} is the total number of particles in the computational domain.

Finally in Chapter 4, we apply the schemes developed in the earlier chapters to performing a laboratory-scale turbulent jet flame calculation (Sandia Flame D) and show that the described implementations yield consistent LES and PDF formulations. Further, the method of cross-validation is presented to assist in the choice of the "optimal" smoothing length scale with LES/PDF calculations of turbulent reacting flames.

CHAPTER 2

TURBULENT DISPERSION FROM LINE SOURCES IN GRID TURBULENCE*

2.1 Introduction

Turbulent mixing and dispersion of passive scalars is of enormous interest in order to understand various phenomena like combustion and pollutant dispersion and is a well researched area. The earliest theoretical studies of turbulent diffusion were performed by G.I.Taylor [79, 80] in his theory of diffusion by continuous movements for self-preserving turbulence. Following his study, a large number of laboratory wind tunnel measurements of diffusion of heat in the thermal wake behind heated line elements were performed, a few of which can be found in [81, 89].

In particular, Stapountzis *et al* [76] analyzed the structure and development of the heated plume behind a single line source in homogeneous turbulence experimentally and theoretically using displacement statistics between pairs of particles, and they noted that the meandering of the thermal wake is the dominant reason for the thermal fluctuations close to the source. Warhaft [89] performed a detailed study of the wake behind a single line source and proceeded to analyze the interference between pairs of line sources using the inference method elaborated in Warhaft(1981) [88] and also noted that a heated *mandoline* can be obtained by superimposing a number of such line sources.

*S. Viswanathan and S.B. Pope, "Turbulent dispersion from line sources in grid turbulence", Phys. Fluids, **20**(**10**), 101513 (2008)

On the modeling side, for chemically inert flows, probability density function (PDF) methods based on the velocity-scalar joint probability density function [50, 61, 54, 55] have been proposed. PDF methods yield the convection terms in closed form while the conditional acceleration and conditional scalar dissipation need to be modeled. The Langevin equation is one among the many stochastic models proposed as a closure for the conditional acceleration term. In order to close the conditional scalar dissipation term, various mixing models have been proposed. In the context of chemical reactor engineering, the Interaction by Exchange with the Mean (IEM) model was postulated by Villermaux and Devillon [82]. Dopazo and O'Brien introduced an identical model in the context of the composition PDF equation in homogeneous turbulence, but referred to it as the linear mean-square estimation model (LMSE) [18].

These models were originally proposed for statistically homogeneous situations, and for inhomogeneous flows they are implemented so as to be local in physical space. The question of the connection between scalar mixing and velocity arises when the joint velocity-scalar PDF is considered.

Pope [52] analyzed the modeling provided by the Langevin equation for velocity combined with Curl's mixing model [16] for composition. His analysis showed that in isotropic turbulence, the predicted decay rate of the velocity-composition correlation coefficient is substantially larger than that observed experimentally. It was also shown that if the scalar mixing is biased towards fluid having similar velocities, then the decay rate of the scalar flux is reduced to be within the experimental range. A velocity-biased mixing model based on these ideas was developed by Song [75].

Pope [56] observed that the combination of Langevin equation and IEM model implies that there is dissipation of the scalar flux and that this is inconsistent with local isotropy. It was observed that this inconsistency is avoided if, in the IEM model, the mean composition is replaced by its mean conditioned on velocity. Although its name arose later, this results in the IECM mixing model (Eq.(2.1)). In the IECM mixing model, the particle's composition $\phi(t)$ relaxes to the local conditional mean according to

$$\frac{d\phi}{dt} = -\omega_m \left(\phi - \langle \phi \mid \mathbf{u}, \mathbf{x} \rangle\right), \tag{2.1}$$

where ω_m is the mixing rate (the inverse of the mixing time scale, t_m), $\mathbf{u}$ and $\mathbf{x}$ are the particle's velocity and position, and $\langle \phi \mid \mathbf{u}, \mathbf{x} \rangle$ denotes the mean composition at $\mathbf{x}$ conditioned on the velocity being $\mathbf{u}$.

Fox [22] introduced the "velocity-conditioned IEM" (VCIEM) model in which the composition relaxes to

$$\zeta \langle \phi \rangle + (1 - \zeta) \langle \phi \mid \mathbf{u}, \mathbf{x} \rangle, \tag{2.2}$$

for $0 \leq \zeta \leq 1$. For $\zeta = 1$ and $\zeta = 0$, this corresponds to the IEM and the IECM models respectively. The DNS data of Overholt and Pope [43] were used to show that ζ decreases towards zero with increasing Reynolds number, consistent with local isotropy. The vanishing effect of molecular diffusivity on the scalar flux was considered further by Pope [58], and apparently in this paper, the name "IECM - Interaction by exchange with the conditional mean" is introduced.

A decade earlier, Anand and Pope [1] applied a velocity-composition PDF model to the problem of dispersion from a line source in grid turbulence, using

a combination of the Langevin equation and the IEM model. With the standard (unconditional) application of the model, the scalar variance greatly exceeds the observed levels. The model was also applied conditioning the scalar mean on the velocity at the source. Close to the source (i.e., for flight times small compared to the Lagrangian integral time scale) the fluid velocity changes little from the value at the source and hence, this conditional model is very similar to the IECM mixing model (in this region).With the conditional model, Anand and Pope were able to match the scalar variance with the experimental data to within a factor of 2 and also proposed a theory that completely predicts the evolution of the mean scalar profile.

Recently, PDF calculations modeling the dispersion behind single and pairs of line sources in decaying turbulence in conjunction with the IECM mixing model were performed by Sawford [70] by using a mixing rate empirically determined to match the experimental data. In that paper, the velocity conditioned scalar mean for the specific case of line sources is also obtained analytically using the backward diffusion of particles.

Other modeling studies that use the IECM model include the work by Luhar and Sawford [35] where they study the dispersion behind line and point sources in inhomogeneous non-Gaussian turbulence in convective boundary layers using a mixing rate that is fit empirically. Sawford [69] also uses the IECM mixing model with the same mixing rate as in Sawford(2004) [70] to analyze the conditional scalar statistics for a line plume in turbulent channel flow comparing against the DNS data of Brethouwer and Nieuswstadt [7].

In order to use the IECM model for a general flow problem, the mixing rate

has to be specified. It is common practice to model the mixing time scale to be proportional to the turbulence time scale. DNS studies of homogeneous turbulence mixing [43, 21, 30] have shown that the mechanical-to-scalar time scale ratio eventually approaches a constant value independent of initial conditions. This is however found to be at variance with the heated-mandoline experiments of Warhaft and Lumley [90] which do not suggest the relaxation of this ratio to an equilibrium value over a period of one turbulence decay time. Hence, the long-time behavior of the mechanical-to-scalar time scale ratio requires further study.

Due to the disparity in the length scales of the initial plume and the turbulence length scale, meandering of the instantaneous plume and the effects of molecular diffusion (in comparison to turbulent diffusion) are dominant [76, 71, 6, 34] in the early stages of the plume development. Conditioning on velocity largely accounts for the fluctuations arising from meandering close to the source, but fluctuations relative to the conditional mean also develop. The IECM mixing model tends to reduce the fluctuations about the conditional mean without affecting the conditional mean itself.

The effects of molecular diffusion are two-fold : transport of the scalar in physical space and mixing in the scalar space. Conventionally, the molecular transport has been modeled by a random walk in physical space [1, 70] but this results in a spurious production term in the scalar variance transport equation. In the context of Filtered Density Function (FDF) methods, McDermott and Pope [37] model the molecular transport by a mean drift term in the scalar evolution equation and the resulting variance equation does not contain spurious production terms.

In the present work, PDF calculations are performed for single and multiple line sources in decaying grid turbulence using a modified IECM mixing model with the effects of molecular diffusion incorporated directly in the mixing model itself. The results of the calculations are compared with the experimental data of Warhaft [89], Sawford and Tivendale [72] and to the recent calculations of Sawford [70]. An array of line sources is also considered with comparison to the experimental data of Warhaft and Lumley [90]. In this paper, the authors show that the passive scalar variance decay rate is uniquely determined by the wavenumber of the initial scalar fluctuations relative to the turbulence integral length scale.

The rest of the paper is organized as follows. Section §2.2 describes the experimental set-up and relevant parameters. Section §2.3 gives a brief overview of the modeling and analysis behind the present work. The implementation details are covered in section §2.4. Section §2.5 presents the model calculations and results along with appropriate discussions for a single line source, a pair of line sources and an array of line sources. The final Section §2.6 summarizes the important conclusions.

2.2 Experimental details

A sketch of the experimental set-up for a single line source in grid turbulence is shown in Fig. 2.1. The turbulence generating grid is taken to be the origin for the downstream distance, x. The flow is in the x-direction as shown in Fig. 2.1 with a mean speed U. A fine heated wire forming a thermal line source is placed

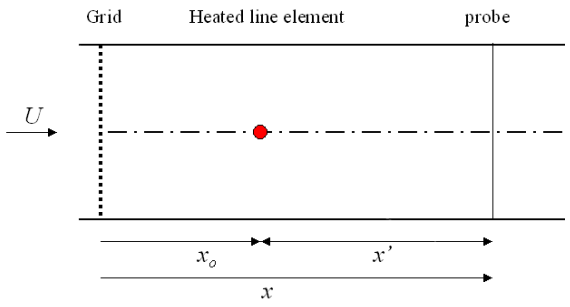

Figure 2.1: Sketch of the experimental set-up showing the wind tunnel. The source (dot) is at a distance x_o from the turbulence generating grid.

normal to the direction of the mean flow at a distance of x_o from the turbulence generating grid. The z-direction is taken parallel to the thermal line source and y is taken to be the third normal direction. The source size is sufficiently small that it does not affect the velocity field and the temperature excess produced by the source heating soon falls to within a few degrees of the mean flow temperature. As a result, the excess temperature is a conserved passive scalar except in the near vicinity of the heated line element. We are interested in understanding the diffusion and mixing of the passive scalar in the wake behind the line source. In particular, we are interested in the scalar mean and variance profiles downstream of the source.

The velocity fluctuations u, v and w are taken to be in the direction of the mean flow, perpendicular to the source and in the direction parallel to the source respectively. The velocity variance decays according to the power law given by

$$\sigma_\alpha^2(x) = \sigma_\alpha^2(M)\left(\frac{x}{M}\right)^{-m}, \tag{2.3}$$

where $\alpha = u, v, w$. The grid mesh spacing is given by M and m is the velocity variance decay exponent. Following Sawford [70], the transverse velocity variance

Table 2.1: Parameters in the laboratory measurements for diffusion behind a single line source in grid turbulence [89]; source diameter, σ_o; mesh spacing, M; position of the source with respect to the grid, x_o/M; mean speed, U; velocity standard deviation at one mesh length from the grid, σ_w, σ_u, σ_v; velocity variance decay exponent, m; molecular diffusivity, κ.

σ_o	1.27×10^{-4}	m
	2.5×10^{-5}	m
M	2.54×10^{-2}	m
x_o/M	20, 52, 60	
U	7	ms^{-1}
σ_w	2.44	ms^{-1}
σ_u, σ_v	2.27	ms^{-1}
m	1.4	
κ	2.1×10^{-5}	m^2s^{-1}

data of Warhaft has been refitted with a decay exponent of $m = 1.4$ to facilitate modeling.

The physical parameters relevant to the laboratory measurements of Warhaft [89] are consolidated in Table 2.1.

2.3 Modeling

2.3.1 Turbulence

In the laboratory frame of reference, the line source is placed at a distance x_o from the turbulence grid. One-point statistics depend solely on x and y and are measured by a stationary probe positioned at various distances downstream of the source. In the reference frame moving with the mean flow, to an excellent approximation, the line source appears as an initial plane area source, and the flow evolves in time. The time t in the moving frame is related to streamwise position x in the laboratory frame by:

$$x(t) = x_o + U\,t. \tag{2.4}$$

Consequently, with the Taylor's hypothesis, only the dispersion perpendicular to this area source is relevant. Thus, in this frame, one-point statistics depend solely on y and t. While the measurements are naturally made in the laboratory frame, it is most convenient to perform the modeling in the moving frame.

For decaying grid turbulence, the rate of decay of the velocity variance (Eq. (2.3)) can be re-expressed as a function of travel time from the source as

$$\sigma_\alpha^2(t) = \sigma_\alpha^2(0)\left(1 + \frac{t}{t_o}\right)^{-m}, \alpha = u, v, w\,, \tag{2.5}$$

where t_o is the flight time to the source from the turbulence generating grid. Using Eq. (2.5), the turbulent kinetic energy $k(t)$ and the turbulent dissipation $\varepsilon(t)$ can therefore be obtained as

$$k(t) = \frac{1}{2}\left(\sigma_u^2(t) + \sigma_v^2(t) + \sigma_w^2(t)\right), \tag{2.6}$$

$$\varepsilon(t) = -\frac{d}{dt}k(t). \tag{2.7}$$

In the Lagrangian PDF modeling framework, the turbulent flow is represented by a large number of particles, all of which are considered to be statistically identical. Each particle carries a set of properties - velocity, $v(t)$; position, $y(t)$; and scalar, $\phi(t)$. Stochastic models are constructed to evolve each of the particle's property in time. The Langevin equation is one of the typical stochastic models used to model the velocity of the particle following the fluid. Conventionally, to model the position, $y(t)$, the evolution equation for fluid particle velocity $dy/dt = v$ is augmented by a random term to account for molecular diffusion. Hence $y(t)$ is a model for the position of a molecule and evolves as

$$dy = v\,dt + \sqrt{2\kappa}\,dW_1, \tag{2.8}$$

where $W_1(t)$ is a Wiener process and κ is the molecular diffusivity. In the present work, the position, $y(t)$ is instead modeled as

$$\frac{dy}{dt} = v, \tag{2.9}$$

and the effects of molecular diffusion are directly incorporated into the mixing model, the details of which are elaborated in Section §2.3.2. While the present model uses Eq. (2.9), the analysis in this section considers both Eqs. (2.8) and (2.9). In both cases the model for $v(t)$ is that for the velocity following a fluid particle (i.e., additional effects due to molecular motion [19] are neglected), and is

$$dv = A(v,t)\,dt + \sqrt{C_0\varepsilon}\,dW = -\left(\frac{1}{2} + \frac{3}{4}C_0\right)\frac{\varepsilon}{k}\,v\,dt + \sqrt{C_0\varepsilon}\,dW, \tag{2.10}$$

where $A(v,t)$ is the drift term and $W(t)$ is a second Wiener process (independent of $W_1(t)$). We use the standard value of 2.1 for C_0, the Langevin equation model constant [59] in all our calculations unless otherwise specified.

Single particle displacement statistics can be used to obtain the mean scalar field. Hence the displacement of a particle from a location at the source at the initial time, defined as $\Delta y(t) = y(t) - y(0)$ can be related to the evolution of the mean scalar profile, which is a Gaussian field with characteristic width, σ_p centered on the plume centerline. Taking into account the effect of the source size σ_o on the evolution of the plume width, σ_p can be written as

$$\sigma_p^2 = \sigma_o^2 + \sigma_y^2, \tag{2.11}$$

where $\sigma_y^2 = \langle \Delta y^2 \rangle$ is the mean-square displacement. Anand and Pope [1] derived σ_y^2 analytically from Eqs. (2.8) and (2.10) to be

$$\sigma_y^2 \;=\; 2\kappa t \;+ \Delta_o^2, \tag{2.12}$$

where the contribution from turbulent dispersion, Δ_o^2 is given by

$$\Delta_o^2 = \; 2\sigma_v^2(t_o) t_o^2 \left[\frac{(1 + t/t_o)^{r-s}}{r(r-s)} + \frac{(1 + t/t_o)^{-s}}{rs} - \frac{1}{s(r-s)} \right], \tag{2.13}$$

with r and s being

$$r = \frac{m}{2}\left(\frac{3}{2}C_0 - 1\right) + 1, \tag{2.14}$$

$$s = \frac{m}{2}\left(\frac{3}{2}C_0 + 1\right) - 1. \tag{2.15}$$

2.3.2 Mixing model

Various mixing models have been proposed [82, 18, 52, 16, 75, 56, 22, 58] as a closure for the conditional scalar dissipation term in the velocity-scalar joint pdf transport equation. The simplest of these is the IEM model [82, 18]. With

the IEM mixing model, the particle's composition $\phi(t)$ relaxes to the local mean as

$$\frac{d\phi}{dt} = -\omega_m \left(\phi - \langle \phi \mid \mathbf{x} \rangle\right), \tag{2.16}$$

where $\mathbf{x}$ is the particle's position, $\langle \phi \mid \mathbf{x} \rangle$ is the mean composition at $\mathbf{x}$, and ω_m is the mixing rate given by

$$\omega_m = \frac{C_\phi \varepsilon}{2k}, \tag{2.17}$$

with $C_\phi \sim 1.2 - 3$ [10]. The IEM model makes an unjustifiable assumption regarding the independence of the scalar mixing term with the velocity field and is inconsistent with local isotropy. On the other hand, conditioning the scalar mean on velocity is consistent with local isotropy and hence corrects the deficiency of the IEM model by performing mixing locally in velocity-physical space (IECM) given by Eq. (2.1).

For a Lagrangian PDF calculation, the Langevin equation coupled with a mixing model comprise a set of stochastic differential equations for velocity, displacement and scalar carried by a particle, from which the transport equation for the Lagrangian joint pdf of velocity and scalar can be derived. The various moment conservation equations can be obtained from the joint pdf transport equation.

2.3.2.1 IECM mixing model

In this sub-section we consider the IECM mixing model as used by Sawford [70] in which the direct effects of molecular diffusivity are modeled by a random walk in position Eq. (2.8). Then in the following sub-section (Sec. §2.3.2.2) we consider the modified IECM model which instead uses Eq. (2.9) and the direct

effects of molecular diffusion are accounted for differently (by Eq. (2.37), below). The analysis shows that the two models yield the same behavior for the mean, $\langle \phi \mid y \rangle$, and the conditional mean, $\langle \phi \mid V, y \rangle$, but a different behavior for the variance,$\langle \phi'^2 \rangle$.

With the IECM mixing model as used by Sawford [70], the transport equation for the joint pdf of velocity, scalar and position, $\tilde{f}(V, \psi, y; t)$ and the joint pdf of velocity and position, $\tilde{g}(V, y; t)$ can be derived from Eqs. (2.1), (2.8) and (2.10), in which the molecular transport is modeled as a random term in the position equation. Here, V and ψ refer to the velocity and scalar sample space variables, respectively. The transport equations for $\tilde{f}$ and $\tilde{g}$ are given by

$$\frac{\partial \tilde{f}}{\partial t} + \frac{\partial V \tilde{f}}{\partial y} + \frac{\partial A(V) \tilde{f}}{\partial V} + \frac{\partial \Phi(V, \psi, y) \tilde{f}}{\partial \psi} = \kappa \frac{\partial^2 \tilde{f}}{\partial y^2} + \frac{1}{2} C_0 \varepsilon(t) \frac{\partial^2 \tilde{f}}{\partial V^2}, \tag{2.18}$$

and

$$\frac{\partial \tilde{g}}{\partial t} + \frac{\partial V \tilde{g}}{\partial y} + \frac{\partial A(V) \tilde{g}}{\partial V} = \kappa \frac{\partial^2 \tilde{g}}{\partial y^2} + \frac{1}{2} C_0 \varepsilon(t) \frac{\partial^2 \tilde{g}}{\partial V^2}, \tag{2.19}$$

where $\Phi(V, \psi, y) = -\omega_m(t) \left(\psi - \langle \phi \mid V, y \rangle\right)$. Note that the coefficients in Eqs. (2.18) and (2.19) depend on time.

From Eq. (2.18), transport equations for the different moments of the scalar can be obtained. In particular, the transport equations for the mean Eq. (2.20) and the mean-square Eq. (2.31) of the scalar are of interest. Multiplying Eq. (2.18) by ψ and integrating over the (ψ, V) sample space, we obtain the transport equation for $\langle \phi \rangle$ to be

$$\frac{\partial \langle \phi \rangle}{\partial t} + \frac{\partial \langle v \phi \rangle}{\partial y} = \kappa \frac{\partial^2 \langle \phi \rangle}{\partial y^2}, \tag{2.20}$$

which is identical to the exact conservation equation. From Eq. (2.20), it is evi-

dent that the IECM mixing model does not affect the mean scalar field as

$$\langle \Phi(\phi) \rangle = \langle \phi - \langle \phi \mid V, y \rangle \rangle = 0. \tag{2.21}$$

Therefore, single particle displacement statistics can be used to obtain the mean scalar field. Hence, the square of the mean plume width σ_p is given by Eq. (2.11) as the sum of σ_o^2 and the particle displacement variance, σ_y^2.

Likewise, the transport equation for the conditional mean, $\tilde{c} = \langle \phi \mid V, y \rangle$ can be obtained from Eqs. (2.18) and (2.19) based on its definition

$$\int_0^\infty \psi \, \tilde{f}(V, \psi, y) \, d\psi = \tilde{c} \, \tilde{g}(V, y), \tag{2.22}$$

as

$$\frac{\partial \tilde{c}}{\partial t} + V \frac{\partial \tilde{c}}{\partial y} + A \frac{\partial \tilde{c}}{\partial V} = \kappa \frac{\partial^2 \tilde{c}}{\partial y^2} + \frac{1}{2} C_0 \varepsilon(t) \frac{\partial^2 \tilde{c}}{\partial V^2} + C_o \varepsilon \frac{\partial \ln \tilde{g}}{\partial V} \frac{\partial c}{\partial V} + \kappa \frac{\partial \ln \tilde{g}}{\partial y} \frac{\partial c}{\partial y}. \tag{2.23}$$

Since the conditional mean is also unaffected by mixing with the IECM model, its transport equation can be obtained from the displacement statistics [70] (in other words, $\tilde{g}$) and the source condition is effected by considering particles that cross the source at the initial time and hence, $\partial g / \partial y$ is non-zero. For the case of a single line source of strength Q in grid turbulence one obtains

$$\langle \phi \mid V, y \rangle = \frac{Q}{\sqrt{2\pi}\tilde{\sigma}} \exp\left[-\frac{1}{2} \left(\frac{y - \tilde{y}}{\tilde{\sigma}} \right)^2 \right], \tag{2.24}$$

where the conditional center $\tilde{y}(V, t)$ is

$$\tilde{y} = \rho_{vy} \, V \, \sigma_y / \sigma_v, \tag{2.25}$$

and the width $\tilde{\sigma}(t)$ is

$$\tilde{\sigma} = \sqrt{\sigma_o^2 + \sigma_y^2 \left(1 - \rho_{vy}^2 \right)}. \tag{2.26}$$

Here $\rho_{vy}(t) = \langle v\Delta y\rangle/\sigma_y\sigma_v$ is defined to be the correlation coefficient between the velocity and displacement from the source and is given by :

$$\rho_{vy} = \frac{1}{\sigma_v\sigma_y}\frac{\sigma_v^2(t_o)t_o}{r}\ \left[(1+t/t_o)^{r-s-1} - (1+t/t_o)^{-s-1}\right]. \tag{2.27}$$

The conditional mean can also be obtained by solving Eq. (2.23) with the appropriate initial condition on $\tilde{c}$. In this case, all particles that are initially distributed in the physical domain are considered and $\partial g/\partial y$ becomes zero. It has been verified that, consistently, this procedure also yields the solution Eq. (2.24).

With $\phi^{'}$ being the fluctuation in ϕ about its mean, the transport equation for the scalar flux $\langle v\phi^{'}\rangle$ can be obtained from Eq. (2.18) by multiplying by $V\psi$ and integrating:

$$\frac{\partial}{\partial t}\langle v\phi^{'}\rangle + \frac{\partial}{\partial y}\langle v^2\phi\rangle = \langle A\phi\rangle + \langle v\Phi\rangle + \kappa\frac{\partial^2}{\partial y^2}\langle v\phi^{'}\rangle. \tag{2.28}$$

A consequence of local isotropy of the velocity and scalar fields is that $\langle v\Phi\rangle$ is zero. For the IEM model we obtain instead

$$\langle v\Phi\rangle = -\omega_m\langle v\ (\phi - \langle\phi\rangle)\rangle = -\omega_m\langle v\phi^{'}\rangle \neq 0, \tag{2.29}$$

while with the IECM model the contribution from the mixing term is

$$\langle v\Phi\rangle = -\omega_m\langle v\ (\phi - \langle\phi \mid v\rangle)\rangle = 0. \tag{2.30}$$

Similarly, the transport equation for the mean-square of the scalar can be obtained by multiplying the joint pdf transport equation, Eq. (2.18), by ψ^2 and integrating over the entire (ψ, V) sample space, which yields

$$\frac{\partial\langle\phi^2\rangle}{\partial t} + \frac{\partial\langle v\phi^2\rangle}{\partial y} = \kappa\frac{\partial^2\langle\phi^2\rangle}{\partial y^2} - 2\omega_m\Theta, \tag{2.31}$$

where Θ is defined by Eq. (2.33). The modeled scalar variance transport equation can be obtained from Eqs. (2.20) and (2.31) as

$$\frac{\partial\langle\phi^{'2}\rangle}{\partial t} + 2\langle v\phi^{'}\rangle\frac{\partial\langle\phi\rangle}{\partial y} + \frac{\partial\langle v\phi^{'2}\rangle}{\partial y} = \kappa\frac{\partial^2\langle\phi^{'2}\rangle}{\partial y^2} + 2\kappa\left(\frac{\partial\langle\phi\rangle}{\partial y}\right)^2 - 2\omega_m\Theta, \tag{2.32}$$

where evidently

$$2\omega_m\Theta = 2\omega_m\left(\langle\phi^2\rangle - \langle\tilde{c}^2\rangle\right), \tag{2.33}$$

is the scalar variance dissipation according to the IECM model. Comparing the IECM model scalar variance transport equation given by Eq. (2.32) against the exact scalar variance transport equation

$$\frac{\partial\langle\phi^{'2}\rangle}{\partial t} + 2\langle v\phi^{'}\rangle\frac{\partial\langle\phi\rangle}{\partial y} + \frac{\partial\langle v\phi^{'2}\rangle}{\partial y} = \kappa\frac{\partial^2\langle\phi^{'2}\rangle}{\partial y^2} - 2\kappa\langle\frac{\partial\phi^{'}}{\partial x_i}\frac{\partial\phi^{'}}{\partial x_i}\rangle, \tag{2.34}$$

it is apparent that the modeled scalar variance transport equation gives rise to a spurious production term $\mathcal{P}$ given by

$$\mathcal{P} = 2\kappa\left(\frac{\partial\langle\phi\rangle}{\partial y}\right)^2. \tag{2.35}$$

2.3.2.2 Modified IECM mixing model

In order to eliminate the spurious production term in the scalar variance transport equation, in the present model, diffusion is removed from the position equation (i.e., Eq. (2.9) is used in place of Eq. (2.8)), and the effects of molecular diffusion are directly incorporated into the mixing model along lines similar to McDermott and Pope [37]. The molecular diffusion is modeled into the IECM mixing model by the addition of a conditional mean scalar drift term, $H(\mathbf{u},\mathbf{x})$ defined as

$$H(\mathbf{u},\mathbf{x}) = \kappa\ \nabla^2\langle\phi\mid\mathbf{u},\mathbf{x}\rangle, \tag{2.36}$$

to obtain the modified IECM mixing model

$$\frac{d\phi}{dt} = H(\mathbf{u}, \mathbf{x}) - \omega_m \left(\phi - \langle \phi \mid \mathbf{u}, \mathbf{x} \rangle\right). \tag{2.37}$$

The transport equations for the joint pdf of position, velocity and scalar, $f(V, \psi, y; t)$, and the joint pdf of position and velocity, $g(V, y; t)$, can be derived from Eqs. (2.9), (2.10) and (2.37) as

$$\frac{\partial f}{\partial t} + \frac{\partial V f}{\partial y} + \frac{\partial A(V) f}{\partial V} + \frac{\partial H(V, y) f}{\partial \psi} + \frac{\partial \Phi(V, y, \psi) f}{\partial \psi} = \frac{1}{2} C_0 \varepsilon(t) \frac{\partial^2 f}{\partial V^2}, \tag{2.38}$$

and

$$\frac{\partial g}{\partial t} + \frac{\partial V g}{\partial y} + \frac{\partial A(V) g}{\partial V} = \frac{1}{2} C_0 \varepsilon(t) \frac{\partial^2 g}{\partial V^2}, \tag{2.39}$$

respectively. Note that we distinguish between the PDFs f and g according to the modified IECM model, and the corresponding PDFs $\tilde{f}$ and $\tilde{g}$ according to the original IECM model. The evolution equation for f Eq. (2.38) contains the term in H, which is absent from Eq. (2.18) for $\tilde{f}$; whereas Eq. (2.19) for $\tilde{g}$ contains the term in κ which is absent from Eq. (2.39) for g.

It is important to observe that the evolution equations for the mean, $\langle \phi \rangle$ and the scalar flux, $\langle v\phi' \rangle$ derived from Eqs. (2.38) and (2.39) agree with Eqs. (2.20) and (2.28), respectively, and so the two model variants yield identical fields of $\langle \phi \rangle$ and $\langle v\phi' \rangle$.

The scalar variance transport equation derived from Eqs. (2.38) and (2.39) contains no production terms and can be written as

$$\frac{\partial \langle \phi'^2 \rangle}{\partial t} + 2\langle v\phi' \rangle \frac{\partial \langle \phi \rangle}{\partial y} + \frac{\partial \langle v\phi'^2 \rangle}{\partial y} = 2\kappa \left[\langle c \frac{\partial^2 c}{\partial y^2} \rangle - \langle \phi \rangle \frac{\partial^2 \langle \phi \rangle}{\partial y^2} \right] - 2\omega_m \left[\langle \phi^2 \rangle - \langle c^2 \rangle \right], \tag{2.40}$$

where $c = \langle \phi \mid V, y \rangle$ is the conditional scalar mean. (Note that we distinguish between the conditional means $\tilde{c}$ and c given by the two model variants.)

The transport equation for the conditional scalar mean can be obtained from Eqs. (2.38) and (2.39) as

$$\frac{\partial c}{\partial t} + \frac{\partial Vc}{\partial y} + A\frac{\partial c}{\partial V} = \kappa\frac{\partial^2 c}{\partial y^2} + \frac{1}{2}C_0\varepsilon(t)\frac{\partial^2 c}{\partial V^2} + C_o\varepsilon\frac{\partial ln\, g}{\partial V}\frac{\partial c}{\partial V}. \tag{2.41}$$

Comparing Eq. (2.41) with Eq. (2.23), we observe that Eq. (2.41) is of the same form as Eq. (2.23) except for the omission of the term in $\partial \ln \tilde{g}/\partial \tilde{g}$. The modified IECM mixing model affects the evolution of the conditional mean through the term $\kappa\partial^2 c/\partial y^2$, and therefore displacement statistics cannot be used to obtain the conditional mean analytically. Since Eq. (2.41) is linear in c, it admits a Gaussian solution with an initial condition, $c = \langle\phi\rangle_{t=0}$ and can be solved for. On the other hand, for the line source, the source condition is effected by the initial condition on the conditional mean and hence, the term $\partial g/\partial y$ becomes zero reducing Eq. (2.23) to Eq. (2.41), implying that $\tilde{c} = c$ for identical initial conditions.

In summary, the two variants of the IECM model lead to identical results for the mean $\langle\phi\rangle$, the conditional mean $\langle\phi \mid V, y\rangle$, and the scalar flux $\langle v\phi'\rangle$. However, the variance $\langle\phi'^2\rangle$ evolves differently (as revealed by the right-hand sides of Eqs. (2.32) and (2.40)). Most importantly, the modified IECM model avoids the spurious production term $\mathcal{P}$.

2.3.3 Laminar Thermal Wake Modeling

There are three relevant length scales in the passive scalar diffusion behind a line source: the instantaneous plume width, σ_p; the Kolmogorov length scale, η; and the turbulence integral length scale, L. The relative magnitudes of the three length scales are summarized in Table 2.2. The source is sufficiently small

Table 2.2: Characteristics of the velocity field corresponding to the parameters in Table 2.1; source size, σ_o; source position relative to grid, x_o/M; Kolmogorov length scale, η; turbulence length scale, L; Integral scale Reynolds number at the source, $Re_L = k_o^2/\varepsilon_o^2\nu$; Taylor scale Reynolds number, $R_\lambda = \sqrt{20/3\, Re_L}$.

σ_o	1.27×10^{-4}	2.5×10^{-5}		(m)
x_o/M	20	52	60	
η	1.99×10^{-4}	3.53×10^{-4}	3.84×10^{-4}	(m)
L	1.02×10^{-2}	1.35×10^{-2}	1.43×10^{-2}	(m)
Re_L	431	294	278	
R_λ	54	44	43	

so as not to affect the underlying velocity field, and it is comparable to the Kolmogorov length scale at the source location. For such small sources with $\sigma_o/L \ll 1$, one of the dominating factors that influence the evolution of the scalar variance in the vicinity of the source is the molecular diffusivity [71]. In addition to the direct effect of molecular processes, the instantaneous plume is affected by the velocity at the source at the initial time [1].

Very close to the source, the scalar field can therefore be locally modeled as evolving due to molecular diffusion in a constant and uniform velocity field, given by the velocity at the source at the initial time, v_o. The instantaneous scalar field can thus be modeled as a Gaussian of width $\sqrt{\sigma_o^2 + 2\kappa t}$ convected by a distance $v_o t$. As a consequence, for a fluid particle with position $y(t)$ and velocity $v(t)$, the scalar carried by the particle is (according to this model at early time) given by

$$\phi(y, v; t) = \frac{Q}{\sqrt{2\pi}\bar{\sigma}} \exp\left[-\frac{1}{2}\left(\frac{y - vt}{\bar{\sigma}}\right)^2\right], \tag{2.42}$$

where the thermal wake thickness $\bar{\sigma}(t)$ is

$$\bar{\sigma} = \sqrt{\sigma_o^2 + 2\kappa t}. \tag{2.43}$$

Thus, the effects of both the molecular diffusion (on the plume width) and the randomness in v_o (on the plume meandering) are accounted for. To evaluate the correctness of the model, the centerline intensity of fluctuations $i(0,t) = \langle \phi'^2 \rangle_{y=0}^{1/2} / \langle \phi \rangle_{y=0}$ is compared to the experimental data and model calculations by Sawford [70] in Fig. 2.2. Including the effects of molecular diffusion in modeling the plume as a laminar thermal wake close to the source gives good agreement with the other two data sets in the initial stages of the plume development. But as may be seen, ignoring molecular diffusion grossly over predicts the scalar variance. From Fig. 2.2, it can also be inferred that, as expected, this model is valid only in the initial stages of the plume development when the ratio of turbulence integral length scale to the plume width is much larger than one.

2.3.4 Mixing rate

In Section §2.3.4.1, the mixing rate ω_m for the IECM model valid at small times is obtained using the laminar wake modeling approach. At large times, the mixing rate is taken to be the standard model Eq. (2.17). Such a specification for the IECM model is compared to the mixing rate used by Sawford [70]. Section §2.3.4.2 derives the mixing rate for the modified IECM mixing model along lines similar to Sec. §2.3.4.1, imposing conditions of realizability and boundedness.

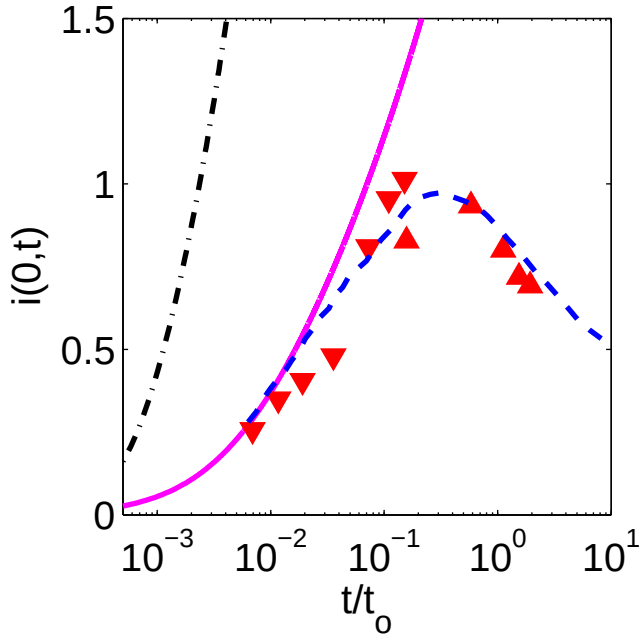

Figure 2.2: Comparison of the centreline intensity of fluctuations obtained using the laminar thermal wake model: $\kappa = 0$ (dot-dashed line); $\kappa = 2.1 \times 10^{-5}\, m^2 s^{-1}$ (solid line); Warhaft data ▼ ; Warhaft data $\sigma_o = 1.27 \times 10^{-4}\, m$ ▲ ; Sawford's model calculations (dashed line) - plotted against flight time from the source, for source position $x_o/M = 52$ and source size $\sigma_o = 2.5 \times 10^{-5}\, m$.

2.3.4.1 IECM model

By definition, the IECM model Eq. (2.1) acts to reduce the fluctuations of the scalar about its conditional mean at a rate given by the mixing rate ω_m (which is the inverse of the mixing time scale). The model has no effect on the scalar mean. Molecular diffusion on the other hand has a direct effect on the scalar mean.

With C_ϕ (in Eq. (2.17)) defined to be a constant, the mixing time scale is proportional to the turbulence time scale for all times during all stages of the plume development. As a consequence, the IECM model (with constant C_ϕ) does not

predict the correct evolution of the scalar variance due to the spurious production term in the scalar variance transport equation.

In order to match the laboratory measurements, Sawford(2004) [70] used experimental data to obtain an empirically fit time scale of the form

$$\frac{t_m}{t_o} = (\omega_m\, t_o)^{-1} = 0.6\frac{t}{t_o}\left[1 + \tanh\left(\frac{\ln(t/t_o) + 2.3}{0.9}\right)\right]. \tag{2.44}$$

We now develop an alternative specification of the mixing rate which is based on an analytic expression for ω_m at small times, obtained from the laminar thermal wake model. Close to the source, the transport equation for the mean-square of the scalar Eq. (2.31) can be integrated over y to give the transport equation for the integral mean-square of the scalar as

$$\int_{-\infty}^{\infty} \frac{\partial\langle\phi^2\rangle}{\partial t}\, dy = -2\,\omega_m \int_{-\infty}^{\infty}\langle\phi^2\rangle\, dy \;+ 2\,\omega_m \int_{-\infty}^{\infty}\int_{-\infty}^{\infty}\langle\phi \mid V, y\rangle^2\, f_v(V)\, dV\, dy. \tag{2.45}$$

At early times, various moments of the scalar can be obtained from Eq. (2.42) using the laminar thermal wake modeling approach described in the previous section and hence the mixing rate close to the source ω_m^0 is obtained as

$$(\omega_m^0)^{-1} = 2\frac{\bar{\sigma}^3}{\kappa}\left[\frac{1}{\bar{\sigma}} - \frac{1}{\sqrt{\sigma_o^2 + \sigma_y^2(1-\rho_{vy}^2)}}\right]. \tag{2.46}$$

Let T denote the turbulence time scale $T = k/\varepsilon$ and L the length scale $L = k^{3/2}/\varepsilon$. At the source location, $T_o \equiv T(t = 0)$ is simply related to the flight time to the source, t_o as $T_o = t_o/m$. The integral length scale at the source, L_o can be obtained as $k_o^{3/2}/\varepsilon_o$ where k_o and ε_o refer to the turbulent kinetic energy and dissipation at the source location respectively. For $t/T_o \ll 1$, Eq. (2.46) can be simplified to

$$\omega_m^0(t)\, T_o \approx \frac{m\kappa}{2\sigma_{v_o}^2 T_o}\left(\frac{T_o}{t}\right)^3. \tag{2.47}$$

The above analysis deduces the appropriate mixing rate $\omega_m^0(t)$ at very early times; whereas the appropriate rate $\omega_m^\infty(t)$ at late times is taken from the standard model Eq. (2.17). Thus, for $t/T_o \gg 1$ we obtain

$$\omega_m^\infty(t)\, T_o = \frac{C_\phi \varepsilon}{2k} = \frac{C_\phi}{2}\left(1 + \frac{t}{mT_o}\right)^{-1} \approx \frac{C_\phi}{2}\frac{T_o}{t}. \tag{2.48}$$

The specification for the mixing rate (for all times)

$$\omega_m(t) = \omega_m^0(t) + \omega_m^\infty(t), \tag{2.49}$$

given in non-dimensional form as

$$\omega_m(t)\, T_o = \frac{m\kappa}{2\sigma_{v_o}^2 T_o}\left(\frac{T_o}{t}\right)^3 + \frac{C_\phi}{2}\left(\frac{T_o}{t}\right), \tag{2.50}$$

i.e., the sum of the rates given by Eqs. (2.47) and (2.48), is comparable to Eq. (2.44) both near to and far from the source.

2.3.4.2 Modified IECM model

As was done in Section §2.3.4.1, an analytic expression for the mixing rate, ω_m^0 at small times, $t/T_o \ll 1$ can be obtained by conserving the integral of the modeled scalar variance transport equation Eq. (2.40) using the laminar thermal wake model. This approach yields ω_m^0 to be

$$\omega_m^0 \approx \frac{3\kappa}{2\sigma_o^2}. \tag{2.51}$$

But at large times $t/T_o \gg 1$, ω_m is taken to be ω_m^∞. Since the two relevant timescales in the passive scalar diffusion from a line source at the source location are the scalar timescale at the source, τ_κ defined as

$$\tau_\kappa = \frac{\sigma_o^2}{\kappa}, \tag{2.52}$$

and the turbulence timescale at the source, T_o, their ratio, γ can be defined as

$$\gamma \equiv \frac{\tau_\kappa}{T_o}. \tag{2.53}$$

From Eqs. (2.48) and (2.51), the mixing rate that is valid for all times can be specified as

$$\frac{1}{\omega_m(t)} = t_m(t) = \frac{2}{3}\tau_\kappa + (T(t) - T_o)\frac{2}{C_\phi}, \tag{2.54}$$

and in non-dimensional form as

$$\frac{1}{\omega_m T_o} = \frac{t_m}{T_o} = \frac{2}{3}\gamma + \left(\frac{T}{T_o} - 1\right)\frac{2}{C_\phi}. \tag{2.55}$$

In order for the modified IECM mixing model Eq. (2.37) to satisfy realizability and boundedness constraints on the scalar, the mixing rate ω_m should be such that $\omega_m \geq \omega_m^{min}$ where

$$\omega_m^{min} = \frac{\kappa}{\tilde{\sigma}^2}, \tag{2.56}$$

and the specification of the mixing rate Eq. (2.55) satisfies realizability and boundedness for $\gamma < 1$. All the calculations reported are performed with the mixing rate specification given using Eq. (2.55). The only adjustable parameter that Eq. (2.55) is dependent on is the model constant, C_ϕ.

Fig. 2.3 compares the different definitions of the mixing rates given by Eqs. (2.44), (2.48) , (2.50) and (2.55). By construction, the specified mixing rates Eqs. (2.50) and (2.55) smoothly blend into the large time asymptote Eq. (2.48) and with Eq. (2.44) for $t/T_o \gg 1$. There is no agreement between Eq. (2.44) and Eq. (2.50) for $t/T_o \ll 1$ because Eq. (2.47) is based on the laminar thermal wake modeling while Eq. (2.44) is empirically fit to match the wind tunnel laboratory data. Also, Eq. (2.55) is derived for an entirely different mixing model.

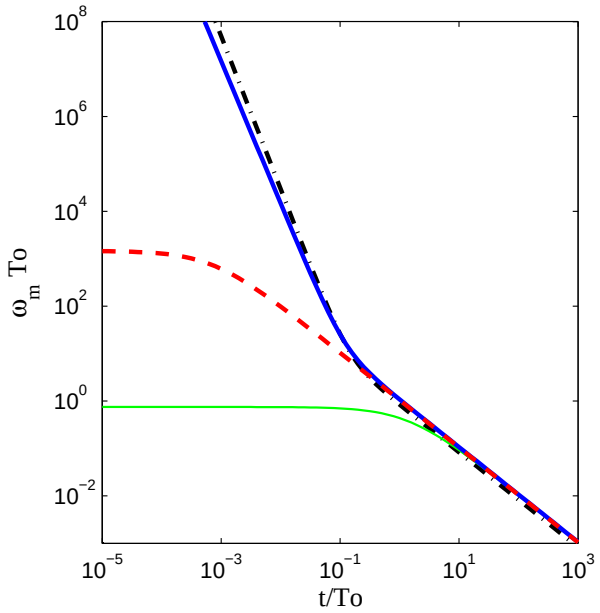

Figure 2.3: Comparison of mixing rate definitions with flight time from the source: Modified mixing model, $\omega_m T_o$ (dashed line); IECM model $\omega_m T_o$ (thick solid line); $\omega_m^\infty T_o$ (thin solid line); Sawford's empirical mixing rate (dot dashed line) .

2.3.5 Summary of the model

In summary, the modified IECM mixing model, which is used to obtain the results presented in the following sections, consists of Eqs. (2.9), (2.10), (2.37) and (2.54) (or equivalently Eq. (2.55) given in non-dimensional form). Unless otherwise stated, the model coefficients take the values $C_0 = 2.1$ and $C_\phi = 1.5$.

2.4 Implementation

We represent the flow by an ensemble of $N = 10,000$ particles, which at time t have properties $y(t)$, $v(t)$ and $\phi(t)$. Initially, the solution domain extends be-

tween $\pm\Delta_y(0)$, where $\Delta_y(0) = 10\,\sigma_o$. The particles are uniformly distributed in the solution domain and are initialized with a Gaussian velocity distribution $\mathcal{N}(0, \sigma_v^2(0))$. The particles' scalar values are initialized to the mean scalar field (which is a Gaussian with characteristic width σ_o).

The particle properties are advanced in time by a first-order explicit Euler scheme with variable time-stepping, the time-step Δt being defined as one-thousandth of the mixing time scale, $t_m = 1/\omega_m$, where ω_m is given by Eq. (2.54). For the line source, the modified IECM mixing model Eq. (2.37) reduces to

$$\frac{d\phi}{dt} = \kappa \frac{\partial^2 c}{\partial y^2} - \omega_m \left(\phi - c\right), \tag{2.57}$$

where c is the conditional scalar mean and is known analytically Eq. (2.24). If the conditional scalar mean is approximated as being a constant across the time-step, then, given $\phi(t)$, $\phi(t + \Delta t)$ is known analytically as the solution to Eq. (2.57):

$$\phi(t + \Delta t) = \phi(t) \exp\left(-\omega_m \Delta t\right) + \Pi(t) \left[1 - \exp\left(-\omega_m \Delta t\right)\right], \tag{2.58}$$

where

$$\Pi(t) = c \left[\frac{\kappa}{\tilde{\sigma}^2(t)\omega_m} \left(\left(\frac{y(t) - \tilde{y}(t)}{\tilde{\sigma}(t)}\right)^2 - 1\right) + 1\right], \tag{2.59}$$

and $\tilde{y}$ and $\tilde{\sigma}$ are given by Eqs. (2.25) and (2.26) respectively. The particle's scalar can be therefore be advanced in time.

The width of the thermal wake is determined from Eqs. (2.11) and (2.12) at the beginning of every time-step. When the width of the thermal wake, σ_p, exceeds a quarter of the current domain half-width, $\Delta_y(t)$, the solution domain is expanded as follows. The size of solution domain is doubled. An additional N particles are temporarily introduced into the expanded domain such that the resulting particle distribution is uniform in physical space. Since the

computational cost scales linearly with the number of particles for a given time-step, to keep the computational cost constant, only every alternate particle of the $2N$ particles is retained in the newly expanded domain. In additional to cost-control, this procedure also ensures that the thermal wake is well resolved within the solution domain. For the time period of the simulation, there are a significant number of particles per unit turbulence integral scale, and hence only the resolution of the thermal wake is of concern. Reflective boundary conditions are applied at the domain boundaries.

Figure 2.4 plots the normalized width of the mean scalar profile (obtained using a Quantile-Quantile plot of particle position compared to an error function) against normalized flight time from the source. The good agreement between the theoretical prediction [1] given by Eqs. (2.11) and (2.12) and model calculations using the modified IECM model verifies the numeric of the calculations - at least for the scalar mean.

The radial profiles of various statistics (shown in the later sections) used to compare the present model calculations with the experimental data are obtained by binning the particles in physical space, in bins of size approximately half of σ_p. Small bins give rise to larger statistical errors while large bins smear out the gradients. This smearing probably explains the small discrepancies between the model calculations and experimental data in regions with steeper gradients (shown in the later sections). Various statistics are obtained by averaging over 20 independent simulations.

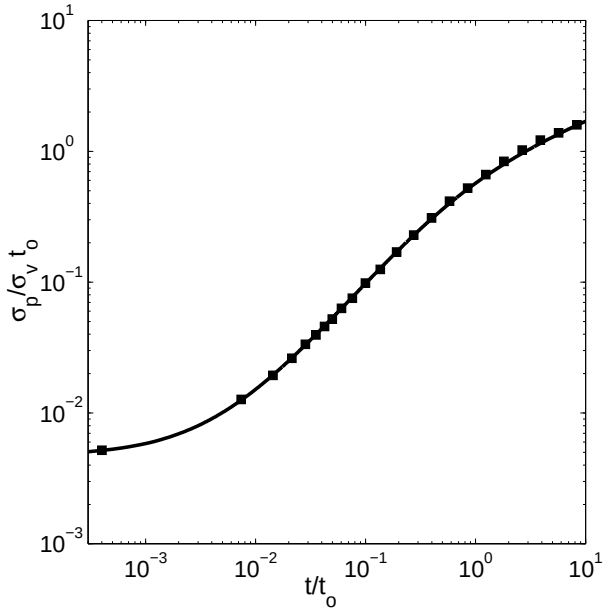

Figure 2.4: Width of the mean scalar profile normalized by the turbulence length scale at the source against normalized flight time from the source for source position $x_o/M = 52$; σ_p from Eq. (2.11) (solid line); σ_p from present model calculations ■.

2.5 Results and Discussion

2.5.1 A single line source

Detailed PDF calculations have been performed with the modified IECM model using the mixing rate given by Eq. (2.55), and the results are compared to the experimental data of Warhaft [89] and the previous calculations of Sawford [70]. Higher-order scalar moments namely skewness and kurtosis are also compared against the experimental data of Sawford and Tivendale [72].

Figure 2.5 plots the centerline intensity of fluctuations, $i(0,t) = \langle \phi'^2 \rangle_{y=0}^{1/2} / \langle \phi \rangle_{y=0}$, against flight time from the source for various source conditions as detailed on

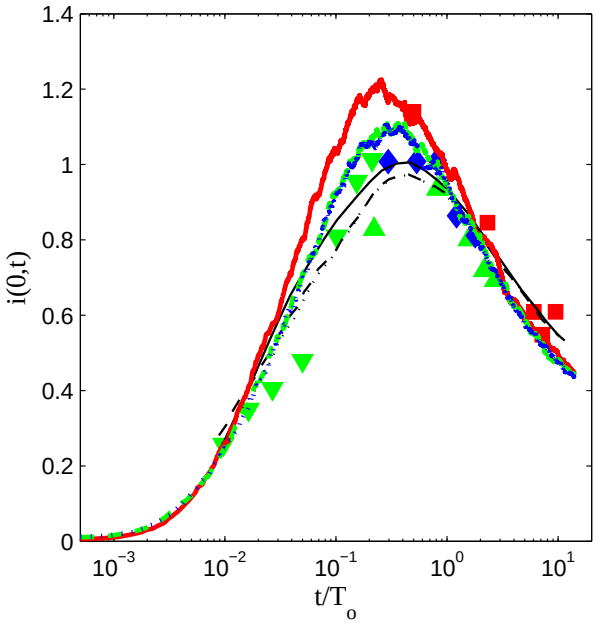

Figure 2.5: Comparison of the centreline intensity of fluctuations, $i(0,t)$ plotted against flight time from the source: Warhaft data $x_o/M = 20,\ \sigma_o = 1.27\times10^{-4}\,m$ ■, $x_o/M = 52,\ \sigma_o = 2.5\times10^{-5}\,m$ ▼, $x_o/M = 52,\ \sigma_o = 1.27\times10^{-4}\,m$ ▲, $x_o/M = 60,\ \sigma_o = 1.27\times10^{-4}\,m$ ◆ ; Sawford's calculations using the mixing rate given by Eq. (2.44) $x_o/M = 20,\ \sigma_o = 1.27\times10^{-4}\,m$ (thin solid line), $x_o/M = 52,\ \sigma_o = 1.27\times10^{-4}\,m$ (thin dashed line); Present calculations $x_o/M = 20,\ \sigma_o = 1.27\times10^{-4}\,m$ (thick solid line), $x_o/M = 52,\ \sigma_o = 1.27\times10^{-4}\,m$ (thick dashed line), $x_o/M = 60,\ \sigma_o = 1.27\times10^{-4}\,m$ (dotted line).

the figure. The experiments are performed with two source sizes. The larger source is used when measurements are taken at distances far away from the source for $x_o/M = 20$ so that the measurements are not corrupted by background noise. Since the model calculations are oblivious to such effects, only one source size is used. The centerline intensity of fluctuations agree well with the experimental data and with the previous model calculations of Sawford [70] throughout the development of the plume. Contrasting this against Fig. 2.6 in which the IECM model with Eq. (2.17) is used and molecular diffusion is ne-

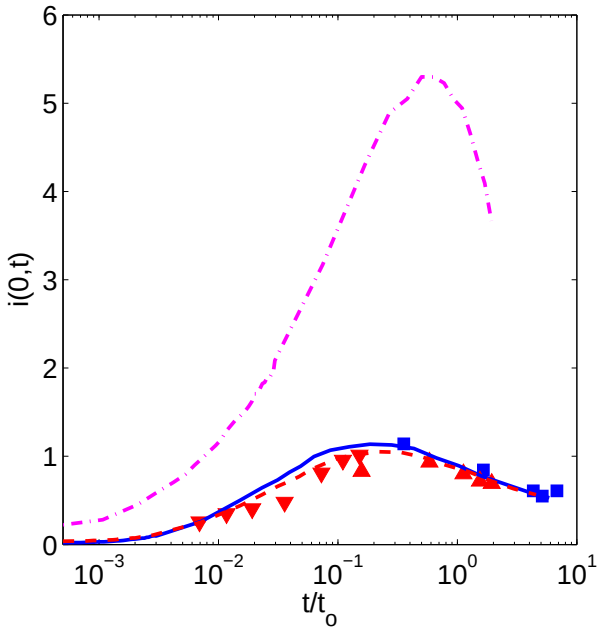

Figure 2.6: Comparison of IECM model calculations with the mixing rate given by Eq. (2.17) with the model calculations done with Eq. (2.50) showing the centreline intensity of fluctuations, $i(0,t)$ against flight time from the source : IECM model calculations using mixing rate given by Eq. (2.17) $x_o/M = 52$, $\sigma_o = 1.27 \times 10^{-4}\, m$ (thick dot dashed line); Warhaft data $x_o/M = 20$, $\sigma_o = 1.27 \times 10^{-4}\, m$ ■, $x_o/M = 52$, $\sigma_o = 2.5 \times 10^{-5}\, m$ ▼, $x_o/M = 52$, $\sigma_o = 1.27 \times 10^{-4}\, m$ ▲; Present calculations $x_o/M = 20$, $\sigma_o = 1.27 \times 10^{-4}\, m$ (thick solid line), $x_o/M = 52$, $\sigma_o = 1.27 \times 10^{-4}\, m$ (thick dashed line).

glected in the scalar evolution equation, we see that molecular diffusion effects are significant in the correct estimation of the evolution of the scalar variance in both near-field and far-field stages of the plume development.

Radial profiles of the normalized *r.m.s.* scalar at four distinct stages of the plume development are plotted in Fig. 2.7 and the integral measure of the variance, $I = \int \langle \phi'^2 \rangle \, dy$ normalized by $2\pi L_o/Q^2$ is plotted in Fig. 2.8. The present calculations are successful in predicting both the shape of the profiles and also

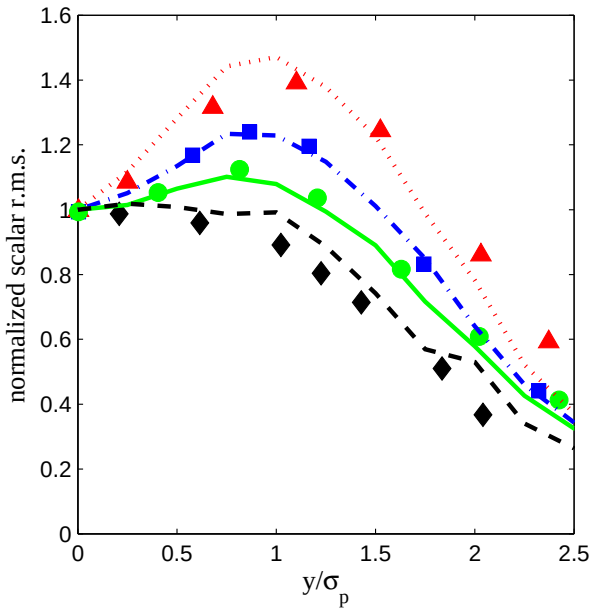

Figure 2.7: Radial profiles of *r.m.s.* scalar normalized by its centerline value at $x_o/M = 52$: Warhaft data $t/t_o = 0.007$ ▲, $t/t_o = 0.012$ ■, $t/t_o = 0.019$ ●, $t/t_o = 1.93$ ◆; Present calculations $t/t_o = 0.007$ (dotted line), $t/t_o = 0.012$ (dot dashed line), $t/t_o = 0.019$ (solid line), $t/t_o = 1.93$ (dashed line).

the locations of the extrema at various time instants in the development of the thermal wake and there is good agreement with the experimental data.

It is also of significant interest to study the model predictions of the higher-order scalar moments especially skewness and kurtosis. Experimental data from Sawford and Tivendale [72] and previous IECM model calculations from Sawford [70] are used to compare with the model predictions. Figure 2.9 plots the the centerline values of skewness, S and kurtosis, K against flight time from the source while Fig. 2.10 compares the radial profiles of the skewness and kurtosis measurements made at three different times, $t/T_o = 0.0014, 0.22, 7.2$ with the experimental data. Even though the centerline values of the moments are not in perfect agreement with the data for all times, the radial profiles match the

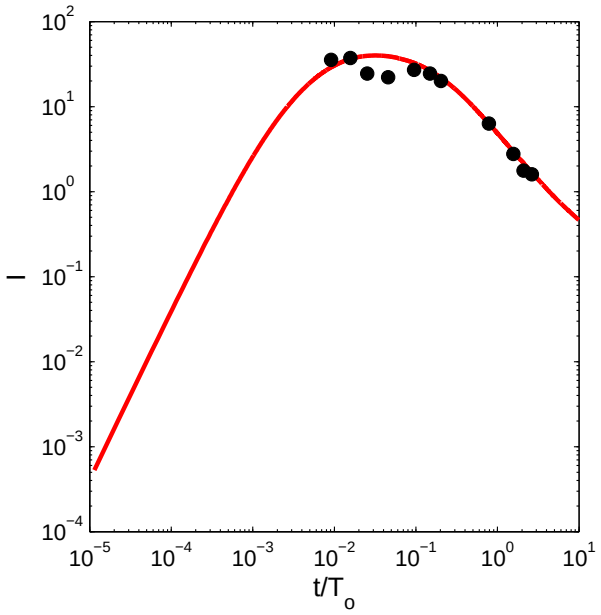

Figure 2.8: Integral measure of the scalar variance, I in non-dimensional form against flight time from the source : Present calculations (solid line); Warhaft data ●; The source of size $\sigma_o = 1.27\times10^{-4}\,m$ is at $x_o/M = 52$.

experimental observations well. However, the centerline predictions are more accurate than the previous model calculations.

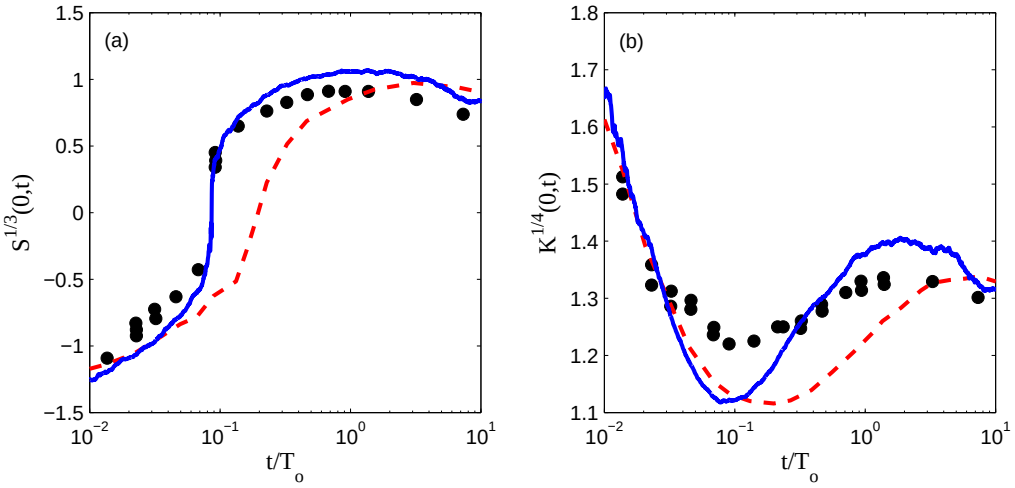

Figure 2.9: Higher moments on the centerline against flight time from the source : Present calculations (solid line); Sawford IECM calculations (Dashed line); Sawford and Tivendale data ●; (a) Skewness, S ; (b) Kurtosis, K.

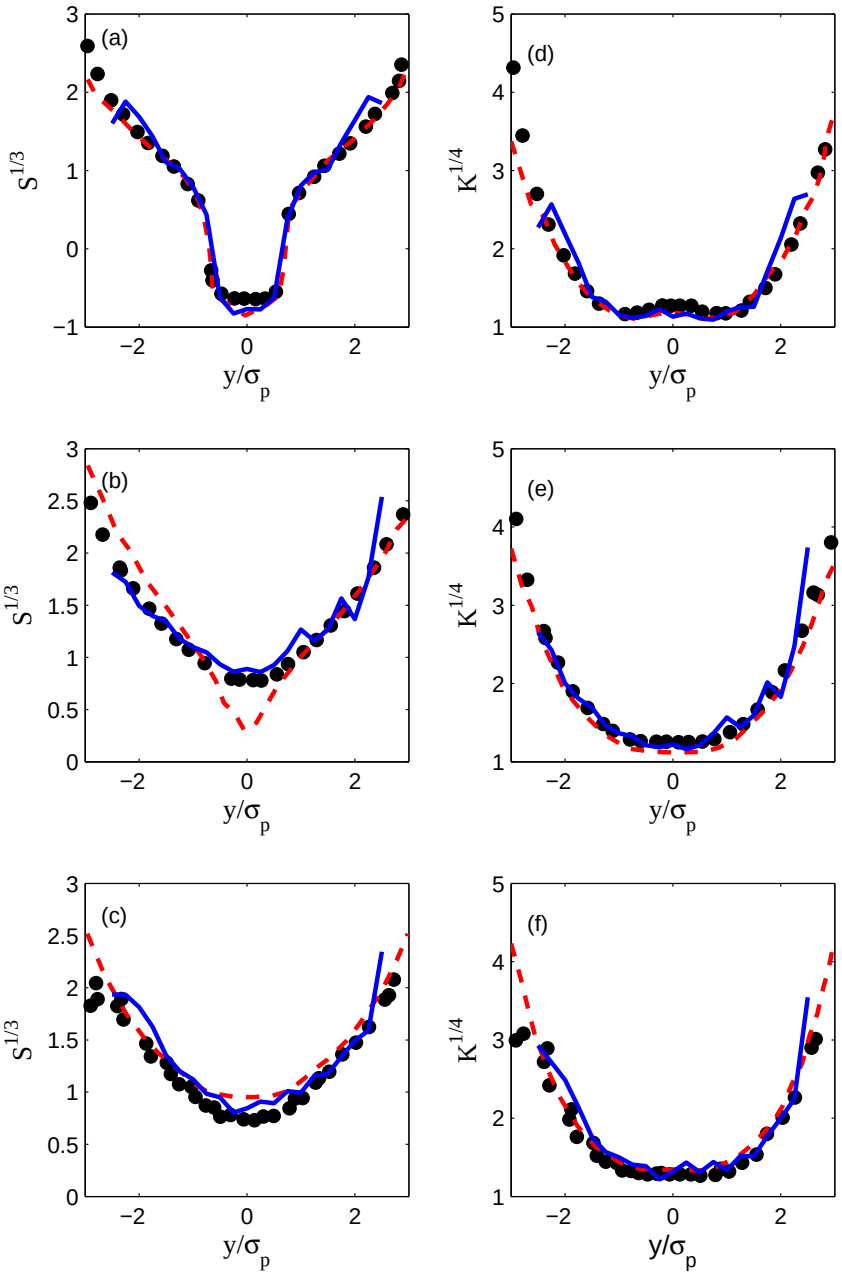

Figure 2.10: Radial profiles of higher order moments measured at varying distances from the source : Present calculations (solid line); Sawford IECM calculations (Dashed line); Sawford and Tivendale data ●; (a) Skewness at $t/T_o = 0.0014$; (b) Skewness at $t/T_o = 0.22$; (c) Skewness at $t/T_o = 7.2$; (d) Kurtosis at $t/T_o = 0.0014$; (e) Kurtosis at $t/T_o = 0.22$; (f) Kurtosis at $t/T_o = 7.2$.

2.5.2 A pair of line sources

A non-trivial extension can be made from a single line source to a pair of line sources in grid turbulence. The two sources, numbered 1 and 2, are placed parallel to each other separated by a distance d_o at a distance x_o from the turbulence generating grid. The origin of the coordinate system is chosen so that the locations of the sources are $(x, y) = (x_o, \pm d_o/2)$. In the experiments, a range of source separations was considered, from $d_o = 1.2\,mm$ to $d_o = 127\,mm$. We are interested in modeling the mixing and interference of the plumes from these two line sources.

The scalar fields corresponding to the two sources 1 and 2 are denoted in the laboratory frame by $\phi_1(x, y)$ and $\phi_2(x, y)$, respectively. The means and variances of ϕ_1 and ϕ_2 are the same as for the single source (with the appropriate shift of origin). In the moving reference frame, the scalar fields are denoted by $\phi_1(y, t)$ and $\phi_2(y, t)$. The correlation coefficient, $\rho_{12}(y, t)$ is defined as

$$\rho_{12} = \frac{\langle \phi_1' \, \phi_2' \rangle}{\langle \phi_1'^{\,2} \rangle^{1/2} \, \langle \phi_2'^{\,2} \rangle^{1/2}}, \tag{2.60}$$

where $\phi_j' = \phi_j - \langle \phi_j \rangle$ is the fluctuation in the jth scalar about its mean.

In the present work, the PDF model using Eq. (2.55) is applied to a pair of line sources, and is used to calculate the correlation coefficient, ρ_{12}. Each particle in the simulation now has two properties, ϕ_1 and ϕ_2, in addition to its velocity and position. Each ϕ_j, $j = 1, 2$, evolves by the modified IECM model equation Eq. (2.37) with conditional means defined similarly to Eq. (2.24) relative to their

Table 2.3: Parameters in the laboratory measurements of Warhaft and Lumley (1978). Definitions are given in Table 2.1.

σ_o	3.21×10^{-4}	m
M	2.54×10^{-2}	m
x_o/M	20	
U	6.5	ms^{-1}
σ_u, σ_v, σ_w	2.275	ms^{-1}
m	1.34	
κ	2.26×10^{-5}	m^2s^{-1}

respective sources. For instance, the conditional mean, $\langle \phi_1 \mid y, v \rangle$ is given by

$$\langle \phi_1 \mid y, v \rangle = \frac{Q}{\sqrt{2\pi}\sqrt{\sigma_o^2 + \sigma_y^2\left(1-\rho_{vy}^2\right)}} \exp\left[-\frac{1}{2}\left(\frac{y - d_o/2 - \rho_{vy}\, v\, \sigma_y/\sigma_v}{\sqrt{\sigma_o^2 + \sigma_y^2\left(1-\rho_{vy}^2\right)}}\right)^2\right], \qquad (2.61)$$

where source 1 is located at a distance, $d_o/2$ from the origin. Thus, the correlation coefficient can be calculated and compared to the detailed laboratory measurements available [89]. The experimental data for the pair of line sources form part of the same data set as the single line source. The relevant parameters are listed in Table 2.1 with $\sigma_o = 1.27 \times 10^{-4}\, m$ and $x_o/M = 20$.

In the experiments, the correlation coefficient can be estimated with multiple sources that are sometimes on or off, using the inference method [88]. For a pair of line sources, let ϕ_B correspond to the scalar field when both the sources are active. Then, with the assumption that the two scalar fields are linearly additive,

we can write

$$\phi_B = \phi_1 + \phi_2, \tag{2.62}$$

$$\phi_B^{'} = \phi_1^{'} + \phi_2^{'}, \tag{2.63}$$

$$\langle \phi_B^{'\,2} \rangle = \langle \phi_1^{'\,2} \rangle + \langle \phi_2^{'\,2} \rangle + 2\langle \phi_1^{'}\, \phi_2^{'} \rangle. \tag{2.64}$$

Therefore, using Eqs. (2.60) and (2.64) the correlation coefficient can be written as,

$$\rho_{12} = \frac{\langle \phi_B^{'\,2} \rangle - \langle \phi_1^{'\,2} \rangle - \langle \phi_2^{'\,2} \rangle}{2 \langle \phi_1^{'\,2} \rangle^{1/2} \langle \phi_2^{'\,2} \rangle^{1/2}}. \tag{2.65}$$

(This technique is used in the experiments; whereas in the calculations joint statistics of the scalars are extracted from the particles' scalar values.)

The evolution of the centerline correlation coefficient between the two sources is plotted in Fig. 2.11 for a range of source separations. The present model calculations are compared to the previous calculations of Sawford and laboratory data of Warhaft. The present model calculations correctly predict the evolution of the centerline correlation coefficient for a range of source separations.

The scalar *r.m.s.* is a relative quantity dependent on the strength of the source. In order to make comparisons with laboratory data, the scalar *r.m.s.* profiles are normalized by the centerline scalar *r.m.s.* for a single source. Figure 2.12 compares the model predictions of the normalized radial profiles of *r.m.s.* scalar with experimental data for three different source spacings, $d_o\,(mm) = 8, 14, 25$. The plots show the *r.m.s.* scalar profiles for ϕ_1, ϕ_2 and $\phi_1 + \phi_2$, assuming that the scalar fields are linearly additive. The present model calculations, as can be seen, correctly reproduce the laboratory measurements.

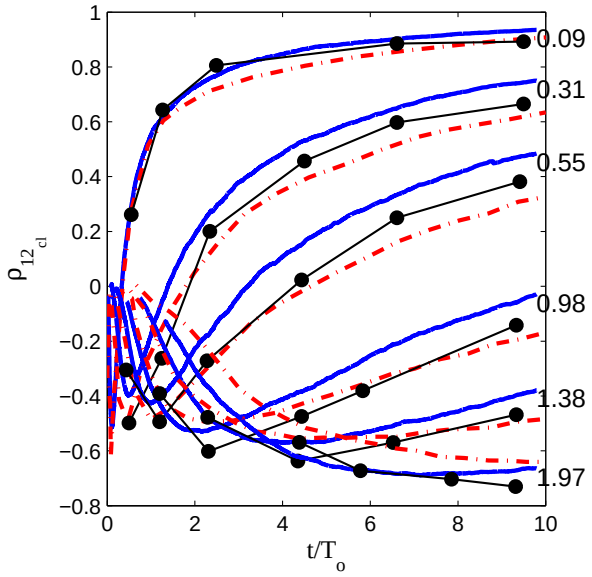

Figure 2.11: Evolution of the centerline cross-correlation coefficient for various source spacings, d_o/M = 0.09, 0.31, 0.55, 0.98, 1.38, 1.97. The sources are placed at a distance of $x_o/M = 20$ from the turbulence generating grid. Warhaft data ●; Sawford model calculations (dot dashed line); Present calculations (solid line).

The radial profiles of the correlation coefficient, ρ_{12} can be obtained using Eq. (2.60) in the model calculations and are plotted in Fig. 2.13 at different stages in the plume development. At every stage, multiple source separations are considered and comparison is made with the experimental data. The agreement is good as regards both the shape of the profile and the location of the minima on the centerline between the two sources. (The over-prediction of ρ_{12} seen at $y/M = 0$ in Fig. 2.13(a) may be due to the smearing introduced by the binning used to extract statistics.)

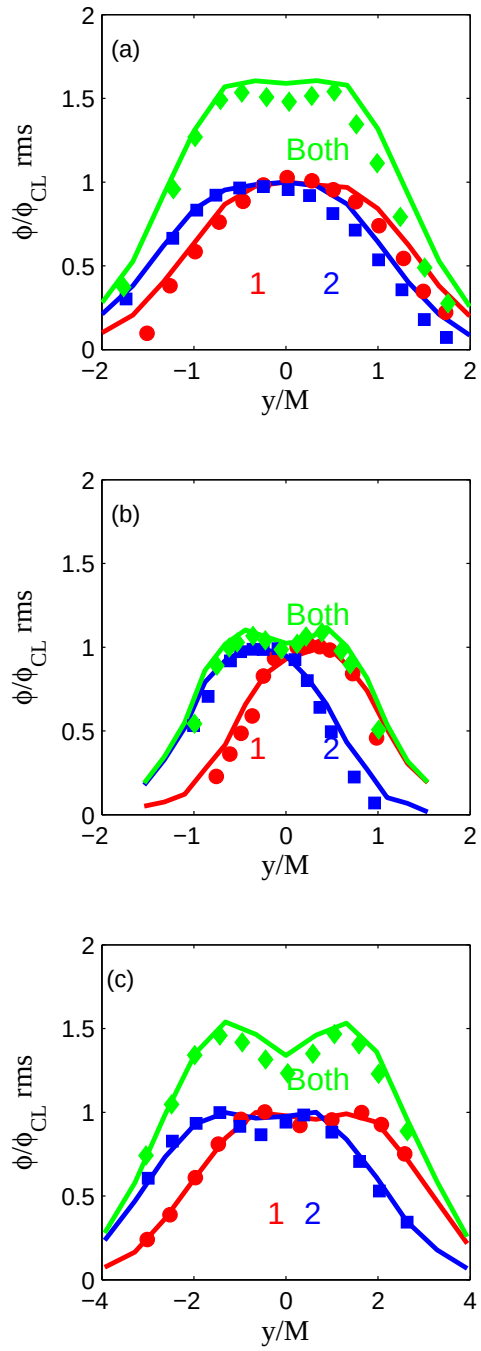

Figure 2.12: Radial profiles of *r.m.s.* scalar normalized by their respective centerline values when the sources are positioned at x_o/M = 20 from the turbulence grid for different spacings between the sources, d_o. (a) d_o/M = 0.31 and t/T_o = 2.31 ; (b) d_o/M = 0.55 and t/T_o = 1.19 ; (c) d_o/M = 0.98 and t/T_o = 9.31 ; Present model calculations (solid line); Warhaft data: ϕ_1, ● ; ϕ_2, ■ ; $\phi_1 + \phi_2$, ◆ ;

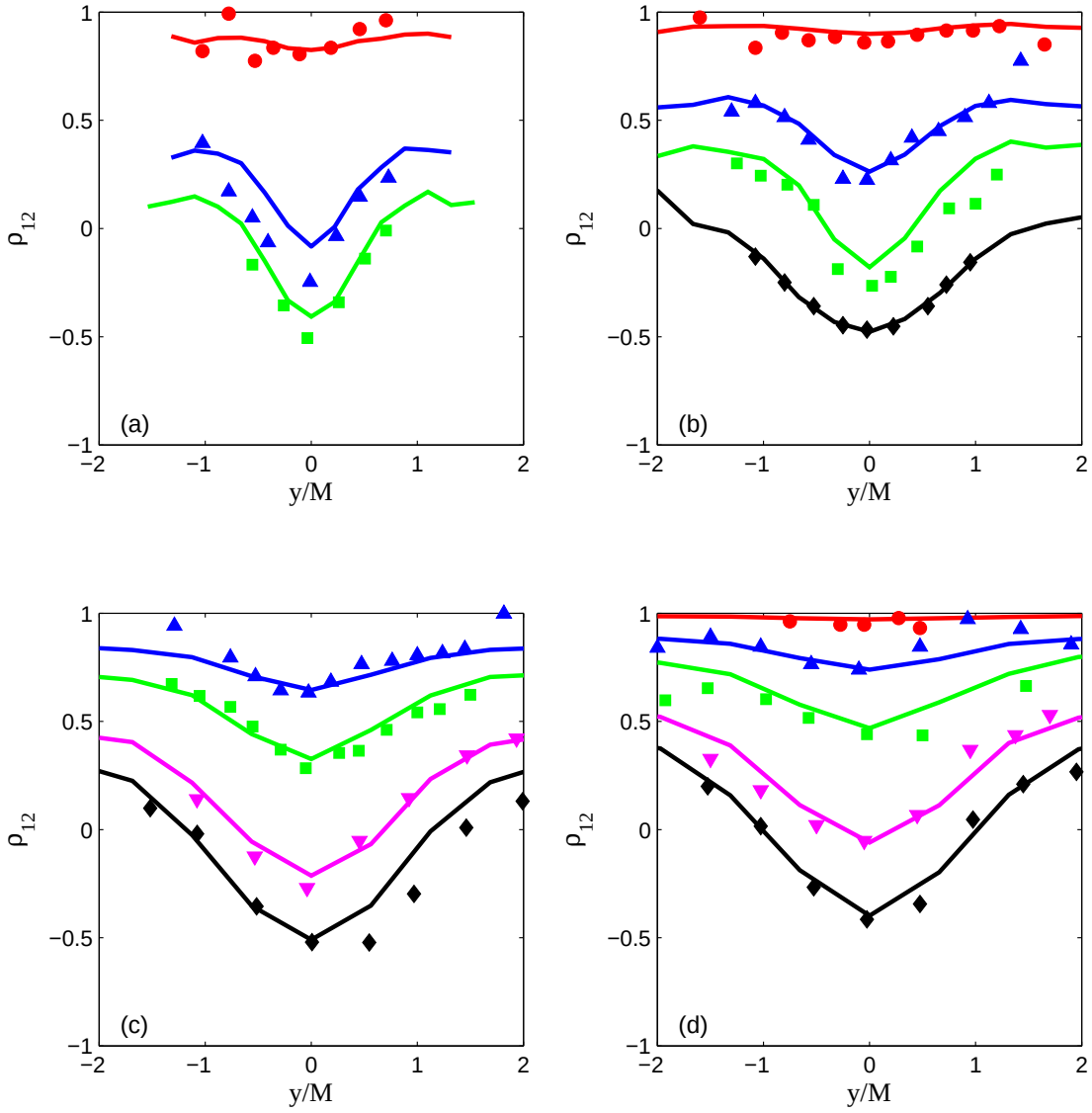

Figure 2.13: Radial profiles of the cross-correlation coefficient, ρ_{12} between the sources 1 and 2, for different spacings between the two sources, d_o/M. The sources are positioned at $x_o/M = 20$ from the turbulence generating grid. (a) : $t/T_o = 1.19$; (b) : $t/T_o = 2.31$; (c) : $t/T_o = 6.51$; (d) : $t/T_o = 9.31$; Present model calculations (solid line); Warhaft data: $d_o/M = 0.05$, ● ; $d_o/M = 0.31$, ▲ ; $d_o/M = 0.55$, ■ ; $d_o/M = 0.98$, ▼ ; $d_o/M = 1.38$, ◆ ;

2.5.3 An array of line sources

The decay of the scalar variance downstream of a heated mandoline (a set of multiple line sources placed parallel to one another a distance x_o downstream of the turbulence generating grid) can be understood by studying the interference between multiple line sources [89].

As a first step, an array of four line sources is considered in place of the pair of sources in the previous section. The relevant parameters for diffusion behind an array of four line sources are listed in Table 2.1 with $\sigma_o = 1.27 \times 10^{-4}\, m$ and $x_o/M = 20$. The distance between adjacent line sources is d_o and will be referred to as the mandoline spacing later on in the section.

As in Section §2.5.2, PDF calculations are performed with the modified IECM model by making a simple extension to four line sources. The sources are located at a distance of $x_o/M = 20$ from the turbulence grid and adjacent sources are separated by a non-dimensional distance of $d_o/M = 1$. The measurements are made at a distance of $x'/M = 63$ from the sources or equivalently at a time instant of $t/T_o = 4.41$. The origin of the coordinate system is defined at the midpoint between the four line sources i.e., the four sources are located at $(x, y) = (x_o, \pm(2j-1)\, d_o/2),\ j = 1, 2.$

Figure 2.14 plots the radial profiles of the normalized scalar *r.m.s*. Normalization is done with respect to the scalar *r.m.s.* value on the centerline of a single source. The radial profiles of the scalar *r.m.s.* corresponding to each source is plotted in (a) for all the four sources numbered $1, 2, 3$ and 4. Each of these profiles is statistically identical to the single line source but shifted in physical

space appropriately. Sub-figures (b,c,d) plot the radial profiles of scalar *r.m.s.* corresponding to $\phi_j + \phi_k$, $|j-k| = 1, 2, 3$ respectively. The profiles are shifted appropriately in physical space depending on the choice of the sources, j and k. Finally sub-figure (e) plots normalized *r.m.s.* scalar profile for $\sum_{j=1}^{4} \phi_j$. The effect of the interference between multiple line sources in reducing the total *r.m.s.* at the centerline between the four sources is captured by the model calculations and the agreement with the experimental data is good.

The radial profiles of the pair-wise correlation coefficients for sources separated by distances $d_o/M = 1, 2, 3$ are plotted in Fig. 2.15-((a),(b),(c)) respectively. Each of the curves here is obtained from the data in Fig. 2.14-((a),(b),(c),(d)). This confirms that the individual *r.m.s.* profiles and the pair-wise correlation coefficients are sufficient to estimate the *r.m.s.* scalar profile corresponding to $\sum_{j=1}^{4} \phi_j$.

2.5.4 The heated mandoline

The decay of scalar variance downstream of a heated mandoline is equivalent to considering the interference between multiple line sources equally spaced and placed parallel to each other at some distance from the turbulence generating grid [89]. Over the downstream range of the experiments, the scalar variance in a given experiment appears to decay according to the power law

$$\frac{\langle \phi'^2 \rangle}{T^2} = B\left(\frac{x}{M}\right)^{-n}, \; x > x_o, \tag{2.66}$$

where x, is measured from a virtual origin (within a few mesh lengths of the grid), T is the mean temperature of the flow without any of the sources being

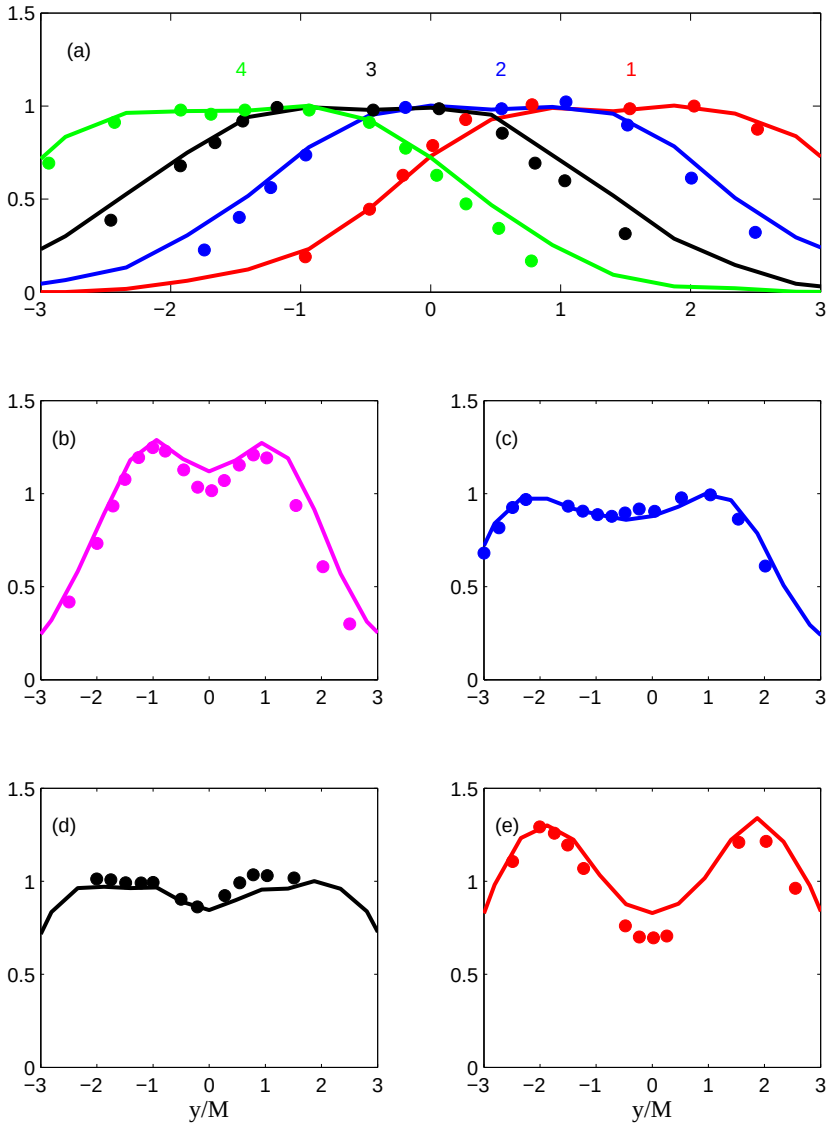

Figure 2.14: (a) Radial profiles of *r.m.s.* scalar corresponding to each of the four sources in an array, normalized by their respective centerline values at $t/T_o = 4.41$; (b) Radial profiles of *r.m.s.* scalar corresponding to $\phi_2 + \phi_3$; (c) Radial profiles of *r.m.s.* scalar corresponding to $\phi_2 + \phi_4$; (d) Radial profiles of *r.m.s.* scalar corresponding to $\phi_1 + \phi_4$; (e) Radial profiles of *r.m.s.* scalar corresponding to all the four sources; The radial profiles in (b)-(e) are normalized by the mean centerline value obtained from (a). Present model calculations (solid line); Warhaft data: ●

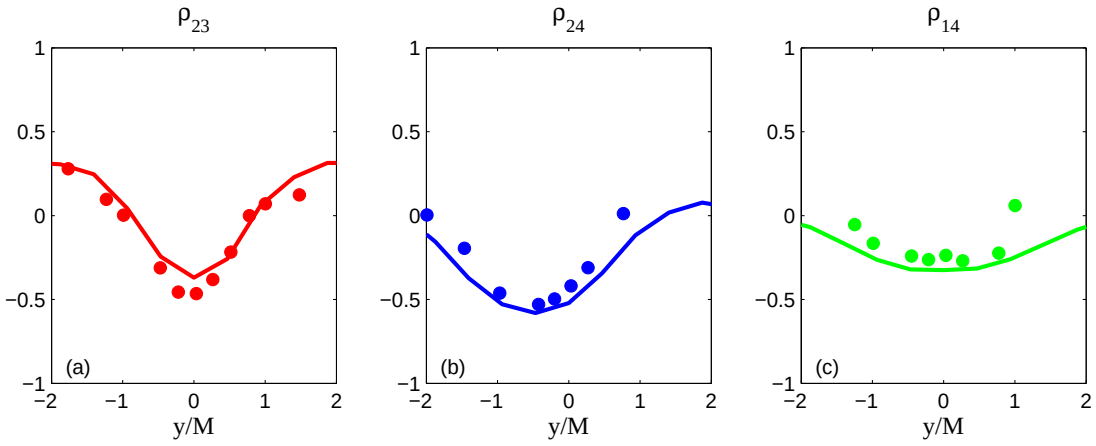

Figure 2.15: Radial profiles of the cross-correlation coefficient, ρ between pairs of sources at $t/T_o = 4.41$. Diffusion behind an array of four sources is considered. The sources are positioned at $x_o/M = 20$ from the turbulence grid. (a) : $d_o/M = 1$, sources 2 & 3; (b) : $d_o/M = 2$, sources 2 & 4 ; (c) : $d_o/M = 3$, sources 1 & 4 ; Present model calculations (solid line); Warhaft data: ●

active, n is the scalar variance decay exponent, and B is a constant. From the experiments of Warhaft and Lumley [90], the scalar variance decay rate was found to be uniquely determined by the length scale of the initial scalar fluctuations relative to the integral turbulence length scale. The scalar variance decay rate, n, was shown to completely depend on the the wavelength of the initial scalar field determined by the mandoline spacing, d_o.

The relevant turbulence parameters characterizing the experimental data are listed in Table 2.3. The experiments were carried out with the mandoline placed a distance $x_o/M = 20$ and for two configurations of the mandoline with spacings of $d_o/M = 1$ and 2. The scalar variance decay exponents were empirically obtained to be $n = 3.20$ and 2.06, respectively, for the two mandoline configurations.

In the present calculations, PDF calculations similar to the array of line sources (described in the previous section) are performed to compare with the experimental data for the two mandoline configurations. The model calculations are performed with a number of line sources n_s such that the addition of any more line sources would hardly affect the scalar variance at the measurement point. Closer to the source (in the laboratory frame of reference), fewer sources are sufficient while farther away, more are required.

Figure 2.16 plots the experimental data from Warhaft and Lumley [90] for $d_o/M = 1, 2$ and Warhaft [89] for $d_o/M = 2/3$, of the decay of the scalar variance downstream of the turbulence grid. Figure 2.17 compares the model calculations against the experimental data and there is clearly a good match between the two. Plotting the scalar variance with distance from the turbulence grid does show a dependence on the ratio of length scale of the initial scalar fluctuations to the integral turbulence length scale. On the other hand, Fig. 2.18 plots the same data, both numerical and experimental, as a function of flight time from the source, t/T_o and the constant decay rate in the scalar fluctuations is apparent across all d_o/M beyond a certain value of t/T_o. For large times, the model predicts a decay exponent of mC_ϕ which evaluates to 2.1 for $C_\phi = 1.5$ and both the calculations and experimental data agree with the model prediction.

2.5.5 The effect of the choices of C_0 and C_ϕ

All results reported so far were performed using the standard values of $C_0 = 2.1$ and $C_\phi = 1.5$, whereas the calculations of Sawford [70] for both the single and pair of line sources are presented for $C_0 = 3$. In order to study the effect of the

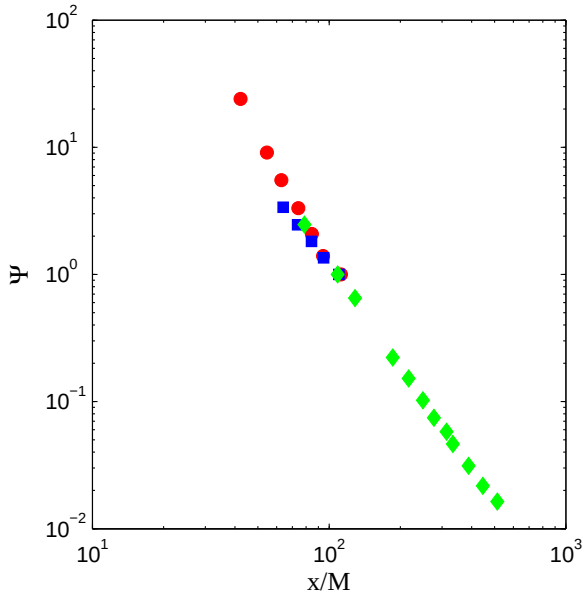

Figure 2.16: Experimental data of decay of normalized scalar fluctuations, $\Psi = \langle\phi'^2\rangle/\langle\phi'^2\rangle_{x/M=100}$ downstream of a heated mandoline from the turbulence generating grid. Relevant parameters are listed in Table 2.3. $d_o/M = 1$ and $x_o/M = 20$ ●; $d_o/M = 2$ and $x_o/M = 20$, ■; $d_o/M = 2/3$ and $x_o/M = 44$, ◆;

choice of the above mentioned model parameters, calculations were repeated for the different combinations of $C_0 = 2.1, 3$ and $C_\phi = 1.3, 1.5, 2$ and compared to the experimental data.

Figure 2.19 compares the centerline intensity of fluctuations, $i(0,t)$ for the six different combinations of C_0 and C_ϕ with the experimental data for three placements of the source, $x_o/M = 20, 52, 60$. Subplot (a) compares the maximum of i observed from the experiments for a given x_o/M to the estimates obtained from the present calculations at the same time. Subplot (b) compares the experimentally observed value of $i(0,t^*)$, where $t^*/T_o \sim 1.82$ to the calculations at the same time. The value $C_\phi = 2$ under predicts the scalar variance irrespective of C_0, whereas $C_\phi = 1.3$ yields better agreement with the experimental data. Our

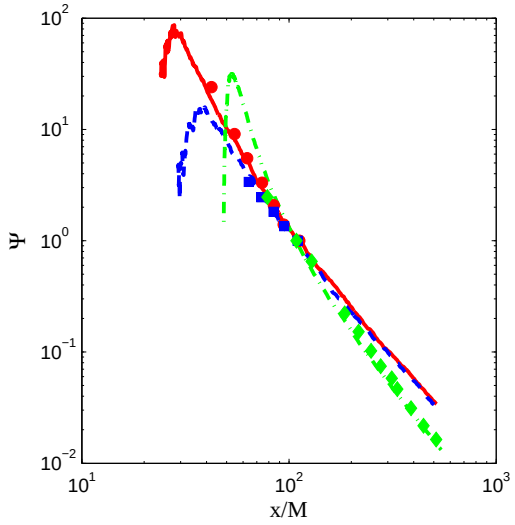

Figure 2.17: Decay of normalized scalar fluctuations, $\Psi = \langle\phi'^2\rangle/\langle\phi'^2\rangle_{x/M=100}$ downstream of a heated mandoline from the turbulence generating grid. Symbols are the same as Fig. 2.16. Present model calculations are denoted by lines. $d_o/M = 1$ and $x_o/M = 20$ (solid line); $d_o/M = 2$ and $x_o/M = 20$, (dashed line); $d_o/M = 2/3$ and $x_o/M = 44$, (dot dashed line);

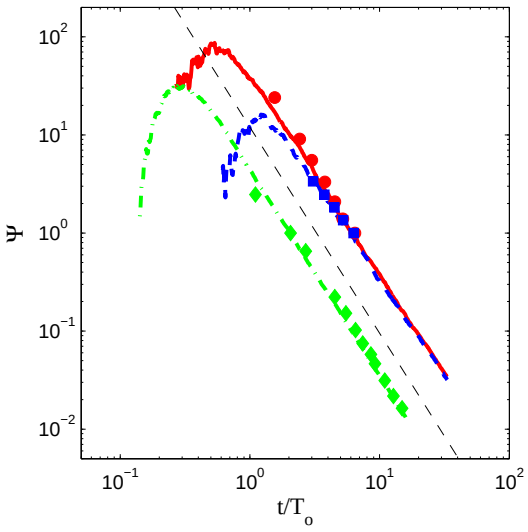

Figure 2.18: Decay of normalized scalar fluctuations, $\Psi = \langle\phi'^2\rangle/\langle\phi'^2\rangle_{x/M=100}$ against flight time from the source. See Fig. 2.17 for an explanation of symbols used. A dashed line of slope $-mC_\phi = -2.1$ is shown for reference.

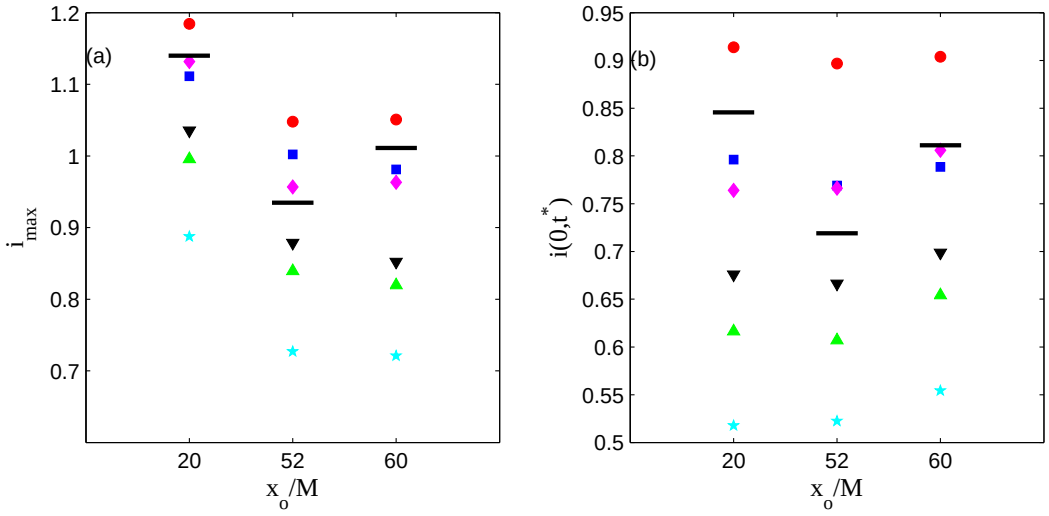

Figure 2.19: Effect of model coefficients C_0 and C_ϕ on scalar fluctuations (a) Maximum centerline intensity of fluctuations, i_{max} against different placements of the source with respect to the turbulence grid, x_o/M. (b) Centerline intensity of fluctuations, $i(0, t^*)$ against x_o/M where $t^*/T_o = 1.82$. Symbols are from present calculations for different combinations of C_0 and C_ϕ : $C_0 = 2.1$ and $C_\phi = 1.3$ ●, $C_0 = 2.1$ and $C_\phi = 1.5$ ■, $C_0 = 2.1$ and $C_\phi = 2$ ▲, $C_0 = 3$ and $C_\phi = 1.3$ ◆, $C_0 = 3$ and $C_\phi = 1.5$ ▼, $C_0 = 3$ and $C_\phi = 2$ ★; Solid horizontal lines correspond to the experimental data.

choice of $C_0 = 2.1$ and $C_\phi = 1.5$ compares well with the $C_0 = 2.1$ and $C_\phi = 1.3$ combination at least for the single line source.

Similarly, Fig. 2.20 compares the estimated centerline correlation coefficient, $\rho_{12_{cl}}$ between a pair of line sources using different combinations of model parameters to the experimentally observed value at the same time instant of $t/T_o \sim 2.8$. The combination of $C_0 = 3$ and $C_\phi = 1.5$ yields the most accurate results but, as for the single line source, our choice of the model parameters gives results with a reasonable accuracy.

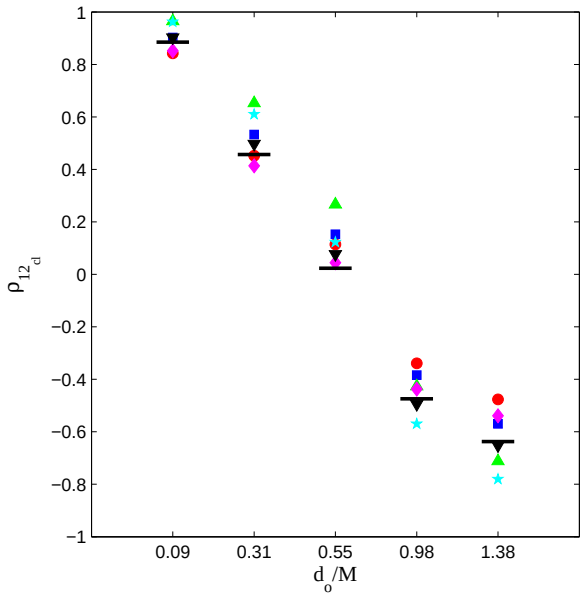

Figure 2.20: Correlation coefficient between a pair of line sources at $t/T_o = 2.8$ plotted for different source separations, $d_o/M = 0.09, 0.31, 0.55, 0.98, 1.38$ for various combinations of C_0 and C_ϕ. Symbols are as defined in Fig. 2.19.

2.5.6 Effect of Reynolds number and source size

Presently, the experimental data available for dispersion studies behind line sources in decaying grid turbulence are at relatively small Taylor scale Reynolds numbers, $R_\lambda \sim 60$. As a natural consequence, it is of significant relevance to be able to understand and predict the behavior of the scalar field at higher Reynolds number.

From the experimentalists' viewpoint, for a grid of fixed geometry, the problem of dispersion from a single line source requires three independent parameters to completely characterize the turbulence field viz., U, M and the viscosity $\nu = \kappa Pr$, where Pr is the Prandtl number, and two independent parameters to completely characterize the source, namely σ_o and x_o. On the other hand, since

dispersion of the scalar plume is only dependent on the turbulence statistics at the source location, the relevant number of independent dimensional parameters required for simulating the dispersion from a single line source reduces to four and these can be taken as - k_o, ε_o, σ_o and κ (for given Pr). Two length scales and two timescales that can be formed given the above four quantities are L_o, σ_o, T_o and τ_κ, from which at most two independent non-dimensional groups can be formed. In this work, we choose to work with the length scale ratio, $\Lambda = \sigma_o/L_o$ and the Taylor scale Reynolds number, R_λ.

In order to understand the effect of each of these non-dimensional quantities on the evolution of the scalar field, the results from a set of five cases are presented for different combinations of Λ and R_λ. Both Λ and R_λ are chosen to vary by an order of magnitude. The value of Λ is typically chosen over a range 5×10^{-5} to 5×10^{-4} whereas R_λ is chosen to vary between 100 and 1000. The details are summarized in Table 2.4.

Additionally, calculations are also performed for larger ranges in both $R_\lambda \sim$ 70 to 7000 and $\Lambda \sim 2\times10^{-5}$ up to 2×10^{-3} with an aim to study the their effects on the centerline intensity of fluctuations. In particular, the maximum value i_{max}, and the large-time asymptote, i_∞, are analyzed in the $\Lambda - R_\lambda$ space.

2.5.6.1 Dependence on Reynolds number, R_λ

As a first step, the dependence of various scalar statistics on R_λ is studied at a given value of Λ. The Langevin model constant, C_0 is taken to be independent of R_λ and equal to 2.1. Figures (2.22-2.24) plot the centerline intensity of fluctuations, the normalized mean plume width, the normalized integral scalar vari-

Table 2.4: Parameters corresponding to the cases performed in Section §2.5.6. Velocity variance at the source location (isotropic turbulence), σ_{vo}^2 ; Velocity variance decay exponent, m; Turbulence mesh spacing, M; Mean speed, U; source size, σ_o; Taylor scale Reynolds number at the source location, R_λ; Ratio of source to turbulence integral scale at the source location, Λ.

	σ_{vo}^2 (m^2/s^2)	m	M (cm)	U (m/s)	σ_o (m)	R_λ	Λ
1	0.45	1.2	11.4	3.66	2.5 x 10^-5	400	5.8 x 10^{-5}
2	0.45	1.2	11.4	3.66	2.01 x 10^-3	400	4.7 x 10^{-4}
3	2.35	1.2	5	8.35	2.5 x 10^-5	400	1.3 x 10^{-4}
4	0.36	1.2	5	3.26	2.5 x 10^-5	250	1.3 x 10^{-4}
5	5.6	1.2	11.4	12.88	5.7 x 10^-5	750	1.3 x 10^{-4}

ance and higher moments of skewness and kurtosis respectively against flight time from the source for $\Lambda = 1.3 \times 10^{-4}$ and for three different values of R_λ - 250, 400 and 750.

Figure 2.21 shows that the normalized mean plume width, σ_p/L_o is independent of R_λ except at small times. Figure 2.21 displays an increase in the peak value of the centerline fluctuation intensity with an increase in R_λ. Additionally, the behavior at very early time ($t/T_o < 3 \times 10^{-5}$) is independent of R_λ. Far downstream, again i seems to be independent of R_λ for a constant C_0 assumption. Figure 2.23 compares the effect of R_λ on the evolution of the normalized integral scalar variance, I. At very small times, I is independent of R_λ. Far downstream also, there is a similar trend. In the intermediate regime, the decay rate of the integral scalar variance is the same and is given by the slope of the curve whereas R_λ has a direct effect on the magnitude. Figure 2.24 exhibits independence of the

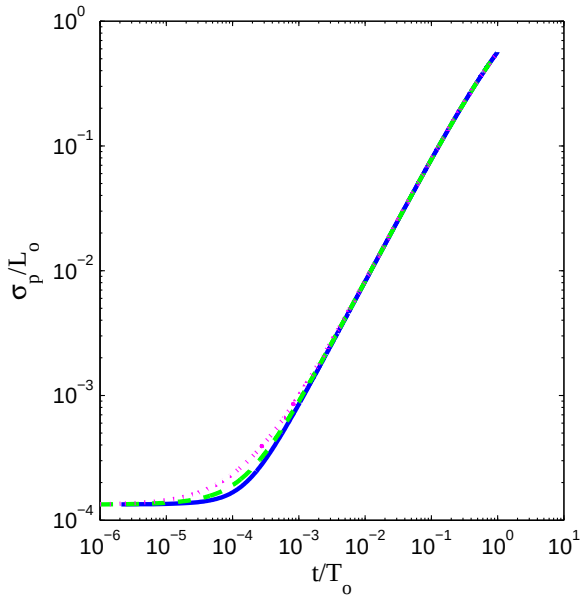

Figure 2.21: Mean plume width normalized by the turbulence integral scale at the source, L_o against flight time from the source for $\Lambda = 1.3 \times 10^{-4}$ and different values of R_λ; (Solid line) $R_\lambda = 750$, (Dashed line) $R_\lambda = 400$, (Dotted line) $R_\lambda = 250$.

higher moments of the scalar from R_λ at very small times. For very large times, an increase in R_λ is equivalent to a shift of the plot to smaller t/T_o.

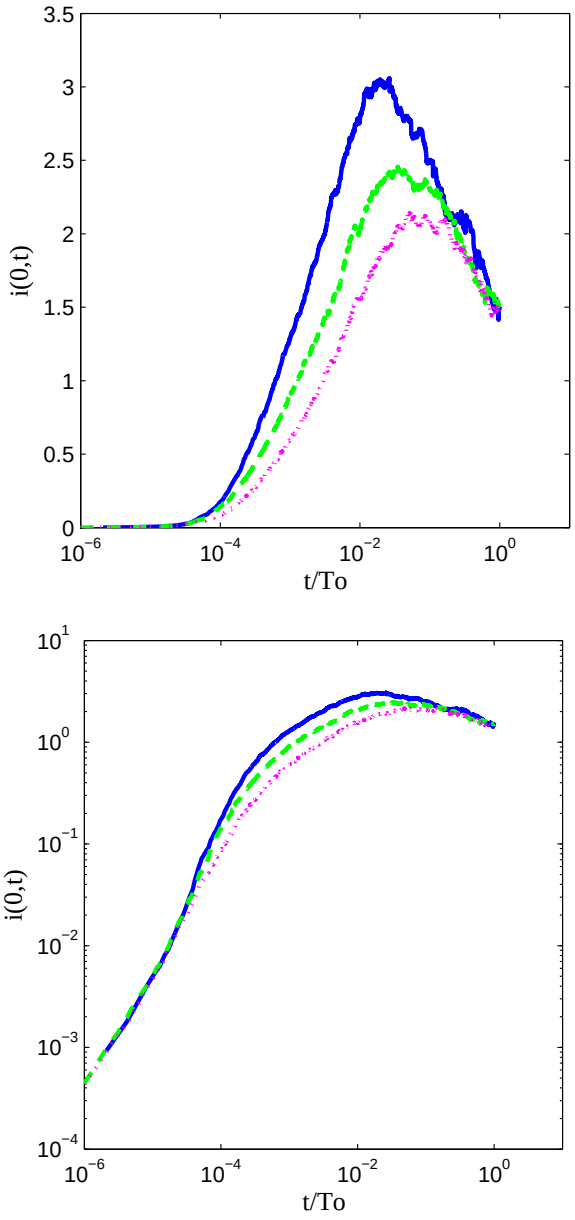

Figure 2.22: Centerline intensity of fluctuations, $i(0,t)$ versus flight time from the source for $\Lambda = 1.3 \times 10^{-4}$ and different values of R_λ; (Solid line) $R_\lambda = 750$, (Dashed line) $R_\lambda = 400$, (Dotted line) $R_\lambda = 250$.

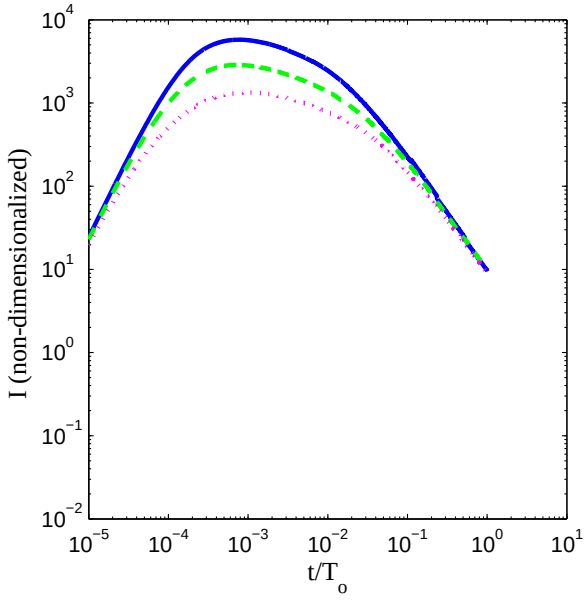

Figure 2.23: Integral of scalar variance, I normalized by $2\pi L_o/Q^2$ against flight time from the source for $\Lambda = 1.3 \times 10^{-4}$ and different values of R_λ; (Solid line) $R_\lambda = 750$, (Dashed line) $R_\lambda = 400$, (Dotted line) $R_\lambda = 250$.

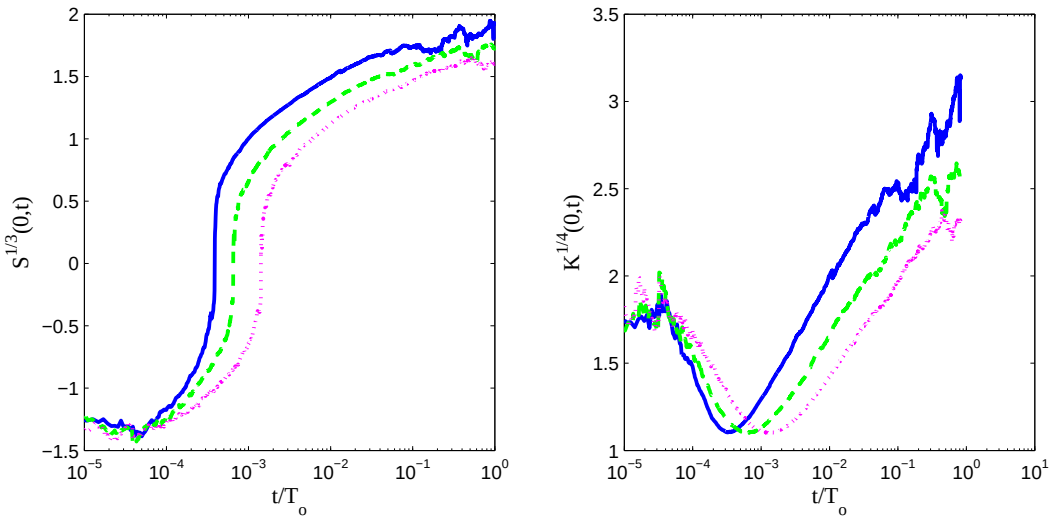

Figure 2.24: Skewness, S and kurtosis, K against flight time from the source for $\Lambda = 1.3 \times 10^{-4}$ and different values of R_λ; (Solid line) $R_\lambda = 750$, (Dashed line) $R_\lambda = 400$, (Dotted line) $R_\lambda = 250$.

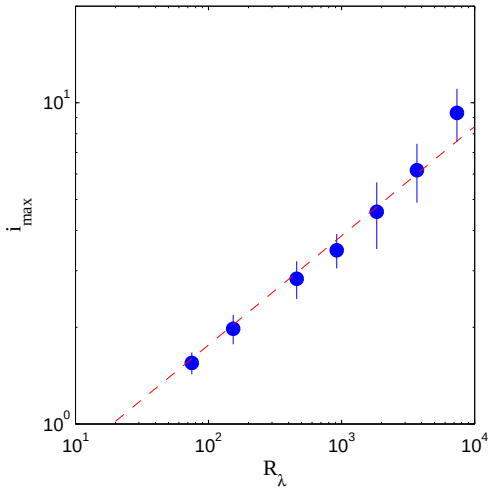

Figure 2.25: Maximum centerline intensity of fluctuation against R_λ for $\Lambda = 1.3 \times 10^{-4}$. The solid lines indicate 95% confidence intervals. Dashed line of slope 1/3 is shown for reference.

Secondly, i is analyzed further over a larger range of R_λ in terms of i_{max} and i_∞, which are the maximum value of i and the large-time asymptote respectively. Figure 2.25 shows a log-log plot of i_{max} versus R_λ. In the range of R_λ considered, i_{max} varies approximately as ${R_\lambda}^{1/3}$ (as is shown by the dashed line) and does not appear to saturate to a constant level. Since, the scalar mean is not affected by R_λ for constant C_0, an increasing trend in i_{max} implies that the scalar fluctuations are increasing. Figure 2.26 is aimed at studying the effect of R_λ on i_∞ and as is evident from the plot, i_∞ is independent of R_λ.

Thirdly, the effect on i_{max} and i_∞ of incorporating a R_λ dependence on C_0 is studied based on Pope [55]. Figure 2.27 compares i_{max} obtained under the assumption that $C_0 = 2.1$ with the estimates made incorporating the R_λ dependence of C_0. The estimates of i_{max} from the two approaches are within the 95% confidence intervals. Figure 2.28 however shows some sensitivity to the value of C_0: including for the R_λ -dependence of C_0 results in a decrease in i_∞ of no

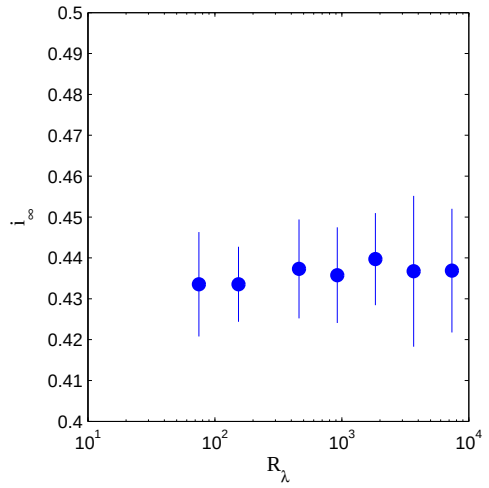

Figure 2.26: Estimate of the centerline intensity of fluctuation as $t \to \infty$ against R_λ for $\Lambda = 1.3\times10^{-4}$. The lines indicate 95% confidence intervals.

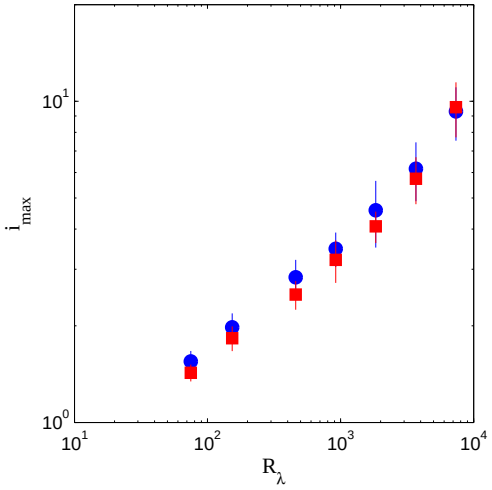

Figure 2.27: Maximum centerline intensity of fluctuation against R_λ for $\Lambda = 1.3 \times 10^{-4}$. ● $C_0 = 2.1$; ■ $C_0(R_\lambda)$; The lines indicate 95% confidence intervals.

more than 10%.

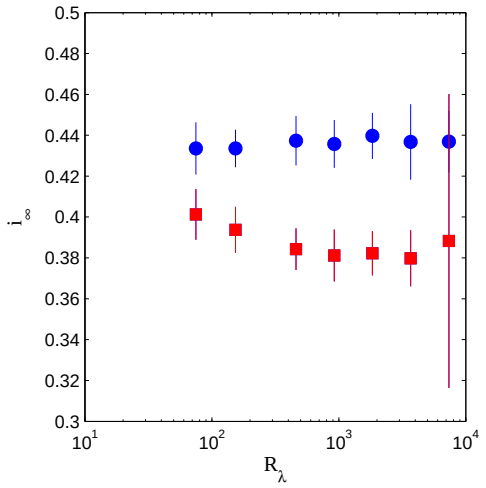

Figure 2.28: Estimate of the centerline intensity of fluctuation as $t \rightarrow \infty$ against R_λ for $\Lambda = 1.3 \times 10^{-4}$. ● $C_0 = 2.1$; ■ $C_0(R_\lambda)$; The lines indicate 95% confidence intervals.

2.5.6.2 Dependence on normalized source size, Λ

Next, the effect of $\Lambda = \sigma_o/L_o$ on the scalar field is studied at a constant value of R_λ of 400. As in Section §2.5.6.1, the centerline intensity of fluctuations, the mean plume width, the integral scalar variance, skewness and kurtosis are probed to understand the effect of Λ on the scalar field.

Figure 2.29 plots the centerline intensity of fluctuations against flight time from the source for three different values of Λ, 5.8×10^{-5}, 1.3×10^{-4} and 4.7×10^{-4}. Except for the effect of the variation in Λ at very early times, there is little dependence of i on Λ. Similar trends are observed in Fig. 2.30 for the normalized mean plume width, σ_p/L_o, in Fig. 2.31 for the normalized integral scalar variance, I and in Fig. 2.32 for skewness and kurtosis.

Since Λ affects the various scalar statistics only at very small times close to the source, each of the quantities can be appropriately scaled to make them

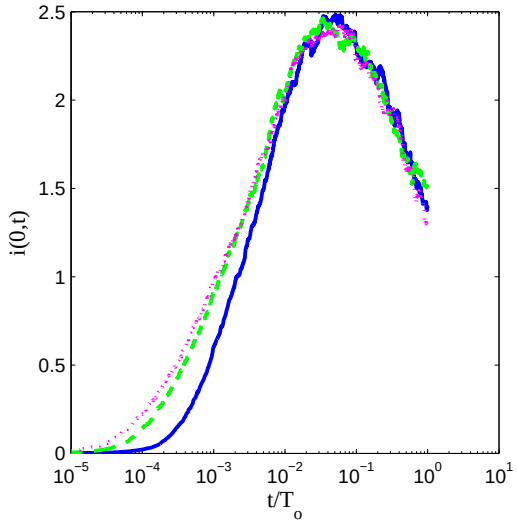

Figure 2.29: Centerline intensity of fluctuations, $i(0,t)$ versus flight time from the source at $R_\lambda = 400$ for different values of Λ; (Solid line) $\Lambda = 4.7 \times 10^{-4}$, (Dashed line) $\Lambda = 1.3 \times 10^{-4}$, (Dotted line) $\Lambda = 5.8 \times 10^{-5}$.

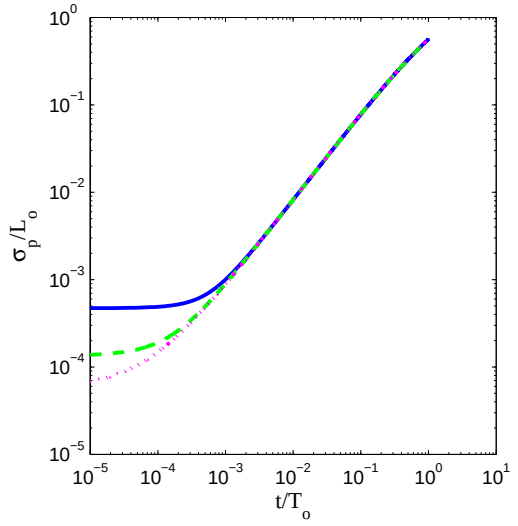

Figure 2.30: Mean plume width normalized by the turbulence integral scale at the source, L_o against flight time from the source at $R_\lambda = 400$ for different values of Λ; (Solid line) $\Lambda = 4.7 \times 10^{-4}$, (Dashed line) $\Lambda = 1.3 \times 10^{-4}$, (Dotted line) $\Lambda = 5.8 \times 10^{-5}$.

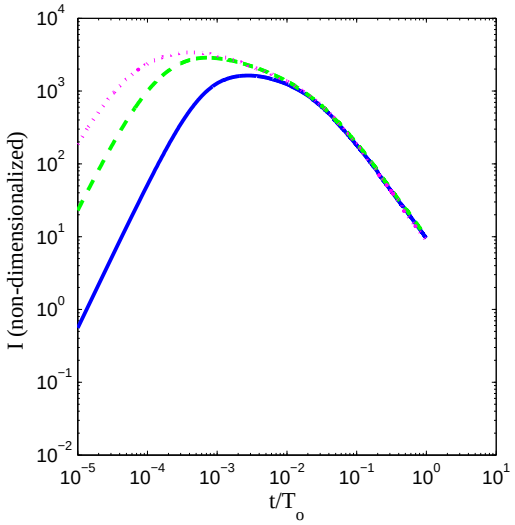

Figure 2.31: Integral of scalar variance, I normalized by $2\pi L_o/Q^2$ against flight time from the source at $R_\lambda = 400$ for different values of Λ; (Solid line) $\Lambda = 4.7 \times 10^{-4}$, (Dashed line) $\Lambda = 1.3 \times 10^{-4}$, (Dotted line) $\Lambda = 5.8 \times 10^{-5}$.

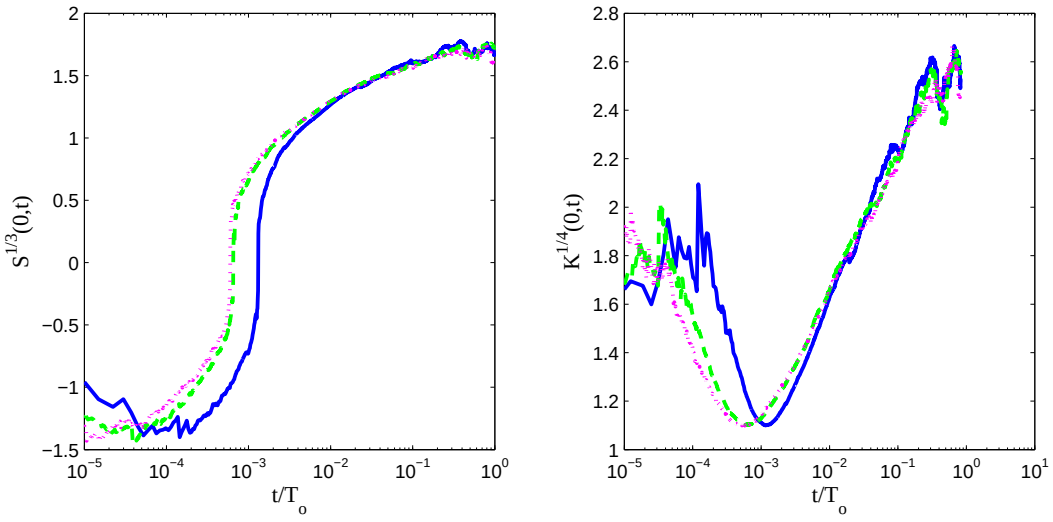

Figure 2.32: Skewness, S and kurtosis, K against flight time from the source at $R_\lambda = 400$ for different values of Λ; (Solid line) $\Lambda = 4.7 \times 10^{-4}$, (Dashed line) $\Lambda = 1.3 \times 10^{-4}$, (Dotted line) $\Lambda = 5.8 \times 10^{-5}$.

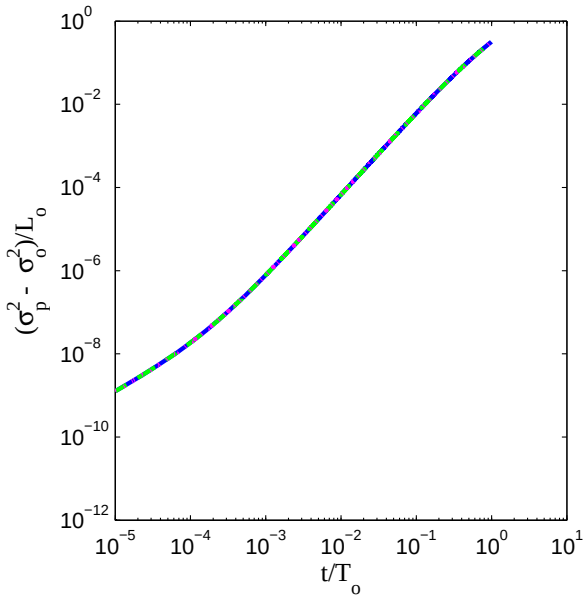

Figure 2.33: Normalized mean plume width minus the effect of the source plotted against flight time from the source at $R_\lambda = 400$ for different values of Λ; (Solid line) $\Lambda = 4.7 \times 10^{-4}$, (Dashed line) $\Lambda = 1.3 \times 10^{-4}$, (Dotted line) $\Lambda = 5.8 \times 10^{-5}$. (The lines are indistinguishable.)

independent of Λ. The effect of the source size on the mean plume width is purely an additive effect as is evident from Eq. (2.11) and therefore, $(\sigma_p^2 - \sigma_o^2)/L_o$ is independent of Λ. Figure 2.33 confirms this observation.

Moreover, the centerline intensity of fluctuations, i at very small times can be analytically obtained using the laminar thermal wake modeling approach to be,

$$i(0,t) = \sqrt{\frac{G^2+1}{\sqrt{2G^2+1}} - 1}, \tag{2.67}$$

where,

$$G(t) = \left(\frac{\sigma_{v_o}^2 T_o}{2\kappa}\right)\left[\frac{t^2}{T_o(t+\frac{1}{2}\tau_\kappa)}\right]. \tag{2.68}$$

Since i is a function of G only at very small times, accurate calculations of i can

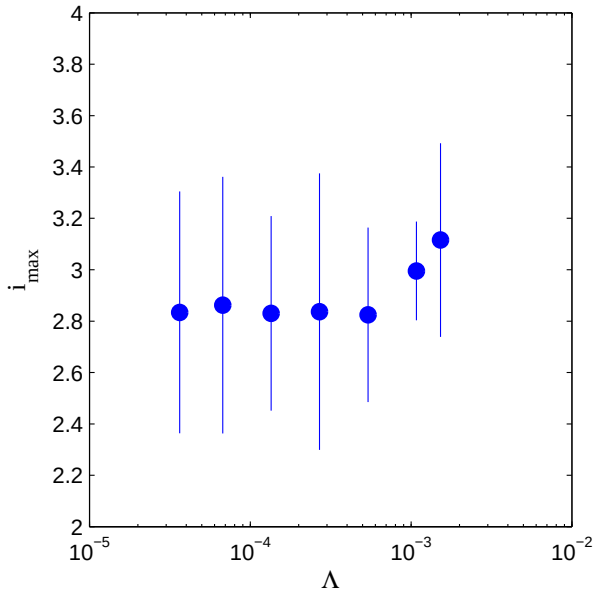

Figure 2.34: Maximum centerline intensity of fluctuation against Λ for $R_\lambda = 460$. The lines indicate 95% confidence intervals.

be expected to scale as G does at small times. Figures 2.34 and 2.35 plot i_{max} and i_∞ respectively over a larger range of Λ at $R_\lambda = 460$. Figure 2.36 shows the plot of i against $t^2/[T_o(t + \tau_\kappa/2)]$ both in linear-log scale and log-log scale, thereby effectively eliminating the influence of Λ on i. Both the figures show no sensitivity to Λ (at least for $\Lambda \leq 10^{-3}$), strengthening the conclusion earlier from this section that Λ affects the statistics only at very early times.

2.6 Conclusions

Detailed PDF calculations have been performed of the dispersion from line sources in grid turbulence. The PDF method uses the modified IECM mixing model, which is summarized in Section §2.3.5. The model calculations are pri-

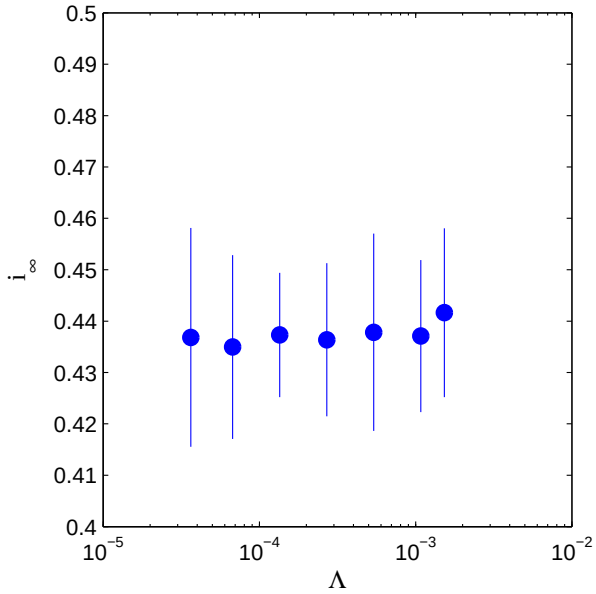

Figure 2.35: Estimate of the centerline intensity of fluctuation as $t \rightarrow \infty$ against Λ for $R_\lambda = 460$. The lines indicate 95% confidence intervals.

marily compared with the experiments of Warhaft [89] and the IECM model calculations of Sawford [70] for single and pairs of line sources. An extension is also made to simulate an array of four line sources and heated mandolines.

Due to the disparity in the length scales of the plume and turbulent energy-containing motions very close to the source, the effects of molecular diffusion have to be accounted for in the scalar evolution equation. However, modeling the molecular diffusion as a random walk in the evolution equation for particle displacement in conjunction with the IECM mixing model gives rise to a spurious production term in the scalar variance transport equation. The spurious production term is avoided by instead incorporating the effects of molecular diffusion directly into the IECM mixing model by the addition of a conditional scalar drift term.

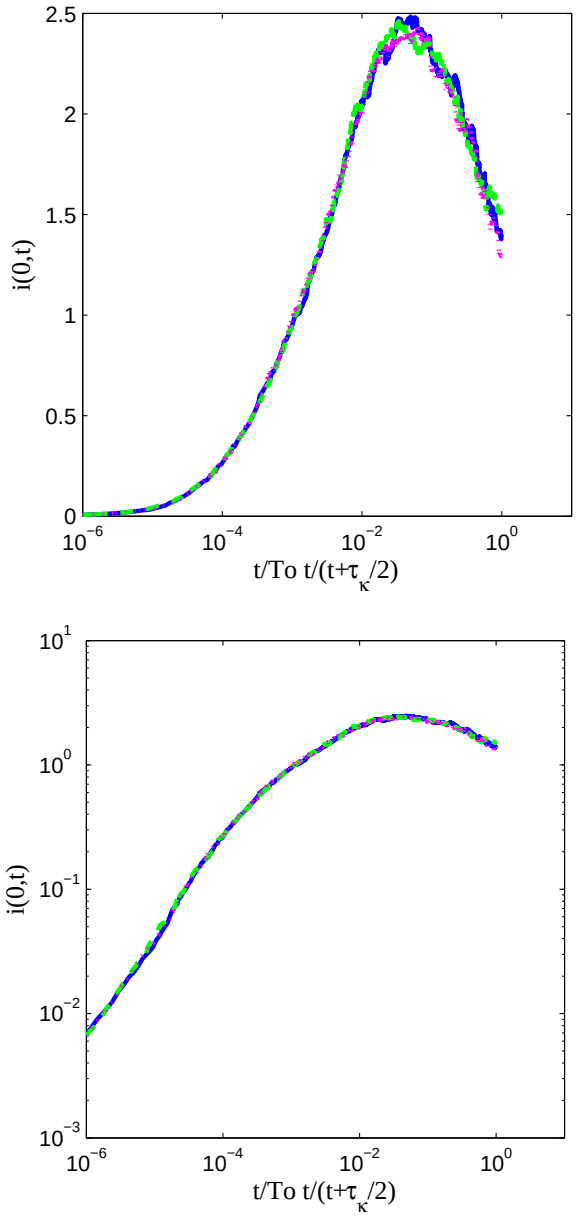

Figure 2.36: Centerline intensity of fluctuations, $i(0,t)$ versus time, $\bar{t} = t^2/[T_o(t + \tau_\kappa/2)]$ at $R_\lambda = 400$ for different values of Λ; (Solid line) $\Lambda = 4.7 \times 10^{-4}$, (Dashed line) $\Lambda = 1.3 \times 10^{-4}$, (Dotted line) $\Lambda = 5.8 \times 10^{-5}$. (The lines are indistinguishable.)

Modeling the instantaneous plume as a laminar thermal wake provides a model for the evolution of the mixing rate very close to the source. This small-time asymptote, $\omega_m^0(t)$ given by Eq. (2.51) provides a non-general model for the early time behavior of the mixing time scale. Far away from the source, all memory about the initial source conditions is lost and the mechanical-to-scalar time scale ratio eventually asymptotes to a constant as determined by various DNS studies. Hence, the large-time asymptote of the mixing rate $\omega_m^\infty(t)$ is retained to be proportional to the turbulence rate ε/k. The new mixing-rate specification used here is simply a blending of the two asymptotic expressions, which is correct in both the limits, $\omega_m = \omega_m^0$ at $t = 0$ and $\omega_m \to \omega_m^\infty$ as $t \to \infty$.

The above mentioned mixing rate involves only one adjustable parameter, that being the time scale ratio, C_ϕ. Even though the proposed timescale was derived from the transport equation of the integral mean-square of the scalar, model calculations using this time scale not only predict different statistics correctly on the plume centreline but also the radial profiles at different stages in the development of the plume, including higher moments, skewness and kurtosis, for which comparisons are made with the experimental data of Sawford and Tivendale [72] and with the previous calculations of Sawford [70] for the single line source.

The PDF model is applied to a pair of line sources and an array of four line sources and is shown to perform well in comparison to the experimental data. The cross-correlation coefficient between any pair of sources gives an indication of the extent of flapping of the wake and inter-wake interference. These accurate predictions suggest that the effects of molecular diffusion have been incorporated accurately. The modified IECM model is also tested to verify the de-

pendence of the scalar variance decay rate on the distance between the sources in the mandoline with respect to the integral turbulence length scale [90]. The present calculations agree with the experimental data and show that at distances far downstream from the mandoline, the scalar variance decay rate is independent of the length scale ratio when plotted against distance from the mandoline.

The choice of standard values for the model parameters, $C_0 = 2.1$ and $C_\phi = 1.5$ compare well with the experimental observations. Additionally, dispersion from a single line source is studied in greater detail over a range of the parameter space. The effect of the source size is only significant at very small times from the source whereas with a constant C_0 assumption, the effects of Reynolds numbers are evident only at intermediate times. The large-time asymptote of the centerline intensity of fluctuations is independent of both the non-dimensional source size and Reynolds number for the range of parameter space explored, while the maximum value of the centerline fluctuation intensity shows a dependence on Reynolds number but not on the source size. Data from experiments and/or DNS are required to corroborate the model predictions at large Reynolds numbers.

2.7 Acknowledgments

SV would like to thank Professor Warhaft for useful pointers and also Prasad Bhave and Haifeng Wang for insightful discussions during the course of this work. This research is supported by Department of Energy under Grant DE-FG02-90ER. This research was conducted using the resources of the Cornell Uni-

versity Center for Advanced Computing, which receives funding from Cornell University, New York State, the National Science Foundation, and other leading public agencies, foundations, and corporations.

CHAPTER 3

NUMERICAL IMPLEMENTATION OF MIXING AND MOLECULAR TRANSPORT IN LES/PDF STUDIES OF TURBULENT REACTING FLOWS*

3.1 Introduction

The world's energy needs are primarily satisfied by processes that convert the chemical energy stored in the fossil fuels into usable thermal energy. Given the high depletion rate of fuels as compared to the increasing energy needs of growing economies, there is a strong focus on improving the efficiencies of existing facilities by augmenting their designs. Better understanding of the underlying physics behind the turbulent combustion processes inherent in these systems paves a path to designing better systems.

Turbulent combustion involves several species interacting with each other via multiple chemical reactions and with the underlying turbulent flow. Computational fluid dynamics (CFD) based tools [5] have been used to provide various levels of description to address the turbulence closure problem [8] encountered in the modeling of turbulent reacting flows. Reynolds Averaged Navier Stokes (RANS) based approaches were historically chosen since the computation of instantaneous flow fields in a turbulent reacting flow was not possible. Given the wide range of temporal and spatial scales inherent in a reacting flow calculation, a DNS (Direct Numerical Simulation) gives the most detailed level

*S. Viswanathan and S.B. Pope, "Numerical implementation of mixing and molecular transport in LES/PDF studies of turbulent reacting flows", J. Comput. Phys., (*submitted*) (2010)

of description possible by resolving all scales [68]. On the other hand, a LES (Large Eddy Simulation) resolves only the large scales of the turbulent flow while modeling the effects of the small scales [59, 47, 67]. In comparison, DNS is still not computationally tractable for high Reynolds number turbulent flow calculations whereas LES is becoming more commonplace with the development and advancement of high performance computing facilities.

In modeling a turbulent reacting flow, the complexity is magnified multifold by large density variations and highly non-linear chemical reaction rates. Probability Density Function (PDF) [59, 52, 53, 25] methods have been proven to be highly successful in addressing most of the closure problems including closure of the non-linear chemical source terms due to reaction. In the context of LES, based on the filtering operation performed, a PDF analogue called the Filtered Density Function (FDF) [53, 23, 13, 27] is defined. Though there are many variants to the definition of LES, the most dominant approach is based on 'filtering'. Recently, Pope [60] introduced the idea of self-conditioned fields as an alternative to the filtering approach. In this work, we use the framework based on self-conditioned fields and hence, the terminology PDF instead of FDF.

The present work improves and extends the numerical implementation of LES/PDF methods. Specifically, we present a smoothing technique for spatial averaging of estimated statistics, an evaluation of three numerical implementations of the mixing model with molecular transport and a brief study of the effects of differential diffusion in a simple non-reacting mixing problem.

In a composition-PDF approach, although the effects of reaction appear in closed form and need no modeling, the effects of turbulent transport and molec-

ular mixing need to be modeled. Typically, the effects of turbulent transport are modeled using a gradient diffusion hypothesis. To model the effects of molecular diffusion which appear as a conditional scalar dissipation term in the PDF transport equation, various mixing models have been developed. The Interaction by Exchange with the Mean (IEM) model was postulated in the context of chemical reactor engineering [82]. An identical model called the linear mean-square estimation model (LMSE) was proposed independently by [18]. These models are implemented as being local in physical space for inhomogeneous flows. The Interaction by Exchange with the Conditional Mean (IECM) mixing model [56, 22] is designed to be local in velocity space while the Euclidean Minimum Spanning Tree (EMST) mixing model [77] models mixing as being local in composition space. Various other mixing models have been developed such as the MC (Modified Curl) mixing model [16, 17, 28, 51] and MMC (Multiple mapping conditioning) mixing models [33, 11]. In PDF methods, the choice of a mixing model is significant, for instance, to predict local extinction in Sandia flames E and F [9]. However, recent studies have shown that in LES/PDF methods, the subgrid-scale mixing closure provided by the IEM mixing model is adequate in most practical situations [38]. Therefore, in the current work, we employ the IEM mixing model to close the conditional dissipation term in the PDF transport equation.

The modeled PDF transport equation is solved using Lagrangian Monte Carlo particle methods. One of the initial works that established a formal relationship between particle models and PDF methods was by Pope [49]. The Lagrangian particle methods associated with the PDF transport in the form in use today are based on Pope's 1985 paper [52]. Here, the turbulent flow is rep-

resented by a large number of notional particles, all of which are considered to be statistically independent. Models are constructed to evolve the properties of the particles in time. The resulting stochastic differential equations (SDE) are solved to account for particle transport, mixing and reaction. Solving for the evolution of these particles corresponds to the solution of the modeled PDF transport equation. The first use of this approach to LES/PDF is due to Colucci *et. al.* [13].

The conditional diffusion term in the PDF transport equation represents both molecular transport in physical space and molecular mixing in composition space. In most previous studies, the effects of molecular transport are incorporated as a random walk term in the particle transport equation, as first proposed by Anand and Pope [1]. Recently, McDermott and Pope [37] show that modeling the effects of molecular transport as a random walk in the particle position equation results in a spurious production of scalar variance in the DNS limit. They propose an alternative approach to modeling molecular transport as a mean drift term in the particle scalar evolution equation, and this avoids the spurious production of variance. LES studies of a laboratory-scale turbulent flame (Sandia flame D) [31] also show that on reasonably resolved grids, the molecular diffusivity is dominant as compared to the subgrid turbulent diffusivity in the near-field of the jet, indicating that the effects of molecular transport need to be treated accurately in LES/PDF models of turbulent reacting flows.

The current work is based on the models and algorithms implemented in the HPDF code described by Wang *et al* [86]. Micro-mixing is modeled using the IEM mixing model and the effects of molecular transport are modeled as a mean drift term as mentioned above [37]. This modeling strategy has the additional

advantage of being able to account for the effects of differential diffusion. The mixing model is implemented such that problems of interest in both Cartesian and cylindrical coordinate systems can be effectively handled. We also require that the numerical schemes used to implement mixing satisfy the following criteria: 1) they satisfy detailed scalar conservation, 2) they ensure realizability, 3) they are stable and 4) they are accurate.

A typical PDF calculation of a turbulent reacting flow is performed with a nominal number, N_{pc}, of 20-50 particles per finite volume cell. In order to maintain an acceptable distribution of particles in space, various particle number control algorithms are used [25, 63]. The numerical errors associated with a hybrid particle/mesh methodology can be classified broadly into statistical error, bias error, spatial truncation error and temporal discretization error. Among these, the statistical error is of a random nature while the latter three are deterministic and cannot be reduced by averaging. The statistical error scales as $N_{pc}^{-1/2}$ and the bias error scales as N_{pc}^{-1}; and both arise due to the finite number of particles used in the PDF calculations [91, 29, 39]. In previous studies, time averaging has been effectively used in PDF methods [91, 29, 40, 85]. But in LES/PDF, since the fields are not stationary, time averaging cannot be used. In this study, we introduce smoothing, a form of spatial averaging.

In this work, we address the following issues. First, we evaluate for accuracy and computational cost of three numerical implementations of the IEM mixing model with molecular transport incorporated as a mean drift term. Secondly, we describe an implicit smoothing algorithm for variance reduction and assess its efficacy. Finally, we develop a methodology for accurately accounting for the effects of differential diffusion and test this implementation in a simple non-

reacting mixing problem. The new implementations developed and evaluated here represent a significant advance in accuracy and computational efficiency over previous methods, and allow for the accurate representation of molecular diffusion, including differential diffusion.

The rest of this paper is organized as follows. Section §3.2 briefly describes the modeling of molecular transport and mixing and the corresponding PDF transport equation. The details of the numerical implementation of mixing and molecular transport along with the smoothing methodology are elucidated in Sec. §3.3. The Method of Manufactured solutions is detailed in Sec. §3.4 followed by the results from the PDF calculations for a suite of test cases in Sec. §3.5. Sections §3.2–§3.5 concentrate on the case of a single scalar, which is readily generalized to a set of scalars with equal diffusivities. The effects of differential diffusion with multiple scalars inclusive of all the pertaining results are dealt with in Sec. §3.6 and finally, the conclusions are drawn in Sec. §3.7.

3.2 Modeling of mixing and molecular transport

This section elaborates on the modeling of molecular transport and mixing in PDF studies and is divided into two parts. The first part under Sec. §3.2.1 briefly describes the set of SDEs used to evolve particle properties in time. Following this, §3.2.2 discusses the implied PDF transport equation and its moments.

3.2.1 Mixing model

Consider a PDF calculation of a turbulent non-reacting flow in which the fluid is represented by N_{tot} particles. We consider here a single composition, ϕ. The extension to multiple compositions ϕ_α with equal molecular diffusivities follows straightforwardly. The case of unequal diffusivities is considered in Sec. §3.6. The general particle has position $\mathbf{x}^*(t)$, mass $m^*(t)$ and a single composition $\phi^*(t)$. These particle properties are advanced in time by the following set of stochastic differential equations,

$$d\mathbf{x}^*(t) = \left[\widetilde{\mathbf{U}} + \frac{\nabla\bar{\rho}\Gamma_T}{\bar{\rho}}\right]^* dt + \sqrt{2\Gamma_T^*}\, d\mathbf{W}, \tag{3.1}$$

$$d\phi^*(t) = -\Omega_m^*\left(\phi^* - \widetilde{\phi}^*\right) dt + \left[\frac{1}{\bar{\rho}}\frac{\partial}{\partial x_j}\left(\bar{\rho}\Gamma\frac{\partial\widetilde{\phi}}{\partial x_j}\right)\right]^* dt + S^*\, dt, \tag{3.2}$$

where $\widetilde{\mathbf{U}}(\mathbf{x},t)$ is the resolved velocity, $\bar{\rho}(\mathbf{x},t)$ is the density, $\Gamma_T(\mathbf{x},t)$ is the turbulent subgrid-scale diffusivity, $\Gamma(\mathbf{x},t)$ is the molecular diffusivity, $\Omega_m(\mathbf{x},t)$ is the mixing frequency, $S(\mathbf{x},t)$ is the source term due to reaction, $\widetilde{\phi}(\mathbf{x},t) = \langle\phi^*(t) \mid \mathbf{x}^*(t) = \mathbf{x}\rangle$ is the mean composition and $d\mathbf{W}$ is the incremental Wiener process. All quantities denoted with a superscript '$*$' are evaluated at $(\mathbf{x}^*(t),t)$ and particle properties are also denoted with a superscript '$*$'. Einstein's summation convention is followed except for repeated indices in parentheses. As is the notation used in standard LES, an over-line '$\bar{}$' denotes filtering operation and a tilde '$\widetilde{}$' is used to denote density-weighted filtering. Or, following [60], $\overline{\phi}$ can be viewed as a conditional mean, and $\widetilde{\phi}$ the density-weighted conditional mean.

As first observed by McDermott and Pope [37], the mixing step corresponding to Eq. (3.2) has several advantages compared to the IEM mixing model. Firstly, it has the capability to include for the effects of differential diffusion di-

rectly into the mixing step: Eq. (3.2) can be written for different scalars, ϕ^*_α, each having its own molecular diffusivity Γ_α. Secondly, as will be re-emphasized in Sec. §3.2.2, this model which is a combination of the IEM mixing,

$$\frac{d\phi^*(t)}{\partial t} = -\Omega^*_m\left(\phi^* - \widetilde{\phi}^*\right), \tag{3.3}$$

and a mean drift term corresponding to

$$\frac{d\widetilde{\phi}}{\partial t} = \frac{1}{\bar{\rho}}\frac{\partial}{\partial x_j}\left(\bar{\rho}\Gamma\frac{\partial\widetilde{\phi}}{\partial x_j}\right), \tag{3.4}$$

does not give rise to spurious production of scalar variance.

3.2.2 The implied PDF transport equation

The corresponding transport equation for the implied scalar PDF $f_\phi(\psi;\mathbf{x},t)$ (where ψ is the sample space variable for the scalar) can be derived from Eqs. (3.1) and (3.2) as

$$\begin{aligned}\frac{\partial f_\phi}{\partial t} + \frac{\partial}{\partial x_j}\left[f_\phi\left(\widetilde{\mathrm{U}}_j + \frac{1}{\bar{\rho}}\frac{\partial\bar{\rho}\Gamma_T}{\partial x_j}\right)\right] &= \frac{\partial^2\left(\Gamma_T f_\phi\right)}{\partial x_j\partial x_j} + \frac{\partial}{\partial\psi}\left[f_\phi\Omega_m\left(\psi - \widetilde{\phi}\right)\right] \\ &- \frac{\partial}{\partial\psi}\left[f_\phi\frac{1}{\bar{\rho}}\frac{\partial}{\partial x_j}\left(\bar{\rho}\Gamma\frac{\partial\widetilde{\phi}}{\partial x_j}\right)\right] + \frac{\partial}{\partial\psi}\left[f_\phi S\right].\end{aligned} \tag{3.5}$$

Given the transport equation for the PDF, the transport equation for the various implied moments can be obtained. Here, we mention the transport equations for the first two moments of the scalar to be:

$$\frac{\partial\bar{\rho}\widetilde{\phi}}{\partial t} + \frac{\partial\bar{\rho}\widetilde{\mathrm{U}}_j\widetilde{\phi}}{\partial x_j} = \frac{\partial}{\partial x_j}\left[\bar{\rho}(\Gamma_T + \Gamma)\frac{\partial\widetilde{\phi}}{\partial x_j}\right] + \bar{\rho}\widetilde{S}, \tag{3.6}$$

$$\begin{aligned}\frac{\partial\bar{\rho}\widetilde{\phi^2}}{\partial t} + \frac{\partial\bar{\rho}\widetilde{\mathrm{U}}_j\widetilde{\phi^2}}{\partial x_j} &= \frac{\partial}{\partial x_j}\left[\bar{\rho}\Gamma_T\frac{\partial\widetilde{\phi^2}}{\partial x_j}\right] + 2\widetilde{\phi}\frac{\partial}{\partial x_j}\left[\bar{\rho}\Gamma\frac{\partial\widetilde{\phi}}{\partial x_j}\right] \\ &- 2\bar{\rho}\Omega_m\left(\widetilde{\phi^2} - \widetilde{\phi}^2\right) + 2\bar{\rho}\widetilde{S\phi}.\end{aligned} \tag{3.7}$$

From Eqs. (3.6) and (3.7), the transport equation for the subgrid variance of the scalar, $Z = \widetilde{\phi^2} - \widetilde{\phi}^2$ can be obtained as,

$$\begin{aligned} \frac{\partial \bar{\rho} Z}{\partial t} + \frac{\partial \bar{\rho} \widetilde{\mathrm{U}}_j Z}{\partial x_j} &= \frac{\partial}{\partial x_j}\left[\bar{\rho}\Gamma_T \frac{\partial Z}{\partial x_j}\right] - 2\bar{\rho}\Omega_m Z \\ &+ 2\bar{\rho}\Gamma_T \frac{\partial \widetilde{\phi}}{\partial x_j}\frac{\partial \widetilde{\phi}}{\partial x_j} + 2\bar{\rho}\left(\widetilde{S\phi} - \widetilde{S}\widetilde{\phi}\right). \end{aligned} \tag{3.8}$$

Equation (3.8) contains a production term due to turbulent subgrid diffusivity but no production term due to molecular diffusivity. In the DNS limit, the production due to turbulent diffusivity vanishes and there is no production of scalar variance, contrary to a model that includes for the effects of molecular diffusivity as a random walk term in the particle position equation.

In summary, it is to be noted that the particle model comprising of Eqs. (3.1) and (3.2) avoids spurious variance production and has the potential to account for differential diffusion effects.

3.3 Numerical implementation of mixing and molecular transport

The numerical method employed here is the hybrid particle/mesh method [59]. A structured mesh is used to store mean quantities estimated from particle data at the cell center locations, which are then interpolated onto particle locations.

To illustrate some of the issues involved, we describe now a crude numerical implementation of the particle mesh method for a simplified problem. We consider constant-density flow in a one-dimensional periodic domain of length

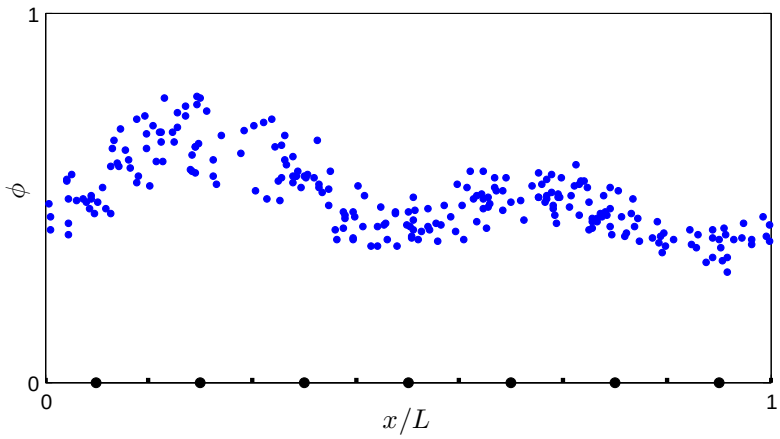

Figure 3.1: Sketch of the periodic domain of length L, showing the particles properties (x^*, ϕ^*); the $N_{cell} = 7$ cells; and the cell centers ●

L with x^* being distributed uniformly. Equations (3.1) and (3.2) reduce to,

$$dx^*(t) = \left[\widetilde{U} + \frac{\partial \Gamma_T}{\partial x}\right]^* dt + \sqrt{2\Gamma_T^*}\, dW, \tag{3.9}$$

$$\frac{d\phi^*(t)}{dt} = -\Omega_m^* \left(\phi^* - \widetilde{\phi}^*\right) + \frac{\partial}{\partial x}\left(\Gamma \frac{\partial \widetilde{\phi}}{\partial x}\right)^* . \tag{3.10}$$

As sketched in Fig. 3.1, the domain is partitioned into N_{cell} cells of width $\Delta x = L/N_{cell}$. Given the particle properties at time t, and given a small time-step Δt, the crude numerical implementation obtains the particle properties at time $t + \Delta t$ through a sequence of processes now described. It is emphasized that this implementation has many deficiencies and is described solely to introduce some of the issues faced in any implementation.

1. Given the values of $\widetilde{U}$, Γ_T and $\partial \Gamma_T / \partial x$ at cell centers, an interpolation scheme is used to obtain the values of the coefficients in Eq. (3.9) at the particle locations. As sketched in Fig. 3.2, possible interpolation schemes

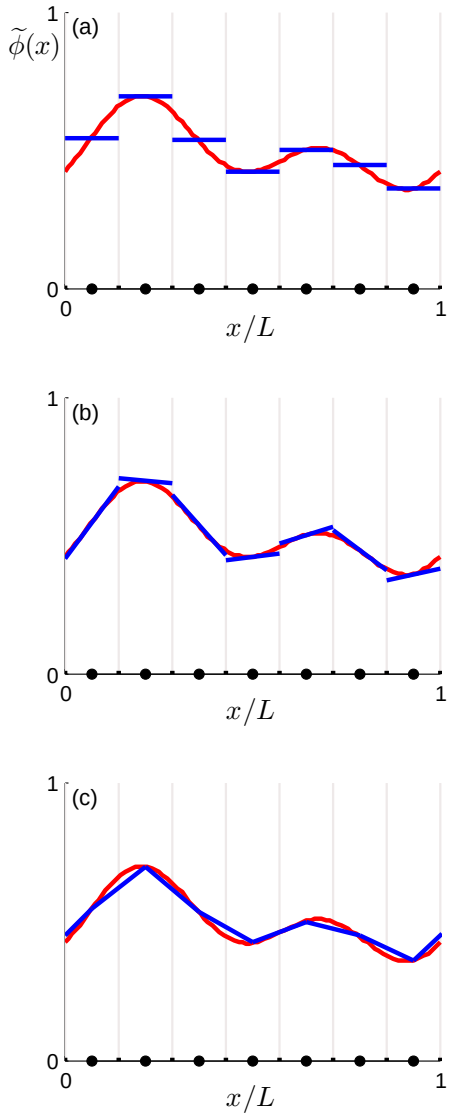

Figure 3.2: Illustration of different interpolation schemes (blue) used to approximate the field $\widetilde{\phi}(x)$ (red). (a) piece-wise constant (PC) (b) piece-wise linear (PL) (c) linear spline (LS)

include: piece-wise constant (PC); piece-wise linear (PL); and linear spline (LS).

2. Advance particle positions by

$$x^*(t+\Delta t) = x^*(t) + \left[\widetilde{\mathrm{U}} + \frac{\partial \Gamma_T}{\partial x}\right]^* \Delta t + (2\Gamma_T^* \Delta t)^{\frac{1}{2}}\, \eta^*, \tag{3.11}$$

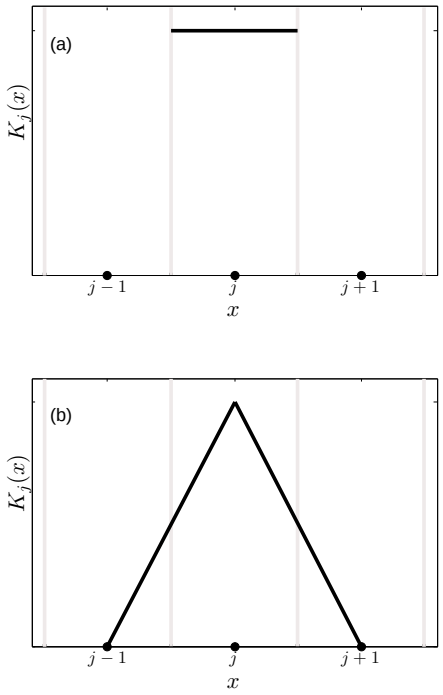

Figure 3.3: Kernels $K_j(x)$ used to estimate means at the center of cell j: (a) PIC (b) CIC.

where η^* is a standardized Gaussian random variable independent for each particle and for each time step.

3. Given the particle compositions $\phi^*(t)$, an estimate $\widehat{\phi}_j$ is made of the mean composition at the j-th cell center. The simplest estimate – termed "particle-in-cell" (PIC) – is the ensemble mean of all particles in the j-th cell. An alternative – termed "cloud-in-cell" (CIC) – is to form the ensemble mean of all particles, weighted by the linear basis function centered at the j-th cell center. Both methods can be viewed as kernel estimators, with the different kernels $K_j(x)$ sketched in Fig. 3.3.

4. To reduce the statistical error in the estimated means at cell centers $\widehat{\phi}_j$, smoothing can be performed, to yield modified estimators $\widetilde{\phi}_j$. This can

most simply be achieved by the explicit three-point smoothing

$$\widetilde{\phi}_j = (1 - 2\beta_s)\widehat{\phi}_j + \beta_s \left(\widehat{\phi}_{j-1} + \widehat{\phi}_{j+1}\right), \tag{3.12}$$

for specified positive β_s (stability requires $\beta_s \leq 0.5$). We can also consider implicit smoothing, the simplest three-point scheme being

$$(1 + 2\alpha_s)\,\widetilde{\phi}_j - \alpha_s \left(\widetilde{\phi}_{j-1} + \widetilde{\phi}_{j+1}\right) = \widehat{\phi}_j, \tag{3.13}$$

for specified positive α_s.

5. Based on the last term in Eq. (3.10), the unsteady heat conduction equation

$$\frac{\partial \widetilde{\phi}}{\partial t} = \frac{\partial}{\partial x}\left(\Gamma \frac{\partial \widetilde{\phi}}{\partial x}\right), \tag{3.14}$$

is integrated for a time Δt by a finite-difference method, starting from the smoothed cell-centered values $\widetilde{\phi}$. The change in the solution over the time-step is referred to as the "mean drift" and its value at the j-th cell center is denoted by $\Delta\widetilde{\phi}_j$.

6. The values of Ω_m, $\widetilde{\phi}$ and $\Delta\widetilde{\phi}$ are interpolated onto the particles, and then Eq. (3.10) is advanced in time by

$$\phi^*(t + \Delta t) = \phi^*(t) + \Delta\widetilde{\phi}^* - \Omega_m^* \Delta t(\phi^*(t) - \widetilde{\phi}^*). \tag{3.15}$$

Having introduced this rudimentary particle-mesh scheme for the simplified one-dimensional problem, we now consider the criteria by which this and other implementations can be appraised.

1. Stability : obviously, unconditional stability is desirable. The above scheme is likely to be unstable if β_s and $\Omega_m \Delta t$ are too large.

2. Accuracy : the numerical errors introduced in this type of particle-mesh scheme include

   (a) A temporal splitting error due to considering simultaneous processes sequentially. The crude splitting scheme above dooms the overall method to first-order temporal accuracy.

   (b) Temporal truncation errors in the sub-steps *e.g.,* Eqs. (3.11), (3.14) and (3.15).

   (c) Spatial truncation errors involved in interpolation and in advancing the heat conduction equation.

   (d) Spatial smearing errors due to the smoothing operation, and the estimation of means.

   (e) Statistical errors due to having a finite total number of particles $\mathrm{N_{tot}}$. For example, the statistical error in the estimated mean $\widehat{\phi}_j$ varies as $\mathrm{N_{pc}^{-1/2}}$, where $\mathrm{N_{pc}} \equiv \mathrm{N_{tot}/N_{cell}}$ is the average number of particles per cell.

   (f) Bias errors, which are deterministic errors due to $\mathrm{N_{tot}}$ being finite.

Thus, a suitably defined root-mean-squared error in the scheme $\mathcal{E}$ can be modeled as

$$\mathcal{E} = a\Delta x^p + b\Delta t^q + c l_s^r + \frac{d}{\mathrm{N_{eff}}} + \frac{e}{\sqrt{\mathrm{N_{eff}}}}, \tag{3.16}$$

where a, b, c, d and e are constants and the terms on the right-hand side represent, respectively: spatial truncation error; temporal errors; smearing error, where l_s is the smearing length-scale associated with the smoothing (determined by α_s and β_s); bias, where $\mathrm{N_{eff}}$ is an effective number of particles used to estimate means; and statistical error. If no smoothing

is used, then N_{eff} equals N_{pc}; with smoothing, N_{eff} increases with l_s. The scheme described above is most likely first-order accurate in space and time ($p = 1, q = 1, r = 1$), whereas the method described below is second-order accurate ($p = 2, q = 2, r = 2$).

3. Computational cost: this is normally dominated by the work that scales linearly with the number of particles, N_{tot}, the work which scales with the number of cells being small in comparison.

4. Conservation : it follows from Eq. (3.10) that the sum of $\phi^*(t)$ over all particles is conserved. It is desirable that a numerical implementation have this same conservation property. The scheme above is not conservative.

5. Boundedness : composition variables such as mixture fraction and species mass fractions are bounded; in particular, they are non-negative. Subject to Ω_m being greater than a known lower limit, Eq. (3.10) satisfies boundedness which can be stated as,

$$\min\{\phi^*(t)\} \leq \phi^*(t + \Delta t) \leq \max\{\phi^*(t)\}. \tag{3.17}$$

6. Continuity: the mean composition $\widetilde{\phi}(x, t)$ implied by Eqs. (3.9) and (3.10) is smooth (as is the PDF of ϕ^*), provided that the coefficients vary smoothly. Discontinuous interpolation schemes (PC and PL) introduce discontinuities in the solution, which may be undesirable.

The most accurate scheme presented below (denoted CIC-LS with smoothing) has the following attributes: it is unconditionally stable, second-order accurate in space and time, the statistical error scales as $N_{tot}^{-1/2}$ (as opposed to $N_{pc}^{-1/2}$), it satisfies conservation and boundedness, and yields continuous solutions.

The following sub-sections describe the details of the numerical method used in this work and is organized as follows. The first part §3.3.1 elaborates on the splitting scheme adopted. The primary focus of this section is on the implementation of mixing and molecular transport. Section §3.3.2 details two mean estimation methods while Sec. §3.3.3 presents three interpolation schemes and finally, the fourth section focuses on the details of the smoothing algorithm.

3.3.1 Splitting Scheme

Given the stochastic differential equations used to advance particle properties in time [Eqs. (3.1) and (3.2)], the following Strang's splitting scheme is used to solve for particle transport $\mathbb{T}$, reaction $\mathbb{R}$ and mixing $\mathbb{M}$. The mixing step here refers to the combination of IEM mixing and the mean drift due to molecular transport. The splitting scheme [87] considered here is of the type, $\mathbb{TMRMT}$, where each of the transport and mixing sub-steps are performed twice each for half the time step, Δt, and the reaction step is performed once for one complete time step. The coefficients in the SDEs are evaluated at the mid-point of the time interval and since the scheme is symmetric, second-order temporal accuracy is achieved [87].

The mixing step $\mathbb{M}$ consists of two sub-steps – IEM mixing $\mathbb{I}$ and estimation of mean drifts due to molecular diffusivity $\mathbb{D}$. Following [37], the mixing step $\mathbb{M}$ is solved using the splitting scheme, $\mathbb{IDI}$. The various quantities required to perform one step of mixing, such as Ω_m and Γ, are evaluated at the particle locations at the mid-point of the time step. This yields a one-step update for the particle scalar ϕ discussed below.

Consider advancing the scalar ϕ^* carried by the particle over a time step of Δt from time $t_n = n\Delta t$ to $t_{n+1} = (n+1)\Delta t$. As mentioned earlier, the mixing frequency Ω_m and molecular diffusivity Γ are known at the time level $t_{n+\frac{1}{2}} = (n+\frac{1}{2})\Delta t$. Given that the scalar mean $\widetilde{\phi}^n$ and the mean drift, $\Delta\widetilde{\phi}^{n+\frac{1}{2}} = \widetilde{\phi}^{n+1} - \widetilde{\phi}^n$ are known at particle locations, the one-step update [37] for the particle scalar can be written as,

$$\phi^{*,n+1} = \phi^{*,n} + c^{*,n+\frac{1}{2}}\left(\widetilde{\phi}^{*,n} - \phi^{*,n}\right) + \Delta\widetilde{\phi}^{*,n+\frac{1}{2}}, \tag{3.18}$$

where

$$c^{n+\frac{1}{2}} = 1 - \exp\left(-\Omega_m^{n+\frac{1}{2}}\Delta t\right). \tag{3.19}$$

With details provided in subsequent subsections, the specific steps involved in implementing Eq. (3.18) to advance the particle scalar over a time step, $\Delta t = t_{n+1} - t_n$ are:

1. The mixing frequency $\Omega_m^{n+\frac{1}{2}}$ available at the cell centers of the PDF mesh is used to calculate $c^{n+\frac{1}{2}}$ at cell centers using Eq. (3.19)
2. The quantity $c^{n+\frac{1}{2}}$ is interpolated onto particle locations to obtain $c^{*,n+\frac{1}{2}}$ using any one of the interpolation methods given by Eqs. (3.25), (3.26) or (3.28).
3. Particle weights w^* defined by

   $$w^* = m^* c^*, \tag{3.20}$$

   are evaluated.
4. Given particle scalar $\phi^{*,n}$ at time level n and the weights w^*, the scalar means $\widehat{\phi}^n$ are estimated at the cell centers (Eq. (3.23)) along with the cell weights w using Eq. (3.24) defined below.

5. The estimates $\widehat{\phi}^n$ of the scalar means are smoothed with weights w to obtain smoothed estimates of the means $\widetilde{\phi}^n$ as given by Eq. (3.32) with $f = \widehat{\phi}^n$ and $g = \widetilde{\phi}^n$ with the specification given by Eq. (3.45-3.48).
6. The mean drifts $\Delta\widetilde{\phi}^{n+\frac{1}{2}}$ are calculated from $\widetilde{\phi}^n$ using Eq. (A.15) elaborated in Appendix A.1.
7. The boundedness condition is imposed on $c^{*,n+\frac{1}{2}}$ using Eq. (C.4).
8. Steps 3-5 are repeated with the modified values of $c^{*,n+\frac{1}{2}}$.
9. The mean drifts $\Delta\widetilde{\phi}^{n+\frac{1}{2}}$ and the smoothed means $\widetilde{\phi}^n$ are interpolated onto particle locations to obtain $\Delta\widetilde{\phi}^{*,n+\frac{1}{2}}$ and $\widetilde{\phi}^{*,n}$, respectively, from Eq. (3.25), (3.26) or (3.28).
10. Finally, the one-step particle scalar update, Eq. (3.18), is performed.

For the most part, we consider the case of uniform particle masses, particularly in the analysis of the scheme. In practice, non-uniform particle masses are used, and there is no difficulty in applying the method in such cases. The algorithm indicates that the following operations need to be performed: 1) Estimation of means given particle properties, 2) Estimation of mean drifts 3) Interpolation of mean quantities to particle locations and 4) Smoothing. The following subsection describes the two numerical schemes used for mean estimation.

3.3.2 Estimation of means

In this section, we present the details of two numerical schemes used to estimate the means from particle properties *viz.*, Particle-in-Cell (PIC) and Cloud-in-Cell

(CIC) based on a uniform Cartesian grid, equal in each direction. However, the methods are not restricted to this specific case. Consider $\mathbf{x}_j$ to denote the cell center locations of the PDF mesh with cell volume Δx^3. Let $\mathbf{e} = (\mathbf{e}_1, \mathbf{e}_2, \mathbf{e}_3)$ denote the unit vectors in the three coordinate directions.

Let us define the indicator function for the cell centered at $\mathbf{x}_j$, denoted $\mathbf{I}_j(\mathbf{y})$ as $\mathbf{I}_j(\mathbf{y}) = \prod_{k=1}^{3} \mathrm{I}_{j,k}(\mathbf{y})$ where,

$$\mathrm{I}_{j,k}(\mathbf{y}) = \begin{cases} 1, \text{ for } \mid (\mathbf{y} - \mathbf{x}_j).\mathbf{e}_k \mid < \Delta x/2 \\ 0, \text{ otherwise.} \end{cases} \tag{3.21}$$

Similarly, consider linear B-spline basis functions $\mathbf{B}_j(\mathbf{y})$ for the cell centered at $\mathbf{x}_j$ to be defined as $\mathbf{B}_j(\mathbf{y}) = \prod_{k=1}^{3} \mathrm{B}_{j,k}(\mathbf{y})$ with

$$\mathrm{B}_{j,k}(\mathbf{y}) = \begin{cases} 1 - \dfrac{\mid (\mathbf{y} - \mathbf{x}_j).\mathbf{e}_k \mid}{\Delta x/2}, \text{ for } \mid (\mathbf{y} - \mathbf{x}_j).\mathbf{e}_k \mid < \Delta x/2 \\ 0, \text{ otherwise.} \end{cases} \tag{3.22}$$

For particle weights w^* given by Eq. (3.20), the mean $\widehat{\phi}_j$, at a cell centered at $\mathbf{x}_j$ is estimated from particles as,

$$\widehat{\phi}_{(j)} w_{(j)} = \sum_p \mathbf{K}_j(\mathbf{x}_p^*) w_p^* \phi_p^*, \tag{3.23}$$

where w_j, the weight associated with that cell is estimated as,

$$w_j = \sum_p \mathbf{K}_j(\mathbf{x}_p^*) w_p^*, \tag{3.24}$$

for some kernel-estimation method with kernel $\mathbf{K}_j$ and the index p runs over all the particles in the PDF domain. We show later in Appendix C.2 that w^* defined by Eq. (3.20) satisfied detailed conservation. The PIC scheme is obtained for $\mathbf{K}_j = \mathbf{I}_j$ and likewise, $\mathbf{K}_j = \mathbf{B}_j$ gives rise to the CIC scheme [37].

3.3.3 Interpolation onto particles

In this section, the three schemes – piecewise-constant (PC), piecewise-linear (PL) and linear splines (LS) – used to interpolate mean quantities onto particle locations are detailed. Piecewise-constant interpolation is the simplest but is only first-order accurate. Piecewise-linear interpolation is second-order accurate and an improvement on piecewise-constant interpolation. Neither piecewise-constant interpolation nor piecewise-linear interpolation results in continuous fields. Interpolation using linear splines satisfies both second-order accuracy and continuity. The details of each of the interpolation schemes are now presented:

Piecewise-constant (PC) interpolation of $\widetilde{\phi}$ onto a particle located at $\mathbf{x}_p^*$ is performed as,

$$\widetilde{\phi}_p^* = \sum_j \mathbf{I}_j(\mathbf{x}_p^*)\widetilde{\phi}_j, \tag{3.25}$$

while interpolation using linear spline basis functions (LS) is achieved by,

$$\widetilde{\phi}_p^* = \sum_j \mathbf{B}_j(\mathbf{x}_p^*)\widetilde{\phi}_j. \tag{3.26}$$

The PC and the LS schemes can be jointly represented using $\mathbf{K}_j$ defined in Sec. §3.3.2 as,

$$\widetilde{\phi}_p^* = \sum_j \mathbf{K}_j(\mathbf{x}_p^*)\widetilde{\phi}_j. \tag{3.27}$$

The third interpolation scheme – the piecewise linear (PL) interpolation – is formulated as,

$$\widetilde{\phi}_p^* = \sum_j \mathbf{I}_j(\mathbf{x}_p^*)\widetilde{\phi}_j + \zeta \sum_j \mathbf{I}_j(\mathbf{x}_p^*)\left(\mathbf{x}_p^* - \bar{\mathbf{x}}_j\right).\boldsymbol{\nu}_j, \tag{3.28}$$

where $\bar{\mathbf{x}}_j$ is given by,

$$\bar{\mathbf{x}}_j = \frac{\sum_p \mathbf{I}_j(\mathbf{x}_p^*) w_p^* \mathbf{x}_p^*}{\sum_p \mathbf{I}_j(\mathbf{x}_p^*) w_p^*}, \tag{3.29}$$

and $\boldsymbol{\nu}_j$ (an approximation to $\nabla\widetilde{\phi}_j$ when the interpolant is $\widetilde{\phi}$) is given by,

$$\boldsymbol{\nu}_j = \mathbf{e}_k \delta_k \widetilde{\phi}_j. \tag{3.30}$$

In Eq. (3.30), δ_k denotes the central-differencing operator in the k-th direction. In Eq. (3.28), the parameter ζ is taken to be the maximum value of $\tilde{\zeta} \in [0, 1]$ such that $\widetilde{\phi}^*$ satisfies the boundedness condition given by Eq. (3.17). To compare the three interpolation schemes, it is to be noted that while both PC and LS interpolation schemes naturally satisfy boundedness criterion, PL requires ζ to explicitly impose the boundedness condition.

Thus, there are two mean estimation methods and three interpolation schemes. Due to the conservation criterion given by Eq. (C.1), only three combinations are considered in this work. The following combinations of schemes satisfy detailed conservation: PIC-PC, PIC-PL and CIC-LS as shown in Appendix C. The properties of each of these schemes are summarized in Table 3.1. All calculations shown in Sec. 3.5.1 are aimed at evaluating these three numerical implementations of mixing and molecular transport for efficiency and accuracy. Next, we present the details of the implicit smoothing scheme developed.

3.3.4 Smoothing

Several 'variance reduction' techniques have been described in previous studies [91, 29, 40, 85]. But these variance reduction techniques are presented as

Table 3.1: Comparison of the various numerical schemes against the set of criteria listed in Sec. §3.3. The symbols refer to: ✔ naturally satisfied; ❍ imposed; ✘ does not satisfy.

Property	PIC-PC	PIC-PL	CIC-LS
Conservation	✔	❍	✔
Boundedness	✔	❍	✔
Continuity	✘	✘	✔
Unconditional Stability	✔	✔	✔
Second order accuracy	✘	✔	✔

time-averaging methods that are suitable to be used with statistically-stationary flows. In LES/PDF methods, the fields are not statistically stationary and therefore, time-averaging cannot be used. Here, we present a smoothing algorithm based on spatial averaging. There are two types of quantities of interest to us that need smoothing - quantities used for output, referred to as "output quantities" and those that are fed back into the calculation, referred to as "feedback quantities". Of specific interest in this work are quantities fed back into the mixing model, such as the scalar means.

A variance reduction method, intended to be used in conjunction with the numerical implementation of a mixing model, should be formulated such that the operation is conservative, ensures boundedness and preserves regularity of the input fields. Moreover, the smearing error incurred (due to spatial averaging) should be small. In this section, we elaborate on an implicit smoothing methodology derived based on the heat diffusion equation. First, Sec. §3.3.4.1 introduces this smoothing scheme. Following this, Sec. §3.3.4.2 lists the properties of the smoothing scheme. Finally, Sec. §3.3.4.3 and §3.3.4.4 elaborate on the

specification of the smoothing operator and its interpretation.

3.3.4.1 A brief introduction

Consider, in one-dimensional space, a periodic domain of size L. Consider a discrete set of points given by $\mathbf{x}_j$ with uniform spacing Δx. We are given a noisy input function, $f_j = f(\mathbf{x}_j)$, at each of these points and we want to form a smoothed version of it, $g_j = g(\mathbf{x}_j)$, such that the variance of g is less than the variance of f. Such a smoothing scheme can be obtained as a solution to the heat conduction equation. It is to be noted that the smoothing operation can be performed either explicitly or implicitly or a combination thereof, as shown in Appendix B.1, but here we focus on the implicit smoothing methodology. Therefore, at each $\mathbf{x}_j$, g_j is defined as

$$(W_{ij} + A_{ij})g_j = W_{ij}f_j, \tag{3.31}$$

which we re-write in an obvious matrix notation as

$$(W + A)g = Wf, \tag{3.32}$$

where $W = \text{diag}(w_i)$ represents the weights ascribed to each of the grid points, $\mathbf{x}_j$ and the matrix A is the implicit smoothing matrix, parametrized by the smoothing parameter α_s. The particulars regarding the specification of each of the matrices are detailed in Sec. 3.3.4.3. Note that Eq. (3.13) is a particular form of Eq. (3.32), in which the weights are unity, and A is symmetric, tri-diagonal, with components $[-\alpha_s \;\; 2\alpha_s \;\; -\alpha_s]$.

For multi-dimensional problems, the smoothing algorithm is implemented using the Locally One Dimensional (LOD) variant of the Alternating Direction

Implicit (ADI) scheme (Appendix A) appropriately adapted to the smoothing methodology. In the LOD scheme, the smoothing algorithm is applied in each direction successively thus approximating the solution to a multi-dimensional problem by a collection of successive solutions to an equivalent system of one-dimensional problems. Therefore, the subsequent sections describe the details of the smoothing methodology in one dimension.

3.3.4.2 Properties

We require the following properties of the smoothing matrix, A, and the weight matrix, W:

$$A_{ij} \leq 0,\ i \neq j \tag{3.33}$$

$$\sum_i A_{ij} = 0 \tag{3.34}$$

$$A_{ij} = A_{ji} \tag{3.35}$$

$$\det(W + A) \neq 0 \tag{3.36}$$

$$W_{ij} = 0,\ i \neq j \tag{3.37}$$

$$W_{ii} \geq 0. \tag{3.38}$$

We then deduce the following properties of g:

- Conservation : Conservation requires that the weighted sum of the input field f equals the weighted sum of the smoothed field g. Consider summing over all rows of Eq. (3.31) as,

$$\sum_i w_i g_i + \sum_j \sum_i A_{ij} g_j = \sum_i w_i f_i. \tag{3.39}$$

Using the property that the elements of a given column of A sum to zero, given by Eq. (3.34), reduces the second term in Eq. (3.39) to zero and therefore,

$$\sum_i w_i g_i = \sum_i w_i f_i, \tag{3.40}$$

showing that smoothing satisfies the conservation criterion.

- Boundedness : The operation of smoothing should preserve the boundedness of the input quantities. Let us again consider Eq. (3.31) to be re-expressed as,

$$(w_i + A_{ii})g_i = w_i f_i - \sum_{j \neq i} A_{ij} g_j \tag{3.41}$$

$$g_i = \mu_i f_i + \sum_{j \neq i} \mu_j g_j, \tag{3.42}$$

where,

$$\mu_i = \frac{w_i}{w_i + A_{ii}} \tag{3.43}$$

$$\mu_j = -\frac{A_{ij}}{w_i + A_{ii}},\ i \neq j. \tag{3.44}$$

It follows that μ is a partition of unity *i.e.* $\mu_j \geq 0$, $\sum_j \mu_j = 1$. Then Eq. (3.42) shows that g_i is a convex combination of f_i and g_j for $i \neq j$ and it follows that g_i cannot be an isolated vertex of the convex hull $\text{conv}(f, g)$ and hence g_i is in $\text{conv}(f)$. Thus g_i satisfies the boundedness condition.

3.3.4.3 Details of the smoothing scheme

Various families of smoothing schemes are briefly mentioned in Appendix B.1 but the three-point implicit smoothing scheme is considered in this work and

is the focus of the current section. Consider a three-point implicit smoothing scheme parametrized by α_s with the following definitions for A and W:

$$A_{j,j-1} = -\alpha_s \frac{w_{j-1} + w_j}{2}, \tag{3.45}$$

$$A_{j,j+1} = -\alpha_s \frac{w_{j+1} + w_j}{2}, \tag{3.46}$$

$$A_{jj} = -(A_{j,j-1} + A_{j,j+1}), \tag{3.47}$$

$$W_{jj} = w_j. \tag{3.48}$$

This specification for A and W is conservative and ensures boundedness. The implication of α_s becomes evident upon considering the length scales associated with the smoothing operation and is elaborated in the following section.

3.3.4.4 Length scales in smoothing

The process of smoothing results in the spatial smearing of the input fields as it achieves a non-trivial reduction in its variance. We define two relevant length scales: l_s associated with smearing; and l_v associated with variance reduction. We perform the analysis for smoothing with unity weights in one-dimension for simplicity but the analysis is not restricted to this specific case.

Consider a three-point implicit smoothing scheme with unity weights in one-dimension such that Eq. (3.32) reduces to

$$(I + A)g = f. \tag{3.49}$$

Further, we define an equivalent explicit smoothing operator $C \equiv (I + A)^{-1}$ and represent Eq. (3.49) as

$$g = Cf, \tag{3.50}$$

whose Fourier transform is given by Eq. (B.12). Given the Fourier transform $\hat{C}(\kappa; \Delta x)$ of C in Eq. (B.13) in terms of the wave-number κ and grid spacing Δx, we deduce the following properties of C:

- The zeroth moment M_0 is unity or equivalently,

$$M_0 = \hat{C}(0; \Delta x) = 1. \tag{3.51}$$

- The second moment evaluates to

$$M_2 = -\left(\frac{\partial^2 \hat{C}}{\partial \kappa^2}\right)_{\kappa=0} = 2\alpha_s \Delta x^2. \tag{3.52}$$

- All the odd moments are zero,

$$M_{2n+1} = \left(\frac{\partial^{2n+1} \hat{C}}{\partial \kappa^{2n+1}}\right)_{\kappa=0} = 0, \text{for } n \geq 0. \tag{3.53}$$

We then define l_s such that the second moment, M_2 is obtained as,

$$M_2 \equiv \frac{1}{8} l_s^2. \tag{3.54}$$

The reason for the proportionality constant of 8 in Eq. (3.54) becomes clear below. Comparing Eq. (3.54) with Eq. (3.52) we obtain l_s to be,

$$\frac{l_s}{\Delta x} = \gamma \equiv 4\sqrt{\alpha_s}. \tag{3.55}$$

Next, the length scale l_v associated with variance reduction V is defined such that the variance reduction :

$$V \equiv \frac{\text{var}(f)}{\text{var}(g)}, \tag{3.56}$$

due to smoothing in a D-dimensional space is obtained as,

$$V \equiv \left(1 + \frac{l_v}{\Delta x}\right)^D. \tag{3.57}$$

The variance reduction is described exactly in B.3. Therefore, by equating Eq. (3.57) with Eq. (B.27), l_v can be obtained as,

$$\frac{l_v}{\Delta x} = \frac{(1+4\alpha_s)^{3/2}}{1+2\alpha_s} - 1, \tag{3.58}$$

for a three-point implicit smoothing operation. With this definition, $l_v/\Delta x$ tends to zero as $l_s/\Delta x$ tends to zero.

An approximation to $l_v/\Delta x$ is,

$$\frac{l_v}{\Delta x} \approx \frac{l_{va}}{\Delta x} \equiv \frac{\gamma^2}{\sqrt{16+\gamma^2}}. \tag{3.59}$$

This approximation is accurate to within 10%, and yields the correct limits for small and large γ. It is to be noted that for large γ, we have $l_v/\Delta x \sim \gamma = l_s/\Delta x$.

Moreover, for the case $f = \widehat{\phi}$, where $\widehat{\phi}$ is the unsmoothed estimate of the scalar mean based on $\mathrm{N_{pc}}$ particles, $\mathrm{var}(f) \sim \mathrm{N_{pc}^{-1}}$. We then define $\mathrm{N_{eff}}$ such that,

$$V = \frac{\mathrm{N_{eff}}}{\mathrm{N_{pc}}}. \tag{3.60}$$

As a result, Eqs. (3.57) and (3.60) yield,

$$\mathrm{N_{eff}} = \mathrm{N_{pc}}\left(1 + \frac{l_v}{\Delta x}\right)^D, \tag{3.61}$$

$$\approx \mathrm{N_{pc}}\left(1 + \frac{\gamma^2}{\sqrt{16+\gamma^2}}\right)^D. \tag{3.62}$$

As presented in Sec. §3.5, we are interested in modeling the error (suitably defined) calculated based on the estimates of mean quantities. Since, the error analysis is more conveniently done with non-dimensional parameters, we define $l = l_s/L$, $h = \Delta x/L$ and $\tau = \Delta t/T$ where T is the total time for which a calculation is performed. Consequently, the effective number of particles, $\mathrm{N_{eff}}$ is

obtained from Eq. (3.62) as,

$$\mathrm{N_{eff}} = \mathrm{N_{tot}} \left(h + \frac{l^2}{\sqrt{16h^2 + l^2}} \right)^D . \tag{3.63}$$

In summary, a three-point implicit smoothing scheme is presented which satisfies conservation and boundedness criteria. Additionally, as is shown in Appendix B.1, the scheme is also successful in handling empty cells properly, and thereby preserves the regularity of input fields. The choice of α_s follows directly from the choice of the normalized smoothing length scale, l. Large values of l (as compared to h) result in large reductions in the variance. But, a large reduction in the variance is always accompanied by a large smearing error indicating the existence of an optimal choice of l (or, equivalently, for α_s).

3.4 The Method of Manufactured Solutions

The Method of Manufactured Solutions (MMS) [64, 65] is extensively used in the current work to appraise the different numerical schemes presented in Sec. §3.3 and this section provides a brief description of the methodology. MMS was originally used to verify the numerical solutions of partial differential equations by manufacturing analytical solutions to the set of equations being solved [66, 20]. In [87], this method is extended for use in the verification of Monte Carlo particle methods. We follow an identical procedure in this work.

In order to advance particle properties in time using Eqs. (3.1) and (3.2), the coefficients $\bar{\rho}$, $\widetilde{\mathrm{U}}$, Γ, Γ_T, Ω_m are required. In the MMS, these quantities are specified as functions of $\mathbf{x}$ and t. Additionally, constants $\mathrm{R_o}$ and $\mathrm{J_o}$ are specified to

facilitate a simple closure for reaction, $S(\phi)$, using a linear model [87]:

$$S(\phi) = \mathrm{R_o}(\phi - \mathrm{J_o}). \tag{3.64}$$

In addition, the manufactured mean $\overline{\phi}_m$ and variance $\overline{\phi'^2}_m$ fields are also specified. Then additional source terms $S_m(\mathbf{x}, t)$ and $S_v(\mathbf{x}, t)$ are defined such that $\overline{\phi}_m$ and $\overline{\phi'^2}_m$ satisfy the following equations:

$$\begin{aligned}
\frac{\partial \bar{\rho}\overline{\phi}_m}{\partial t} + \frac{\partial \bar{\rho}\widetilde{\mathrm{U}}_j\overline{\phi}_m}{\partial x_j} &= \frac{\partial}{\partial x_j}\left[\bar{\rho}(\Gamma_T + \Gamma)\frac{\partial \overline{\phi}_m}{\partial x_j}\right] + \bar{\rho}\mathrm{R_o}(\overline{\phi}_m - \mathrm{J_o}) + \bar{\rho}S_m, && (3.65)\\
\frac{\partial \bar{\rho}\overline{\phi'^2}_m}{\partial t} + \frac{\partial \bar{\rho}\widetilde{\mathrm{U}}_j\overline{\phi'^2}_m}{\partial x_j} &= \frac{\partial}{\partial x_j}\left[\bar{\rho}\Gamma_T\frac{\partial \overline{\phi'^2}_m}{\partial x_j}\right] - 2\bar{\rho}\Omega_m\overline{\phi'^2}_m + 2\bar{\rho}\Gamma_T\frac{\partial \overline{\phi}_m}{\partial x_j}\frac{\partial \overline{\phi}_m}{\partial x_j} \\
&+ 2\bar{\rho}\mathrm{R_o}\overline{\phi'^2}_m + \bar{\rho}S_v. && (3.66)
\end{aligned}$$

These equations correspond to Eqs. (3.6) and (3.7) but with the addition of the source terms. The second moment is then obtained as,

$$\overline{\phi^2}_m = \overline{\phi}_m^2 + \overline{\phi'^2}_m. \tag{3.67}$$

The transport equation for the corresponding PDF, $g_\phi(\psi; \mathbf{x}, t)$ is obtained as,

$$\begin{aligned}
\frac{\partial g_\phi}{\partial t} + \frac{\partial}{\partial x_j}\left[g_\phi\left(\widetilde{\mathrm{U}}_j + \frac{1}{\bar{\rho}}\frac{\partial \bar{\rho}\Gamma_T}{\partial x_j}\right)\right] &= \frac{\partial^2\left(\Gamma_T g_\phi\right)}{\partial x_j \partial x_j} + \frac{\partial}{\partial \psi}\left[g_\phi\Omega_m\left(\psi - \widetilde{\phi}\right)\right] - \frac{1}{\bar{\rho}}\frac{\partial}{\partial x_j}\left[\bar{\rho}\Gamma\frac{\partial \widetilde{\phi}}{\partial x_j}\right]\frac{\partial g_\phi}{\partial \psi} \\
&+ \frac{\partial}{\partial \psi}\left(g_\phi S\right) - S_m\frac{\partial g_\phi}{\partial \psi} + \frac{\partial}{\partial \psi}\left[g_\phi\Omega_v\left(\psi - \widetilde{\phi}\right)\right], \qquad (3.68)
\end{aligned}$$

where $\Omega_v = -S_v/2\overline{\phi'^2}_m$ and the implied particle model for scalar evolution can be derived to be,

$$\begin{aligned}
d\phi^*(t) &= -\Omega_m^*\left(\phi^* - \widetilde{\phi}^*\right)dt + \left[\frac{1}{\bar{\rho}}\frac{\partial}{\partial x_j}\left(\bar{\rho}\Gamma\frac{\partial \widetilde{\phi}}{\partial x_j}\right)\right]^* dt + S(\phi^*)\,dt \\
&\quad -\Omega_v^*\left(\phi - \widetilde{\phi}^*\right)dt + S_m^* dt. \qquad (3.69)
\end{aligned}$$

The particle position equation given by Eq. (3.1) does not change with the method of manufactured solutions. Given Eq. (3.1) and (3.69), the particle

evolution is implemented using the second order accurate splitting scheme $\mathbb{T}\mathbb{M}^s\mathbb{V}^s\mathbb{M}\mathbb{R}\mathbb{M}\mathbb{V}^s\mathbb{M}^s\mathbb{T}$, where $\mathbb{M}^s$ refers to the increment due to the mean source term S_m and $\mathbb{V}^s$ refers to the increment due to the variance source term S_v. Finally, the implementation is verified by investigating the convergence properties in the first and second moments of the scalar against the analytical solutions manufactured by MMS.

3.4.1 Definition of error

Next, we define a measure of error used for weak convergence studies. The error is measured on the same mesh as the PDF mesh and, typically, multiple independent trials are performed to estimate various statistics. The error is defined based on the volume averaged estimate (over a PDF cell) of the scalar moments and their exact MMS counterparts identical to the definition presented in [87]. Consider T to be the time over which the convergence study is performed and $\langle . \rangle$ to represent volume-averaged quantities. Let $\langle \overline{\phi_m^q} \rangle_i$ denote the volume-averaged manufactured q-th scalar moment (for $q = 1$ and 2) at time T in the i-th cell and let $\langle \overline{\phi^q} \rangle_{i,k}$ be the corresponding smoothed (with smoothing length scale l) estimate of the q-th scalar moment obtained by averaging ϕ^q at the same time T over an ensemble of $\mathrm{N_{i,k}}$ particles in the i-th cell in the k-th trial defined by:

$$\langle \overline{\phi^q} \rangle_{i,k} = \left[\frac{1}{\mathrm{N}_{i,k}} \sum_{p=1}^{\mathrm{N}_{i,k}} \left(\phi_p^*(T) \right)^q \right]_l , \tag{3.70}$$

We define the error in the estimated q-th scalar moment at time T in the i-th cell on the k-th trial as,

$$e_{q,i,k} = \langle \overline{\phi_m^q} \rangle_i - \langle \overline{\phi^q} \rangle_{i,k}. \tag{3.71}$$

A PDF calculation is performed with a finite number of particles and the local error $e_{q,i,k}$ can be approximated to be a random variable with a normal distribution as,

$$e_{q,i,k} = \mu_{q,i} + \sigma_{q,i}\,\eta_{q,i,k} \quad \text{with} \tag{3.72}$$

$$\eta_{q,i,k} \overset{\text{D}}{=} \mathcal{N}(0,1). \tag{3.73}$$

The deterministic error $\mu_{q,i}$ is comprised of contributions primarily from three sources: spatial discretization error, temporal discretization error and bias error which scales as $\mathrm{N}_{\mathrm{pc}}^{-1}$ for $l = 0$. The smoothing operation incurs an additional smearing error. The random error $\sigma_{q,i}$ is a measure of the statistical error in the estimate (Eq. 3.70) and it scales as $\mathrm{N}_{\mathrm{pc}}^{-1/2}$ for $l = 0$. We now define the following three global errors with $\mathrm{N}_{\mathrm{cell}}$ being the total number of cells:

$$\mathcal{E}_{d,q} = \left[\frac{1}{\mathrm{N}_{\mathrm{cell}}}\sum_{i=1}^{\mathrm{N}_{\mathrm{cell}}}\mu_{q,i}^2\right]^{\frac{1}{2}}, \tag{3.74}$$

$$\mathcal{E}_{s,q} = \left[\frac{1}{\mathrm{N}_{\mathrm{cell}}}\sum_{i=1}^{\mathrm{N}_{\mathrm{cell}}}\sigma_{q,i}^2\right]^{\frac{1}{2}}, \tag{3.75}$$

$$\begin{aligned}\mathcal{E}_q &= \left[\mathcal{E}_{d,q}^2 + \mathcal{E}_{s,q}^2\right]^{\frac{1}{2}} \\ &= \left[\frac{1}{\mathrm{N}_{\mathrm{cell}}}\sum_{i=1}^{\mathrm{N}_{\mathrm{cell}}}\left(\mu_{q,i}^2 + \sigma_{q,i}^2\right)\right]^{\frac{1}{2}}.\end{aligned} \tag{3.76}$$

The definition of the global error given by Eq. (3.74) is a measure of the deterministic global error in the estimate of the q-th scalar moment and is used for convergence studies. Equation (3.75) is a measure of the global statistical error in the q-th moment of the scalar. The definition in Eq. (3.76) is a measure of the root-mean-squared error in the q-th moment of the scalar and is used to study the efficacy of smoothing.

It is to be noted that in statistical sciences, typically, the mean squared error

is used for all analyzes for it is more convenient to perform optimization using the mean squared error. On the other hand, the root mean squared error has the advantage of having the same units as the quantity under consideration. Therefore, in this study, we choose the root-mean-squared error for all further purposes.

In summary, this section presents the numerical methodologies developed as part of this work for the implementation of the mixing step given by Eq. (3.2) and its evaluation, in the context of LES/PDF methods. The following section describes the results obtained from using these schemes in a suite of test problems manufactured using the MMS.

3.5 Results and Discussion

This section is arranged in two subsections. Section §3.5.1 demonstrates the accuracy of the various implementation methodologies described in Sec. §3.3 while Sec. §3.5.2 elaborates on the benefits of using smoothing.

3.5.1 Accuracy and computational cost

Here we present the results that probe the numerical implementation of mixing and molecular transport in the HPDF code for order of accuracy, agreement between the modeled error and the data from numerical tests and computational cost. This section is categorized into four parts: First, we present results for a test case defined in a 3D Cartesian coordinate system (see Appendix D.1), with

purely mixing and molecular transport, comparing the order of accuracy of the three schemes - PIC-PC, PIC-PL and CIC-LS. Next, the aforementioned three schemes are evaluated for accuracy in a 3D Cartesian system with all processes - transport, mixing and reaction and we also compare the cost incurred by each scheme. Finally, the method is verified in a cylindrical coordinate system based on a 3D test problem described in Appendix D.2.

3.5.1.1 Cartesian - Mixing and molecular transport

The implementation of mixing and molecular transport is verified using the MMS for a single scalar. Given $\widetilde{\mathbf{U}}$, $\bar{\rho}$, Γ, Γ_T and Ω_m, analytical solutions are manufactured for the scalar mean $\overline{\phi}_m$ and variance $\overline{\phi'^2}_m$. The details of the test case are described in Appendix D.1. The three numerical schemes : PIC-PC, PIC-PL and CIC-LS are evaluated for accuracy (spatial, temporal and bias error) in the first two scalar moments using the global error defined by Eq. (3.74).

First, the three schemes are evaluated with the coefficients $\mathrm{U_o}$, $\mathrm{D_{o,t}}$ and $\mathrm{R_o}$ taken to be zero. In such a case, the only processes relevant are mixing, molecular transport and the source terms S_m and S_v. The splitting scheme described in Sec. §3.3.1 reduces to being $\mathbb{M}^s\mathbb{V}^s\mathbb{M}\mathbb{M}\mathbb{V}^s\mathbb{M}^s$. The normalized smoothing length scale l is set to zero *i.e.,* no smoothing is performed. The deterministic global error in the absence of smoothing is modeled as,

$$\dot{\mathcal{E}}_d = ah^2 + b\tau^2 + \frac{c}{\mathrm{N_{pc}}}, \tag{3.77}$$

where the first term on the right-hand side represents the spatial truncation error due to finite grid size, $h = \Delta x/L$; the second term models the temporal error

due to $\tau = \Delta t/T$; and the final term models the bias error due to a finite number of particles per cell, N_{pc}. The dot '$\cdot$' indicates modeled quantities. Each of the coefficients a, b and c is obtained from a weighted least-squares fit to the data obtained from the calculations.

Figure 3.4 compares the global error, defined by Eq. (3.74), in the three schemes PIC-PC, PIC-PL and CIC-LS in terms of accuracy in spatial truncation error, temporal discretization error and bias error in the first two scalar moments. From the sub-figures (1a-1b) it can be inferred that CIC-LS incurs more error as compared to the two other schemes. The bias error is small as compared to the spatial and temporal errors and is dominated by spatial and temporal discretization error in sub-figures (3a-3b). The differences between the schemes PIC-PC and PIC-PL are small.

Next, Figs. 3.5, 3.6 and 3.7 compare the global errors incurred by each of the schemes – PIC-PC, PIC-PL and CIC-LS respectively – against the model for that error given by Eq. (3.77). The symbols are from the PDF calculation and the solid line corresponds to the model for the global error. The sub-figures (a) are at $\tau = 0.03$ and $N_{pc} = 100$; sub-figures (b) at $h = 0.06$ and $N_{pc} = 50$; and sub-figures (c) at $h = 0.06$ and $\tau = 0.03$. As can be observed, the model agrees very well with the data showing that the numerical implementation of mixing and molecular transport is second-order accurate in space and time for each of the three numerical methods. The bias error is small in comparison.

Table 3.2 lists the set of coefficients a, b and c estimated for each of the schemes for both the first and the second scalar moments indicating the following. The CIC-LS scheme incurs approximately thrice the spatial truncation error

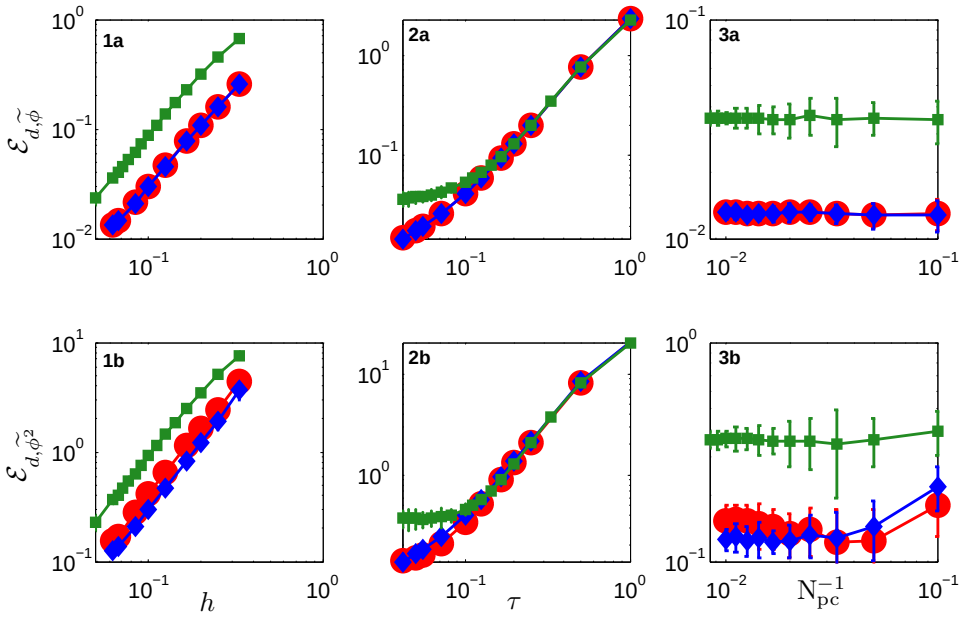

Figure 3.4: Comparison between the three numerical schemes : PIC-PC ●, PIC-PL◆, CIC-LS ■ in terms of the estimated global error. The sub-figures (1) plot convergence of spatial discretization error, sub-figures (2) plot convergence of temporal discretization error, and sub-figures (3) plot bias convergence. The sub-figures marked (a) correspond to the convergence for the first scalar moment and those marked (b) to the scalar second moment. The symbols correspond to the data obtained from PDF calculation (refer Appendix D.1 for test case with U_o, $D_{o,t}$ and R_o taken to be zero).

as the other two schemes. The schemes should not affect the temporal accuracy and the data confirm this. Additionally, the data also confirm that the bias error is small in comparison to the spatial truncation and temporal discretization errors.

In the following subsection, we study the three schemes using a test case incorporating all the processes - mixing, molecular transport, transport in physical space and reaction.

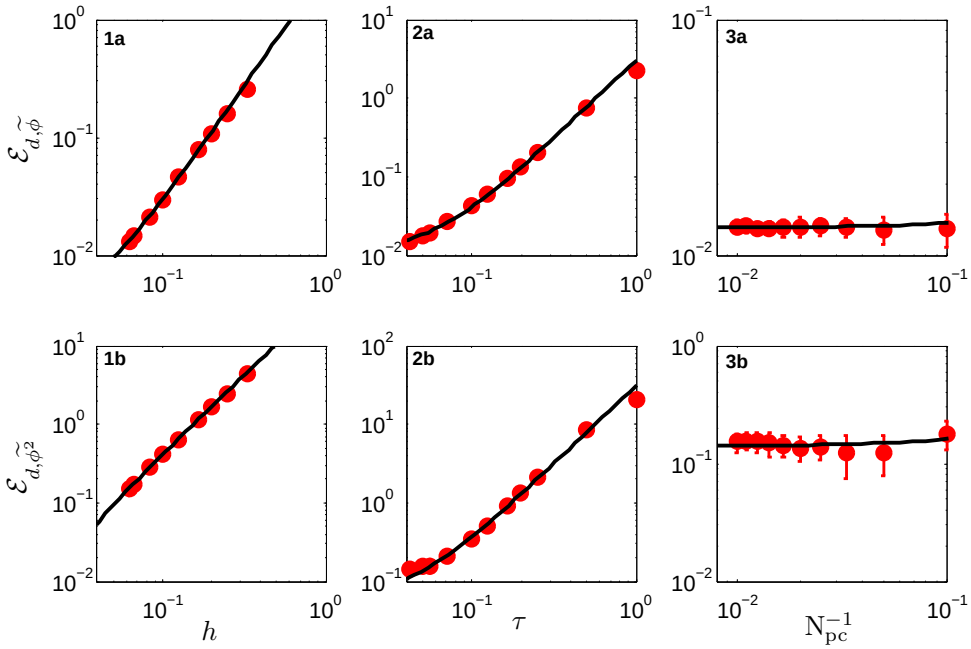

Figure 3.5: Comparison of estimated global error given by Eq. (3.74) obtained from PDF calculations (refer Appendix D.1 for test case with U_o, $D_{o,t}$ and R_o taken to be zero) using the scheme PIC-PC, against the model for the error given by Eq. (3.77). Details of the sub-figures are identical to the description given in Fig. 3.4.

Table 3.2: Table listing the values of the coefficients a, b, and c in Eq. (3.77) estimated for the first and the second moments of the scalar across each of the three schemes: PIC-PC, PIC-PL and CIC-LS. The test problem is described in Appendix D.1 with U_o, $D_{o,t}$ and R_o set to zero.

	$\widetilde{\phi}$			$\widetilde{\phi^2}$		
Scheme	a	b	c	a	b	c
PIC-PC	2.5	3.0	0.02	39.2	32.6	−1.5
PIC-PL	2.5	3.0	0.02	29.0	32.9	−0.1
CIC-LS	7.6	2.8	0.04	83.4	31.3	−1.3

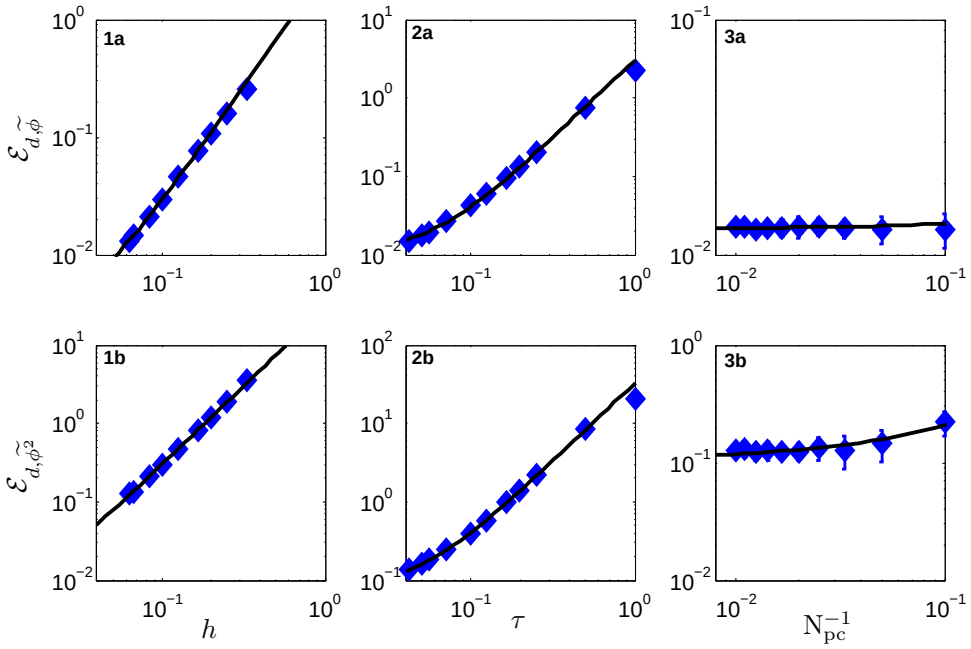

Figure 3.6: Comparison of estimated global error given by Eq. (3.74) obtained from PDF calculations (refer Appendix D.1 for test case with U_o, $D_{o,t}$ and R_o taken to be zero) using the scheme PIC-PL, against the model for the error given by Eq. (3.77). Details of the sub-figures are identical to the description given in Fig. 3.4.

3.5.1.2 Cartesian - Mixing, molecular transport, transport and reaction

In this section, the three numerical schemes are evaluated for accuracy in a manner identical to the previous section but with the default values for the U_o, $D_{o,t}$ and R_o mentioned in Appendix D.1.

Figure 3.8 compares the global error, defined by Eq. (3.74), in the three schemes PIC-PC, PIC-PL and CIC-LS in terms of accuracy in spatial discretization error, temporal discretization error and bias error for the test problem with non-trivial transport and reaction. Under such circumstances, there is no significant difference between the three schemes. Sub-figure (3b) indicates that

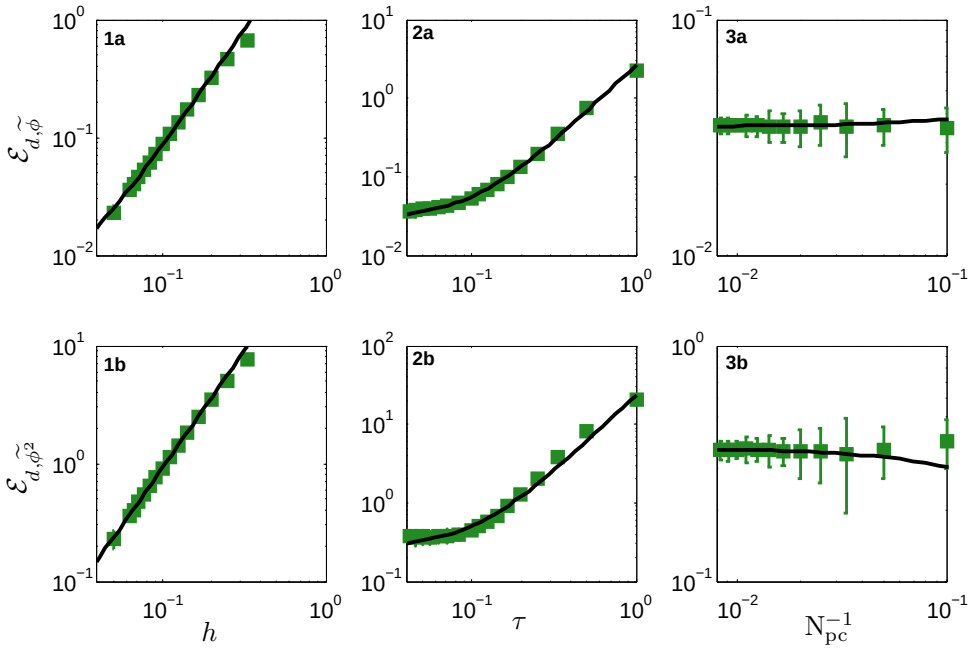

Figure 3.7: Comparison of estimated global error given by Eq. (3.74) obtained from PDF calculations (refer Appendix D.1 for test case with U_o, $D_{o,t}$ and R_o taken to be zero) using the scheme CIC-LS, against the model for the error given by Eq. (3.77). Details of the sub-figures are identical to the description given in Fig. 3.4.

the CIC-LS scheme incurs slightly smaller bias error as compared to the other two schemes since the mean estimate is based on $2\mathrm{N_{pc}}$ particles in each direction. Figures 3.9, 3.10 and 3.11 compare the global error incurred by each of the schemes against the model for that error given by Eq. (3.77). The symbols are from the PDF calculation and the solid line corresponds to the model for the global error. The sub-figures (a) are at $\tau = 0.03$ and $\mathrm{N_{pc}} = 100$; sub-figures (b) at $h = 0.06$ and $\mathrm{N_{pc}} = 50$; and sub-figures (c) at $h = 0.1$ and $\tau = 0.05$. As can be observed, the model agrees very well with the data showing that second-order accuracy in space and time is preserved for each of the three models with non-trivial transport and reaction. The bias error in the second moment is significant

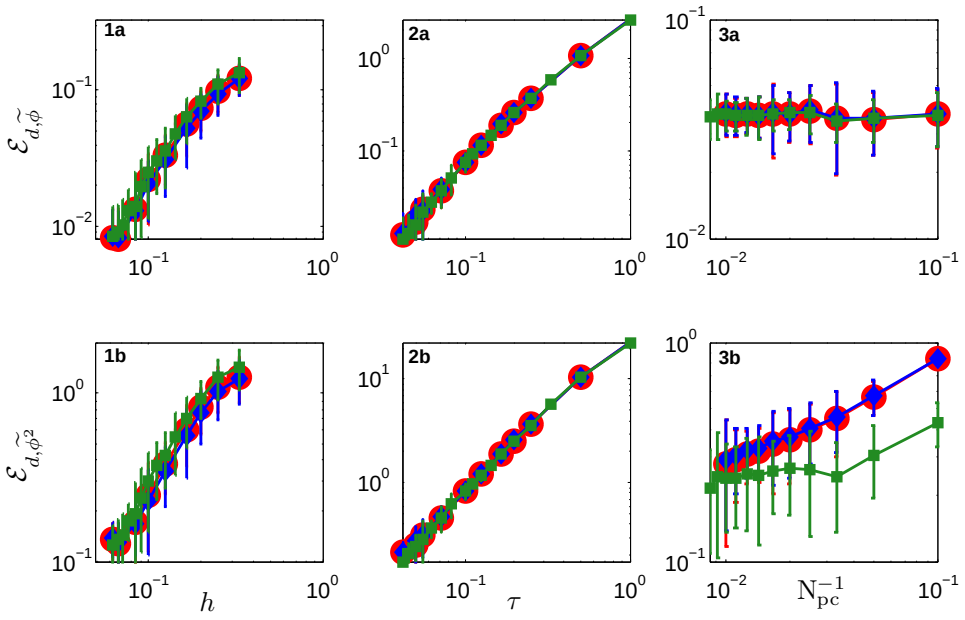

Figure 3.8: Comparison between the three numerical schemes : PIC-PC ●, PIC-PL◆, CIC-LS ■ in terms of the estimated global error. The sub-figures (1) plots convergence of spatial discretization error, sub-figures (2) plot convergence of temporal discretization error, and sub-figures (3) plot bias convergence. The sub-figures marked (a) correspond to the convergence for the first scalar moment and those marked (b) to the scalar second moment. The symbols correspond to the data obtained from PDF calculation (refer Appendix D.1 for test case).

and the data show that bias error scales as $\mathrm{N}_{\mathrm{pc}}^{-1}$.

Table 3.3 lists the set of coefficients a, b and c estimated for each of the schemes for both the first and the second scalar moments. This data suggest the following. Firstly, although small in comparison to the other two errors, the bias error is significant unlike the observations in Sec. §3.5.1.1. Secondly, there are negligible differences in the spatial truncation errors between the schemes indicating that the dominant contribution to spatial errors is due to transport and reaction.

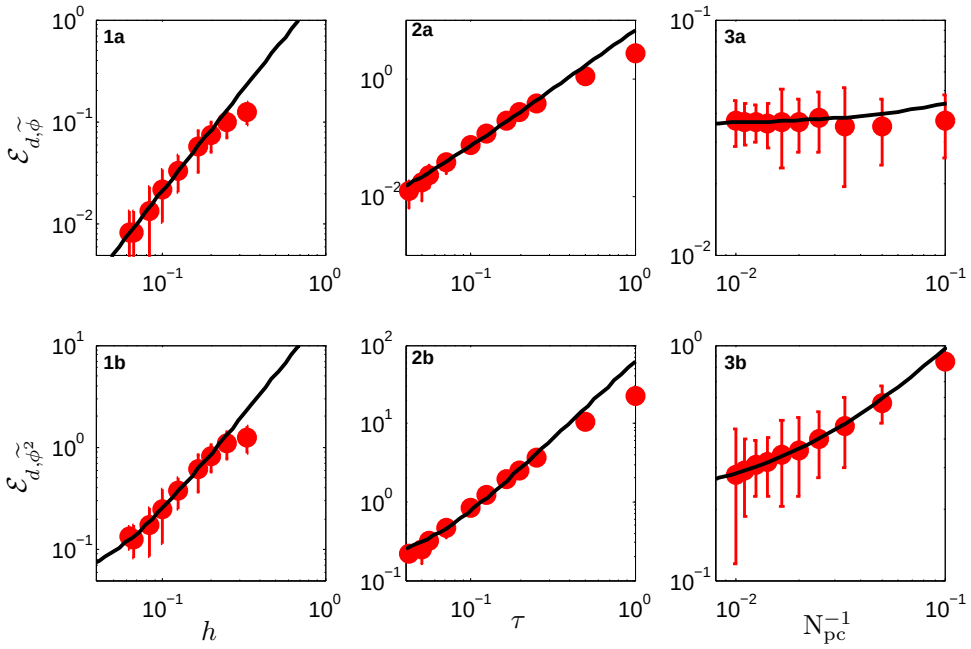

Figure 3.9: Comparison of estimated global error given by Eq. (3.74) obtained from PDF calculations (refer Appendix D.1 for test case with non-trivial transport and reaction) using the scheme PIC-PC, against the model for the error given by Eq. (3.77). Details of the sub-figures are identical to the description given in Fig. 3.8.

Table 3.3: Table listing the values of the coefficients a, b, and c in Eq. (3.77) estimated for the first and the second moments of the scalar across each of the three schemes: PIC-PC, PIC-PL and CIC-LS. The test problem is described in Appendix D.1.

	$\widetilde{\phi}$			$\widetilde{\phi^2}$		
Scheme	a	b	c	a	b	c
PIC-PC	1.5	6.0	0.4	15.9	56.7	8.0
PIC-PL	1.4	5.9	0.4	14.6	57.0	8.3
CIC-LS	1.7	5.3	0.5	20.0	52.9	4.6

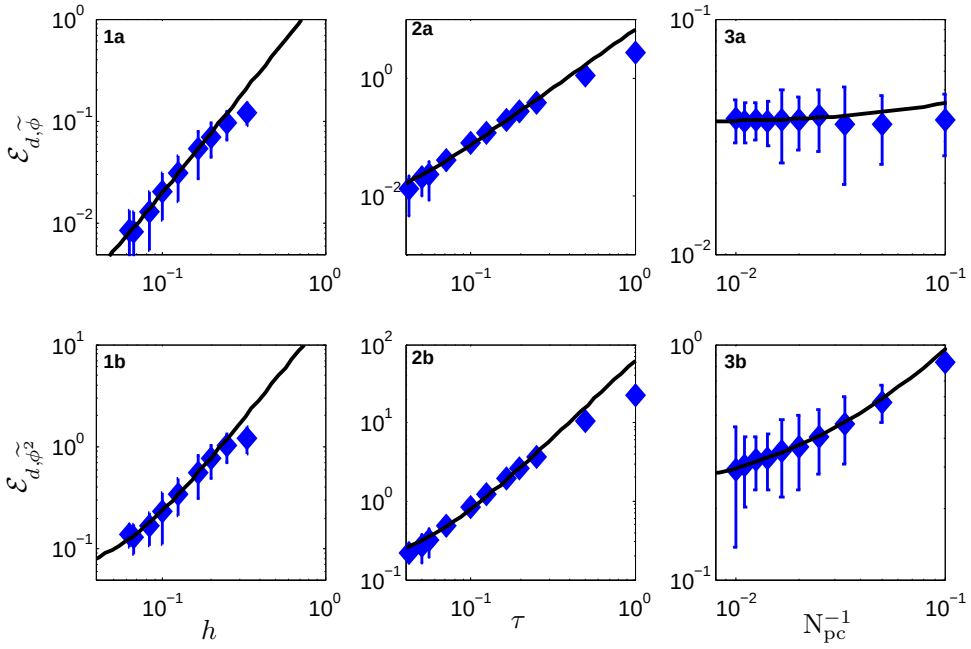

Figure 3.10: Comparison of estimated global error given by Eq. (3.74) obtained from PDF calculations (refer Appendix D.1 for test case with non-trivial transport and reaction) using the scheme PIC-PL, against the model for the error given by Eq. (3.77). Details of the sub-figures are identical to the description given in Fig. 3.8.

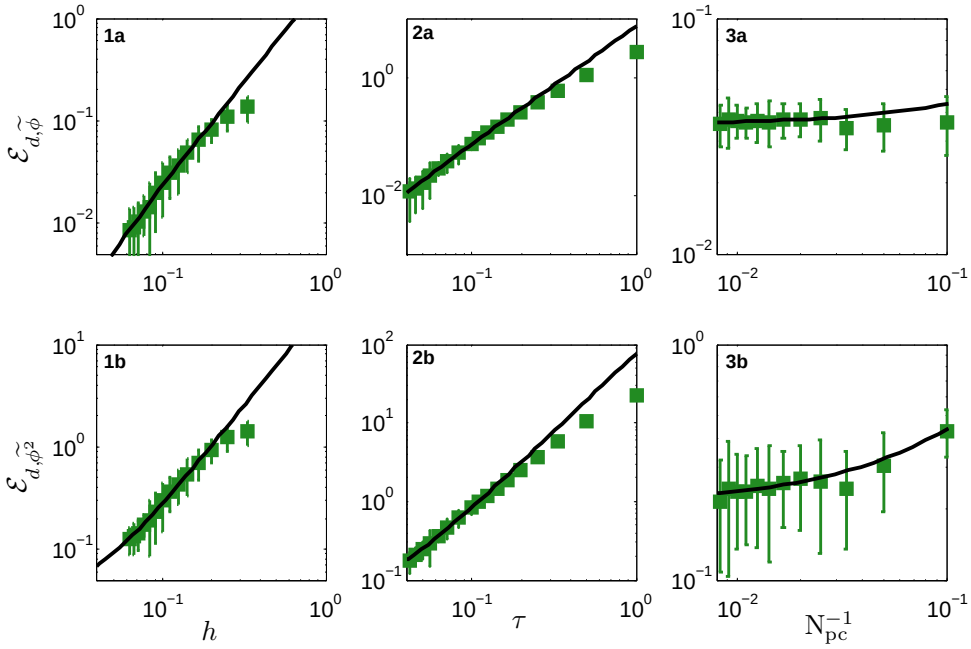

Figure 3.11: Comparison of estimated global error given by Eq. (3.74) obtained from PDF calculations (refer Appendix D.1 for test case with non-trivial transport and reaction) using the scheme CIC-LS, against the model for the error given by Eq. (3.77). Details of the sub-figures are identical to the description given in Fig. 3.8.

3.5.1.3 Computational cost

Given that there is very little difference in accuracy across the three numerical implementation described in Sec. §3.3, here we compare the cost of implementing each scheme. Since the only difference in each of these schemes is in the implementation of mixing (mean estimation and interpolation methods), the cost of each scheme is compared by looking at the CPU time per particle step spent on mixing in comparison to the time spent per particle step. The CPU time per particle step of mixing is further split to see the cost of the various mean estimation and interpolation methods. Note that each set of calculations was performed using 32 processors on an HPC cluster of 36 Dell servers, each featuring dual, dual-core 3GHz Intel Xeon "Woodcrest" processors with 8 GB RAM, tied together using a QLogic 4X SDR InfiniBand interconnect.

Figure 3.12 plots the CPU time per particle step (in μ seconds) for each of the three schemes. The figure indicates that the CIC-LS scheme incurs almost three times the cost as either of the other two schemes. This is due to the fact that in CIC-LS, for each particle, the basis functions are evaluated in each of the neighboring 26 cells (in 3D) in addition to one to which the particle belongs. In contrast, in PIC-PC and PIC-PL, the indicator function is evaluated just once per particle. While in these tests the smoothing length-scale is set to zero, nevertheless the smoothing operations are performed (yielding the trivial results $g = f$). This enables the measurement of the CPU time required for smoothing (which is independent of l). As may be seen, the CPU time requirement that pertains to smoothing is modest, amounting to less than 3% of the total for CIC-LS.

The results from the numerical tests presented above indicate that the differ-

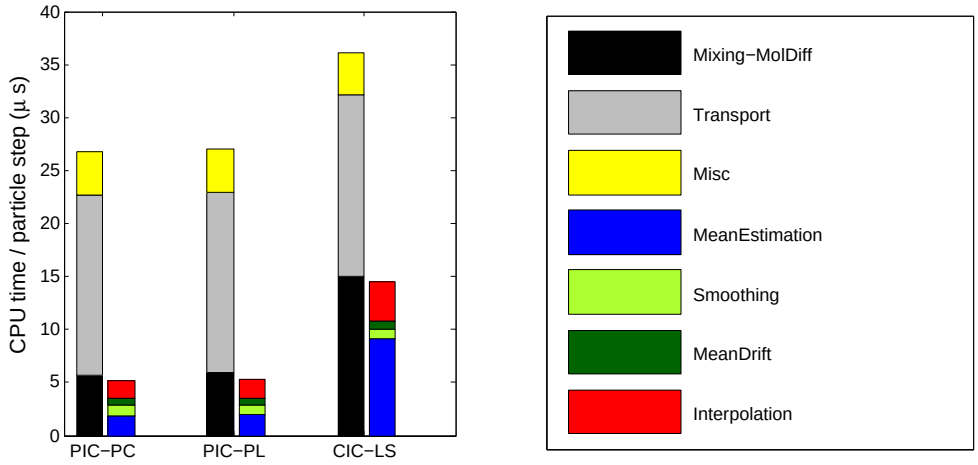

Figure 3.12: Comparison in the computational cost across the three numerical schemes : PIC-PC, PIC-PL and CIC-LS in terms of the CPU time per particle step (in micro seconds). The first stack under each scheme splits the cost into mixing $\mathbb{M}$, transport $\mathbb{T}$ and other steps. The second stack splits the time spent within mixing $\mathbb{M}$ into mean estimation, smoothing, molecular transport to obtain the mean drifts and interpolation.

ences in accuracy across the three schemes for a 3D Cartesian MMS test problem are small. The CIC-LS scheme has two advantages over the other two schemes since the resulting fields are always continuous and bounded. Therefore, although the CIC-LS scheme is relatively expensive in comparison to the other two schemes, we choose the CIC-LS scheme for all the following tests.

3.5.1.4 Cylindrical - Mixing, molecular transport, transport and reaction

In this section, the CIC-LS scheme is evaluated for accuracy in spatial discretization, temporal discretization and bias for the MMS test problem in a cylindrical coordinate system described in Appendix D.2. Figure 3.13 plots the estimate for global error obtained from the PDF calculation against h, τ and N_{pc}^{-1}. The model

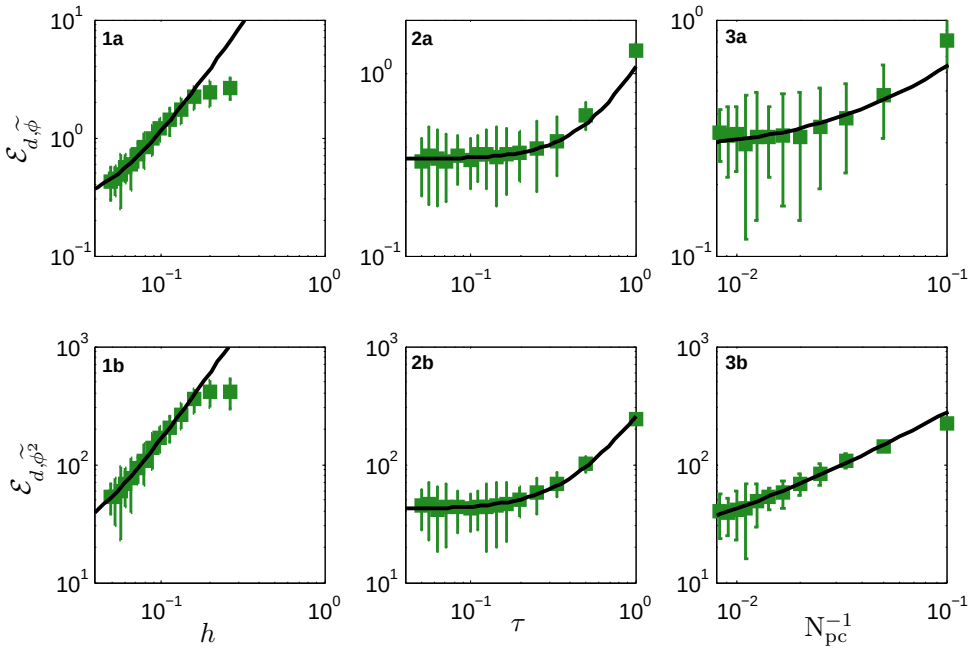

Figure 3.13: Comparison of estimated global error given by Eq. (3.74) obtained from PDF calculations (refer Appendix D.2 for test case with non-trivial transport and reaction in cylindrical coordinate system) using the scheme CIC-LS, against the model for the error given by Eq. (3.77). Details of the sub-figures are identical to the description given in Fig. 3.8.

for the error given by Eq. (3.77) is plotted so that a comparison can be made between the model predictions and the data from calculations. As is seen from the figure, the implementation is second-order accurate in space and time and the model for the error agrees well with the data for spatial and temporal truncation errors. Additionally, the model for the bias error agrees with the data as well.

In summary, the data from PDF calculations using the MMS testing methodology confirm that the numerical implementation of mixing and molecular transport is second-order accurate in space and time in both the Cartesian and

the cylindrical coordinate systems. There are insignificant differences between the three schemes in terms of accuracy, and for reasons mentioned in the previous section, we choose the CIC-LS scheme for all our results henceforth.

3.5.2 Smoothing

Smoothing, as described in Sec. §3.3.4, is presented as a technique for reducing the variance in the estimated statistics by spatial averaging. In this section, we study the efficacy of incorporating smoothing by analyzing the behavior of the root-mean-squared error in the estimated statistics of "output" quantities. The test case used is the MMS problem defined in a 3D Cartesian domain (Appendix D.1) without transport and reaction. The numerical scheme used for implementation is the CIC-LS scheme.

As mentioned previously, the root-mean-squared error consists of two components - the deterministic part and the random part. The deterministic error is composed of contributions from a) spatial truncation error due to finite grid spacing, b) temporal truncation error due to finite time step, and c) smearing error due to smoothing. Additionally, using a finite number of particles in the Monte-Carlo particle method gives rise to a deterministic bias error and a random statistical error. Consequently, the fundamental numerical parameters relevant to this study in the analysis of the model for error are the normalized grid spacing h, time step τ, normalized smoothing length scale l, and the total number of particles N_{tot}.

Typically, in LES/PDF studies, the choice of the time step is restricted to very

small values due to considerations of stability and the CFL number criterion. It has been observed in the numerical studies done as part of this work using MMS and in flame calculations done by Wang *et al.* [86] that, for the values of τ used in practice, the temporal error is negligible compared to the contributions from other errors. Therefore, we confine our analysis to the 3-D numerical parametric space characterized by h, l and N_{tot}. The MMS calculations are performed for h ranging between 10^{-2} and 1; for l between 0 and 1; and for N_{tot} between 10^3 and 10^7.

Figure 3.14 plots an estimate of the global errors as defined by Eq. (3.74-3.76) in the scalar mean and scalar second moment obtained from PDF calculations (shown as symbols) against the smoothing length scale, l for given h and N_{tot}. The normalized grid spacing h is fixed at 0.05 and the number of particles per cell, N_{pc} is fixed at unity ($N_{tot} = 8,000$). The filled circles represent the estimate for the global error given by Eq. (3.74) and correspond to the deterministic error, the filled squares represent the estimate for the global error given by Eq. (3.75) corresponding to the statistical error and the filled diamonds correspond to the root-mean-squared error given by Eq. (3.76). It can be inferred that the global estimate for the deterministic error decreases with decreasing l for large l values, reaches a minimum and then increases before leveling off. On the other hand, the global estimate for the statistical error decreases for increasing l. Since the root-mean-squared error is defined to be a combination of the deterministic and statistical errors, there exists a minimum and the corresponding value of l represents optimal smoothing.

We are interested in modeling the root-mean-squared error as a function of the three numerical parameters h, l and N_{tot} across the range of parametric space

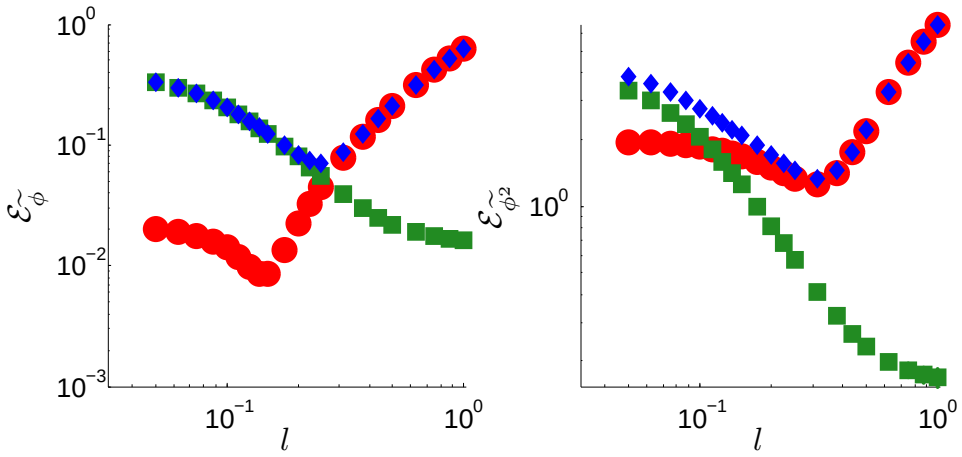

Figure 3.14: Global error in the scalar mean and the second moment against l for fixed $h = 0.05$ and $\mathrm{N_{tot}} = 8,000$. Symbols are results of PDF calculations and correspond to $\mathcal{E}_d$ ● (Eq. 3.74), $\mathcal{E}_s$ ■ (Eq. 3.75), $\mathcal{E}$ ◆ (Eq. 3.76).

considered in this study. Consequently, in the following paragraphs, we present models for the statistical error and the deterministic error in terms of h, l and $\mathrm{N_{tot}}$ and derive a model for the root-mean-squared error based on these models for the statistical and deterministic errors. While we focus on the scalar mean, the model is itself general and is extensible to any measured statistic.

Considering the statistical error first, we model the global statistical error as

$$\dot{\mathcal{E}}_s = c_0 \mathrm{N_{eff}}^{-\frac{1}{2}}, \tag{3.78}$$

where the effective number of particles, $\mathrm{N_{eff}}$ is defined in Eq. (3.63). The definition of $\mathrm{N_{eff}}$ given by Eq. (3.63) implies that for $l = 0$, $\mathrm{N_{eff}} = \mathrm{N_{tot}} h^D = \mathrm{N_{pc}}$ while for $h = 0$, $\mathrm{N_{eff}} = \mathrm{N_{tot}} l^D$ with $D = 3$. Figure 3.15 presents the estimate of the global statistical error obtained from PDF calculations as symbols and the solid lines to represent the model given by Eqs. (3.63) and (3.78) with $c_0 = 0.8$. The sub-figures (1) correspond to $\mathrm{N_{tot}} = 8,000$; sub-figures (2) correspond to $\mathrm{N_{tot}} = 128,000$; and

sub-figures (3) correspond to $N_{tot} = 1,638,400$. The figure labels (a) consider the variation of the statistical error with l and (b) consider the variation with h. The primary observation is that the model for the statistical error given by Eq. (3.78) agrees well with the data across the parametric space explored. It can be inferred that given h, for values of l larger than 10^{-2}, the statistical error is reduced significantly as compared to when no smoothing is performed *i.e.,* for $l = 0$. Similarly, for a given value of N_{tot} with $l = 0$, grid refinement results in the statistical error scaling as $h^{-\frac{3}{2}}$ or ${N_{pc}}^{-\frac{1}{2}}$ (denoted by the red line). On the other hand, for non-trivial smoothing ($l > 0$), the statistical error asymptotes to a constant given by $c_0(N_{tot} l^3)^{-\frac{1}{2}}$.

Next, we examine the data for the estimate of the global deterministic error in Fig. 3.16. The sub-figure (a) plots the deterministic error against l at a given value of h for the three values of N_{tot} while (b) plots against h at a given value of l for the same three values of N_{tot}. The data show no dependence on N_{tot} indicating that the bias error is negligible in comparison to the smearing and spatial discretization errors. A striking feature of the plot of $\mathcal{E}_d$ vs l (Fig. 3.16) is the sharp minimum around $l \approx 0.5$, for which we offer the following explanation.

Prior to smoothing, the deterministic error is dominated by spatial truncation error and as mentioned previously, smoothing introduces additional smearing errors. Smoothing tends to smear both the underlying field (which is undesirable) and the spatial truncation error (which is desirable). For small values of the smoothing length scale $l \leq h$, the smearing error is smaller or comparable to the spatial truncation error. As we increase the smoothing length scale, there exists an optimal value of l at which the smearing of the underlying field is compensated for by the smearing of the spatial truncation error, resulting in

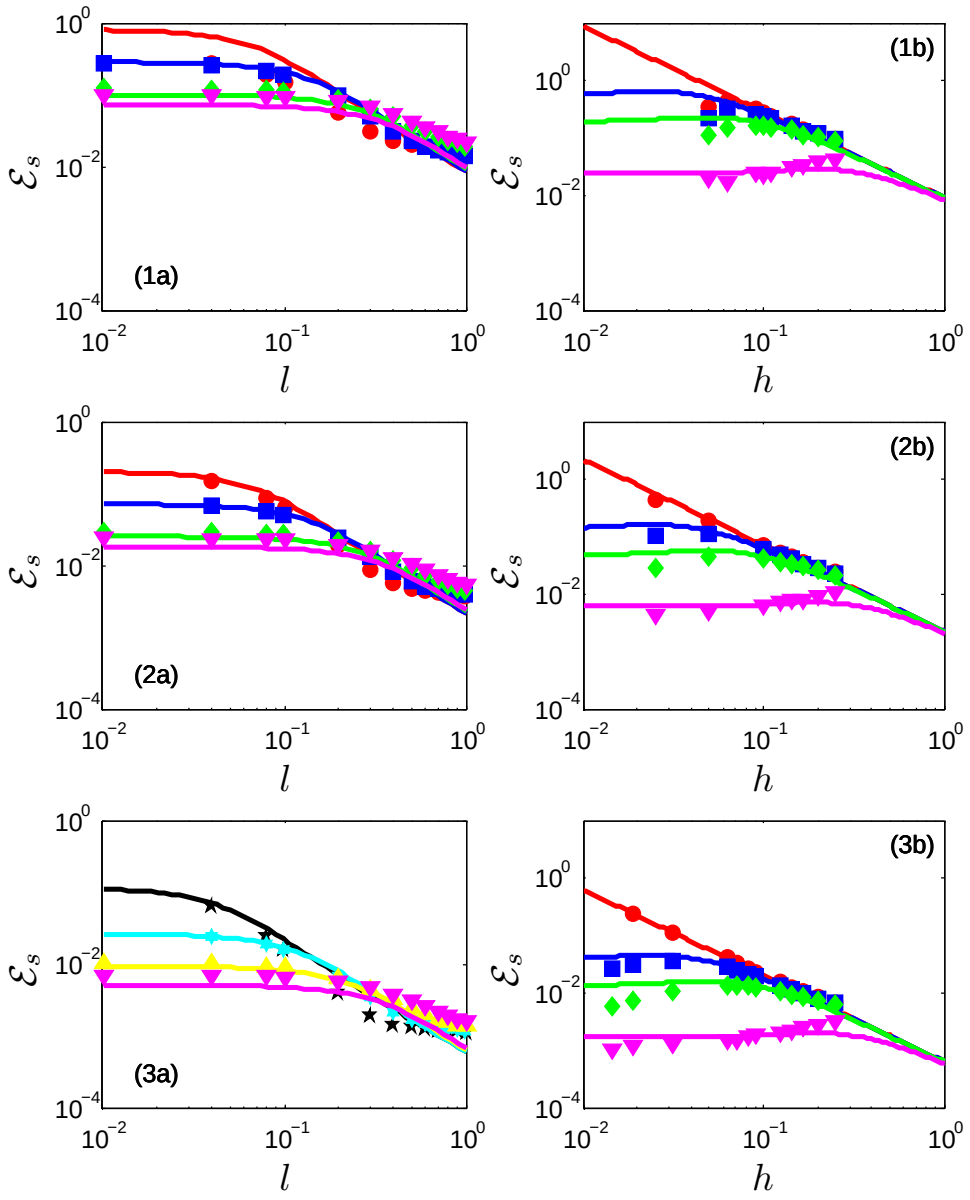

Figure 3.15: Comparison between the estimate of the global statistical error in the scalar mean obtained from the PDF calculations (symbols) and its model given by Eq. (3.78). Sub-figures (1) are at $N_{tot} = 8,000$, (2) at $N_{tot} = 128,000$ and (3) at $N_{tot} = 1,638,400$. Sub-figures (a) plot against l for fixed h (note that data for $l = 0$ is in fact plotted at $l = 10^{-2}$) and (b) plots against h given l. Plots under sub-figures (b) follow the legend: ● $l = 0$, ■ $l = 0.5$, ◆ $l = 0.125$, ▼ $l = 0.0625$. Plots under sub-figures (a) follow the legend: ● $h = 0.05$, ■ $h = 0.1$, ◆ $h = 0.2$, ▼ $h = 0.25$, ★ $h = 0.03125$, ✶ $h = 0.083$, ▲ $h = 0.16$.

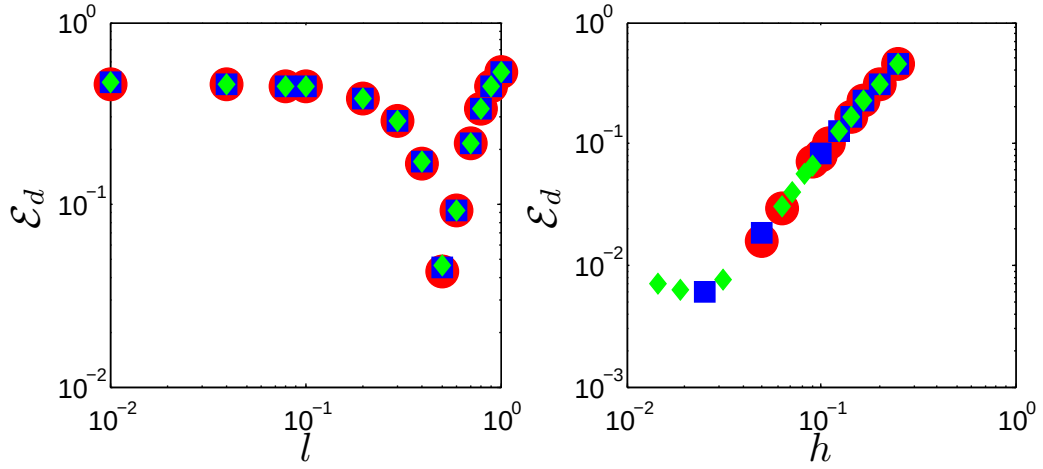

Figure 3.16: Comparison between the estimate of the global deterministic error in the scalar mean obtained from the PDF calculations against l for $h = 0.25$ and against h for $l = 0.0625$. The legend is as follows : ● $N_{tot} = 8,000$, ■ $N_{tot} = 128,000$, ◆ $N_{tot} = 1,638,400$.

a minimum deterministic error. This behavior is well portrayed in the left-hand plot of Fig. (3.16).

Appendix B.2 analyzes the smearing error incurred due to smoothing and presents approximate models for the same in Eqs. (B.23) and (B.24) for two specific cases (see the appendix for details). This analysis is used to suggest a form for a model of the deterministic error incurred after smoothing, and we accordingly model the global deterministic error as:

$$\begin{aligned} \dot{\mathcal{E}}_d^2 &= \left(\frac{\dot{a}_1\alpha_s h^2 - \dot{a}_2 h^2}{1 + \dot{a}_5\alpha_s h^2}\right)^2 + \left(\frac{\dot{a}_4 h^2}{1 + \dot{a}_3\alpha_s}\right)^2, \\ &= \left(\frac{a_1 l^2 - a_2 h^2}{1 + a_5 l^2}\right)^2 + \left(\frac{a_4 h^4}{h^2 + a_3 l^2}\right)^2, \end{aligned} \tag{3.79}$$

where the second line is obtained using Eq. (3.55) as a model for α_s and a_i are empirical constants. Fitting the model given by Eq. (3.79) to the data for the estimate of the deterministic error obtained from PDF calculations, we obtain

$a_1 = 1.52$, $a_2 = 7.27$, $a_3 = 0.75$, $a_4 = 1.76$ and $a_5 = 0.98$.

Figure 3.17 plots the deterministic error against l in sub-figures marked (a) and against h in sub-figures marked (b) for the three values of N_{tot} values. The data from PDF calculations correspond to the symbols and the lines represent the model given by Eq. (3.79). The model is successful in predicting the behavior exhibited by the data across the range of parameters studied. In particular, in most cases, the model prediction of location of the optimal error is in good agreement with the data.

Given the models for the statistical error in Eq. (3.78) and the deterministic error in Eq. (3.79), the model for the global estimate of the corresponding root-mean-squared error is obtained as,

$$\dot{\mathcal{E}}^2 = \dot{\mathcal{E}}_d^2 + \dot{\mathcal{E}}_s^2. \tag{3.80}$$

Figure 3.18 compares the model given by Eq. (3.80) against the data from PDF calculations for the three values of N_{tot} analyzed. As is evident, the model agrees well with the PDF simulations and is successful in predicting their behavior quantitatively. As with the deterministic error, the model for the root-mean-squared error is successful in predicting the location of the optimal error.

The deterministic error given by Eq. (3.79) is modeled based on the analysis performed in Appendix B.2 for the smearing error due to smoothing. Consider making the following approximation to Eq. (3.79) where we force the coefficient a_5 (in Eq. (3.79)) to zero to obtain:

$$\dot{\mathcal{E}}_d^2 = \left(c_1 l^2 - c_2 h^2\right)^2 + \left(\frac{c_4 h^4}{h^2 + c_3 l^2}\right)^2, \tag{3.81}$$

for a different set of coefficients c_i. The motivation behind this approximation

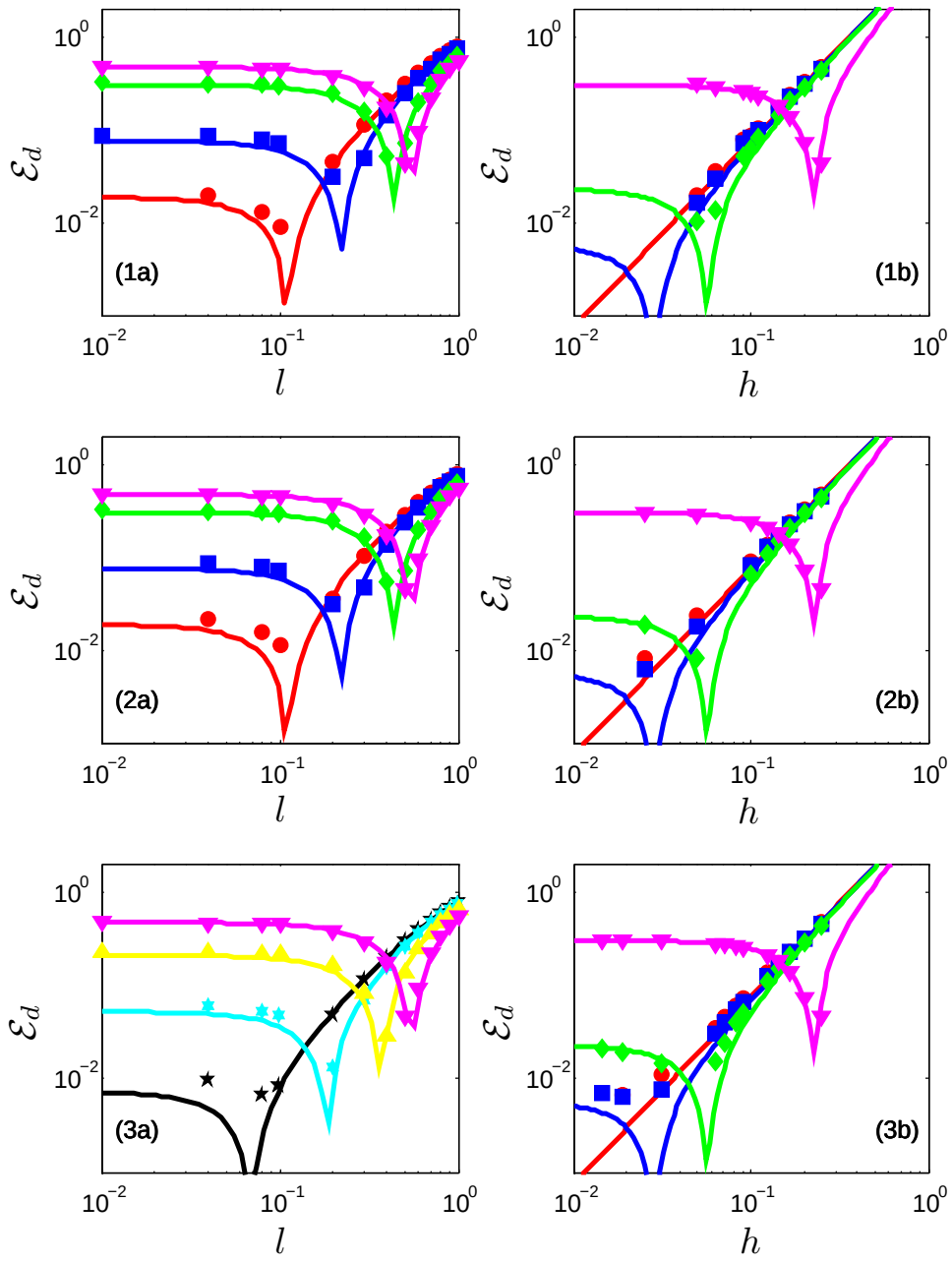

Figure 3.17: Comparison between the estimate of the global deterministic error in the scalar mean obtained from the PDF calculations (symbols) and its model given by Eq. (3.79). The figure description is the same as in Fig. 3.15.

becomes clear in the following paragraphs. Note that this approximation likely tends to affect choices of smoothing length scale on the order of unity. Smoothing length scale l of unity implies that smoothing is performed over the entire computational domain.

Fitting this model given by Eq. (3.81) to the data for the estimate of the deterministic error obtained from PDF calculations, we obtain $c_1 = 0.82$, $c_2 = 3.89$, $c_3 = 0.49$ and $c_4 = 6.45$. Figure 3.19 compares the root-mean-squared error obtained using the models for the deterministic error given by Eqs. (3.79) (thin solid lines) and (3.81) (thick dashed lines). The discrepancy between the two models are observed for values of l comparable to unity. Barring this drawback, the model corresponding to Eq. (3.81) yields to elegant inferences as shown below.

Our studies show that the computing time is dominated by particle work and therefore we model the cost, C to scale with $\mathrm{N_{tot}}$. We now use the model Eq. (3.81) in the definition of the global root-mean-squared error Eq. (3.80) to investigate the selection of the optimal value of l. We write this error as $\dot{\mathcal{E}}(h, l, \mathrm{N_{tot}})$ and, as a preliminary step we define $\hat{h}(\mathrm{N_{tot}})$ to be the optimal normalized grid spacing when no smoothing is used, and $\hat{l}(\mathrm{N_{tot}})$ to be the optimal amount of smoothing on an infinitely fine grid. Thus, $\hat{h}(\mathrm{N_{tot}})$ is the minimizer of $\dot{\mathcal{E}}(h, 0, \mathrm{N_{tot}})$, and this minimum error is denoted by $\dot{\mathcal{E}}_h(\mathrm{N_{tot}}) = \dot{\mathcal{E}}(\hat{h}, 0, \mathrm{N_{tot}})$. Similarly $\hat{l}(\mathrm{N_{tot}})$ is the minimizer of $\dot{\mathcal{E}}(0, l, \mathrm{N_{tot}})$ and this minimum error is denoted by $\dot{\mathcal{E}}_l(\mathrm{N_{tot}}) \equiv \dot{\mathcal{E}}(0, \hat{l}, \mathrm{N_{tot}})$. A simple analysis of Eq. (3.80) obtained using Eqs. (3.78)

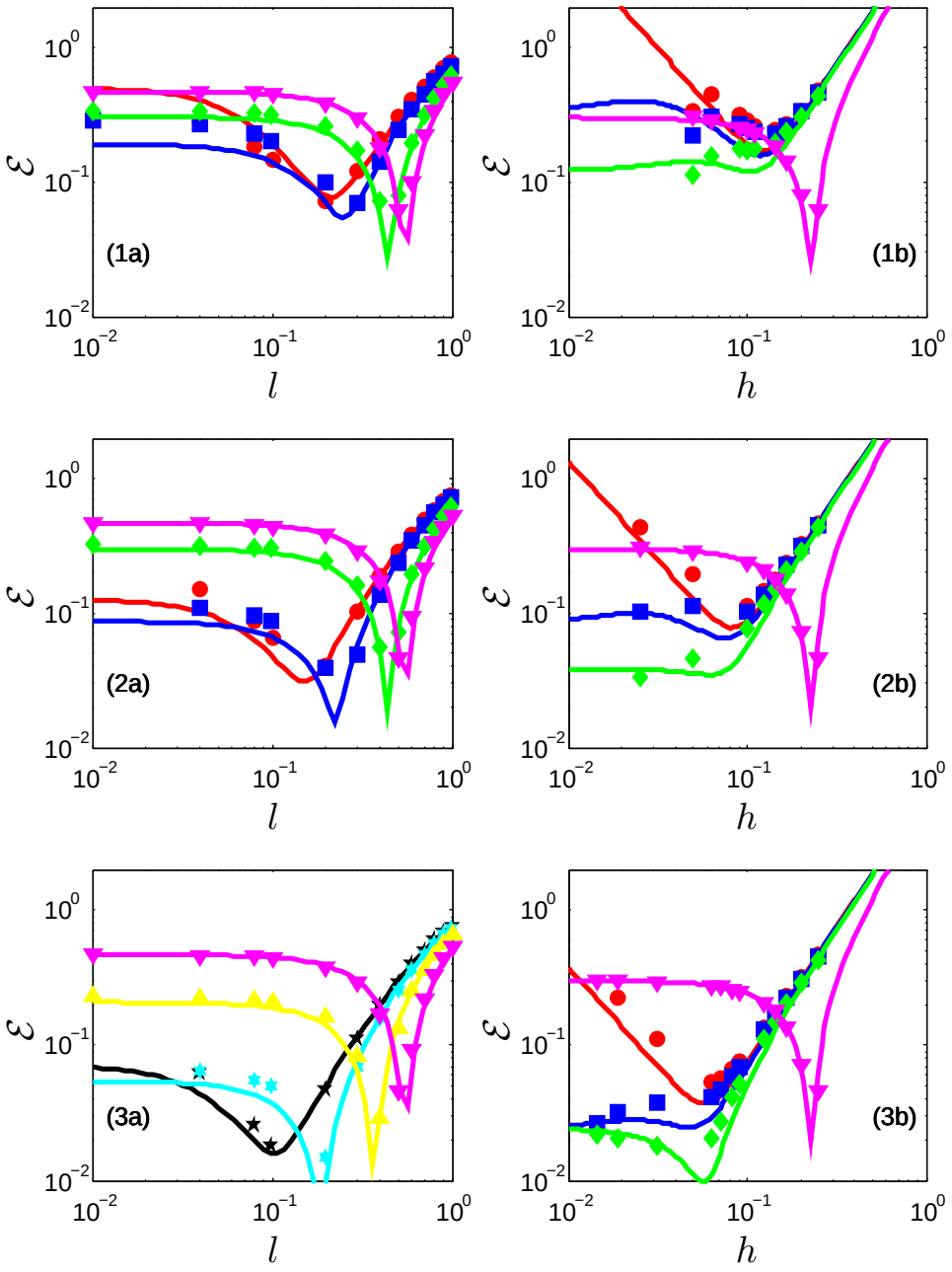

Figure 3.18: Comparison between the estimate of the global root-mean-squared error in the scalar mean obtained from the PDF calculations (symbols) and its model given by Eq. (3.80). The figure description is the same as in Fig. 3.15.

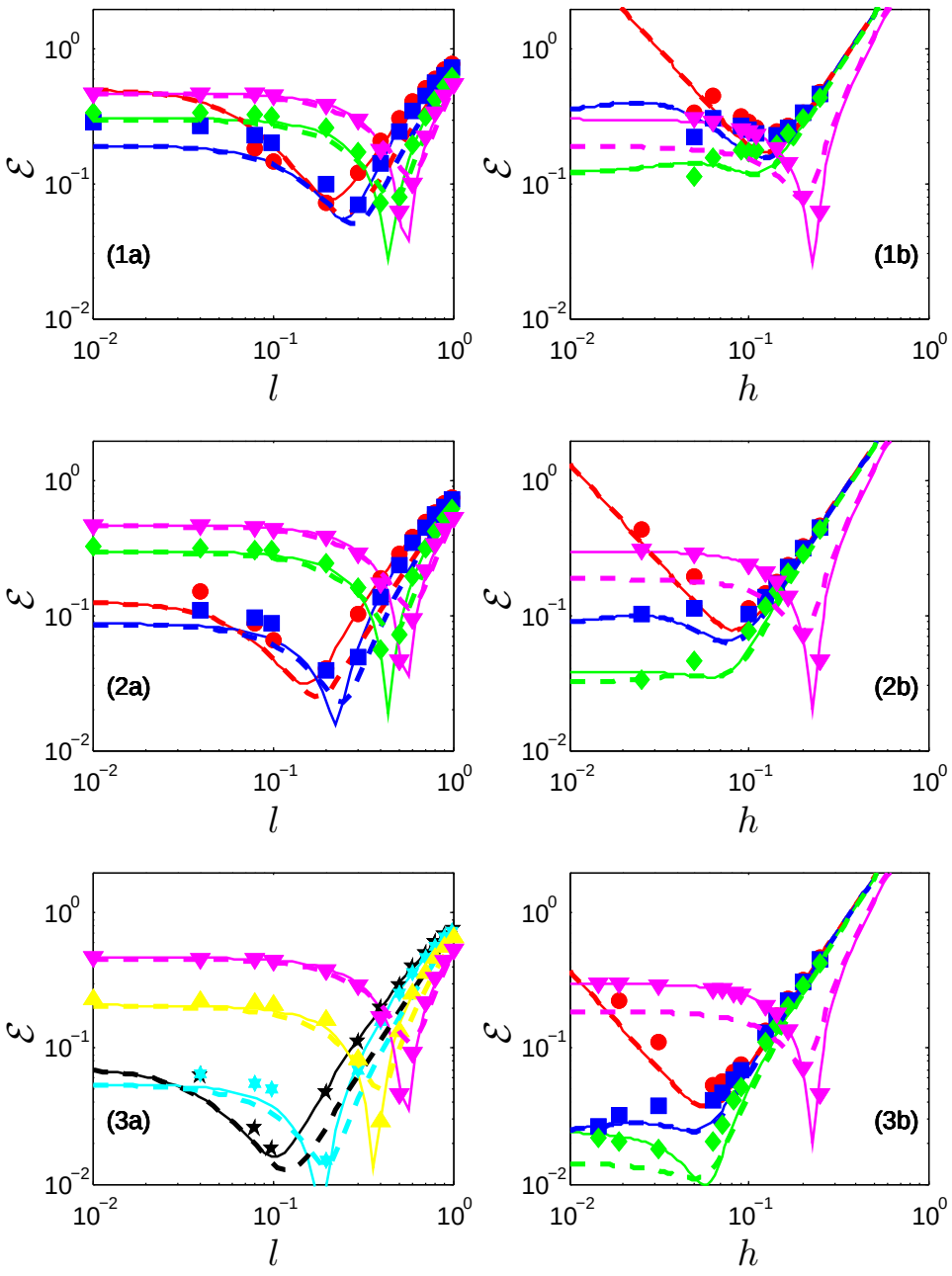

Figure 3.19: Comparison between the estimates of the global root-mean-squared error in the scalar mean obtained from the PDF calculations (symbols) against the root-mean-squared error modeled based the two models for the deterministic error corresponding to Eqs. (3.79) (thin solid lines) and (3.81) (thick dashed lines). The figure description is the same as in Fig. 3.15.

and (3.81) shows that,

$$\hat{h} = \left(\frac{\mathrm{N_{tot}}}{\widetilde{N}_h}\right)^{-q}, \tag{3.82}$$

$$\hat{l} = \left(\frac{\mathrm{N_{tot}}}{\widetilde{N}_l}\right)^{-q}, \tag{3.83}$$

with $\widetilde{N}_h = c_0^2 D/4c^2$ for $c^2 \equiv c_2^2 + c_4^2$, $\widetilde{N}_l = c_0^2 D/4c_1^2$, and $q^{-1} = 4 + D$. Thus, $\hat{h}$ and $\hat{l}$ decrease at the same slow rate with increasing $\mathrm{N_{tot}}$, as $\mathrm{N_{tot}^{-1/7}}$ for $D = 3$.

Now, given the definitions of $\hat{l}$ and $\hat{h}$ above, Eqs. (3.78) and (3.81) can be re-expressed in terms of $\tilde{l} \equiv l/\hat{l}$ and $\tilde{h} \equiv h/\hat{h}$ to obtain for the root-mean-squared error an expression of the form:

$$\dot{\mathcal{E}}^2 = \mathrm{N_{tot}^{-4q}} \mathcal{F}\left(\tilde{l}, \tilde{h}\right), \tag{3.84}$$

for the set of coefficients c_i where with $r \equiv (c_1/c)^{2q}$ we have,

$$\begin{aligned} \mathcal{F} &= c_0^2 \widetilde{N}_l^{-qD} \left(\tilde{h} r + \frac{\tilde{l}^2}{\sqrt{16 r^2 \tilde{h}^2 + \tilde{l}^2}}\right)^{-D} \\ &\quad + \widetilde{N}_l^{4q} \left[\left(c_1 \tilde{l}^2 - c_2 r^2 \tilde{h}^2\right)^2 + \left(\frac{c_4 r^4 \tilde{h}^4}{r^2 \tilde{h}^2 + c_3 \tilde{l}^2}\right)^2\right]. \end{aligned} \tag{3.85}$$

In other words, $\dot{\mathcal{E}}\mathrm{N_{tot}^{2q}}$ is known completely in terms of the parameters $\tilde{h}$ and $\tilde{l}$ given the coefficients c_i.

Figure 3.20 plots the filled contours of $\log_{10}\left(\dot{\mathcal{E}}\mathrm{N_{tot}^{2q}}\right)$ in $\tilde{h}$–$\tilde{l}$ space using model coefficients c_i estimated using the data from PDF calculations. Note that $\tilde{l} = 1$ and $\tilde{h} = 1$ are special values. Let $\mathcal{F}_{\min}(\tilde{h})$ be the minimum value of $\mathcal{F}$ over all $\tilde{l}$ *i.e.*,

$$\mathcal{F}_{\min}(\tilde{h}) = \min_{\tilde{l}} \mathcal{F}(\tilde{l}, \tilde{h}), \tag{3.86}$$

and let $\tilde{l}_{\min}$ be defined such that

$$\mathcal{F}_{\min}(\tilde{h}) = \mathcal{F}(\tilde{l}_{\min}, \tilde{h}). \tag{3.87}$$

Further let us define $\mathcal{F}_o$ to be the global minimum over all $\tilde{l}$ and $\tilde{h}$. The following observations can be made.

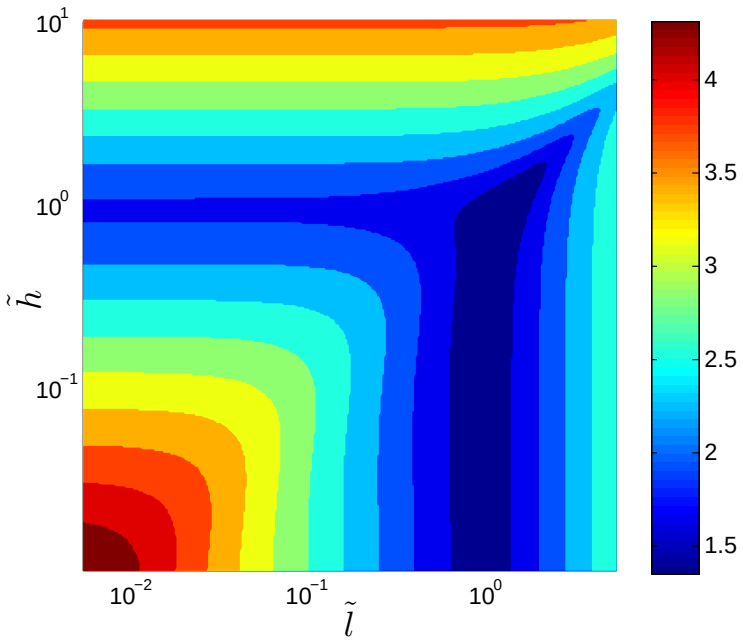

Figure 3.20: Contours of the modeled error $\log_{10}\left(\dot{\mathcal{E}}\mathrm{N}_{\mathrm{tot}}^{2q}\right)$ given by Eq. (3.84) in $\tilde{h}$-$\tilde{l}$ space.

First, consider Fig. 3.21(a) which plots the variation of $\tilde{l}_{\min}$ against $\tilde{h}$. For $\tilde{h}$ tending to zero, the optimal error is obtained at $\tilde{l} = 1$. Next, for all values of $\tilde{h} \leq 1$, $\tilde{l} = 1$ is a reasonable choice for minimizing the error. For values of $\tilde{h}$ greater than unity, $\tilde{l}$ is directly proportional to $\tilde{h}$. Secondly, consider Figure 3.21(b) which plots $\mathcal{F}_{\min}/\mathcal{F}(0,\tilde{h})$ against $\tilde{h}$ suggesting that given $\mathrm{N}_{\mathrm{tot}}$ and $\tilde{h}$, the minimum root-mean-squared error in an estimated statistic $\mathcal{F}_{\min}$ after smoothing with $\tilde{l}_{\min}$ is smaller than the error incurred $\mathcal{F}(0,\tilde{h})$ before smoothing is performed. The error is reduced significantly for $\tilde{h} < 1$. In other words, smoothing with an appropriate value of $\tilde{l}$ is always beneficial. Finally, Figure 3.21(c) indicates that to a good approximation, the global minimum $\mathcal{F}_o$ occurs at $\tilde{h} = 1$

and $\tilde{l} = 1$. For $\tilde{h} < 1$, $\mathcal{F}_{\min}$ is approximately 26% larger than $\mathcal{F}_o$. For large $\tilde{h}$ (compared to unity) values, $\mathcal{F}_{\min}$ is proportional to $\tilde{h}$. Moreover, for a value of N_{tot} infinitely large, provided that $\tilde{l}$ and $\tilde{h}$ are chosen such that $\mathcal{F}$ is essentially constant, then

$$\dot{\mathcal{E}} \sim N_{tot}^{-2q} = N_{tot}^{-2/7} \text{ in 3D.} \tag{3.88}$$

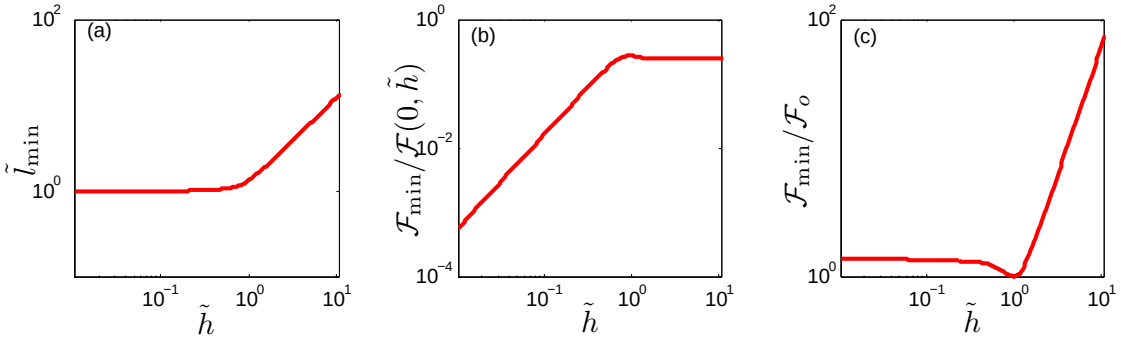

Figure 3.21: (a) Variation of $\tilde{l}_{\min}$ given by Eq. (3.87) against $\tilde{h}$ (b) Variation of $\mathcal{F}_{\min}/\mathcal{F}(0,\tilde{h})$ (Eq. (3.86)) with $\tilde{h}$ and (c) Variation of $\mathcal{F}_{\min}/\mathcal{F}_o$ with $\tilde{h}$.

Finally, one could also study the effect of grid refinement on the root-mean-squared error for a fixed number of particles per cell N_{pc}. Figure 3.22 plots the statistical error against N_{tot} with smoothing (open symbols) and without smoothing (filled symbols) for a fixed value of l. The solid lines correspond to the model given by Eq. (3.78). This shows that the statistical error scales as $N_{pc}^{-1/2}$ with no smoothing and as $N_{tot}^{-1/2}$ with non-trivial smoothing.

In summary, the results suggest the following. Smoothing can be used for two purposes. It can be applied to quantities that are estimated primarily for output purposes. Or it can be applied to quantities that are fed back into the PDF calculations as coefficients of SDEs. Smoothing output quantities reduces the

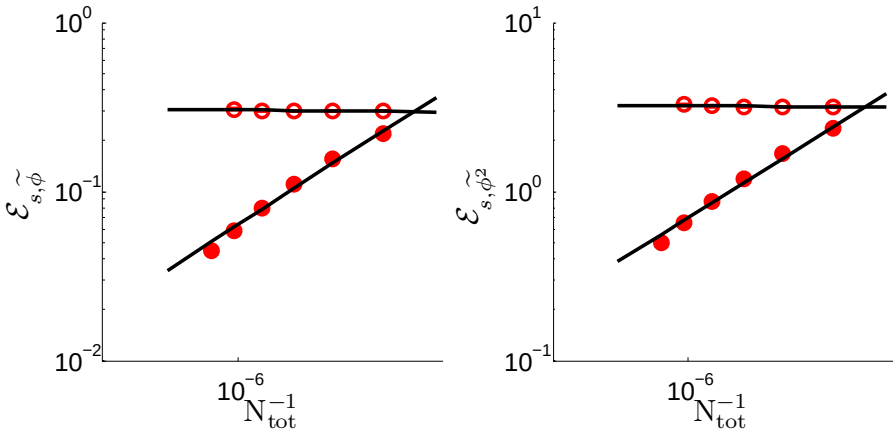

Figure 3.22: Global error in the scalar mean and the second moment against N_{tot}^{-1} for fixed N_{pc}. Symbols are results of PDF calculations. Solid lines correspond to the model for the global error given by Eq. (3.78). ● corresponds to a non-dimensional $l = 0.04$ and ❍ corresponds to $l = 0$

statistical error in their estimate and the error with smoothing scales as $N_{tot}^{-1/2}$ instead of as $N_{pc}^{-1/2}$. When smoothing is applied to feedback quantities, it is evident that the bias error now scales as N_{tot}^{-1} instead of N_{pc}^{-1}. An appropriate amount of smoothing is also beneficial in reducing the deterministic error incurred. Therefore, smoothing allows us to decrease the root-mean-squared error incurred for an appropriate choice of the smoothing length scale, l given a total number of particles N_{tot} and h.

3.6 Differential diffusion

Many mixing and combustion models in turbulence make the assumption of equal molecular diffusivities of all species. This may be justified when the molecular diffusivity is smaller than the turbulent diffusivity. However, in a

DNS this assumption is not justified, and in LES/PDF methods, the DNS limit is significant. Sutherland *et. al.* [78] analyzed spatially–filtered DNS data of $CH_4/H_2/N_2$–air and $CO_4/H_2/N_2$–air flames to show that the importance of differential diffusion increases as the filter size decreases. Kemenov and Pope [31] show from LES studies of a laboratory-scale jet flame (Sandia flame D) that molecular diffusivity is dominant in the near-field of the jet in comparison to the subgrid-scale turbulent diffusivity on reasonably sized grids. The equal diffusivity assumption in such cases might lead to inaccurate predictions for various statistics of interest. In this section, we study the ability of the modified IEM mixing model to account for the effects of differential diffusion.

The current section is organized as follows. In Sec. §3.2, it was shown that the mixing model given by Eq. (3.2) has the capability to account for the effects of differential diffusion. Here, in sub-section §3.6.1, we extend the mixing model given by Eq. (3.2) to multiple scalars with equal diffusivities. The modified form of Fick's law is briefly mentioned in Sec. 3.6.2. Following this, an extension to multiple scalars with differential diffusion is made in Sec. §3.6.3 with the results of a test case that considers mixing of three species with different diffusivities presented in Sec. §3.6.4.

3.6.1 Multiple scalars with equal diffusivities

Consider a PDF calculation of a non-reacting turbulent flow with n_s species each with the same molecular diffusivity $\Gamma(\mathbf{x}, t)$. Then, the mixing model given by

Eq. (3.2) can simply be extended to this case of multiple species as,

$$\frac{d\phi_\alpha^*(t)}{dt} = -\Omega_m^* \left(\phi_\alpha^* - \widetilde{\phi}_\alpha^*\right) + \left[\frac{1}{\bar{\rho}}\frac{\partial}{\partial x_j}\left(\bar{\rho}\Gamma\frac{\partial\widetilde{\phi}_\alpha}{\partial x_j}\right)\right]^*, \tag{3.89}$$

where ϕ_α for $\alpha = 1, 2, ..., n_s$ is the set of species mass fractions. It should be noted that the above Eq. (3.89) is easily obtained by replacing ϕ in Eq. (3.2) with ϕ_α.

Given that ϕ_α is the set of species mass fractions, a mixing model should satisfy the normalization condition on mass fractions $\sum_\alpha \phi_\alpha = 1$. Now, let $\phi^o = \mathbf{\Theta}^T\boldsymbol{\phi}$, where $\mathbf{\Theta}$ is any constant and uniform vector. Then it is evident that ϕ^o also satisfies Eq. (3.89). Note that $\mathbf{\Theta}$ can be chosen so that ϕ^o represents conserved quantities: element mass fractions, mixture fractions and the sum of species mass fractions (= 1). If ϕ^o is initially constant and uniform, then its value does not change both according to Eq. (3.89) and in any numerical implementation that guarantees boundedness (since $\min\{\phi^o\} = \max\{\phi^o\}$). Thus the normalization condition on mass fractions is satisfied.

3.6.2 Modified Fick's Law

For a non-reacting flow with n_s species and unequal molecular diffusivities, we consider molecular diffusion to be represented by a modified form of Fick's law in which the diffusion velocity $\mathbf{V}_\alpha$ of species α is given by

$$\phi_{(\alpha)}\left(\mathrm{V}_{(\alpha),j} + \mathrm{V}_{c,j}\right) = -\Gamma_{(\alpha)}\frac{\partial\phi_{(\alpha)}}{\partial x_j}, \tag{3.90}$$

where $\Gamma_\alpha(\mathbf{x}, t)$ is the mixture-averaged diffusivity of species α, and $\mathbf{V}_c$ is the correction velocity [42, 12] given by,

$$\mathrm{V}_{c,j} = -\sum_{\alpha=1}^{n_s}\Gamma_\alpha\frac{\partial\phi_\alpha}{\partial x_j}. \tag{3.91}$$

The suffixes in parentheses are excluded from the summation convention. The correction velocity is thus defined so that the Fick's law model for the mass-averaged diffusion velocity is zero, and therefore the sum of the species mass fraction equations correctly reduces to the mass conservation equation.

3.6.3 Multiple scalars with unequal diffusivities

For the case of multiple species with unequal molecular diffusivities $\Gamma_\alpha(\mathbf{x}, t)$, a mixing model is defined that is consistent with the modified Fick's law:

$$\frac{d\phi_\alpha^*(t)}{dt} = -\Omega_m^*\left(\phi_\alpha^* - \widetilde{\phi}_\alpha^*\right) + \left[\frac{1}{\bar{\rho}}\frac{\partial}{\partial x_j}\left(\bar{\rho}\Gamma_{(\alpha)}\frac{\partial\widetilde{\phi}_\alpha}{\partial x_j}\right)\right]^* - \left[\frac{1}{\bar{\rho}}\frac{\partial\bar{\rho}\widetilde{\phi}_\alpha V_{c,j}}{\partial x_j}\right]^*. \tag{3.92}$$

It should be noted that Eq. (3.92) differs from Eq. (3.89) in the last two terms on its right-hand side: the second term involves Γ_α in place of a single diffusivity Γ for all species, and the final term includes the correction velocity $\mathbf{V}_c$. It is evident that given ϕ^o denotes the sum of species mass fractions (= 1), ϕ^o satisfies Eq. (3.92), indicating that the mixing model given by Eq. (3.92) satisfies the normalization condition on mass fractions. Realizability of species mass fractions is guaranteed when $\phi_\alpha \geq 0$ for each α in addition to the normalization condition. Boundedness ($\phi_\alpha \geq 0$) can be imposed by fixing a lower limit on the mixing frequency [37] the details of which are presented in Appendix C.

Let us consider the transport equations for the first two scalar moments – the mean and the variance of mass fractions. The transport equation for any scalar moment can be derived from the corresponding PDF transport equation. The modeled PDF transport equation that corresponds to Eqs. (3.1) and (3.92) is

obtained as,

$$\begin{aligned}\frac{\partial f_\phi}{\partial t}+\frac{\partial}{\partial x_j}\left[f_\phi\left(\widetilde{\mathrm{U}}_j+\frac{1}{\bar{\rho}}\frac{\partial\bar{\rho}\Gamma_T}{\partial x_j}\right)\right] &= \frac{\partial^2\left(\Gamma_T f_\phi\right)}{\partial x_j\partial x_j}+\frac{\partial}{\partial\psi_\alpha}\left[f_\phi\Omega_m\left(\psi_\alpha-\widetilde{\phi}_\alpha\right)\right]\\ &- \frac{\partial}{\partial\psi_\alpha}\left[f_\phi\frac{1}{\bar{\rho}}\frac{\partial}{\partial x_j}\left(\bar{\rho}\Gamma_{(\alpha)}\frac{\partial\widetilde{\phi}_\alpha}{\partial x_j}\right)\right]\\ &+ \frac{\partial}{\partial\psi_\alpha}\left[f_\phi\frac{1}{\bar{\rho}}\frac{\partial}{\partial x_j}\left(\bar{\rho}\widetilde{\phi}_\alpha V_{c,j}\right)\right]. \end{aligned} \tag{3.93}$$

First, we consider the transport equation for the first moment of the scalar $\widetilde{\phi}_\alpha$:

$$\frac{\partial\bar{\rho}\widetilde{\phi}_\alpha}{\partial t}+\frac{\partial\bar{\rho}\widetilde{\mathrm{U}}_j\widetilde{\phi}_\alpha}{\partial x_j}=\frac{\partial}{\partial x_j}\left[\bar{\rho}(\Gamma_T+\Gamma_{(\alpha)})\frac{\partial\widetilde{\phi}_{(\alpha)}}{\partial x_j}\right]-\frac{\partial}{\partial x_j}\left[\bar{\rho}\widetilde{\phi}_\alpha V_{c,j}\right]. \tag{3.94}$$

Given Eq. (3.91) and realizable initial and boundary conditions, Eq. (3.94) guarantees

$$\frac{D}{Dt}\sum_\alpha\widetilde{\phi}_\alpha=0, \tag{3.95}$$

where D/Dt is the substantial derivative following a particle and $\widetilde{\phi}_\alpha\geq 0$. It should be noted that $\widetilde{\phi}_\alpha\geq 0$ and $\sum_\alpha\widetilde{\phi}_\alpha=1$ implies $\widetilde{\phi}_\alpha\leq 1$. Thus, the mixing model given by Eq. (3.92) guarantees realizability and boundedness of mean mass fractions. The transport equation for the scalar variance remains unchanged from Eq. (3.8) (with $S=0$) *i.e.,* according to the model, the variances are not directly affected by molecular diffusivities.

The following paragraphs detail an algorithm for the numerical implementation of Eq. (3.92). Given the pair of equations Eqs. (3.1) and (3.92), we adopt a splitting scheme of type $\mathbb{TMRMT}$ to solve for particle transport $\mathbb{T}$, mixing $\mathbb{M}$ and reaction $\mathbb{R}$. While the mixing step was split into IEM mixing step $\mathbb{I}$ and estimation of mean drifts due to molecular transport $\mathbb{D}$ as $\mathbb{IDI}$ in Sec. §3.3.1 for the case of equal diffusivities, with differential diffusion we adopt a scheme denoted as $\mathbb{IDCI}$ for the mixing step where $\mathbb{C}$ denotes the correction imposed to

satisfy the normalization condition on species mass fractions (corresponding to Eq. (3.91)). It should be noted that the mixing step given by the splitting scheme $\mathbb{IDCI}$ is not symmetric and therefore, the overall scheme reduces to first-order temporal accuracy in the presence of differential diffusion.

The one-step update for the particle scalar with differential diffusion is numerically implemented similar to Eq. (3.18) for a single scalar as:

$$\phi_\alpha^{*,n+1} = \phi_\alpha^{*,n} + c^{*,n+\frac{1}{2}} \left(\widetilde{\phi}_\alpha^{*,n} - \phi_\alpha^{*,n} \right) + \Delta\widetilde{\phi}_\alpha^{*,n+\frac{1}{2}}, \tag{3.96}$$

with the mean drift $\Delta\widetilde{\phi}_\alpha$ now defined in terms of the change in solution over a time-step of the heat conduction equation $\Delta\widetilde{\phi}_\alpha^h$ and the correction to the mean drift $\Delta\widetilde{\phi}_\alpha^c$ as,

$$\Delta\widetilde{\phi}_\alpha^{*,n+\frac{1}{2}} \equiv \Delta\widetilde{\phi}_\alpha^{h,*,n+\frac{1}{2}} - \Delta\widetilde{\phi}_\alpha^{c,*,n+\frac{1}{2}}. \tag{3.97}$$

Note that $\Delta\widetilde{\phi}_\alpha^{h,*,n+\frac{1}{2}}$ is the change in the solution over one time-step, in species α estimated at particle locations, obtained using Eq. (3.4) given $\widetilde{\phi}_\alpha^n$ and $\Delta\widetilde{\phi}_\alpha^{c,*,n+\frac{1}{2}}$ is the correction to the mean drift and is obtained as the change in solution to

$$\frac{\partial \bar{\rho}\widetilde{\phi}_\alpha}{\partial t} = \frac{\partial \bar{\rho}\widetilde{\phi}_\alpha V_{c,j}}{\partial x_j}, \tag{3.98}$$

over the same time-step given $\widetilde{\phi}_\alpha^n$ and $\mathbf{V}_c^{n+\frac{1}{2}}$. The precise details of the numerical implementation are provided in Appendix A. In Appendix C, it is shown that this numerical implementation satisfies conservation and realizability.

In summary, we present a model for scalar mixing that incorporates differential diffusion effects correctly. A splitting scheme is presented that satisfies conservation and realizability constraints (shown in Appendix C) but reduces to first-order temporal accuracy in the presence of differential diffusion. The following section analyzes this model and its implementation using a three-species

mixing problem with differential diffusion.

3.6.4 Results and discussion

We study the model and its implementation presented in Sec. §3.6.3 for incorporating the effects of differential diffusion by considering a three-species pure mixing problem in one dimension as described below. The Schmidt numbers of the three species are taken to be Sc = $[1\ \frac{1}{4}\ \frac{1}{10}]$ with reference to a constant viscosity of unity. The governing equations for the mean and the variance of species mass fractions given by Eqs. (3.94) and (3.8) respectively reduce to,

$$\frac{\partial \widetilde{\phi}_\alpha}{\partial t} = \frac{\partial}{\partial x}\left[\Gamma_{(\alpha)}\frac{\partial \widetilde{\phi}_{(\alpha)}}{\partial x}\right] - \frac{\partial}{\partial x}\left[\widetilde{\phi}_\alpha \sum_\beta \Gamma_\beta \frac{\partial \widetilde{\phi}_\beta}{\partial x}\right] \tag{3.99}$$

$$\frac{\partial \widetilde{\phi''^2_\alpha}}{\partial t} = -2\Omega_m \widetilde{\phi''^2_\alpha}, \tag{3.100}$$

with the mixing frequency Ω_m being set to unity. Equation (3.99) is solved with zero Neumann boundary conditions on each $\widetilde{\phi}_\alpha$ and the domain in x-direction is chosen to be sufficiently large such that the value of each $\widetilde{\phi}_\alpha$ near the boundary does not change significantly. The mean mass fractions are initialized at time $t = 0$ as,

$$\widetilde{\phi}_1 = \frac{13}{40}\left[\tanh(20x + 8) - \tanh(20x - 8)\right], \tag{3.101}$$

$$\widetilde{\phi}_2 = \frac{7}{13}\widetilde{\phi}_1, \tag{3.102}$$

$$\widetilde{\phi}_3 = 1 - \widetilde{\phi}_1 - \widetilde{\phi}_2. \tag{3.103}$$

Given the constraint $\sum_\alpha \phi_\alpha = 1$, the realizable region in 3D composition space is a 2D simplex with vertices at $\phi_\beta = \delta_{(\alpha)\beta}$ for each α (δ denotes the Kronecker

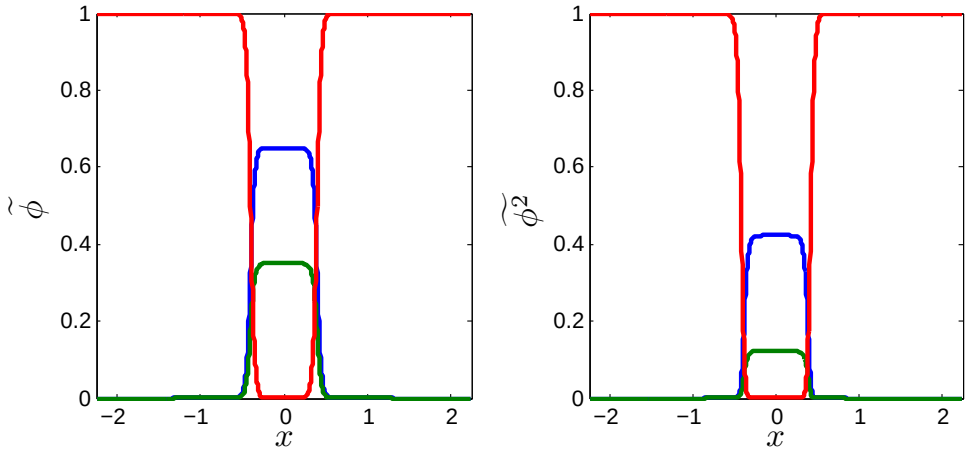

Figure 3.23: Mean and mean square of species mass fractions at $t = 0$ for the three species with Schmidt numbers $\mathrm{Sc}_1 = 1$, $\mathrm{Sc}_2 = \frac{1}{4}$ and $\mathrm{Sc}_3 = \frac{1}{10}$

delta). We initialize the particles in composition space by distributing them on the realizable plane uniformly around a mean composition $\widetilde{\boldsymbol{\phi}}$ in a circle of radius ρ_c. As a result, the variance of mass fraction for each species can be shown to be equal to $\rho_c^2/6$. The initial conditions for the mean and mean square of mass fractions are illustrated in Fig. 3.23.

Since the solution to Eq. (3.99) is not known analytically, the results of the PDF calculation are compared to an accurate numerical solution. A numerically accurate solution is obtained by solving Eq. (3.99) using the Crank-Nicolson method in conjunction with Richardson extrapolation over 512 time steps and on two grids with 512 and 1536 cells for a total time T of $\Omega_m \mathrm{T} = 3$. For constant Ω_m, the solution to Eq. (3.100) and the mean square mass fraction are obtained as,

$$\widetilde{\phi_\alpha''^2}(t) = \widetilde{\phi_\alpha''^2}\Big|_{t=0} \exp\left(-2\Omega_m t\right), \tag{3.104}$$

$$\widetilde{\phi_\alpha^2} = \widetilde{\phi_\alpha''^2} + \widetilde{\phi}_\alpha^2. \tag{3.105}$$

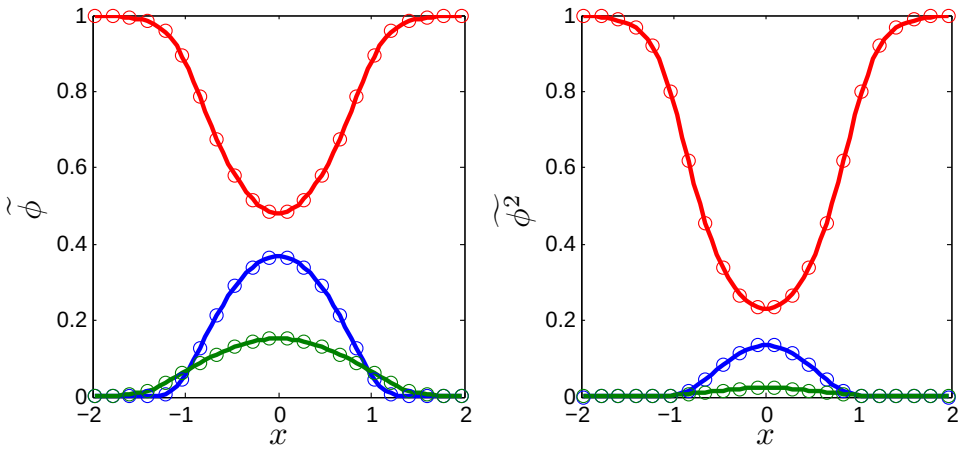

Figure 3.24: Mean and mean square of species mass fraction at $\Omega_m t = 3$ for the three species with Schmidt numbers $\mathrm{Sc}_1 = 1$, $\mathrm{Sc}_2 = \frac{1}{4}$ and $\mathrm{Sc}_3 = \frac{1}{10}$. Solid line corresponds to PDF calculations and the symbols are sampled from the accurate solution obtained using Crank-Nicolson method.

Figure 3.24 plots the mean and mean-squared mass fractions at $\Omega_m t = 3$. The solid line corresponds to the PDF calculation and the symbols are sampled from the solution obtained from Crank-Nicolson method. Figure 3.25 plots the particles in composition space at the same time on the realizable plane. As can be observed, the implementation ensures that the particles evolve on the realizable plane through the progress of the calculation.

We define mixture fraction based on individual species as,

$$\xi_\alpha = \frac{\phi_\alpha - \phi_{\alpha,0}}{\phi_{\alpha,\infty} - \phi_{\alpha,0}}, \tag{3.106}$$

where ξ_α is the mixture fraction based on species α, $\phi_{\alpha,0}$ is the mass fraction of species α at $x = 0$ and $t = 0$, and $\phi_{\alpha,\infty}$ is at $x = \infty$ and $t = 0$. In the case of equal Schmidt numbers, the mixture fractions based on individual species is identical and the ratio of any two mass fractions remains constant. In the current test problem with non-unity Schmidt numbers, differential diffusion of individual

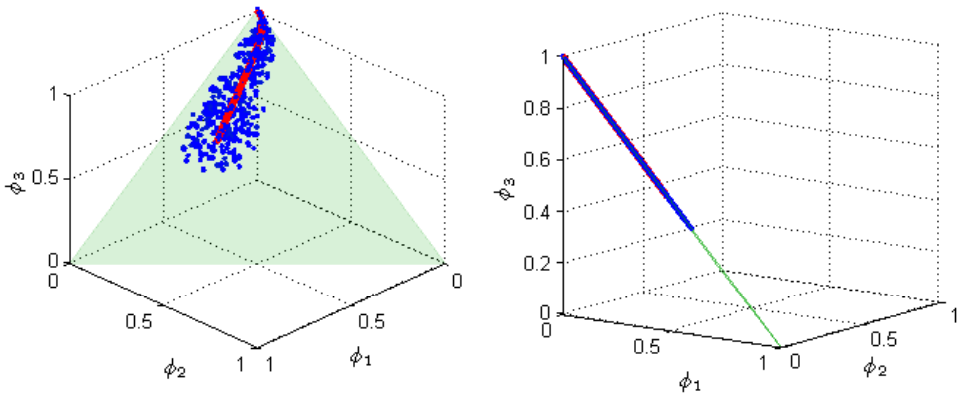

Figure 3.25: Distribution of particle compositions in composition space at $\Omega_m t = 3$. The green plane is the realizable region. The red solid line corresponds to the mean composition field and the blue dots represent particle compositions. The second figure is identical to the first one but is rotated such that the line of sight is along the plane of the realizable region confirming that the numerical implementation preserves realizability.

species yields distinct definitions of mixture fractions. Figure 3.26 compares the estimated mean mixture fractions defined based on the three species taken two at a time. As is evident, differential diffusion effects are significant as the results from the PDF calculations deviate strongly from the line of slope 1.

In summary, we see that differential diffusion effects can be significant and the current implementation of molecular transport is successful in capturing these effects accurately while ensuring realizability.

3.7 Conclusions

In this work, we present a model for mixing and molecular transport in the context of PDF methods for turbulent reacting flows based on the work of Mc-

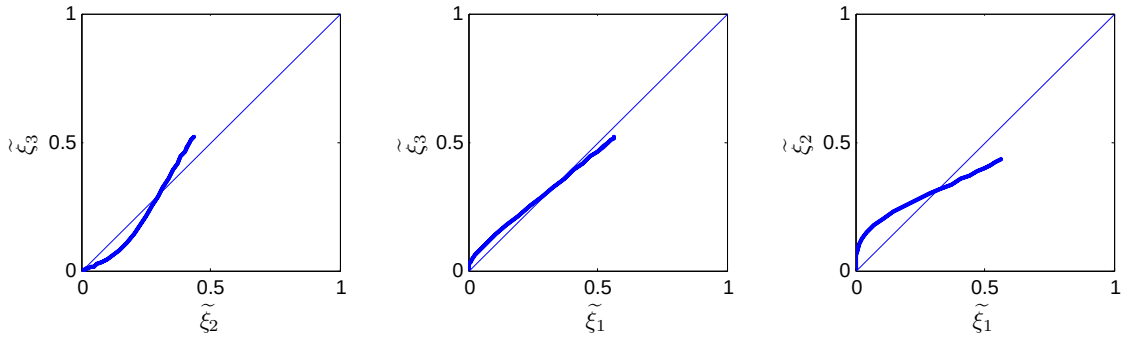

Figure 3.26: Comparison of mean mixture fractions defined based on each species using Eq. (3.106) at $\Omega_m t = 3$ is shown in blue. The thin solid blue line is of slope 1.

Dermott and Pope [37]. Mixing is modeled using the IEM model while the effects of molecular transport are directly incorporated as a mean drift term in the scalar evolution equation by Eq. (3.2). This modeling strategy avoids spurious production of scalar variance even though it neglects the molecular transport of variance in physical space. In high-Reynolds-number flows, transport in physical space by molecular diffusion can be justified as being negligible. Additionally, this model provides an easy route to incorporating the effects of differential diffusion (Eq. (3.92)).

We show that the algorithm described for the numerical implementation of the above-mentioned model is second-order accurate in space and time (except for first-order temporal accuracy in the implementation of the convection velocity in the case of differential diffusion). Specifically, three numerical schemes (PIC-PC, PIC-PL and CIC-LS) for the implementation of mixing and molecular transport are evaluated. All the numerical schemes used for the implementation are unconditionally stable and conservative. For a pure mixing problem,

the CIC-LS scheme incurs a larger error as compared to the other two schemes whereas there is insignificant difference between the schemes when all processes - transport, mixing and reaction - are treated. For a given accuracy, the CIC-LS scheme is almost thrice as expensive as the other two schemes. Yet, since CIC-LS naturally ensures boundedness of scalars and yields continuous estimated fields, it is preferred over other schemes.

We also present a new variance-reduction methodology by performing implicit smoothing operations. The three-point smoothing scheme is adopted in this work and is shown to satisfy conservation and boundedness criteria. It is also shown to preserve regularity of smooth fields via appropriate handling of empty cells. The accuracy of estimated statistics can be improved significantly for an appropriate choice of the smoothing parameter for very little increase in computational cost. Smoothing can be applied on either the "output" quantities or "feedback" quantities. In this work, a detailed analysis of the root-mean-squared error is performed while smoothing "output" quantities and we infer that the statistical error scales inversely with the total number of particles as $N_{tot}^{-1/2}$ instead of the number of particles per cell $N_{pc}^{-1/2}$ (as is the case with no smoothing). This implies that with smoothing of "feedback" quantities, the bias error scales inversely with the total number of particles, N_{tot}^{-1} in the domain instead of the number of particles per cell N_{pc}^{-1}. Moreover, we present a model for the root-mean-squared error obtained after smoothing of the "output" quantities that is successful in explaining the behavior portrayed by the data obtained from PDF calculations. One of the primary predictions of this model is that the root-mean-squared error after smoothing depends weakly on N_{tot} as $N_{tot}^{-2/7}$ in 3D.

Finally, we present a model (and a numerical implementation) that accounts

for differential diffusion effects in the scalar evolution equation. We show that this model and the corresponding numerical algorithm described in this work satisfy conservation and realizability constraints but the asymmetry of the splitting scheme reduces the temporal accuracy to first-order in the presence of differential diffusion. The model and the algorithm are studied in one dimension considering pure mixing of three non-unity Schmidt number scalars. It is shown that the effects of differential diffusion can be significant and the current implementation is successful in capturing these effects accurately while ensuring realizability.

3.8 Acknowledgments

We would like to thank Haifeng Wang and Steve R. Lantz for useful pointers through this work. This research is supported by the Department of Energy under Grant DE-FG02-90ER14128. This research was conducted using the resources of the Cornell University Center for Advanced Computing, which receives funding from Cornell University, New York State, the National Science Foundation, and other leading public agencies, foundations, and corporations.

CHAPTER 4

PRELIMINARY INVESTIGATION OF MIXING, MOLECULAR TRANSPORT AND SMOOTHING IN LES/PDF STUDIES OF SANDIA FLAME D*

Turbulence is one of the most complex unsolved research areas and the challenges in understanding turbulent combustion is further compounded due to the complicated chemical kinetics and highly non-linear turbulence-chemistry interactions. Qualitative and quantitative understanding of turbulent combustion therefore requires sound physical models and efficient numerical implementation methodologies.

Given the recent advancements made in the development of high-performance computing facilities, Large Eddy Simulations (LES) are emerging as the preferred Computational Fluid Dynamics (CFD) methodology to provide a detailed description of a wide range of turbulent flows. This is because, in comparison to Reynolds-Averaged Navier Stokes (RANS) approaches, LES resolves the largest scales inherent in the flow that are problem and geometry specific while modeling only the smallest scales of turbulence which, to some extent, feature universal properties. On the other hand, Direct Numerical Simulations (DNS) are currently computationally intractable for high Reynolds number turbulent flows and realistic geometries.

However, in LES studies of turbulent reacting flows, mixing and subgrid scale reaction have to be modeled. Various models have been devel-

*S. Viswanathan and S.B. Pope, "Preliminary investigation of mixing, molecular transport and smoothing in LES/PDF studies of Sandia Flame D", Cornell University Report, (*in preparation*) (2010)

oped in providing closure for sub-grid scale combustion, the most notable amongst which are the laminar flamelet model [14], Conditional Moment Closure (CMC) [41, 32] and Probability Density Function (PDF) methods [53, 23, 13]. PDF methods have proven to be successful in the context of both RANS and LES studies of turbulent reacting flows. The modeled PDF transport equations are solved using Lagrangian Monte Carlo particle methods [13, 49, 52] where the turbulent flow is represented by a set of statistically independent notional particles. Models are constructed to evolve particle properties in time and the resulting set of Stochastic Differential Equations (SDEs) are solved for particle transport, mixing and reaction.

In this work, we present results of a preliminary investigation of the numerical implementation of mixing and molecular transport detailed in Viswanathan and Pope [83] in LES/PDF study of a laboratory-scale turbulent jet flame. We choose the Sandia Flame D [2, 3] for this study since it is a very well documented and researched turbulent reacting jet flame with minimal levels of local extinction (in the Sandia Flame series). Further, we present an algorithm based on cross-validation to assist in the choice of a smoothing length scale for performing smoothing on estimated statistics.

Mixing is modeled using the Interaction by Exchange with the Mean (IEM) model and the effects of molecular diffusion are incorporated as a mean drift term in the particle scalar equation. As McDermott and Pope [37] point out, this modeling strategy has the advantage of avoiding spurious production of scalar variance, thereby achieving consistency between LES and PDF formulations in the DNS limit. Additionally, Kemenov and Pope [31] observe in their LES calculations of the same flame that on reasonably resolved grids, molecular

diffusivity is dominant compared to the sub-grid scale turbulent diffusivity in the near-field of the jet. Moreover, since the effects of molecular diffusion are not modeled as a stochastic Wiener process using a single diffusivity, differential diffusion is more readily incorporated [37, 83].

The rest of this study is organized as follows. Section §4.1 describes the the details of the LES/PDF method used in current work. Following this, Sec. §4.2 provides a brief overview of the three-point implicit smoothing scheme detailed in [83] and describes an algorithm based on the method of cross-validation used in the choice of a smoothing length scale. Finally, Sec. §4.3 provides the experimental and computational details on Flame D before presenting the results of this study in Sec. §4.4 and conclusions in Sec. §4.6.

4.1 Details of the LES/PDF method

In this section, we present the details of the numerical scheme employed to obtain the LES and PDF solutions. A hybrid particle/mesh method is used with a fractional step scheme, the details of which are described below. Section §4.1.1 presents the details regarding the algorithm used in obtaining the LES solution and Sec. §4.1.2 briefly gives details about the the methodology used to solve for the PDF transport equation.

4.1.1 LES solution

The LES algorithm used in this work is based on the Stanford LES code, the details of which can be found in [46, 45]. We briefly mention the significant relevant details here. The LES model equations for mass, momentum and scalars are solved using a finite-difference scheme in a cylindrical coordinate system on a structured non-uniform grid with second-order spatial and temporal accuracy. The pressure projection method is used to enforce continuity. The SGS eddy viscosity μ_{sgs} and the diffusivity Γ_{sgs} are both obtained using the dynamic Smagorinsky model [73].

Transport equations are solved for both the resolved mixture fraction $\widetilde{\xi}$ and the resolved mixture fraction square $\widetilde{\xi^2}$ and the dissipation rate $\widetilde{\chi}$ of the residual variance of mixture fraction is modeled as [86],

$$\widetilde{\chi} = \Gamma \nabla\widetilde{\xi}.\nabla\widetilde{\xi} + \frac{\left(2\Gamma + \Gamma_{sgs}\right)\widetilde{\xi''^2}}{\Delta^2}, \tag{4.1}$$

where $\widetilde{\xi''^2} = \widetilde{\xi^2} - \widetilde{\xi}^2$ is the residual mixture fraction variance, Δ is the filter size and Γ is the molecular diffusivity. Note that a "$\widetilde{\ }$" denotes density-weighted filtered quantities.

The various compositions are obtained using the laminar flamelet model. A single laminar flamelet profile is obtained as a function of instantaneous mixture fraction from an OPPDIF [36] calculation using CHEMKIN performed at a nominal strain rate of $25s^{-1}$. The chemical mechanism used is GRI3.0 [74]. Molecular transport is treated using mixture-averaged diffusivities. A presumed beta-function PDF for the SGS mixture fraction fluctuations is used to tabulate the resolved quantities as functions of $\widetilde{\xi}$ and $\widetilde{\xi^2}$. All the resolved species mass frac-

tions $\widetilde{Y}$, the resolved temperature $\widetilde{T}$ and the filtered density $\overline{\rho}$ in the LES are retrieved from this pre-computed table given $\widetilde{\xi}$ and $\widetilde{\xi^2}$. The molecular transport properties of viscosity μ and diffusivity Γ are approximated to be functions of $\widetilde{T}$ and $\overline{\rho}$ using empirical relations fit to the laminar flame calculations as [86]:

$$\mu = \nu_0 \overline{\rho} \left(\frac{\widetilde{T}}{T_0} \right)^{1.66}, \tag{4.2}$$

$$\Gamma = c_0 \nu_0 \left(\frac{\widetilde{T}}{T_0} \right)^{1.69}, \tag{4.3}$$

where $\nu_0 = 2.22 \times 10^{-5} m^2/s$, $T_0 = 300K$ and $c_0 = 1.22$.

4.1.2 PDF and Lagrangian Monte Carlo particle methods

In the PDF method, we solve the scalar PDF transport equation by numerically integrating the following set of modeled SDEs forward in time:

$$d\mathbf{x}^*(t) = \left[\widetilde{\mathbf{U}} + \frac{\nabla(\overline{\rho}\Gamma_{\text{sgs}})}{\overline{\rho}} \right]^* dt + \sqrt{2\Gamma^*_{\text{sgs}}} d\mathbf{W}, \tag{4.4}$$

$$\frac{d\xi^*(t)}{dt} = -\Omega^* \left(\xi^* - \widetilde{\xi}^* \right) + \left[\frac{1}{\overline{\rho}} \frac{\partial}{\partial x_j} \left(\overline{\rho} \Gamma \frac{\partial \widetilde{\xi}}{\partial x_j} \right) \right]^*, \tag{4.5}$$

where $\mathbf{x}^*$ denotes the particle position, $\widetilde{\mathbf{U}}$ is the resolved velocity field, $\mathbf{W}$ is the Wiener process, and Ω is the mixing frequency. All particle properties and quantities evaluated at $(\mathbf{x}^*(t), t)$ are denoted using a superscript "$*$". Note that the first term on the right-hand side of Eq. (4.5) represents mixing due to the IEM model and the second term represents the mean drift term due to molecular transport [37, 83]. All the coefficients required for integrating Eqs. (4.4) and (4.5) are obtained by interpolating the grid-based LES fields to particle locations. Evolution equations for $\widetilde{\xi}(\mathbf{x}, t)$ and $\widetilde{\xi^2}(\mathbf{x}, t)$ can be deduced from Eqs. (4.4) and (4.5), and

these are identical to those solved in the LES in the limit of vanishing molecular diffusivity. It should be noted that the LES and PDF grids are identical in this study.

Various first and second-order accurate numerical schemes can be constructed to numerically integrate Eqs. (4.4) and (4.5) in time [87]. LES/PDF studies based on this algorithm [86] indicate that for the values of the time steps typically encountered in a jet flame calculation, the differences between a first-order and second-order temporally accurate schemes are negligible. Therefore, a first-order accurate Strang's splitting scheme of type $\mathbb{TMR}$ is used to integrate the set of Eqs. (4.4) and (4.5) forward in time. The transport step is integrated numerically using the first-order Euler scheme and the "Cloud-in-cell (CIC) - Linear Spline (LS)" combination of schemes is used in the implementation of the mixing step. The details of the numerical implementation can be found in [83]. The mixing frequency Ω is obtained as $\Omega = (2\Gamma + \Gamma_{sgs})/\Delta^2$ to ensure consistency between LES and PDF formulations.

In summary, a brief description of the algorithm used in the numerical solution of the LES/PDF method is provided in this section.

4.2 Smoothing

In PDF methods, typically a nominal number N_{pc} of 20-50 particles per computational cell are used in a numerical calculation and the associated numerical errors can be broadly classified into spatial and temporal truncation errors, bias errors and statistical errors. The last two arise due to a finite number of particles

in the simulation. Various time-averaging methods [29, 40, 85, 91] have been developed in the context of RANS based PDF methods to control the statistical and bias errors encountered in these calculations.

However in LES/PDF methods, since time-averaging cannot be used on instantaneous fields, Viswanathan and Pope [83] present a spatial averaging methodology formulated as a three-point implicit smoothing technique (in 1D) parametrized by a single smoothing parameter α_s. It is shown in this work that with smoothing the statistical error scales as $N_{tot}^{-1/2}$ and bias as N_{tot}^{-1} where N_{tot} is the total number of particles used in the calculation, while with no smoothing the statistical and bias errors scale as $N_{pc}^{-1/2}$ and N_{pc}^{-1}, respectively. Moreover, their model for the root-mean-squared error in estimated statistics indicates that, upon smoothing with an appropriate value for the smoothing parameter, the method yields root-mean-squared errors scaling as $N_{tot}^{-2/7}$ in 3D.

The problem of choosing the smoothing length scale depends on the interpretation of smooth. However, a reliable automatically chosen parameter is a good initial guess. In this section, we present an algorithm based on the method of cross-validation to assist in the choice of the smoothing length scale based on the data from the PDF calculations. Section §4.2.1 presents the details of a technique of cross-validation implemented in this study.

4.2.1 Cross-validation assisted smoothing

Cross-validation is a well researched statistical method that is used to assess the predictive capabilities of a model [84, 15, 26, 24]. The general idea is to di-

vide the available data set into a *training* set and a *testing* set. The model is then built using the training set and is evaluated on the testing set. There exist many variants of the cross-validation algorithm that include leave-one-out (LOO) cross-validation, K-fold cross-validation and hold-out cross-validation. Studies performed (not reported here) indicate that there are negligible differences in accuracy between these different variants – LOO, K-fold and hold-out – for the current purpose and therefore in this study, we use the hold-out cross-validation. The details are presented below.

Consider a uniform grid with N_{cell} cells in a 1D Cartesian coordinate system with cell-centers of the grid located at uniform x_i for $i = 1, 2, ..., N_{cell}$. Let f_i be the estimate of a statistic $F(x)$ at these cell-centers obtained as

$$f_i \equiv F(x_i) + \sigma\eta_i, \tag{4.6}$$

where σ^2 is the variance in the estimation of f_i and η is a normal random variable with zero mean and unit variance. Given the smoothing parameter α_s, we perform a three-point implicit smoothing [83] of the form,

$$(A_{ij} + W_{ij})g_j = W_{ij}f_j, \tag{4.7}$$

to obtain smoothed estimates g_i at the same locations x_i, where the tri-diagonal matrix A depends on α_s and W is the diagonal weight matrix. The details regarding the specifications of A and W and the treatment in higher dimensions can be found in [83]. We present the method of cross-validation employed in this work for this simple set-up of a 1D uniform grid in Cartesian system with unity smoothing weights $W = I$ (I is the identity matrix) but the method itself is not restricted to this specific case. The assumption of unity weights reduces

Eq. (4.7) to

$$(A_{ij} + I_{ij})g_j = f_j. \tag{4.8}$$

As mentioned before, we adopt the hold-out cross-validation method in this study. Consider W_1 and W_2 to be defined as follows:

$$W_{1ij} = \delta_{ij} \text{ for } i, j = 2p,\ p = 1, 2, ..., \mathrm{N_{cell}}/2, \tag{4.9}$$

$$W_{2ij} = \delta_{ij} \text{ for } i, j = 2p + 1,\ p = 0, 1, 2, ..., \mathrm{N_{cell}}/2 - 1, \tag{4.10}$$

where δ is the Kronecker symbol. Note that $W_1 + W_2 = I$, $W_1^T W_1 = W_1$ and $W_1^T W_2 = 0$, where W_1^T denotes the transpose of W_1.

Let f be divided into two subsets of $\bar{f}_1$ and $\bar{f}_2$ obtained from f as,

$$\bar{f}_1 = W_1 f, \tag{4.11}$$

$$\bar{f}_2 = W_2 f. \tag{4.12}$$

Consider obtaining smoothed estimates g_1 and g_2 of $\bar{f}_1$ and $\bar{f}_2$ respectively using Eq. (4.8) given the smoothing parameter α_s as:

$$(A + I)g_1 = \bar{f}_1, \tag{4.13}$$

$$(A + I)g_2 = \bar{f}_2. \tag{4.14}$$

The cross-validation error, $Z(\alpha_s)$ is defined as the mean-squared error between the smoothed data set and the data set not used in its determination and is calculated as:

$$Z(\alpha_s) = \|W_1 (f - g_2) + W_2 (f - g_1)\|, \tag{4.15}$$

where $\|.\|$ represents the two-norm. The value of α_s that minimizes Eq. (4.15) is chosen to be the optimal choice of the smoothing parameter.

Note that in a PDF calculation, f is any statistic such as the scalar mean estimated from particles. In the current study, cross-validation is applied to the smoothing of "output" fields and these fields are estimated using the PIC method [83] *i.e.*, f is estimated using all the N_{pc} particles in a given computational cell and $\bar{f}_1$ and $\bar{f}_2$ are then obtained from f using Eqs. (4.11) and (4.12). This methodology does not detect the noise-free $2\Delta x$ wave (where $\Delta x = x_{i+1} - x_i$ for uniform x_i) and will likely smooth it out. Instead, an alternative is to estimate $\bar{f}_1$ (and $\bar{f}_2$) using only half the number of particles in each cell.

The value α_s that minimizes Z can be calculated using any standard algorithm applied to an optimization problem. Specifically, we mention two such algorithms – the golden section search and Newton's method. The Golden Section Search [62] is the analog of the bisection method applied to a minimization problem where the minimum is repeatedly bracketed in an interval $a < b < c$ where $\alpha_s \in [a\ c]$. The name *golden section* search is due to the fact that the middle point b is chosen to be a fractional distance 0.38197 from one end, say a, and 0.61803 from the other end, say c and these fractions are those of the *golden mean* or *golden section*. The golden section search converges linearly. Moreover, it is very straight-forward to extend the algorithm to estimate the smoothing parameter for smoothing higher dimensional fields and is therefore used in this work.

However, there are other algorithms that can be used in place of the golden section search and we mention Newton's method here in 1D. The extension of Newton's method to multiple dimensions requires further thought. Newton's method requires the knowledge of the first two derivatives of Z with respect to α_s for iterative convergence and are readily obtained. Consider A to be ex-

pressed as $A \equiv \alpha_s B$ for some tri-diagonal matrix B. To simplify the notation we have

$$(\alpha_s B + I)\, g = f. \tag{4.16}$$

Thus, differentiating with respect to α_s,

$$(\alpha_s B + I)\, \frac{dg}{d\alpha_s} = -Bg. \tag{4.17}$$

Thus, once g is obtained, the same system of equations is again solved with $-Bg$ in place of f on the right-hand-side to obtain $dg/d\alpha_s$. Differentiating Eq. (4.17) again,

$$(\alpha_s B + I)\, \frac{d^2 g}{d\alpha_s^2} = -2B\frac{dg}{d\alpha_s}. \tag{4.18}$$

Once again, the second derivative is obtained by solving the same system of equations for a different RHS as shown in Eq. (4.18).

Let us define $R = Z^T Z$ and given Eqs. (4.17) and (4.18), we obtain the first and second derivatives of R with respect to α_s as

$$\begin{aligned} R' &= \frac{dR}{d\alpha_s} \\ &= -2(f - g_2)^T W_1 \frac{dg_2}{d\alpha_s} - 2(f - g_1)^T W_2 \frac{dg_1}{d\alpha_s}, \end{aligned} \tag{4.19}$$

$$\begin{aligned} R'' &= \frac{d^2 R}{d\alpha_s^2} \\ &= 2\frac{dg_2^T}{d\alpha_s} W_1 \frac{dg_2}{d\alpha_s} - 2(f - g_2)^T W_1 \frac{d^2 g_2}{d\alpha_s^2} \\ &+ 2\frac{dg_1^T}{d\alpha_s} W_2 \frac{dg_1}{d\alpha_s} - 2(f - g_1)^T W_2 \frac{d^2 g_1}{d\alpha_s^2}. \end{aligned} \tag{4.20}$$

Then, given an initial guess for α_s, say α_s^n, Newton's iteration yields

$$\alpha_s^{n+1} = \alpha_s^n - \frac{R'}{R''}. \tag{4.21}$$

In summary, we present the hold-out cross-validation method and its numerical implementation used in this work to assist in the automatic choice of the smoothing parameter in a LES/PDF turbulent reacting jet flame calculation.

4.3 Computational details of the Sandia Flame D

Extensive research amongst members of the turbulent combustion community has led to the development of a wide variety of turbulent jet flames useful for model development, testing and other benchmarking studies. The Sandia Flame D is one of the Sandia Flame series A-F [2, 3, 4]. The experimental database available for the Sandia Flames is comprehensive and detailed numerical studies have been performed on these flames previously by other researchers. We choose flame D for our studies in this work due to the relatively low levels of extinction observed in these flames.

Flame D is a piloted methane/air diffusion flame at a Reynolds number of $22,400$ based on the jet bulk exit velocity, the nozzle diameter and the kinematic viscosity of the fuel jet. The jet fluid consists of 1:3 volumetric ratio of methane and air with a stoichiometric mixture fraction $\xi_{st} = 0.351$. The pilot stream is a lean premixed gas mixture of C_2H_2, H_2, CO_2, N_2 and air at an equivalence ratio of 0.77 and an equilibrium composition similar to the jet fuel with $\xi = 0.271$. The details regarding the operating conditions and geometry are listed in Table 4.1.

The computational domain is setup to extend between [0 80D] in the axial (x) direction, [0 20D] in the radial (r) direction and [0 2π] in the azimuthal (θ) direction, where D is the jet diameter. A non-uniform structured grid of size

$256 \times 128 \times 32$ (in x, r, θ) is used. The LES and PDF grids are identical. A constant CFL condition (CFL = 0.5 and based on the axial velocity) is imposed and the time step is determined given this condition. The LES equations and the PDF counter-parts are then numerically integrated forward in time over this same time step. A nominal number of $N_{pc} = 40$ particles per cell is used in the solution of the PDF transport equation. A statistically stationary solution is used for initialization of the LES solution and the LES fields are used to initialize the particles in the PDF method. Convective boundary conditions are imposed on the outflow boundaries. The simulation is carried out for around 6 flow-through times (estimated based on the jet centerline velocity) to attain a statistically stationary state. Then, statistics are collected for an additional 6

Table 4.1: Operating conditions and the geometry of Sandia Flame D.

Jet bulk velocity	(m/s)	49.6(±2)
Pilot gas velocity	(m/s)	11.4(±0.2)
Co-flow velocity	(m/s)	0.9(±0.05)
Reynolds number		22,400
Inner jet diameter (D)	(mm)	7.2
Inner pilot diameter	(mm)	7.7
Outer pilot diameter	(mm)	18.2
Pressure	(bar)	1.006
Fuel stream	(K,–)	T = 291, $Y_{CH_4} = 0.156$, $Y_{O_2} = 0.196$, $Y_{N_2} = 0.648$
Oxidizer stream	(K,–)	T = 291, $Y_{O_2} = 0.233$, $Y_{N_2} = 0.767$

flow-through times after statistical stationarity. This corresponds to 3000 time steps of a single calculation. Each calculation is performed on an HPC cluster of 32 Dell servers, each featuring dual, dual-core 3GHz Intel Xeon "Woodcrest" processors with 8 GB RAM, tied together using a QLogic 4X SDR InfiniBand interconnect for approximately 28 hours of wall-clock time.

4.4 Results

The implementation of mixing, molecular transport and smoothing (with and without cross-validation) in LES/PDF methods is validated against the experimental data available for Sandia Flame D [2] and LES/PDF calculations based on the algorithm described in [86] (henceforth referred to as W-PDF). In these calculations denoted W-PDF, the IEM model is used for mixing while the effects of molecular transport are modeled as a random walk term in the particle position equation. In other words, Eqs. (4.4) and (4.5) are replaced with

$$d\mathbf{x}^*(t) = \left[\widetilde{\mathbf{U}} + \frac{\nabla(\overline{\rho}(\Gamma_{\rm sgs}+\Gamma))}{\overline{\rho}}\right]^* dt + \sqrt{2(\Gamma^*_{\rm sgs}+\Gamma^*)}d\mathbf{W}, \tag{4.22}$$

$$\frac{d\xi^*(t)}{dt} = -\Omega^*\left(\xi^* - \widetilde{\xi}^*\right), \tag{4.23}$$

in the PDF particle method. For consistency between the LES and W-PDF solutions in the DNS limit, the mixing frequency in Eq. (4.23) is obtained as $\Omega = \widetilde{\chi}/\widetilde{\xi''^2}$ where $\widetilde{\chi}$ is given by Eq. (4.1). Note that the differences between the current PDF calculations and W-PDF calculations arise in the treatment of molecular transport and the numerical implementation of the IEM mixing model. The W-PDF calculations are performed on the same grid as the current PDF studies, for the same number of time steps and with the same number of particles per cell. The

models and boundary conditions used for transport and reaction sub-steps are the same. The algorithm used in obtaining the solution to the LES set of equations (in conjunction with the W-PDF calculations) is identical to the method used in the current study.

The results of this study are presented in two parts. Section §4.4.1 compares the radial profiles of time-averaged statistics of various quantities obtained using Eqs. (4.4) and (4.5) with the experimental data, the LES solution and W-PDF calculations. No smoothing is performed in any of these calculations. Section §4.4.2 describes the effect of the choice of the smoothing parameter on the "output" and "feedback" quantities and additionally also demonstrates the efficacy of using cross-validation assisted smoothing.

4.4.1 Mixing and molecular transport

This section presents results of the LES/PDF calculations of Sandia Flame D performed based on Eqs. (4.4) and (4.5) for the evolution of particle properties in the PDF method. Specifically, we report radial profiles of time-averaged statistics at various axial locations downstream of the jet exit plane. All time-averaged quantities are denoted using $\langle . \rangle$ and the different statistics considered include resolved mixture fraction $\langle \widetilde{\xi} \rangle$, total mixture fraction variance $\langle \xi'' \rangle_m^2 = \langle \widetilde{\xi^2} \rangle - \langle \widetilde{\xi} \rangle^2$, resolved density $\langle \overline{\rho} \rangle$, resolved temperature $\langle \widetilde{T} \rangle$, resolved species mass fractions $\langle \widetilde{Y} \rangle$, resolved temperature fluctuation $\langle T'' \rangle_W = \left(\langle \widetilde{T}^2 \rangle - \langle \widetilde{T} \rangle^2 \right)^{1/2}$ and resolved fluctuations in species mass fractions $\langle Y'' \rangle_W = \left(\langle \widetilde{Y}^2 \rangle - \langle \widetilde{Y} \rangle^2 \right)^{1/2}$.

Figure 4.1 plots the radial profiles of time-averaged mixture fraction $\langle \widetilde{\xi} \rangle$, to-

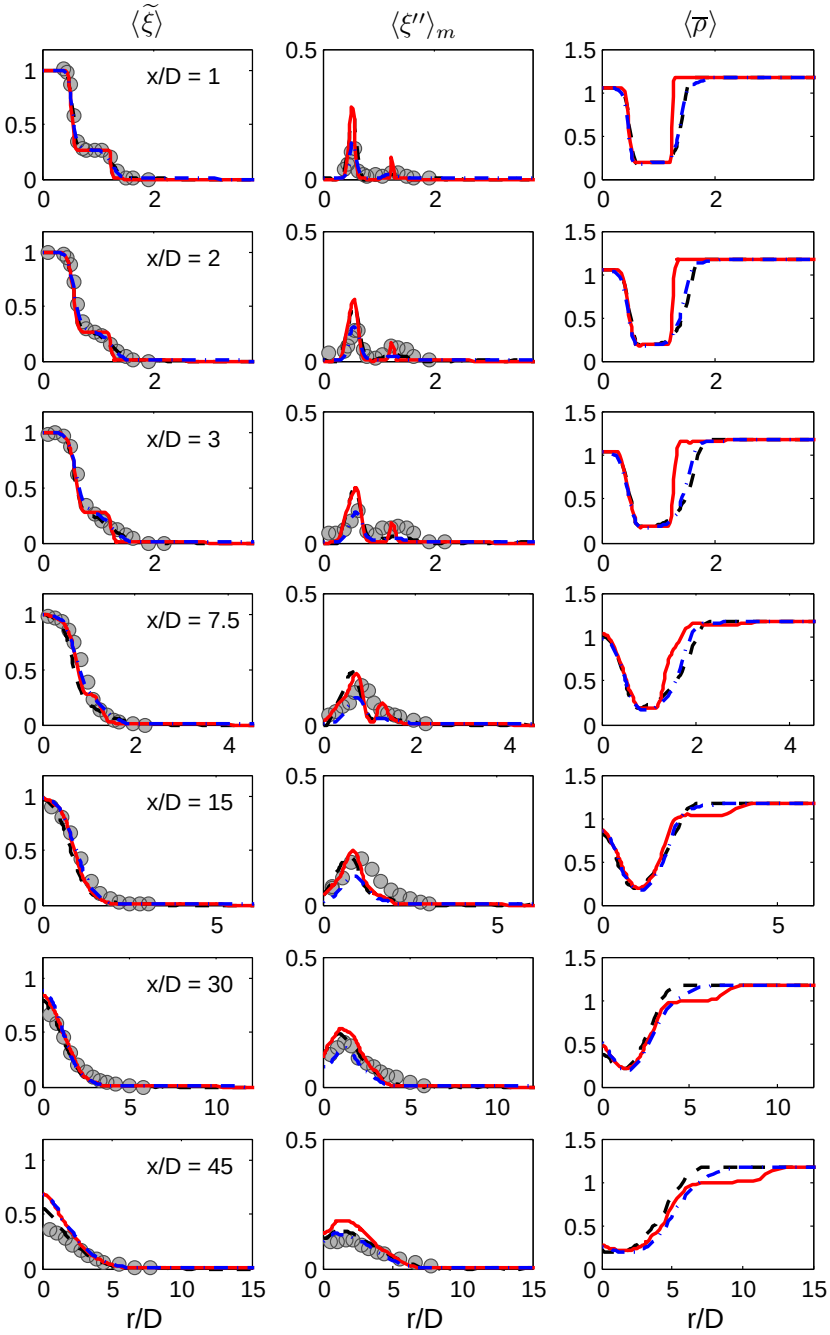

Figure 4.1: Radial profiles of time-averaged quantities – mixture fraction $\langle\widetilde{\xi}\rangle$, total mixture fraction variance $\langle\xi''\rangle_m^2$ and resolved density $\langle\overline{\rho}\rangle$ – at various axial locations x/D. Symbols represent experimental data [2], black dashed line are results of current LES calculations, blue dash-dotted lines are W-PDF calculations and red solid lines are current PDF calculations.

tal mixture fraction variance $\langle \xi'' \rangle_m^2$ and resolved density $\langle \overline{\rho} \rangle$ at various axial locations. The data sets included on this figure are results of current PDF calculations (red solid line), current LES calculations (dash black line), W-PDF calculations (blue dash-dotted line) and experimental data (symbols) [2]. First, considering the first column of sub-figures which compare the radial profiles of $\langle \widetilde{\xi} \rangle$, we note that there is good agreement between the all the four data sets except at $x/D = 45$. The same is true with the second column of sub-figures corresponding to $\langle \xi'' \rangle_m^2$. It is evident that the LES results are consistent in $\langle \widetilde{\xi} \rangle$ and $\langle \xi'' \rangle_m^2$ of the current PDF calculations. However, at axial distances very close to the jet exit plane, $\langle \overline{\rho} \rangle$ from the current PDF calculations deviate from the W-PDF and current LES calculations at radial locations corresponding to the pilot-coflow region.

Next we consider the resolved mean and resolved fluctuations in temperature and species mass fractions at two axial locations – close to the jet exit plane at $x/D = 3$ and at an intermediate distance of $x/D = 30$.

Figure 4.2 compares the radial profiles of resolved temperature $\langle \widetilde{T} \rangle$ and resolved species mass fractions $\langle \widetilde{Y} \rangle$ at $x/D = 3$ between experiments (symbols), W-PDF calculations (blue solid line), current PDF calculations (red solid line) and current LES calculations (black dashed line). The general agreement between the numerical calculations is reasonable. In specific, the following points are noted. The W-PDF calculations compare well with the LES calculations whereas the radial profiles of the current PDF calculations do not agree with the LES perfectly in the pilot-coflow mixing region. However the peak values predicted by both the current PDF and LES match. However, the agreement between the various sets of data is good at a downstream locations of $x/D = 30$ as is shown in

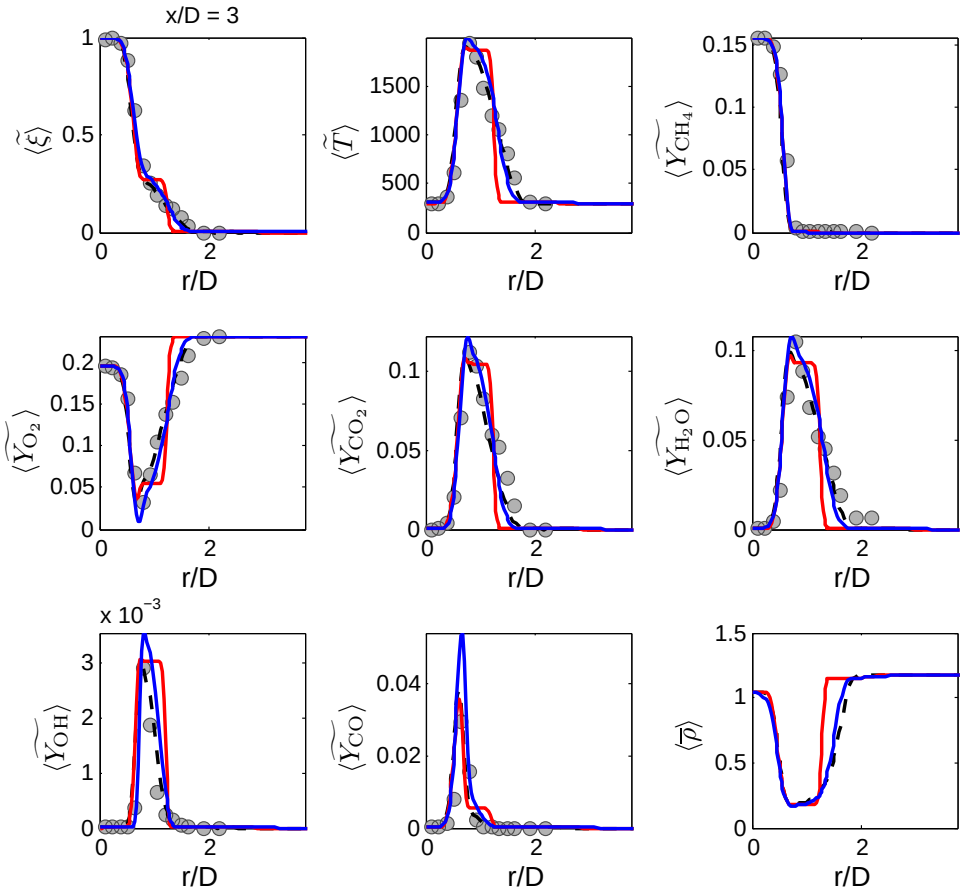

Figure 4.2: Radial profiles of time-averaged resolved mixture fraction $\langle\widetilde{\xi}\rangle$, resolved temperature $\langle\widetilde{T}\rangle$ and species mass fractions $\langle\widetilde{Y}\rangle$ at $x/D = 3$. Symbols represent experimental data [2], black dashed line are results of current LES calculations, blue solid lines correspond to W-PDF calculations and red solid lines are current PDF calculations.

Fig. 4.3.

The following two figures probe the radial profiles of resolved fluctuations in these same quantities.

Figure 4.4 compares the time-averaged resolved fluctuations in temperature $\langle T'' \rangle_W$ and species mass fractions $\langle Y'' \rangle_W$ at $x/D = 3$ between the experiments,

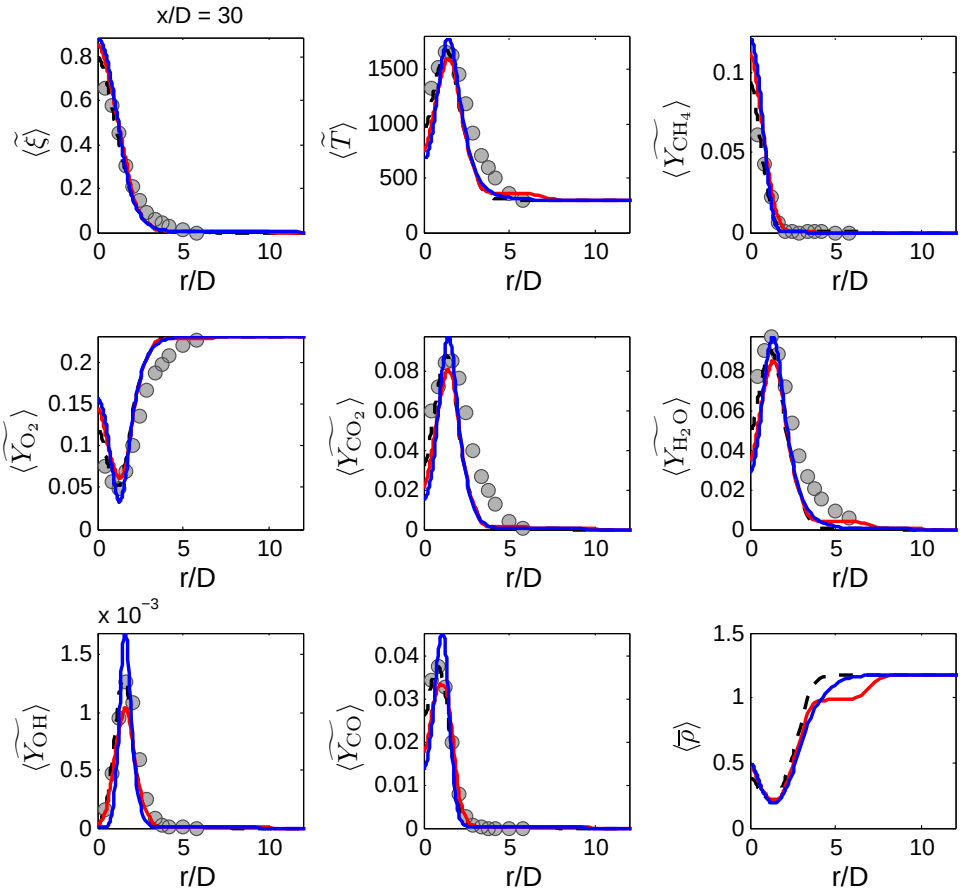

Figure 4.3: Radial profiles of time-averaged resolved mixture fraction $\langle\widetilde{\xi}\rangle$, resolved temperature $\langle\widetilde{T}\rangle$ and species mass fractions $\langle\widetilde{Y}\rangle$ at $x/D = 30$. The notation is the same as in Fig. 4.2.

W-PDF calculations, current LES and PDF calculations. The current PDF calculations over predict the peak values in comparison to the LES whereas the agreement between the W-PDF and LES is better. However, the current PDF calculations agree in the magnitude of the peak value with the experiments. Additionally, the current PDF calculations portray the existence of two peaks (except in CH_4) of very narrow spread in contrast to the experiments which demonstrate a much wider spread in the data.

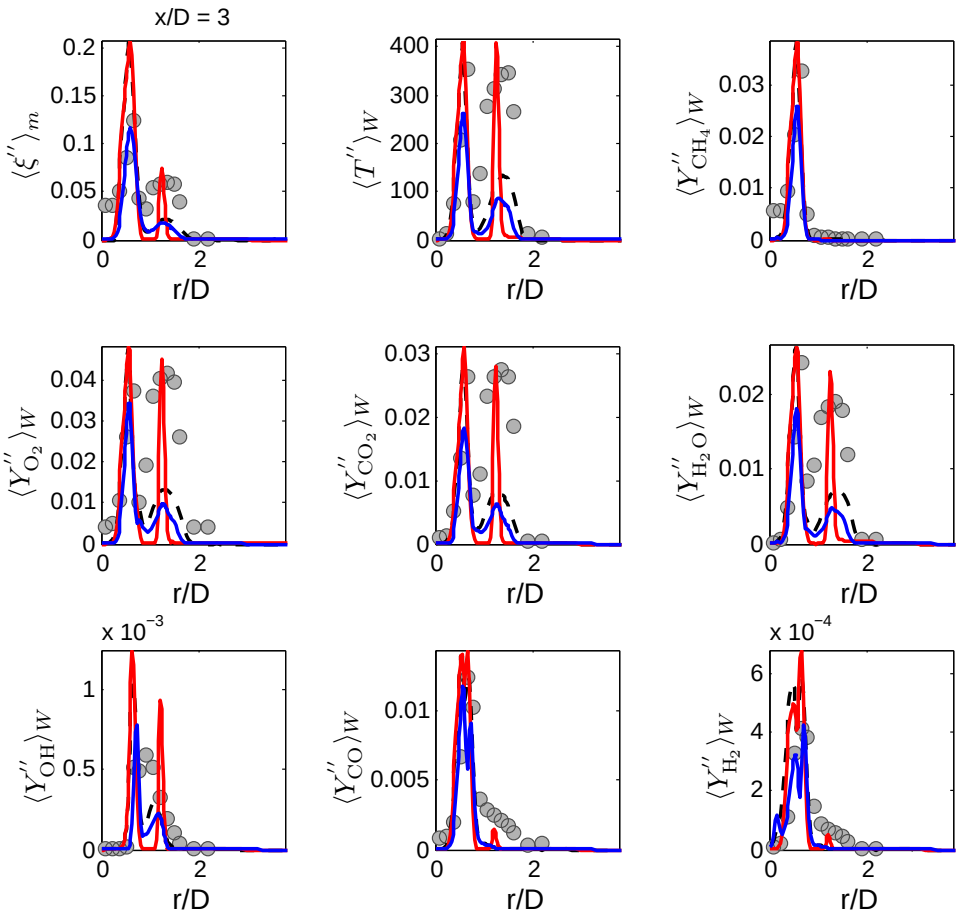

Figure 4.4: Radial profiles of time-averaged resolved fluctuations in temperature $\langle T'' \rangle_W$ and species mass fractions $\langle Y'' \rangle_W$ and total fluctuations in mixture fraction $\langle \xi'' \rangle_m$ at $x/D = 3$. The notation is the same as in Fig. 4.2.

As with the resolved mean quantities, the agreement in the resolved fluctuations of various statistics is better farther downstream of the jet exit plane as is evident in Fig. 4.5.

In summary, the current implementation of mixing and molecular transport is consistent with the previous calculations, LES and experiments. However, further research is required to further understand and quantify the behavior of

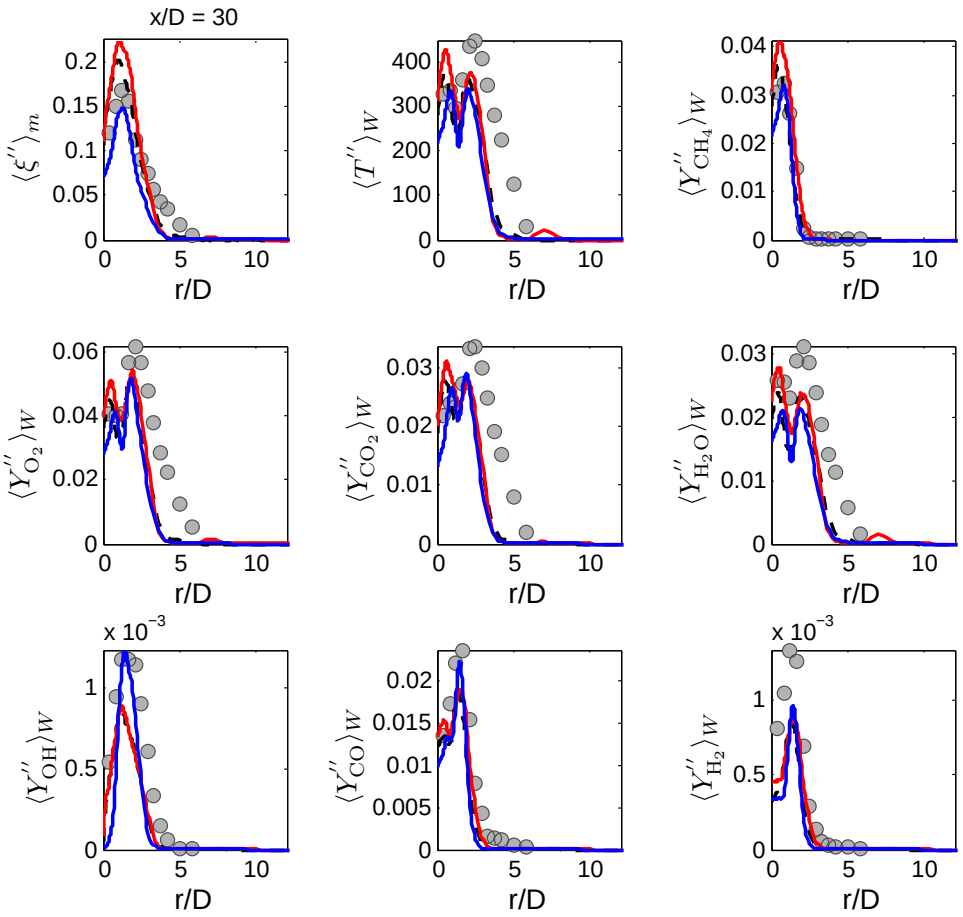

Figure 4.5: Radial profiles of time-averaged resolved temperature $\langle \widetilde{T} \rangle$ and species mass fractions $\langle \widetilde{Y} \rangle$ and total fluctuations in mixture fraction $\langle \xi'' \rangle_m$ at $x/D = 30$. The notation is the same as in Fig. 4.2.

the various statistics closer to the jet exit plane in the mixing layer between the pilot and the co-flow. Note that no smoothing has been performed on any of the quantities through the simulation.

4.4.2 Smoothing

In this section, we study the effect of the choice of the smoothing parameter α_s (or equivalently the smoothing length scale $l_s = 4\sqrt{\alpha}_s\Delta x$, where Δx is the local nominal grid size) on the resolved PDF fields such as mixture fraction $\widetilde{\xi}$, mixture fraction square $\widetilde{\xi^2}$ and density $\overline{\rho}$.

As detailed in [83], the numerical errors involved in PDF methods include spatial discretization errors, temporal truncation errors, bias errors and statistical errors. The last two are due to the finite number of particles used in the calculation. Time-averaging has been used in previous hybrid RANS/PDF methods to control the statistical and bias errors arising in these calculations. Since, instantaneous fields cannot be time-averaged, we use smoothing [83] in LES/PDF methods. Smoothing has a two-fold effect: reduction in the variance and spatial smearing of the corresponding fields. Small values of α_s (or $l_s \ll \Delta x$) result in lower amount of variance reduction and smearing, while large values of α_s (or $l_s \gg \Delta x$) lead to higher reduction in the variance accompanied by large smearing errors.

In the following paragraphs, we study the effect of the choice of α_s on "output" fields alone. Then we employ the method of cross-validation to assist in the choice of α_s and compare the smoothed PDF fields to the corresponding unsmoothed LES fields.

Figure 4.6 compares the smoothed (PDF) profiles of $\widetilde{\xi}$, $\widetilde{\xi^2}$ and $\overline{\rho}$ for various values of $\alpha_s = \{0, 1.5, 6.5, 26\}$. The top four rows are radial profiles at four axial locations as indicated on the figures (for one t and θ). Each row corresponds

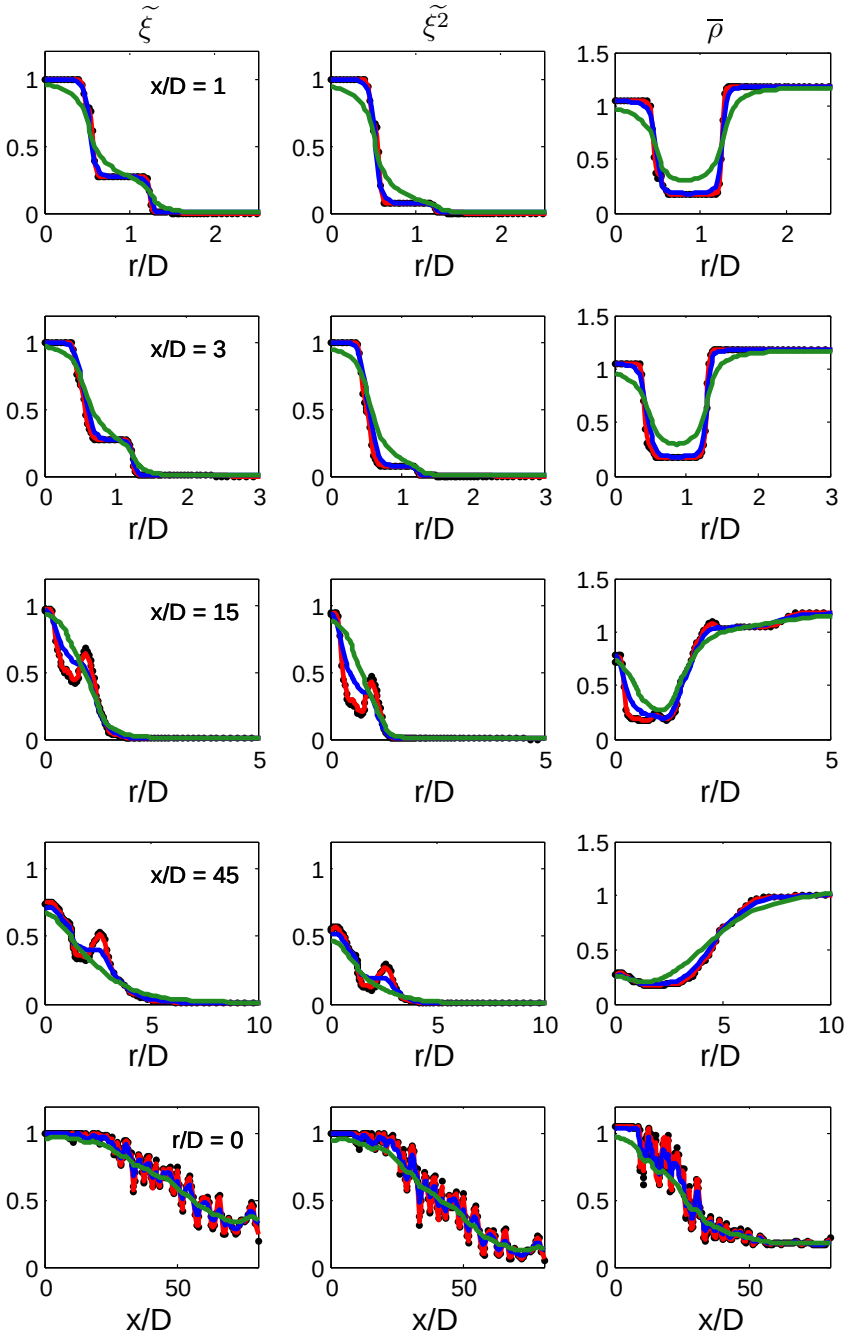

Figure 4.6: Radial profiles of resolved mixture fraction $\widetilde{\xi}$, mixture fraction square $\widetilde{\xi^2}$ and density $\overline{\rho}$ at four axial locations (top four rows) and centerline axial profiles of the same quantities (bottom row) for various value of the smoothing parameter α_s: $\alpha_s = 0$, black dots; $\alpha_s = 1.5$, red line; $\alpha_s = 6.5$, blue line; and $\alpha_s = 26$, green line.

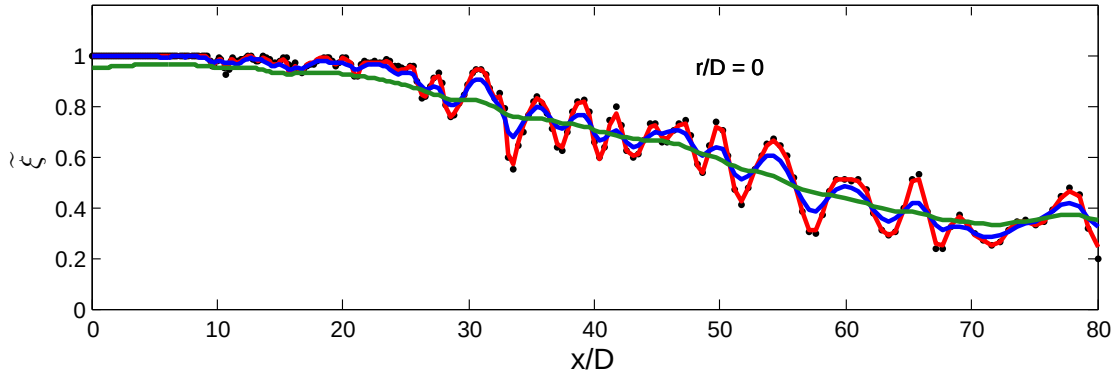

Figure 4.7: Axial profile of resolved mixture fraction $\widetilde{\xi}$ on the centerline for various value of the smoothing parameter α_s: $\alpha_s = 0$, black dots; $\alpha_s = 1.5$, red line; $\alpha_s = 6.5$, blue line; and $\alpha_s = 26$, green line.

to a same axial location. The bottom row compares the axial profiles on the centerline. Note that there are negligible differences between the lines for $\alpha_s = 0$ and $\alpha_s = 1.5$. The effects of smoothing become evident for $\alpha_s = 6.5$ and large smearing errors are clear in the profiles for $\alpha_s = 26$. The effect of the choice of the smoothing parameter is more evident in Fig. 4.7 which plots the centerline axial profiles of $\widetilde{\xi}$ for the various values of α_s mentioned previously.

Since, *a priori* determination of the optimal smoothing parameter is unclear in these PDF calculations of turbulent flames, the method of cross-validation provides a convenient initial guess for the smoothing parameter that minimizes the cross-validation error defined in Eq. (4.15). We use the golden section search algorithm for optimization and a unique smoothing parameter is determined for each of the PDF fields to be smoothed.

Cross-validation is applied on the "output" PDF fields of $\widetilde{\xi}$, $\widetilde{\xi^2}$ and $\overline{\rho}$ to determine optimal values of the smoothing parameter for each PDF field considered.

The optimal values of α_s determined by the algorithm for each of the PDF fields considered are: $\alpha_s = 4.2$ for $\widetilde{\xi}$; $\alpha_s = 3.8$ for $\widetilde{\xi^2}$; and $\alpha_s = 5.2$ for $\overline{\rho}$.

Figure 4.8 compares the smoothed PDF (green) fields of $\widetilde{\xi}$, $\widetilde{\xi^2}$ and $\overline{\rho}$ with the corresponding unsmoothed PDF (red) and LES (black) fields. Smoothing with α_s values determined by cross-validation does not affect the fields mentioned above at distances close to the jet exit plane. At distances greater than $x/D = 15$, the smearing error incurred due to smoothing is evident and at $x/D = 45$. Figure 4.9 compares the effect of smoothing on the centerline profiles of $\widetilde{\xi}$ and we note that the level of fluctuations between the LES and smoothed PDF fields is in better agreement (than without smoothing). Finally, there is no substantial effect of smoothing on the radial profiles of the density fields.

To briefly describe the computational cost of performing cross-validation, since smoothing work incurred is proportional to the number of computational cells independent of the number of particles, we consider the CPU time per iteration per cell of cross-validation against the CPU time taken per cell for one operation of smoothing. The smoothing operation takes 50μ seconds per computational cell on an average while one iteration of cross-validation takes 7.5μ seconds on an average. We observe that convergence is achieved after approximately 15 iterations for the termination condition defined by $\mid a - c \mid < \tau \mid b \mid$ for a tolerance $\tau = 0.01$ *i.e.,* the iterations are terminated when the above condition evaluates to true.

Finally, we consider the effect of smoothing quantities that are fed back into the PDF calculations, also referred to as "feedback" quantities. Figure 4.10 compares the radial profiles of time-averaged $\widetilde{\xi}$, $\widetilde{\xi^2}$ and $\overline{\rho}$ at various axial locations as

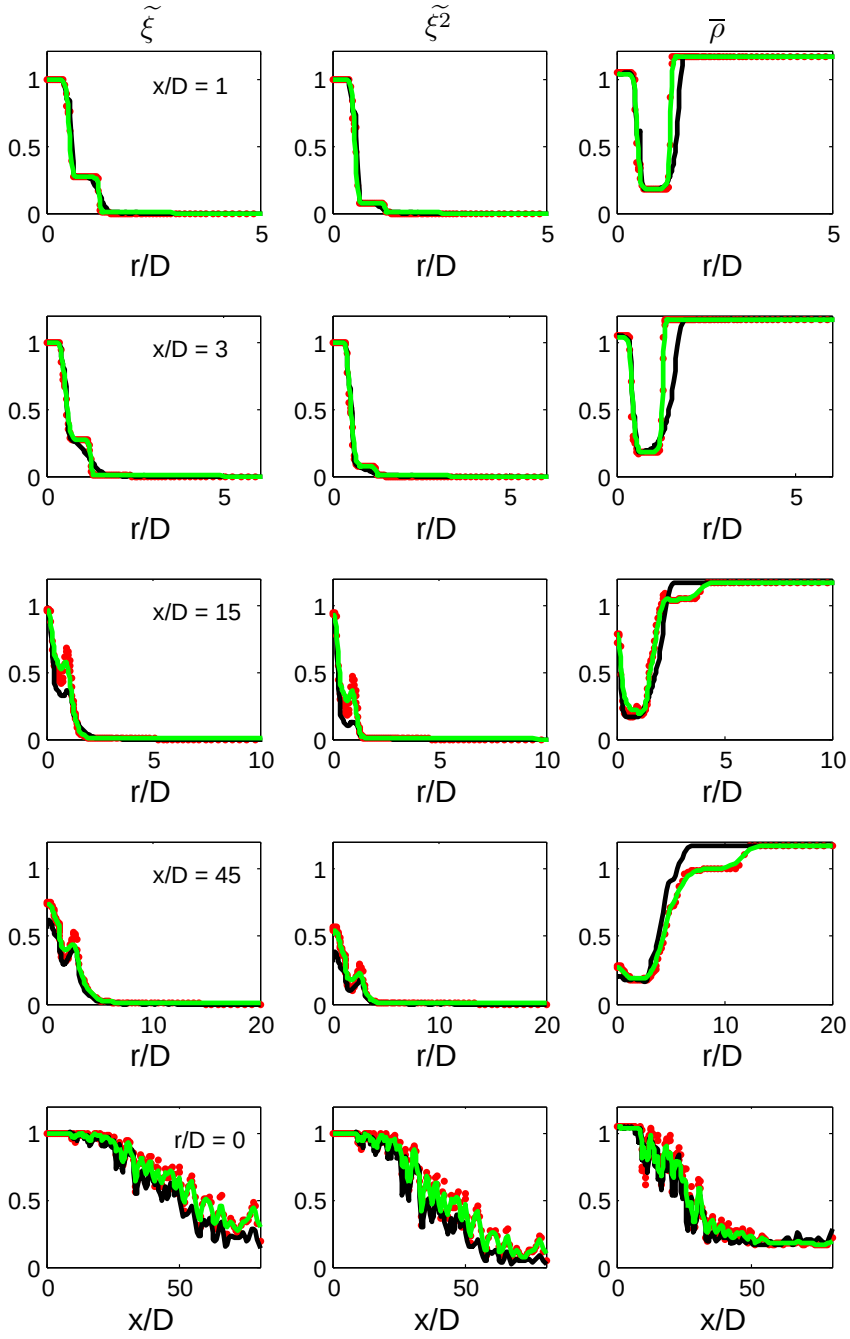

Figure 4.8: Radial profiles of resolved mixture fraction $\widetilde{\xi}$, mixture fraction square $\widetilde{\xi^2}$ and density $\overline{\rho}$ at four axial locations (top four rows) and centerline axial profiles of the same quantities (bottom row). Unsmoothed LES fields are represented by black lines, unsmoothed PDF fields by red dots and the cross-validation assisted smoothed PDF fields are in green color.

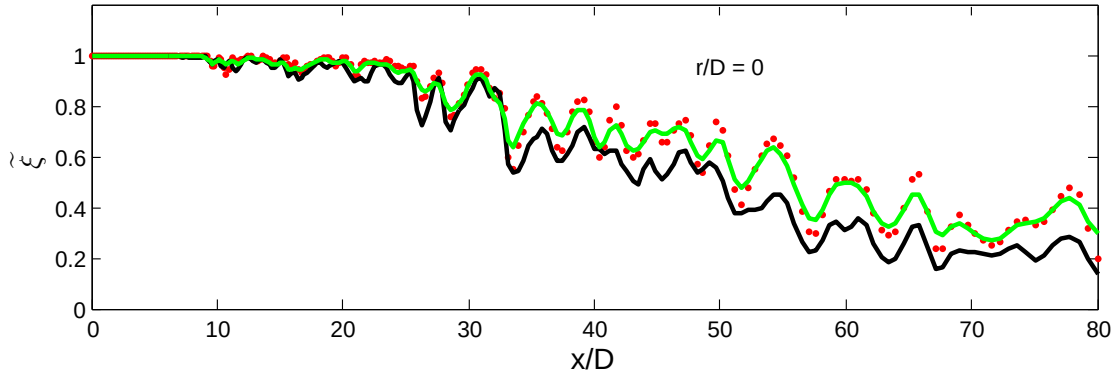

Figure 4.9: Centerline axial profile of resolved mixture fraction $\widetilde{\xi}$. Unsmoothed LES fields are represented by black lines, unsmoothed PDF fields by red dots and the cross-validation assisted smoothed PDF fields are in green color.

obtained from experiments (circles), LES (black dashed lines), PDF calculations with no smoothing (red dots) and PDF calculations with smoothing of feedback quantities (green lines). Smoothing is performed for a fixed value of $\alpha_s = 3.0$ for all fields. We note that there are no gross errors in the implementation of smoothing used for feedback quantities. The differences between the time-averaged unsmoothed PDF statistics and time-averaged smoothed statistics are insignificant and the effect of smoothing is marginally evident for $x/D \geq 3$.

In summary, an optimal choice of the smoothing parameter helps in reducing the variance in estimated statistics while minimizing the smearing error incurred. Cross-validation is a useful numerical tool that can be used to estimate the value of this optimal smoothing parameter.

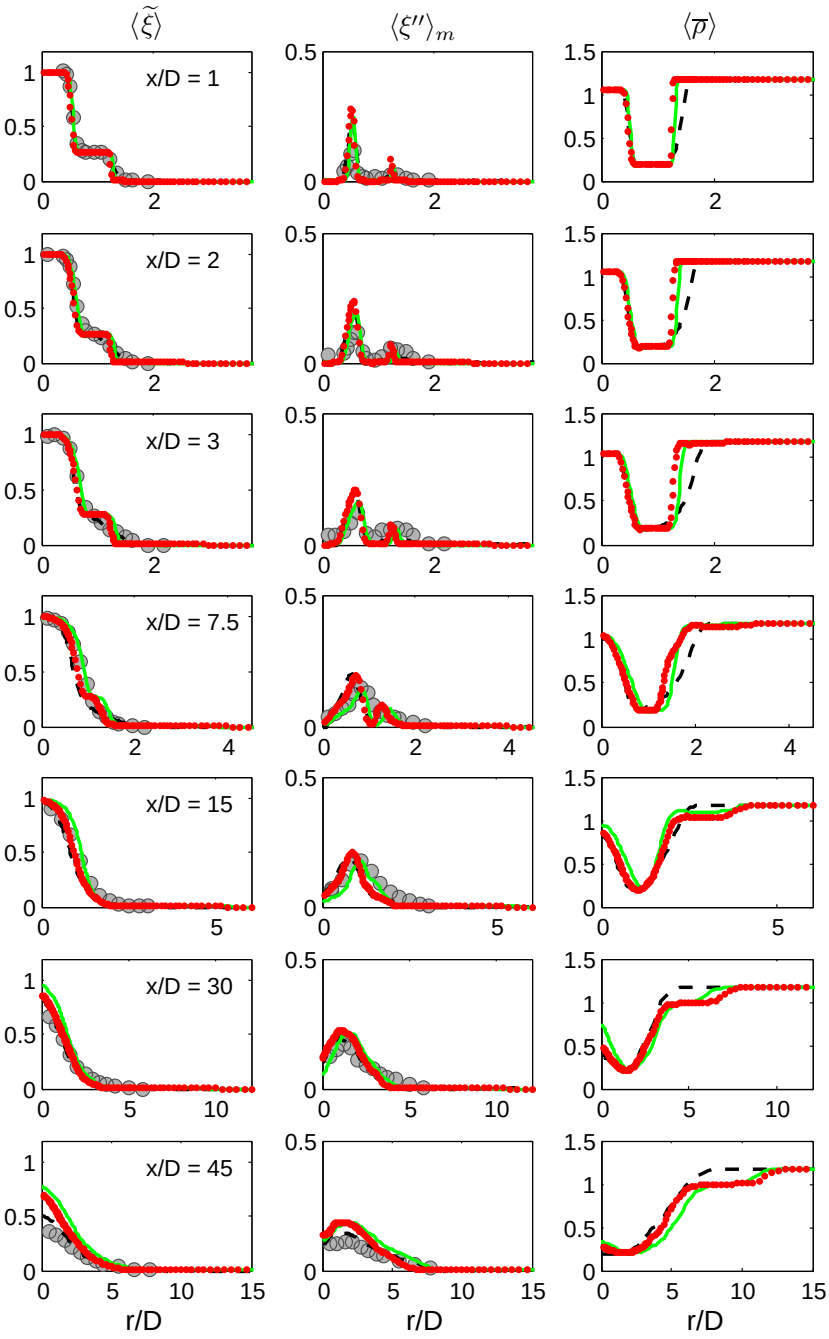

Figure 4.10: Radial profiles of time-averaged quantities – mixture fraction $\langle\widetilde{\xi}\rangle$, total mixture fraction fluctuations $\langle\xi''\rangle_m$ and resolved density $\langle\overline{\rho}\rangle$ – at various axial locations x/D. Symbols represent experimental data [2], black dashed line are results of current LES calculations, red dots are current PDF calculations with no smoothing and green solid lines are current PDF calculations with smoothing of feedback quantities.

4.5 Suggestions for future work

In this study, we have performed preliminary investigations of the implementation of mixing, molecular transport and smoothing in LES/PDF studies of turbulent reacting flows (Flame D). We also show that cross-validation is a convenient methodology to automatically choose the value of the smoothing parameter for a given field. But further research is required to completely understand the discrepancies observed between the current PDF calculations and W-PDF.

To summarize briefly, the primary differences between the two implementations are in the treatment of molecular transport and the numerical implementation of the IEM mixing model. Molecular transport is modeled as a Wiener process in the W-PDF calculations while it is modeled as a mean drift term in the current PDF calculations. This difference in the modeling of molecular transport has the following effects. The corresponding modeled transport equation for the resolved mixture fraction is identical in both cases. Modeling molecular transport as a mean drift term neglects the molecular transport of the mixture fraction variance. On the other hand, modeling molecular transport as a random walk term results in a spurious production of the variance. Further, in each PDF calculation, the mixing frequency is defined so as to ensure consistency between the modeled LES transport equation of mixture fraction square and the corresponding PDF study.

Figures (4.2) and (4.3) indicate significant deviations in the radial profiles of $\langle\widetilde{\xi}\rangle$ between the current PDF calculations and W-PDF calculations. In a PDF study, quantities such as temperature, density and species mass fractions are derived from the mixture fraction using a flamelet table as $\phi = \mathbb{F}(\xi)$, where ϕ

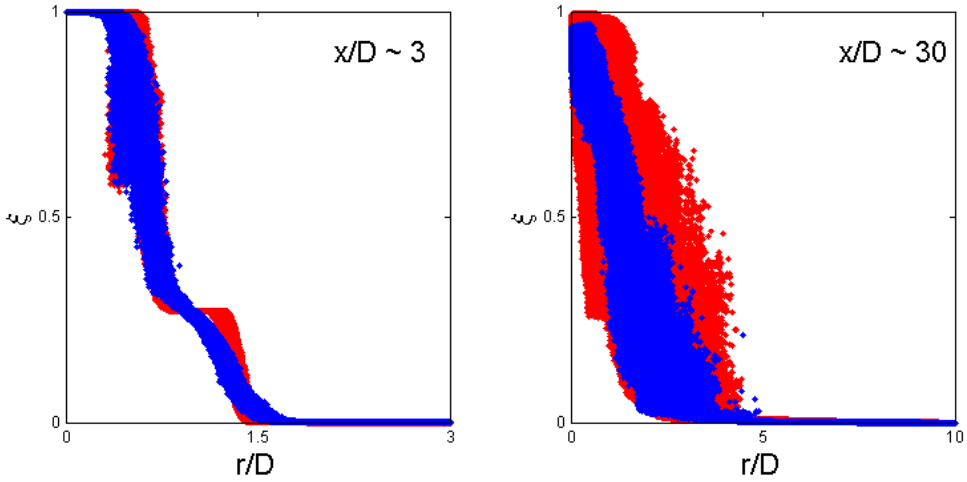

Figure 4.11: Scatter plot of particle mixture fraction in the radial direction at $x/D = 3$ (left) and $x/D = 30$ (right) between the current PDF calculations (red) and W-PDF calculations (blue)

denotes quantities such as temperature, density or species mass fractions. This suggests that the relevant quantity to be considered first is the particle mixture fraction.

Figure (4.11) compares the scatter plot of particle mixture fraction in the radial direction at $x/D = 3$ on the left and $x/D = 30$ on the right between the current PDF calculations (red) and W-PDF calculations (blue). Let us first consider the sub-figure on the left at $x/D = 3$. There is an obvious difference in the scatter plots between the two calculations around $r/D = 1.2$ and this region corresponds to the mixing layer between the pilot and the coflow. Further, at $x/D = 30$, we observe that the mixture fraction variance predicted in the current PDF calculations is much larger than in the W-PDF calculations.

As mentioned previously, the discrepancy in the mixture fraction variance could be either due to the neglect of the transport of variance in physical space

by molecular diffusion in the current PDF calculations or due to the spurious production in the W-PDF calculations. The exact reasons for this are not clear from this study. Moreover, reasonable agreement is expected in the time-averaged resolved mixture fraction fields obtained from the two sets of calculations barring numerical inconsistencies. Since the IEM mixing model and its numerical implementation does not affect the mean, the implementation of molecular transport needs to be investigated in detail.

Finally, once these concerns are addressed, the molecular transport model may be studied in the context of a flow where the effects of molecular diffusion dominate in comparison to the subgrid scale diffusivity. Further, differential diffusion effects may be investigated in combination with a more detailed model for chemistry such as ISAT [57].

4.6 Conclusions

The numerical implementation of mixing, molecular transport and smoothing as detailed in [83] is applied in the study of a laboratory-scale turbulent reacting jet flame (Sandia Flame D). It is seen that the various time-averaged statistics calculated from both the LES and the PDF methods are consistent with each other and with the experimental data available (except around $r/D = 1.2$ close to the jet exit plane). It is also shown that the predictions of current implementation of molecular transport and mixing for the resolved fluctuations of temperature and species mass fractions are in better agreement with the experimental data at distances close to the jet exit plane.

Further, cross-validation is presented as a numerical technique to aid in the choice of a smoothing parameter in these turbulent reacting flow calculations. The smoothing algorithm [83] is applied to the output instantaneous resolved PDF fields of mixture fraction, mixture fraction square and density. It is shown that cross-validation assisted smoothing results in better (marginal) consistency between LES and PDF fields.

4.7 Acknowledgments

SV would like to thank Haifeng Wang for his numerous inputs during the course of this work. This research is supported by the Department of Energy under Grant DE-FG02-90ER14128. This research was conducted using the resources of the Cornell University Center for Advanced Computing, which receives funding from Cornell University, New York State, the National Science Foundation, and other leading public agencies, foundations, and corporations.

CHAPTER 5
CONCLUSIONS

The primary focus of this work has been towards the modeling and numerical implementation of the effects of molecular diffusion and mixing in PDF methods of turbulent flows.

In Chapter 2, the dispersion from line sources in decaying grid turbulence is studied using PDF methods. Mixing is modeled using the IECM mixing model with molecular transport modeled as a conditional scalar drift term in the scalar evolution equation. Comparison is made extensively against the experimental data of Warhaft [89] and the previous calculations of Sawford [70] for the case of single and pair of line sources. The model presented is also verified using a heated mandoline [90]. The following conclusions are drawn from the work reported in this chapter.

1. Turbulent dispersion from a line source is characterized by two length scales: one due to turbulence and one due to molecular diffusion. Due to the disparity between these two length scales close to the source, the effects of molecular diffusivity is significant.

2. However, modeling molecular transport as a random walk in the particle position equation gives rise to spurious production of scalar variance. In contrast, modeling it as a conditional mean scalar drift term in the scalar evolution equation avoids this spurious production.

3. Modeling the plume as a laminar wake at distances close to the source provides a non-general model for the mixing frequency at early times.

However, the large-time asymptote of the mixing frequency is independent of the source conditions and is modeled as being proportional to the turbulence frequency ε/k.

4. The data from PDF calculations based on this combination of models for mixing, mixing frequency and molecular transport agree well with the experimental data observed for both the centerline and radial profiles of various statistics such as the mean, the variance, skewness and kurtosis. Additionally, the model is extended to multiple line sources and also to a heated mandoline and is observed to agree well with experimental data. For the heated mandoline, the decay rate of the scalar fluctuations is found to be independent of the conditions at the source.

5. Finally, analysis of dispersion from a single line source over a range of the parameter space indicates that the effect of the source size is only significant at very small times from the source whereas with a constant C_0 assumption, the effects of Reynolds numbers are evident only at intermediate times. The large-time asymptote of the centerline intensity of fluctuations is independent of both the non-dimensional source size and Reynolds number for the range of parameter space explored, while the maximum value of the centerline fluctuation intensity shows a dependence on Reynolds number but not on the source size.

In addition to other studies performed [37, 31], the results from the study of dispersion from line sources indicates that modeling of molecular diffusion is significant. The work detailed in Chapter 3 focuses on the numerical implementation of the IEM mixing model in combination with the mean drift term (for molecular transport) in the context of LES/PDF methods. The following

inferences can be drawn based on this chapter:

1. Three numerical schemes – PIC-PC, PIC-PL, CIC-LS – are analyzed for accuracy, stability, efficiency, conservation and realizability. It is shown that all the schemes result in second-order spatial and temporal accuracy. Moreover, each implementation is shown to preserve detailed conservation and realizability criteria. The CIC-LS scheme is observed to be three times more computationally expensive as compared to the other two schemes but has the additional advantages of yielding continuous estimates of estimated statistics and naturally preserving boundedness.

2. A methodology is presented to account for the effects of differential diffusion in the scalar evolution equation consistent with the requirements of detailed conservation and realizability. Tests performed on a three-species mixing problem, with each species having a unique, constant and uniform molecular diffusivity, confirm that the implementation described satisfies these criteria.

3. Finally, a three-point implicit smoothing algorithm is detailed as a method to reduce the variance in estimated statistics. This scheme is also shown to satisfy conservation and boundedness criteria. It is further shown that the optimal value of the root-mean-squared error in estimated statistics is achieved with smoothing *i.e.,* for a non-trivial value of the smoothing length scale $l > 0$. In other words, it is beneficial to perform smoothing on an estimated statistic as compared to no smoothing at all.

4. The model for the root-mean-squared error is shown to agree well with the data for the estimated statistics. The model predicts that with smooth-

ing, the bias error scales as N_{tot}^{-1} whereas the statistical error scales as $N_{tot}^{-1/2}$ where N_{tot} is the total number of particles in the computational domain.

In Chapter 4, the numerical implementation described in the previous chapter is applied to the study of a turbulent reacting jet flame (Sandia Flame D) calculation. This chapter can be summarized as:

1. The numerical implementation of mixing and molecular transport described previously is validated against previous LES/PDF calculations (done using the IEM mixing and the random walk models) and the experimental data for the Sandia Flame D. The current implementation described is shown to result in statistics and instantaneous fields of various resolved quantities that agree reasonably well with the experiments and previous calculations.
2. An implementation of the method of cross-validation is presented to assist with the choice of the smoothing length scale (or smoothing parameter) in the study of a turbulent reacting jet flame calculation. This algorithm is then applied to smooth "output" PDF fields in a LES/PDF study of the Sandia Flame D. Smoothing is shown to improve (though marginally) the agreement between the LES and PDF fields.

In summary, we show that the effects of molecular diffusion can be significant and needs to be modeled correctly. Further we present various numerical schemes for the implementation of mixing, molecular transport and differential diffusion in LES/PDF methods. Additionally, we describe a smoothing scheme to reduce the root-mean-squared error in estimated statistics and present an im-

plementation of cross-validation to assist in the choice of the smoothing length scale. Finally, we validate the described implementation by applying it to a LES/PDF study of a turbulent reacting jet flame (Sandia Flame D).

APPENDIX A

NUMERICAL SOLUTION OF THE HEAT CONDUCTION EQUATION

The numerical solution to the heat conduction equation is required both in the estimation of mean shifts due to molecular transport (Sec. §3.3) and in performing the smoothing operation (Sec. §3.3.4). This appendix details the methodology used in obtaining the numerical solution of the 3D variable-property heat conduction equation using the Crank-Nicolson Finite Volume (CN-FV) scheme, and it is organized as follows. First, we consider the numerical solution to the 3D variable-property heat conduction equation for a single species. Next, we present a description of the Locally One Dimensional (LOD) scheme (a variant of the Alternating Direction Implicit (ADI) scheme) used to simplify the numerical solution of the 3D variable-property heat conduction equation. Finally, we conclude this appendix by extending this algorithm to incorporate the general case of multiple species with different diffusivities.

A.1 Crank-Nicolson Finite Volume Scheme

The primary object of discussion in this section is the numerical solution of the 3D variable-property heat conduction equation:

$$\frac{\partial \rho \widetilde{\phi}}{\partial t} = \frac{\partial}{\partial x_j}\left(\rho \Gamma \frac{\partial \widetilde{\phi}}{\partial x_j}\right), \tag{A.1}$$

where ρ is the density, $\widetilde{\phi}$ is the conserved scalar being diffused (the scalar mean, for instance) and Γ is its conductivity or diffusivity.

The formulation of the finite-volume equation here (A.1) and their solution

(A.2) is standard. It is necessary, however, to develop the equations involved in order to establish the conservation and boundedness properties of operations involved.

Consider a closed domain of volume L^3 in a Cartesian coordinate system. Consider this volume to be discretized into $\mathrm{N_{cell}} = \mathrm{N_x N_y N_z}$ sub-volumes (or cells) where each coordinate direction x, y and z is discretized into $\mathrm{N_x}$, $\mathrm{N_y}$ and $\mathrm{N_z}$ 1D-cells respectively. Let $\mathbf{x}_p = (x_i, y_j, z_k)$ for $i = 1, 2, ..\mathrm{N_x}$, $j = 1, 2, ..\mathrm{N_y}$ and $k = 1, 2, ..\mathrm{N_z}$ denote the center of the p-th cell where a lexicographical reordering is used to obtain the index p as $p = (k-1)\mathrm{N_x N_y} + (j-1)\mathrm{N_x} + i$. Further, let $\bar{x}_i$, $\bar{y}_j$ and $\bar{z}_k$ denote the vertices in each direction with $i = 0, 1, 2, ..\mathrm{N_x}$, $j = 0, 1, 2, ..\mathrm{N_y}$ and $k = 0, 1, 2, ..\mathrm{N_z}$. The cell width in each direction is obtained as,

$$\Delta x_i = \bar{x}_i - \bar{x}_{i-1} \tag{A.2}$$

$$\Delta y_j = \bar{y}_j - \bar{y}_{j-1} \tag{A.3}$$

$$\Delta z_k = \bar{z}_k - \bar{z}_{k-1}, \tag{A.4}$$

for $i = 1, 2, ..\mathrm{N_x}$, $j = 1, 2, ..\mathrm{N_y}$ and $k = 1, 2, ..\mathrm{N_z}$. For simplicity of illustration, Fig. A.1 presents a pictorial representation of the notation described above in a 2D Cartesian system for $\mathrm{N_x} = 4$ and $\mathrm{N_y} = 3$.

Consider obtaining a numerical solution $\widetilde{\phi}_p$ defined at cell-centers $\mathbf{x}_p$ to the 3D heat conduction equation given by Eq. (A.1) using the Crank-Nicolson Finite Volume scheme by advancing $\widetilde{\phi}$ across a time step Δt from a time level $t_n = n\Delta t$ to $t_{n+1} = (n+1)\Delta t$. The coefficients are frozen at a time level of $n + \frac{1}{2}$ and any

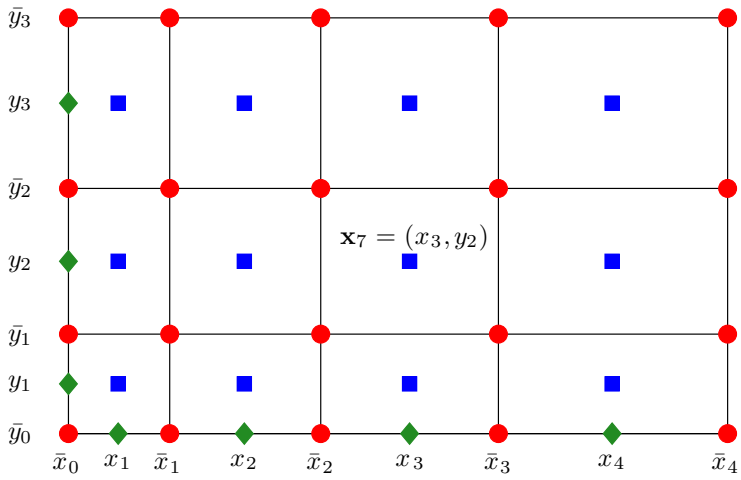

Figure A.1: Illustration of a 2D grid with $\mathrm{N_x} = 4$ and $\mathrm{N_y} = 3$. The physical domain considered is of size L^2 with $\bar{x}_0 = 0$, $\bar{x}_{\mathrm{N_x}} = L$, $\bar{y}_0 = 0$, $\bar{y}_{\mathrm{N_y}} = L$. The vertices $\bar{x}$ and $\bar{y}$ are denoted using ●; the cell centers x and y (in 1D) are denoted using ◆; and the cell-center of the p-th cell $\mathbf{x}_p$ is denoted using ■. To illustrate the lexicographical re-ordering used, $\mathbf{x}_7$ is denoted on the plot.

quantity Q is obtained as,

$$Q^{n+\frac{1}{2}} = \frac{Q^n + Q^{n+1}}{2}, \tag{A.5}$$

$$Q_{i-\frac{1}{2},j,k} = \frac{Q_{i,j,k}\Delta x_{i-1} + Q_{i-1,j,k}\Delta x_i}{\Delta x_i + \Delta x_{i-1}}, \tag{A.6}$$

$$Q_{i,j-\frac{1}{2},k} = \frac{Q_{i,j,k}\Delta y_{j-1} + Q_{i,j-1,k}\Delta y_j}{\Delta y_j + \Delta y_{j-1}}, \tag{A.7}$$

$$Q_{i,j,k-\frac{1}{2}} = \frac{Q_{i,j,k}\Delta z_{k-1} + Q_{i,j,k-1}\Delta z_k}{\Delta z_k + \Delta z_{k-1}}. \tag{A.8}$$

Let W be a diagonal matrix with $W_{pp} = m_p = m_{i,j,k}$, where m_p (defined below in C) is the mass of the cell centered at $\mathbf{x}_p$ and let M be a banded matrix with

bandwidth of at most $2N_xN_y$ with off-diagonal entries:

$$M_{p,p-1} = m_{i-\frac{1}{2},j,k}\Gamma^{n+\frac{1}{2}}_{i-\frac{1}{2},j,k}/\Delta x^2_{i-\frac{1}{2}} \tag{A.9}$$

$$M_{p,p+1} = m_{i+\frac{1}{2},j,k}\Gamma^{n+\frac{1}{2}}_{i+\frac{1}{2},j,k}/\Delta x^2_{i+\frac{1}{2}} \tag{A.10}$$

$$M_{p,p-N_x} = m_{i,j-\frac{1}{2},k}\Gamma^{n+\frac{1}{2}}_{i,j-\frac{1}{2},k}/\Delta y^2_{j-\frac{1}{2}} \tag{A.11}$$

$$M_{p,p+N_x} = m_{i,j+\frac{1}{2},k}\Gamma^{n+\frac{1}{2}}_{i,j+\frac{1}{2},k}/\Delta y^2_{j+\frac{1}{2}} \tag{A.12}$$

$$M_{p,p-N_xN_y} = m_{i,j,k-\frac{1}{2}}\Gamma^{n+\frac{1}{2}}_{i,j,k-\frac{1}{2}}/\Delta z^2_{k-\frac{1}{2}} \tag{A.13}$$

$$M_{p,p+N_xN_y} = m_{i,j,k+\frac{1}{2}}\Gamma^{n+\frac{1}{2}}_{i,j,k+\frac{1}{2}}/\Delta z^2_{k+\frac{1}{2}}, \tag{A.14}$$

where $2\Delta x_{i-\frac{1}{2}} = \Delta x_i + \Delta x_{i-1}$. The definitions for $\Delta y_{j-\frac{1}{2}}$ and $\Delta z_{k-\frac{1}{2}}$ follow similarly and by construction, $\sum_q M_{pq} = 0$.

Given $\widetilde{\phi}^n_p$, W, and M, the change in solution $\Delta\widetilde{\phi}^h$ to the heat conduction equation given by Eq. (A.1) over a time-step Δt can be written in matrix form as,

$$W\Delta\widetilde{\phi}^{h,n+\frac{1}{2}} = \Delta t M\widetilde{\phi}^{n+\frac{1}{2}}, \tag{A.15}$$

where $\Delta\widetilde{\phi}^{h,n+1/2} = \widetilde{\phi}^{n+1} - \widetilde{\phi}^n \equiv \Delta\widetilde{\phi}^{n+\frac{1}{2}}$. Or equivalently, we can re-write Eq. (A.15) in index notation as,

$$m_{(p)}\Delta\widetilde{\phi}^{n+\frac{1}{2}}_p = \Delta t M_{pq}\widetilde{\phi}^{n+\frac{1}{2}}_q, \tag{A.16}$$

where indices in parentheses are not included in the summation convention. By the definition of M,

$$\sum_p m_p\Delta\widetilde{\phi}^{n+\frac{1}{2}}_p = \Delta t \underbrace{\sum_p M_{pq}}_{0}\widetilde{\phi}^{n+\frac{1}{2}}_q = 0. \tag{A.17}$$

Further Eq. (A.15) can be re-arranged in-terms of known quantities to give,

$$\left[W - \frac{\Delta t}{2}M\right]\widetilde{\phi}^{n+1} = \left[W + \frac{\Delta t}{2}M\right]\widetilde{\phi}^n. \tag{A.18}$$

The CN-FV scheme detailed above is second-order accurate in space and time and is unconditionally stable.

A.2 Locally One Dimensional ADI scheme

As mentioned in the previous section, the bandwidth of the system of equations considered (Eq. A.18) is at most $2N_xN_y$ and we approximate it as the product of tri-diagonal matrices (and permutations) by incorporating Alternating Direction Implicit (ADI) methods. There are many variants of the ADI scheme but the Locally One Dimensional (LOD) scheme is of interest here and is described below. The LOD scheme has the additional advantage of resulting in a numerical solution procedure equivalent to solving a 1D heat conduction equation successively in each direction.

Consider X to be a tri-diagonal square matrix of size N_x defined by:

$$\begin{aligned} X_{i,i-1} &= \frac{m_{i-\frac{1}{2},j,k}\Gamma^{n+\frac{1}{2}}_{i-\frac{1}{2},j,k}}{\Delta x^2_{i-\frac{1}{2}}} \\ X_{i,i+1} &= \frac{m_{i+\frac{1}{2},j,k}\Gamma^{n+\frac{1}{2}}_{i+\frac{1}{2},j,k}}{\Delta x^2_{i+\frac{1}{2}}} \\ X_{i,i} &= -X_{i,i-1} - X_{i,i+1}, \end{aligned} \tag{A.19}$$

with $i = 1, 2, ..., N_x$ for every j and k. Similarly, Y and Z of sizes N_y and N_z respectively are defined as:

$$\begin{aligned} Y_{j,j-1} &= \frac{m_{i,j-\frac{1}{2},k}\Gamma^{n+\frac{1}{2}}_{i,j-\frac{1}{2},k}}{\Delta y^2_{j-\frac{1}{2}}} \\ Y_{j,j+1} &= \frac{m_{i,j+\frac{1}{2},k}\Gamma^{n+\frac{1}{2}}_{i,j+\frac{1}{2},j,k}}{\Delta y^2_{j+\frac{1}{2}}} \\ Y_{j,j} &= -Y_{j,j-1} - Y_{j,j+1}, \end{aligned} \tag{A.20}$$

and

$$
\begin{aligned}
Z_{k,k-1} &= \frac{m_{i,j,k-\frac{1}{2}}\Gamma^{n+\frac{1}{2}}_{i,j,k-\frac{1}{2}}}{\Delta z^2_{k-\frac{1}{2}}} \\
Z_{k,k+1} &= \frac{m_{i,j,k+\frac{1}{2}}\Gamma^{n+\frac{1}{2}}_{i,j,k+\frac{1}{2}}}{\Delta z^2_{k+\frac{1}{2}}} \\
Z_{k,k} &= -Z_{k,k-1} - Z_{k,k+1},
\end{aligned} \tag{A.21}
$$

with $j = 1, 2, ..., \mathrm{N_y}$ and $k = 1, 2, ..., \mathrm{N_z}$.

We approximate the numerical solution obtained by solving Eq. (A.18) by the solving each of the following three sub-steps given by the LOD scheme successively in each direction:

$$\left[W - \frac{\Delta t}{2}X\right]\widetilde{\phi}^{s1} = \left[W + \frac{\Delta t}{2}X\right]\widetilde{\phi}^{n}, \tag{A.22}$$

$$\left[W - \frac{\Delta t}{2}Y\right]\widetilde{\phi}^{s2} = \left[W + \frac{\Delta t}{2}Y\right]\widetilde{\phi}^{s1}, \tag{A.23}$$

$$\left[W - \frac{\Delta t}{2}Z\right]\widetilde{\phi}^{n+1} = \left[W + \frac{\Delta t}{2}Z\right]\widetilde{\phi}^{s2}. \tag{A.24}$$

Each sub-step of the LOD scheme given corresponding to Eqs. (A.22-A.24) is equivalent to solving the one-dimensional heat conduction equation successively and can be numerically solved using the Tri-Diagonal Matrix Algorithm (TDMA) in $O(N)$ operations. For periodic problems, the Sherman-Morrison-Woodbury formula is used. It should be noted that the transition between the sub-steps occurs with appropriate permutations on $\widetilde{\phi}$. Additionally, note that the LOD scheme is unconditionally stable and conservative.

To summarize, thus far we present a methodology to estimate the mean drifts for the special case of either a single species or multiple species with the same molecular diffusivity. The following section describes an algorithm to cal-

culate the mean drifts in the presence of differential diffusion.

A.3 Differential diffusion

In this section, we present a numerical implementation of the variable-property heat conduction equation in the presence of differential diffusion of multiple species mass fractions. The algorithm is presented in one-dimension but is easily extended to multiple dimensions without any violation of the properties of the scheme.

Consider a set of n_s transport equations for species mass fractions $\widetilde{\phi}_\alpha$ for $\alpha = 1, 2, ..., n_s$ in the x-direction:

$$\frac{\partial \rho \widetilde{\phi}_\alpha}{\partial t} + \frac{\partial \rho V_{(\alpha)} \widetilde{\phi}_\alpha}{\partial x} = 0, \tag{A.25}$$

where V_α is the diffusion velocity in the x-direction. Note that indices in parentheses are excluded from the summation convention. We consider modeling diffusion velocities using Fick's law as

$$(V_{(\alpha)} + V_c)\, \widetilde{\phi}_\alpha = -\Gamma_{(\alpha)} \frac{\partial \widetilde{\phi}_\alpha}{\partial x}, \tag{A.26}$$

where Γ_α is the mixture-averaged diffusivity of species α and the correction velocity V_c is given by

$$V_c = -\sum_\alpha \Gamma_\alpha \frac{\partial \widetilde{\phi}_\alpha}{\partial x}. \tag{A.27}$$

Given Eqs. (A.26) and (A.27), Eq. (A.25) can be written as,

$$\frac{\partial \rho \widetilde{\phi}_\alpha}{\partial t} = \frac{\partial}{\partial x}\left(\rho \Gamma_{(\alpha)} \frac{\partial \widetilde{\phi}_\alpha}{\partial x}\right) - \frac{\partial}{\partial x}\left(\rho \widetilde{\phi}_\alpha \sum_\beta \Gamma_\beta \frac{\partial \widetilde{\phi}_\beta}{\partial x}\right). \tag{A.28}$$

The numerical solution to Eq. (A.28) is obtained in two steps. First, given $\widetilde{\phi}_\alpha^n$, the heat conduction equation without the correction term:

$$\frac{\partial \rho \widetilde{\phi}_\alpha}{\partial t} = \frac{\partial}{\partial x}\left(\rho \Gamma_{(\alpha)} \frac{\partial \widetilde{\phi}_\alpha}{\partial x}\right), \tag{A.29}$$

is solved to obtain the increment $\Delta\widetilde{\phi}_\alpha^{h,n+\frac{1}{2}} = \widetilde{\phi}_\alpha^{h,n+1} - \widetilde{\phi}_\alpha^n$ over a time-step Δt using the CN-FV scheme as

$$W\Delta\widetilde{\phi}_\alpha^{h,n+\frac{1}{2}} = \Delta t X_{(\alpha)} \widetilde{\phi}_\alpha^{h,n+\frac{1}{2}}, \tag{A.30}$$

for each α with $2\widetilde{\phi}_\alpha^{h,n+\frac{1}{2}} = \widetilde{\phi}_\alpha^{h,n+1} + \widetilde{\phi}_\alpha^n$ where X_α is given by Eq. (A.19) with Γ replaced by Γ_α. This step is implicit and second-order accurate in space and time. Note that summing Eq. (A.30) over all rows yields,

$$\sum_p W_{pp}\Delta\widetilde{\phi}_{\alpha,p}^{h,n+\frac{1}{2}} = \Delta t \underbrace{\sum_p X_{\alpha;pq}}_{=0} \widetilde{\phi}_{\alpha,q}^{h,n+\frac{1}{2}} = 0. \tag{A.31}$$

Equation (A.30) can be represented in terms of known quantities as:

$$\left(W - \frac{\Delta t}{2} X_\alpha\right)\widetilde{\phi}_\alpha^{h,n+\frac{1}{2}} = \left(W + \frac{\Delta t}{2} X_\alpha\right)\widetilde{\phi}_\alpha^n. \tag{A.32}$$

Secondly, given $\widetilde{\phi}_\alpha^{h,n+\frac{1}{2}}$, we define V for each $j = 1, 2, ..., \mathrm{N_y}$ and $k = 1, 2, ..., \mathrm{N_z}$ as:

$$V_{i+\frac{1}{2}} = \sum_\alpha X_{\alpha;i,i+1}\left(\widetilde{\phi}_{\alpha;i+1,j,k}^{h,n+\frac{1}{2}} - \widetilde{\phi}_{\alpha;i,j,k}^{h,n+\frac{1}{2}}\right). \tag{A.33}$$

Using $\widetilde{\phi}_\alpha^n$ and V, we solve

$$\frac{\partial \rho \widetilde{\phi}_\alpha}{\partial t} = \frac{\partial (\rho \widetilde{\phi}_\alpha V_c)}{\partial x}, \tag{A.34}$$

over the time-step Δt explicitly to obtain the correction $\Delta\widetilde{\phi}_\alpha^{c,n+\frac{1}{2}}$ as,

$$W\Delta\widetilde{\phi}_\alpha^{c,n+\frac{1}{2}} = \Delta t N \widetilde{\phi}_\alpha^n, \tag{A.35}$$

where N is a tri-diagonal matrix defined as:

$$N_{i-1,i} = \frac{V_{i-\frac{1}{2}}}{2}, \tag{A.36}$$

$$N_{i+1,i} = -\frac{V_{i+\frac{1}{2}}}{2}. \tag{A.37}$$

Note that by construction, $\sum_i N_{ij} = 0$. This implies that the summation over all rows of Eq. (A.35) yields zero.

Finally, the increment $\Delta\widetilde{\phi}_\alpha^{n+\frac{1}{2}}$ is obtained as,

$$\Delta\widetilde{\phi}_\alpha^{n+\frac{1}{2}} = \Delta\widetilde{\phi}_\alpha^{h,n+\frac{1}{2}} - \Delta\widetilde{\phi}_\alpha^{c,n+\frac{1}{2}}, \tag{A.38}$$

based on which, the following observations can be made:

1. Summing Eq. (A.38) over all species α yields zero *i.e.,*

$$\sum_\alpha \Delta\widetilde{\phi}_\alpha^{n+\frac{1}{2}} = 0. \tag{A.39}$$

2. Summing Eq. (A.38) weighted by W over all rows sums to zero as well,

$$\sum_p W_{pp}\Delta\widetilde{\phi}_{\alpha,p}^{n+\frac{1}{2}} = 0, \tag{A.40}$$

since summing over all rows of both N and X_α is zero.

In summary, this section presents an implementation methodology that accounts for differential diffusion effects in one-dimension. In higher dimensions, the LOD scheme is used and the correction $\Delta\widetilde{\phi}_\alpha^c$ is applied at each sub-step of the LOD scheme.

APPENDIX B

SMOOTHING

Many families of smoothing schemes can be formulated originating from the generalized variable-property heat conduction equation by implementing various numerical schemes such as the implicit Euler scheme. In B.1, a brief mention is made about the various smoothing schemes derived from the heat-conduction equation with specific reference to the three-point implicit smoothing methodology. Following this, B.2 presents a detailed analysis (in wave number space) of the smearing error incurred upon smoothing and the corresponding variance reduction achieved for the three-point implicit smoothing scheme.

B.1 Explicit smoothing vs. Implicit smoothing

In this section of the appendix on smoothing, we present a class of implicit-explicit smoothing schemes derived from the variable-property heat conduction equation using the Crank-Nicolson scheme. The three-point implicit smoothing scheme is of particular interest in this work.

Let us consider formulating a smoothing scheme starting with the variable-property heat equation in 1D given by Eq. (A.29). As described in A.1, the discrete representation of the heat equation using the CN-FV scheme yields Eq. (A.32), which when adapted to smoothing becomes,

$$(W + A)\, g = (W + B)\, f. \tag{B.1}$$

The noisy input field f and the smoothed output field g are both weighted by

the diagonal matrix W. The matrix A performs the implicit smoothing operation and B corresponds to the explicit smoothing operation. Each specification for the matrices A and B, that satisfies the set of properties mentioned in Sec. 3.3.4.2, yields a family of smoothing schemes. In this work, we are interested in a smoothing scheme with a three-point stencil that yields A and B in tri-diagonal form. Computational algorithms such as the tri-diagonal matrix solvers can be used to solve the resulting linear system relatively inexpensively.

The three-point scheme is parametrized by two parameters: α_s parametrizes the smoothing matrix A, and β_s parametrizes the smoothing matrix B. The following specification for A and B,

$$A_{j,j-1} = -\alpha_s, \quad A_{j,j+1} = -\alpha_s, \quad A_{j,j} = 2\alpha_s, \tag{B.2}$$

$$B_{j,j-1} = \beta_s, \quad B_{j,j+1} = \beta_s, \quad B_{j,j} = -2\beta_s, \tag{B.3}$$

satisfies the properties listed in Sec. 3.3.4.2 for non-negative α_s and β_s and this is identical to the specification introduced in Eqs. (3.12) and (3.13). The process of smoothing not only achieves a reduction in variance *i.e.*, $\text{var}(g) \leq \text{var}(f)$ but also incurs a spatial smearing error. A simple analysis (not shown here) in wave number space shows that for a given reduction in variance, minimal smearing error is incurred for $\beta_s = 0$. Henceforth, we consider only the three-point implicit smoothing scheme given by Eq. (3.32) repeated here for coherence:

$$(W + A)g = Wf.$$

It should be noted that in Eq. (3.32), f enters solely as Wf. Consequently, if $w_i = 0$ then $(Wf)_i = 0$ regardless of the value of f_i. In a situation where the i-th cell is devoid of particles and is empty, $w_i = 0$ and therefore g_i contains no contribution from the undefined f_i.

B.2 Smearing error in smoothing

The operation of smoothing has a two-fold effect on the smoothed fields g in comparison to the fields input for smoothing f: variance reduction and spatial smearing. Here, we present an analysis in wave number space to estimate the smearing error incurred given the three-point implicit smoothing scheme parametrized by α_s. This analysis is later used towards the end of this section to model the smearing error due to smoothing of "output" quantities in a PDF calculation.

Consider a periodic function $H(x)$, in one dimension with period L, to be specified. We sample $H(x)$ at N equally spaced points x_j for $j = 0, 1, ..., N-1$ to get

$$H_j \equiv H(x_j), \tag{B.4}$$

and define $\Delta x = L/N$ such that $x_j = j\Delta x$. The discrete inverse Fourier transform of H_j is obtained as

$$H_j = \sum_{k=1-\frac{N}{2}}^{\frac{N}{2}} \hat{H}_k e^{i\kappa_k x_j}, \tag{B.5}$$

where $\kappa_k = 2\pi k/L$ and

$$\hat{H}_k = a_{H,k} + ib_{H,k}. \tag{B.6}$$

Since H_j is real, $\hat{H}_k$ satisfies conjugate symmetry resulting in $a_{H,k} = a_{H,-k}$ and $b_{H,k} = -b_{H,-k}$.

Next, consider $f(x)$ to be an estimate of $H(x)$ and $f_j \equiv f(x_j)$ such that

$$f_j = H_j + \mu_j, \tag{B.7}$$

for some deterministic error $\mu_j \equiv \mu(x_j)$. As in Eq. (B.5), the discrete inverse Fourier transforms of μ_j and f_j are obtained as,

$$\mu_j = \sum_{k=1-\frac{N}{2}}^{\frac{N}{2}} \hat{\mu}_k e^{i\kappa_k x_j}, \tag{B.8}$$

and

$$\hat{f}_k = \hat{H}_k + \hat{\mu}_k, \tag{B.9}$$

respectively with

$$\hat{\mu}_k = a_{\mu,k} + ib_{\mu,k}. \tag{B.10}$$

As with H_j, since μ_j is real, conjugate symmetry implies that $a_{\mu,k} = a_{\mu,-k}$ and $b_{\mu,k} = -b_{\mu,-k}$.

We perform a three-point implicit smoothing operation on f_j using Eq. (3.50) to obtain g_j as

$$g_i = C_{ij} f_j, \tag{B.11}$$

the Fourier transform of which results in

$$\hat{g}_k = \hat{C}_k \hat{f}_k, \tag{B.12}$$

where $\hat{g}_k$ is the Fourier transform of g_j and $\hat{C}_k$ is that of C_{ij}. For A defined by Eq. (B.2), it can be shown that

$$\hat{C}_k = \frac{1}{1 + 2\alpha_s E_k}, \tag{B.13}$$

where

$$E_k = 1 - \cos(\kappa_k \Delta x). \tag{B.14}$$

Note that given Eqs. (B.13) and (B.14) , $\hat{C}$ has zero phase.

Let us define the Fourier transform $\hat{S}_k$ of the smearing error $S_j \equiv S(x_j) = g_j - H_j$ as

$$\begin{aligned} \hat{S}_k &= \hat{g}_k - \hat{H}_k, & \text{(B.15)} \\ &= \left(\hat{C}_k - 1\right)\hat{H}_k + \hat{C}_k\hat{\mu}_k, & \text{(B.16)} \end{aligned}$$

where the last line is obtained by substituting Eqs. (B.9) and (B.12) in Eq. (B.15). Now, consider $\mathcal{S}$ to be the global estimate of the smearing error S_j given by

$$\begin{aligned} \mathcal{S}^2 &= \sum_{j=0}^{N-1} S_j^2, \\ &= \sum_{k=1-\frac{N}{2}}^{\frac{N}{2}} \hat{S}_k \hat{S}_k^* \\ &= \sum_{k=1-\frac{N}{2}}^{\frac{N}{2}} \mid \hat{S}_k \mid^2, & \text{(B.17)} \end{aligned}$$

where $\hat{S}_k^*$ is the complex conjugate of $\hat{S}_k$. The second line in Eq. (B.17) follows from Parseval's theorem and the last line is obtained by using $\mid \hat{S}_k \mid^2 = \hat{S}_k\hat{S}_k^*$. Since $\mid \hat{S}_k \mid^2 = \mid \hat{S}_{-k} \mid^2$, using Eqs. (B.6), (B.10), (B.13) and (B.16) in Eq. (B.17), we obtain the global estimate of the smearing error to be

$$\begin{aligned} \mathcal{S}^2 = \mid \hat{\mu}_0 \mid^2 &+ 2\sum_{k=1}^{\frac{N}{2}} \left(\frac{2\alpha_s E_k}{1 + 2\alpha_s E_k}\right)^2 \mid \hat{H}_k \mid^2 \\ &+ 2\sum_{k=1}^{\frac{N}{2}} \left(\frac{1}{1 + 2\alpha_s E_k}\right)^2 \mid \hat{\mu}_k \mid^2 \\ &- 2\sum_{k=1}^{\frac{N}{2}} \frac{4\alpha_s E_k}{(1 + 2\alpha_s E_k)^2} \left(a_{H,k}a_{\mu,k} + b_{H,k}b_{\mu,k}\right). & \text{(B.18)} \end{aligned}$$

Note that $A_\mu^2 \equiv \mid \hat{\mu}_k \mid^2 = a_{\mu,k}^2 + b_{\mu,k}^2$. The definition for $A_H^2 \equiv \mid \hat{H}_k \mid^2$ follows.

Equation (B.18) can be used to obtain the global estimate of the smearing error due to smoothing f_j implicitly with parameter α_s when $\hat{H}$ and $\hat{\mu}$ are known.

Typically, in a PDF calculation, neither of these are known *a priori* and in the following paragraphs, we present an approximate model for $\mathcal{S}$ under the assumption that H_j and μ_j consist of a single mode each at wave-numbers κ_H and κ_μ respectively.

Given H_j, κ_H and A_H are known. Consider μ_j to arise primarily due to spatial truncation errors (second-order accurate in this work). Then, the following can be inferred:

$$E_{\kappa_H} \sim \Delta x^2, \tag{B.19}$$

$$A_\mu \sim \Delta x^2, \tag{B.20}$$

$$\kappa_\mu \sim \frac{1}{\Delta x}, \tag{B.21}$$

$$E_{\kappa_\mu} \sim \text{constant}. \tag{B.22}$$

We present models for $\mathcal{S}^2$ for the following two cases:

1. When $\kappa_H \neq \kappa_\mu$, the global estimate of the smearing error $\mathcal{S}$ given by Eq. (B.18) can be simplified to get

$$\mathcal{S}^2 = \left(\frac{c_1\alpha_s\Delta x^2}{1 + c_2\alpha_s\Delta x^2}\right)^2 + \left(\frac{c_3\Delta x^2}{1 + c_4\alpha_s}\right)^2, \tag{B.23}$$

   for some c_i.

2. When $\kappa_H = \kappa_\mu$, $\mathcal{S}$ in Eq. (B.18) is simplified to get

$$\mathcal{S}^2 = \left(\frac{c_1\Delta x^2 - c_2\alpha_s\Delta x^2}{1 + c_3\alpha_s\Delta x^2}\right)^2 + \left(\frac{c_4\Delta x^2 - c_5\alpha_s\Delta x^2}{1 + c_3\alpha_s\Delta x^2}\right)^2, \tag{B.24}$$

   for some other c_i.

It should be noted however, that the preceding analysis yields an approximate model for $\mathcal{S}$ since only one or two modes were considered to obtain Eqs. (B.24) and (B.23).

B.3 Variance reduction in smoothing

We briefly present an expression for the reduction in variance achieved due to smoothing in this section of B. Let V denote the ratio $\text{var}(f)/\text{var}(g)$. An exact expression for V is easily obtained in 1D using Eq. (B.12) as

$$V^{-1} = \frac{1}{\kappa}\int_0^{\kappa} \hat{C}(\hat{\kappa})^2 d\hat{\kappa}, \tag{B.25}$$

$$= \frac{1+2\alpha_s}{(1+4\alpha_s)^{3/2}}. \tag{B.26}$$

Since LOD is used to perform smoothing in higher dimensions, it follows that in a D-dimensional space the variance reduction is obtained as,

$$V = \left[\frac{(1+4\alpha_s)^{3/2}}{1+2\alpha_s}\right]^D. \tag{B.27}$$

In summary, B presents a brief introduction to the various explicit and implicit smoothing methodologies followed by an analysis of the smearing error due to smoothing in wave-number space, concluding with approximate models for the smearing error and an exact expression for the variance reduction.

APPENDIX C

PROPERTIES OF VARIOUS SCHEMES

Consider $\phi^{*,n}_{\alpha,p}$ to represent the mass fraction of species α for a general particle p at a time level n. All particle properties are denoted with a superscript '$*$'. Any numerical scheme presented for the implementation of mixing must satisfy the following three criteria:

1. Detailed conservation at the particle level given by

$$\sum_p m_p \phi^{*,n+1}_{\alpha,p} = \sum_p m_p \phi^{*,n}_{\alpha,p}, \tag{C.1}$$

   where m_p is the mass of the particle p.

2. Boundedness of species mass fractions which requires that mass fractions be positive at all times:

$$\phi_\alpha \geq 0. \tag{C.2}$$

3. Normalization constraint on species mass fractions:

$$\sum_\alpha \phi_\alpha = 1. \tag{C.3}$$

A set of mass fractions is realizable if both the normalization condition and boundedness is satisfied. Boundedness can be imposed by fixing a lower limit on the mixing frequency [37] while considering the implementation of IEM mixing and molecular transport together. Therefore, this section is divided into two parts: the first analyzes each of the schemes *viz.*, PIC-PC, PIC-PL and CIC-LS for realizability and the second part concentrates on the conservation properties of each scheme.

C.1 Realizability

Realizability is satisfied if both the boundedness and normalization conditions are satisfied. Consider Eq. (3.96) repeated here for convenience,

$$\phi_{\alpha,p}^{*,n+1} = \phi_{\alpha,p}^{*,n} + c_p^{*,n+\frac{1}{2}} \left(\widetilde{\phi}_{\alpha,p}^{*,n} - \phi_{\alpha,p}^{*,n} \right) + \Delta\widetilde{\phi}_{\alpha,p}^{*,n+\frac{1}{2}},$$

where $\Delta\widetilde{\phi}_p^{*,n+\frac{1}{2}}$ is given by Eq. (A.38). McDermott and Pope [37] show that boundedness can be achieved by imposing a lower limit on the mixing frequency as:

$$c_p^{*,n+\frac{1}{2}} \geq c_{\min}^{n+\frac{1}{2}} \equiv \max_{p,\alpha} \left[\frac{\Delta\widetilde{\phi}_{\alpha,p}^{*,n+1/2}}{\phi_{\max}^n - \phi_{\alpha,p}^{*,n}}, \frac{\Delta\widetilde{\phi}_{\alpha,p}^{*,n+1/2}}{\phi_{\min}^n - \phi_{\alpha,p}^{*,n}} \right], \tag{C.4}$$

where $\phi_{\min}^n \leq \phi_{\alpha,p}^{*,n} \leq \phi_{\max}^n$. Given that boundedness is satisfied by imposing a lower limit on the mixing frequency, realizability is achieved by satisfying the normalization condition given by Eq. (C.3).

We show that, given that $\phi_{\alpha,p}^{*,n}$ satisfies the normalization condition, a necessary and sufficient condition for $\phi_{\alpha,p}^{*,n+1}$ to satisfy the normalization condition is that $\widetilde{\phi}_{\alpha,p}^{*,n}$ also satisfy the normalization condition. Consider summing Eq. (3.96) over all species:

$$\sum_\alpha \phi_{\alpha,p}^{*,n+1} = \underbrace{\sum_\alpha \phi_{\alpha,p}^{*,n}}_{1} + c_p^{*,\frac{1}{2}} \left(\sum_\alpha \widetilde{\phi}_{\alpha,p}^{*,n} - \underbrace{\sum_\alpha \phi_{\alpha,p}^{*,n}}_{1} \right) + \underbrace{\sum_\alpha \Delta\widetilde{\phi}_{\alpha,p}^{*,\frac{1}{2}}}_{0}.$$

where the last term stems from Eq. (A.39) since interpolation preserves the normalization condition. As elaborated in Sec. §3.3.3, $\widetilde{\phi}_{\alpha,p}^{*,n}$ (or $\Delta\widetilde{\phi}_{\alpha,p}^{*,n}$) is obtained by interpolating $\widetilde{\phi}_{\alpha,j}^n$ (or $\Delta\widetilde{\phi}_{\alpha,j}^n$) to particle locations using one of the three interpolation schemes: PC, LS or PL.

Note that $\widetilde{\phi}^n_{\alpha,j}$ is the smoothed estimate of the mean of species α obtained by smoothing $\widehat{\phi}^n_{\alpha,j}$ using the implicit smoothing scheme represented by Eq. (3.32). If $f_j \equiv \sum_\alpha \widehat{\phi}_{\alpha,j} = 1$, then $g_j \equiv \sum_\alpha \widetilde{\phi}_{\alpha,j} = 1$ because of boundedness (shown in Sec. §3.3.4.2), *i.e.*, $\min_j f_j = 1 \leq g_j \leq \max_j f_j = 1$. Therefore, smoothing preserves the normalization condition.

Finally, the unsmoothed mean estimates $\widehat{\phi}^n_{\alpha,j}$ are obtained from $\phi^{*,n}_{\alpha,p}$ using one of the two mean estimation methods elaborated in Sec. §3.3.2 – PIC or CIC. Let us define $\mathbf{K}_j$ to denote $\mathbf{I}_j$ (Eq. (3.21)) in case of the PIC scheme and $\mathbf{B}_j$ (Eq. (3.22)) in case of the CIC scheme. We now show that mean estimation given by Eq. (3.23) preserves the normalization condition:

$$\sum_\alpha \widehat{\phi}_{\alpha,j} = \frac{\displaystyle\sum_p \mathbf{K}_j(\mathbf{x}_p) m^*_p c^*_p \sum_\alpha \phi^*_{\alpha,p}}{\displaystyle\sum_p \mathbf{K}_j(\mathbf{x}_p) m^*_p c^*_p} = 1. \tag{C.5}$$

Therefore, in summary, the numerical implementation of Eq. (3.96) satisfies realizability.

C.2 Conservation

We consider the conservation properties of the three numerical schemes – PIC-PC, CIC-LS and PIC-PL – for the case of a single scalar first. Conservation at the level of multiple species is addressed in C.2.3.

Consider the one-step update for the IEM mixing model given by Eq. (3.18) repeated here for convenience,

$$\phi^{*,n+1}_p = \phi^{*,n}_p + c^{*,n+\frac{1}{2}}_p \left(\widetilde{\phi}^{*,n}_p - \phi^{*,n}_p\right) + \Delta\widetilde{\phi}^{*,n+\frac{1}{2}}_p,$$

where $\Delta\widetilde{\phi}_p^{*,n+\frac{1}{2}}$ is the mean drift obtained using Eq. (A.15). Conservation requires that,

$$\begin{aligned}\sum_p m_p^* \left(\phi_p^{*,n+1} - \phi_p^{*,n}\right) &= \sum_p m_p^* \Delta\widetilde{\phi}_p^{*,n+\frac{1}{2}} + \sum_p m_p^* c_p^{*,n+1/2} \left(\widetilde{\phi}_p^{*,n} - \phi_p^{*,n}\right) \\ &= 0. \end{aligned} \tag{C.6}$$

It is therefore sufficient to satisfy the following:

$$\sum_p m_p^* \Delta\widetilde{\phi}_p^{*,n+\frac{1}{2}} = 0, \tag{C.7}$$

$$\sum_p m_p^* c_p^{*,n+1/2} \widetilde{\phi}_p^{*,n} = \sum_p m_p^* c_p^{*,n+1/2} \phi_p^{*,n} = 0. \tag{C.8}$$

The outline of this appendix is as follows. Since both the PIC-PC and the CIC-LS schemes are similar in mathematical form, we define $\mathbf{K}_j$ to denote $\mathbf{I}_j$ in case of the PIC-PC scheme and $\mathbf{B}_j$ in case of the CIC-LS scheme, as was done in C.1 and address the conservation properties of both these schemes in C.2.1 using $\mathbf{K}_j$. The PIC-PL scheme is dealt with in C.2.2 as an extension of the PIC-PC scheme. Finally, C.2.3 probes for detailed conservation with differential diffusion.

C.2.1 PIC-PC/CIC-LS

We consider the conservation properties of both the PIC-PS and CIC-LS schemes together in this section of C using $\mathbf{K}_j$ to denote $\mathbf{I}_j$ in case of the PIC-PC scheme and $\mathbf{B}_j$ in case of the CIC-LS scheme. Furthermore, conservation in terms of Eq. (C.7) and Eq. (C.8) is considered separately.

We define the mass m_j of a cell centered at $\mathbf{x}_j$ to be,

$$m_j = \sum_p m_p^* \mathbf{K}_j(\mathbf{x}_p^*). \tag{C.9}$$

Now, consider Eq. (C.7), which can be re-expressed as,

$$\begin{aligned} \sum_p m_p^* \Delta\widetilde{\phi}_p^{*,n+1/2} &= \sum_p m_p^* \sum_j \mathbf{K}_j(\mathbf{x}_p^*) \Delta\widetilde{\phi}_j^{n+1/2}, \\ &= \sum_j m_j \Delta\widetilde{\phi}_j^{n+1/2}, \\ &= 0. \end{aligned} \tag{C.10}$$

The first line is obtained by using Eq. (3.27) to interpolate $\Delta\widetilde{\phi}_j^{n+1/2}$ to particle locations. The second line comes by substituting m_j using Eq. (C.9). The last line is obtained due to the formulation of the Crank-Nicolson scheme given by Eq. (A.17). Thus, Eq. (C.7) is satisfied by both the PIC-PC and the CIC-LS schemes.

Next, we prove Eq. (C.8). Consider weights w to be defined as $w = mc$. Starting from the left-hand-side of Eq. (C.8) (and ignoring the time-levels for brevity),

$$\begin{aligned} \sum_p m_p^* c_p^* \widetilde{\phi}_p^* &= \sum_p w_p^* \widetilde{\phi}_p^*, \\ &= \sum_p w_p^* \sum_j \mathbf{K}_j(\mathbf{x}_p^*) \widetilde{\phi}_j, \\ &= \sum_j w_j \widetilde{\phi}_j, \end{aligned} \tag{C.11}$$

$$\tag{C.12}$$

where the first line comes by using $w = mc$. The second line follows when interpolating $\widetilde{\phi}_j$ to particle locations using Eq. (3.27) and the last line comes from Eq. (3.24). Note that $\widetilde{\phi}_j$ is obtained by smoothing the unsmoothed estimates of

the mean scalar $\widehat{\phi}_j$ using weights w_j. As shown in sec. (3.3.4.2), smoothing is conservative *i.e.*, $\sum_j w_j \widetilde{\phi}_j = \sum_j w_j \widehat{\phi}_j$ and therefore we can write,

$$\begin{aligned}\sum_p m_p^* c_p^* \widetilde{\phi}_p^* &= \sum_j w_j \widehat{\phi}_j, \\ &= \sum_j \sum_p \mathbf{K}_j(\mathbf{x}_p^*) w_p^* \phi_p^*, \\ &= \sum_p w_p^* \phi_p^* = \sum_p m_p^* c_p^* \phi_p^*, \end{aligned} \tag{C.13}$$

where the first line comes from using the conservation property of the smoothing operation. The second line follows from the mean estimation procedure given by Eq. (3.23) and third line comes because the summation of $\mathbf{K}_j$ over all j is unity. Thus we obtain the right hand side, showing that the PIC-PC/CIC-LS schemes are conservative.

C.2.2 PIC-PL

The conservation properties of the PIC-PL scheme are addressed in this section as an extension to the PIC-PC scheme. Given that the cell mass is defined by Eq. (C.9), with Eq. (3.28) the left hand side of Eq. (C.7) becomes,

$$\begin{aligned}\sum_p m_p^* \Delta\widetilde{\phi}_p^* &= \sum_p m_p^* \sum_j \mathbf{I}_j(\mathbf{x}_p^*) \Delta\widetilde{\phi}_j + \zeta \sum_p m_p^* \sum_j \mathbf{I}_j(\mathbf{x}_p^*) \left(\mathbf{x}_p^* - \bar{\mathbf{x}}_j^\Delta\right) . \boldsymbol{\nu}_j^\Delta, \\ &= \sum_p m_p^* \sum_j \mathbf{I}_j(\mathbf{x}_p^*) \Delta\widetilde{\phi}_j, \end{aligned} \tag{C.14}$$

by the definition of $\bar{\mathbf{x}}_j^\Delta$ given by,

$$\bar{\mathbf{x}}_j^\Delta = \frac{\sum_p \mathbf{I}_j(\mathbf{x}_p^*) m_p^* \mathbf{x}_p^*}{\sum_p \mathbf{I}_j(\mathbf{x}_p^*) m_p^*}, \tag{C.15}$$

and $\boldsymbol{\nu}_j^\Delta = \mathbf{e}_k \delta_k \Delta\widetilde{\phi}_j$ is an approximation to $\nabla\Delta\widetilde{\phi}_j$. As shown in C.2.1,

$$\sum_p m_p^* \sum_j \mathbf{I}_j(\mathbf{x}_p^*) \Delta\widetilde{\phi}_j = 0.$$

Next we consider Eq. (C.8) for the PIC-PL scheme. Using Eq. (3.28), the left hand side of Eq. (C.8) is written as,

$$\begin{aligned}\sum_p m_p^* c_p^* \widetilde{\phi}_p^* &= \sum_p m_p^* c_p^* \sum_j \mathbf{I}_j(\mathbf{x}_p^*)\widetilde{\phi}_j + \zeta \sum_p m_p^* c_p^* \sum_j \mathbf{I}_j(\mathbf{x}_p^*)\left(\mathbf{x}_p^* - \bar{\mathbf{x}}_j\right)\nu_j, \\ &= \sum_p m_p^* c_p^* \sum_j \mathbf{I}_j(\mathbf{x}_p^*)\widetilde{\phi}_j, \end{aligned} \tag{C.16}$$

by the definition of $\bar{\mathbf{x}}_j$ which is given by,

$$\bar{\mathbf{x}}_j = \frac{\sum_p \mathbf{I}_j(\mathbf{x}_p^*) m_p^* c_p^* \mathbf{x}_p^*}{\sum_p \mathbf{I}_j(\mathbf{x}_p^*) m_p^* c_p^*}. \tag{C.17}$$

As shown in C.2.1,

$$\sum_p m_p^* c_p^* \sum_j \mathbf{I}_j(\mathbf{x}_p^*)\widetilde{\phi}_j = \sum_p m_p^* c_p^* \phi_p^{*,n}.$$

This shows that the PIC-PL scheme is also conservative.

C.2.3 Multiple species with unequal diffusivities

While considering multiple species each with different diffusivity, conservation requires that

$$\sum_p m_p^* \Delta\widetilde{\phi}_{\alpha,p}^{*,n+\frac{1}{2}} = 0, \tag{C.18}$$

where $\Delta\widetilde{\phi}_{\alpha,p}^{*,n+\frac{1}{2}}$ is obtained by interpolating $\Delta\widetilde{\phi}_{\alpha,j}^{n+\frac{1}{2}}$ given by Eq. (A.38) to particle locations. Equation (A.40) suggests that conservation is satisfied at the cell level. Since interpolation from estimates at the cell level to particle locations satisfies conservation criterion, we conclude that detailed conservation is satisfied in the case of multiple species with different diffusivities.

In summary, C presents evidence to show that the numerical implementation detailed in Sec. §3.3 satisfies conservation and realizability.

APPENDIX D

DESCRIPTION OF TESTS

The formulations of test cases using the Method of Manufactured Solutions are described here in the following two sections. D.1 details the constant-density test case in a Cartesian coordinate system, and D.2 provides specifications for the test problem in a cylindrical system.

D.1 Cartesian system

The manufactured solutions used in this work are defined in terms of several constants which are ascribed the values:

$$\omega = \frac{10}{2\pi},\ \mathrm{L} = 2\pi,\ \phi_{m,o} = \frac{1}{45},\ \phi_{v,o} = \frac{1}{125},\ \Omega_o = \frac{1}{2}$$
$$\mathrm{D_o} = \frac{1}{4},\ \mathrm{D_{o,t}} = \frac{4}{5},\ \mathrm{U_o} = 1,\ \mathrm{R_o} = 1,\ \mathrm{J_o} = 1. \tag{D.1}$$

Given the constants above, the manufactured solutions to Eqs. (3.65) and (3.66) are specified as functions of the three spatial coordinates x, y and z in a 3D Cartesian coordinate system and time t:

$$\overline{\phi}_m = \phi_{\mathrm{m,o}}\, \mathrm{e}^{4\,\omega t}\, (\cos(x) + \cos(z) + \sin(y) + 4)\,, \tag{D.2}$$
$$\overline{\phi'^2}_m = \phi_{\mathrm{v,o}}\left(4 - \mathrm{e}^{-3\,\omega t}\right) (\cos(y) + \sin(x) + \sin(z) + 4)\,, \tag{D.3}$$

respectively where $\{x, y, z\} \in [0\ L]$ and $\omega t \in [0\ 1]$. The second moment is then obtained as a sum of the variance and the square of the mean. The effective diffusivity $\Gamma_{\mathrm{eff}} = \Gamma + \Gamma_T$, sub-grid scale turbulent diffusivity Γ_T and molecular

diffusivity Γ are given by,

$$\Gamma_{\text{eff}} = \mathrm{D_o}\left(\mathrm{e}^{-4\,\omega\,t} + \frac{\mathrm{e}^{4\,\omega\,t}}{20}\right)(4\,\cos(y)\,\sin(x)\,\sin(z) - 4\, + 24)\,, \tag{D.4}$$

$$\Gamma_T = \mathrm{D_{o,t}}\,\Gamma_{\text{eff}}, \tag{D.5}$$

$$\Gamma = (1 - \mathrm{D_{o,t}})\,\Gamma_{\text{eff}}. \tag{D.6}$$

Finally, the mixing frequency Ω_m and velocity $\widetilde{\mathbf{U}}$ as given below,

$$\Omega_m = -\frac{2\,\Omega_\mathrm{o}\,\left(\cos\left(\pi\,\omega\,\left(2\,t - \frac{1}{5}\right)\right) + \frac{6}{5}\right)\left(\cos(z) + \sin(x) + \sin(y) + \frac{51}{5}\right)}{5\,\left(\mathrm{e}^{-3\,\omega\,t} - 4\right)}, \tag{D.7}$$

$$\widetilde{\mathrm{U}}_x = \mathrm{U_o}\left(\frac{4}{\mathrm{e}^{4\,\omega\,t}} + \frac{\mathrm{e}^{4\,\omega\,t}}{10}\right)(\cos(x)\,\cos(y) + \sin(x)\,\sin(z))\,, \tag{D.8}$$

$$\widetilde{\mathrm{U}}_y = \mathrm{U_o}\left(\frac{4}{\mathrm{e}^{4\,\omega\,t}} + \frac{\mathrm{e}^{4\,\omega\,t}}{10}\right)(\cos(y)\,\cos(z) + \sin(x)\,\sin(y))\,, \tag{D.9}$$

$$\widetilde{\mathrm{U}}_z = \mathrm{U_o}\left(\frac{4}{\mathrm{e}^{4\,\omega\,t}} + \frac{\mathrm{e}^{4\,\omega\,t}}{10}\right)(\cos(x)\,\cos(z) + \sin(y)\,\sin(z))\,, \tag{D.10}$$

and the source terms S_m and S_v can be obtained from Eqs. (3.65) and (3.66) respectively.

Figure D.1 plots the contours of various quantities at x = 0.4L and ωt = 0.25.

D.2 Cylindrical system

In the cylindrical coordinate system, the manufactured solutions are defined in terms of several constants that are ascribed values:

$$\omega = \frac{1}{4\pi},\ \mathrm{L} = 2\pi,\ \phi_{m,o} = 2,\ \phi_{v,o} = 200,\ \Omega_o = \frac{2}{100}$$
$$\mathrm{D_o} = \frac{5}{100},\ \mathrm{D_{o,t}} = \frac{2}{10},\ \mathrm{U_o} = -\frac{2}{100},\ \mathrm{R_o} = -\frac{5}{100},\ \mathrm{J_o} = 10. \tag{D.11}$$

The manufactured solutions to Eqs. (3.65) and (3.66) are specified as,

$$\overline{\phi}_m = \frac{\phi_{\mathrm{m,o}}\ (\cos(x)+2)\left(r^2\ (\cos(\theta)+1)\left(\cos\left(\frac{r}{2}\right)+1\right)+20\right)\left(\mathrm{e}^{-5\,\omega\,t}+\frac{\mathrm{e}^{5\,\omega\,t}}{100}\right)}{2} + 5, \tag{D.12}$$

$$\overline{\phi'^2}_m = \frac{\phi_{\mathrm{v,o}}\ (\cos(x)+2)\left(r^2\ (\cos(\theta)+1)\left(\cos\left(\frac{r}{2}\right)+1\right)+20\right)\left(\mathrm{e}^{-5\,\omega\,t}+\frac{\mathrm{e}^{5\,\omega\,t}}{100}\right)}{20} + \frac{1571}{5000}, \tag{D.13}$$

respectively where $\{x, r, \theta\} \in [0\ L]$ and $\omega t \in [0\ 1]$. The other properties and the velocity field are given by,

$$\Gamma_{\mathrm{eff}} = \frac{\mathrm{D_o}\ (\cos(x)+2)\left(r^2\ (\cos(\theta)+1)\left(\cos\left(\frac{r}{2}\right)+1\right)+20\right)\left(\mathrm{e}^{-5\,\omega\,t}+\frac{\mathrm{e}^{5\,\omega\,t}}{100}\right)}{2}, \tag{D.14}$$

$$\Omega_m = \frac{\Omega_{\mathrm{o}}\ (\cos(x)+2)\left(r^2\ (\cos(\theta)+1)\left(\cos\left(\frac{r}{2}\right)+1\right)+20\right)\left(\mathrm{e}^{-5\,\omega\,t}+\frac{\mathrm{e}^{5\,\omega\,t}}{100}\right)}{4}, \tag{D.15}$$

$$\widetilde{\mathrm{U}}_x = \mathrm{U_o}\ \sin(x)\left(\frac{r^3\ \sin\left(\frac{r}{2}\right)}{2} - 3\,r^2\left(\cos\left(\frac{r}{2}\right)+1\right)\right), \tag{D.16}$$

$$\widetilde{\mathrm{U}}_r = \mathrm{U_o}\,r^3\ \cos(x)\left(\cos\left(\frac{r}{2}\right)+1\right), \tag{D.17}$$

$$\widetilde{\mathrm{U}}_\theta = 2\,\mathrm{U_o}\,r\left(\cos\left(\frac{r}{2}\right)+1\right). \tag{D.18}$$

The sub-grid scale diffusivity, Γ_T and molecular diffusivity Γ are obtained using Eqs. (D.5-D.6) respectively and the source terms S_m and S_v can be obtained from Eqs. (3.65) and (3.66) respectively.

The contours of various quantities at $x = 0.4$L and ωt $= 0.5$ are plotted in Fig. D.2.

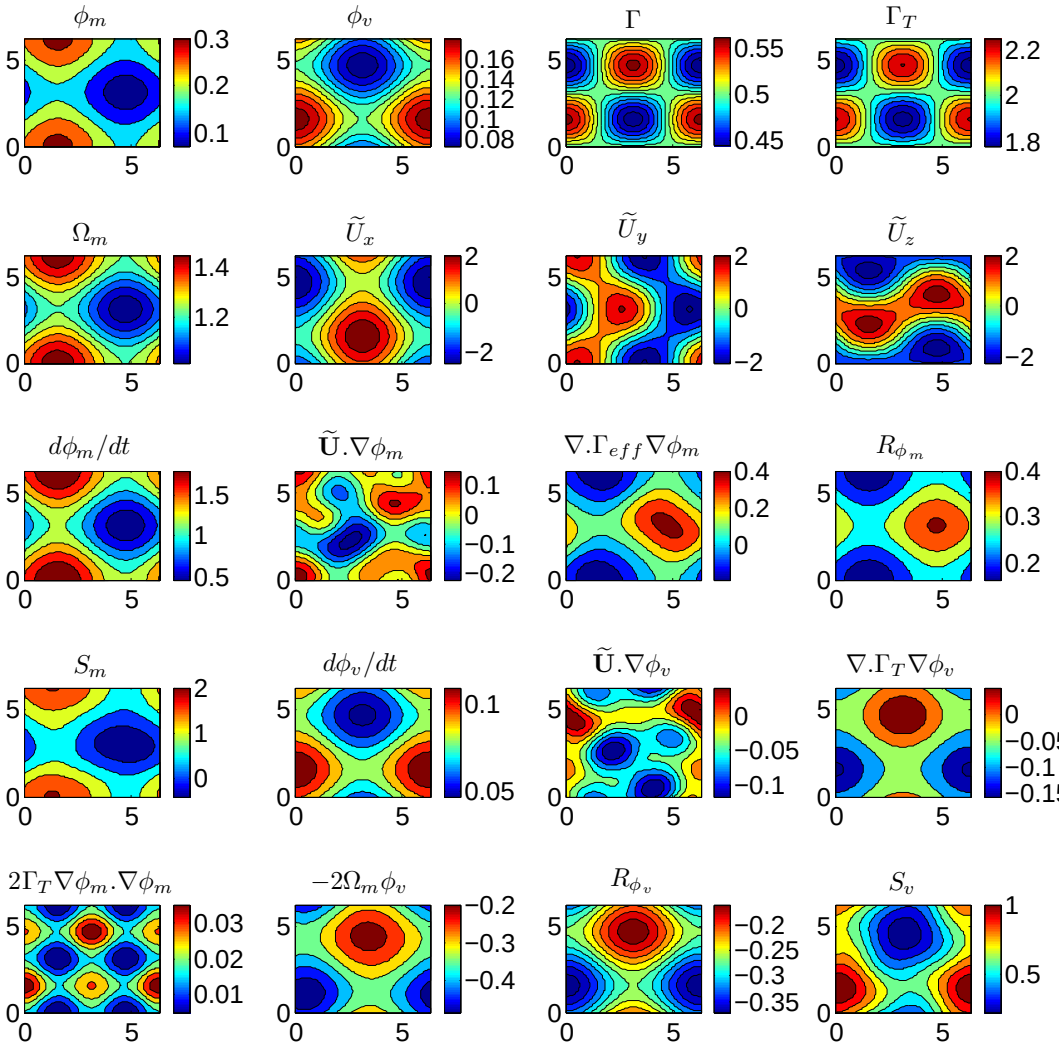

Figure D.1: Contour plots of the various MMS quantities in y-z plane at x = 0.4L and ωt = 0.25

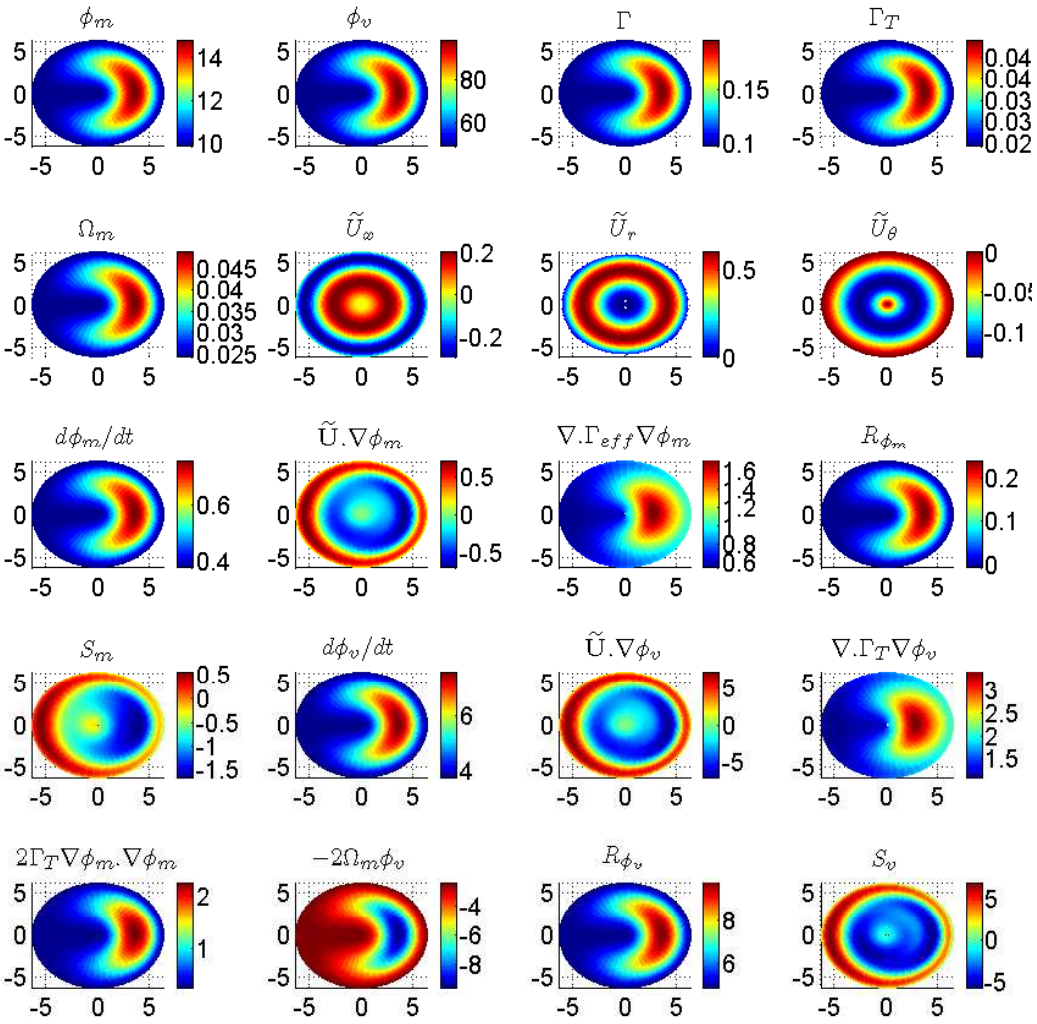

Figure D.2: Contour plots of the various MMS quantities in *r*-θ plane at x = 0.4L and ωt = 0.5

BIBLIOGRAPHY

[1] M.S. Anand and S.B. Pope. Diffusion behind line source in grid turbulence. Turbulent Shear Flows, 4:46–61, 1985.

[2] R.S. Barlow. Web site for the International Workshop on Measurement and Computation of Turbulent Non-premixed Flames (TNF), http://www.ca.sandia.gov/TNF/, 1996.

[3] R.S. Barlow and J.H. Frank. Effects of turbulence on species mass fractions in methane/air jet flames. Proceedings of the Combustion Institute, 27(1):1087 – 1095, 1998.

[4] R.S. Barlow, J.H. Frank, A.N. Karpetis, and J.-Y. Chen. Piloted Methane/Air Jet Flames: Scalar Structure and Transport Effects. Combustion and Flame, 143:433–449, 2005.

[5] R.W. Bilger, S.B. Pope, K.N.C. Bray, and J.F. Driscoll. Paradigms in turbulent combustion research. Proceedings of the Combustion Institute, 30:21–42, 2005.

[6] M.S. Borgas and B.L. Sawford. Molecular diffusion and viscous effects on concentration statistics in grid turbulence. Journal of Fluid Mechanics, 324:25–54, 1996.

[7] G. Brethouwer and F.T.M. Nieuwstadt. DNS of mixing and reaction of two species in a turbulent channel flow : A validation of the conditional moment closure. Flow, Turbulence and Combustion, 66:209–239, 2001.

[8] R.S. Cant and E. Mastorakos. An introduction to turbulent reacting flows. Imperial College Press, London, 2008.

[9] R. Cao, H. Wang, and S.B. Pope. The effect of mixing models in PDF calculations of piloted jet flames. Proceedings of the Combustion Institute, 31:1543–1550, 2007.

[10] M. Cassiani, P. Franzese, and U. Giostra. A PDF micromixing model of dispersion for atmospheric flow. Part I: Development of the model, application to homogeneous turbulence and to neutral boundary layer. Atmospheric Environment, 39:1457–1469, 2005.

[11] M.J. Cleary and A.Y. Klimenko. A generalized multiple mappling conditioning approach for turbulent comsbution. Flow, Turbulence and Combustion, 82:477–491, 2009.

[12] T.P. Coffee and J.M. Heimerl. Transport algorithms for premixed, laminar steady-state flames. Combustion and Flame, 43:273–289, 1981.

[13] P.J. Colucci, F.A. Jaberi, P. Givi, and S.B. Pope. Filtered density function for large eddy simulation of turbulent reacting ows. Physics of Fluids, 10(2):499–515, 1998.

[14] A.W. Cook, J.J. Riley, and G. Kosly. A laminar flamelet approach to subgrid-scale chemistry in turbulent flows. Combustion and Flame, 109(3):332 – 341, 1997.

[15] P. Craven and G. Wahba. Smoothing noisy data with spline functions. Numerische Mathematik, 31:377–403, 1978.

[16] R.L. Curl. Dispersed phase mixing I: Theory and effects in simple reactors. AIChE Journal, 9(2):175–181, 1963.

[17] C. Dopazo. Relaxation of initial probability density function in the turbulent convection of scalar elds. Physics of Fluids, 22:20–30, 1979.

[18] C. Dopazo and E.E. O'Brien. An approach to the autoignition of a turbulent mixture. Acta Astronautica, 1:1239–1266, 1974.

[19] T.D. Dreeben and S.B. Pope. Probability density function/Monte Carlo simulation of near wall turbulent flows. Journal of Fluid Mechanics, 357:141–166, 1998.

[20] L. Eça, M. Hoekstra, A. Hay, and D. Pelletier. Verication of RANS solvers with manufactured solutions. Engineering with computers, 23:253–270, 2007.

[21] V. Eswaran and S.B. Pope. Direct numerical simulations of the turbulent mixing of a passive scalar. Physics of Fluids, 31:506–520, 1988.

[22] R.O. Fox. On velocity conditioned scalar mixing in homogeneous turbulence. Physics of Fluids, 8:2678–2691, 1996.

[23] F. Gao and E.E. OBrien. A large-eddy simulation scheme for turbulent reacting ows. Physics of Fluids A, 5:1282–1284, 1993.

[24] G.H. Golub, M. Heath, and G. Wahba. Generalized cross-validation as a method for choosing a good ridge parameter. Technometrics, 21(2):215–223, 1979.

[25] D.C. Haworth. Progress in probability density function methods for turbulent reacting flows. Progress in energy and combustion science, 36:168–259, 2010.

[26] M. F. Hutchinson and F. R. de Hoog. Smoothing noisy data with spline functions. Numerische Mathematik, 47:99–106, 1985.

[27] F.A. Jaberi, P.J. Colucci, S. James, P. Givi, and S.B. Pope. Filtered mass density function for large-eddy simulation of turbulent reacting ows. Journal of Fluid Mechanics, 401:85–121, 1999.

[28] J. Janicka, W. Kolbe, and W. Kollmann. Closure of the transport equation for the probability density function of turbulent scalar elds. Journal of Non-Equilibrium Thermodynamics, 4:47–66, 1979.

[29] P. Jenny, S.B. Pope, M. Muradoglu, and D.A. Caughey. A hybrid algorithm for the joint PDF equation for turbulent reactive flows. Journal of Computational Physics, 166:281–252, 2001.

[30] A. Juneja and S.B. Pope. A DNS study of turbulent mixing of two passive scalars. Physics of Fluids, 8:2177–2184, 1996.

[31] K.A. Kemenov and S.B. Pope. Molecular diffusion effects in LES of a piloted methane-air flame. Combustion and Flame, 2010. (to be published).

[32] S.H. Kim and H. Pitsch. Conditional filtering method for large-eddy simulation of turbulent nonpremixed combustion. Physics of Fluids, 17(10):105103, 2005.

[33] A.Y. Klimenko and S.B. Pope. A model for turbulent reactive flows based on multiple mapping conditioning. Physics of Fluids, 15:1907–1925, 2003.

[34] D. Livescu, F.A. Jaberi, and C.K. Madnia. Passive-scalar wake behind a line source in grid turbulence. Journal of Fluid Mechanics, 416:117–149, 2000.

[35] A. Luhar and B.L. Sawford. Micro-mixing modeling of concentration fluctuations in inhomogeneous turbulence in the convective boundary layer. Boundary Layer meteorology, 114:1–30, 2005.

[36] A.E. Lutz, R.J. Kee, J.F. Grcar, and Fran M. Rupley. Oppdif: A fortran program for computing opposed-flow diffusion flames. Technical report, Sandia National Laboratories, 1997.

[37] R. McDermott and S.B. Pope. A particle formulation for treating differential diffusion in filtered density function methods. Journal of Computational Physics, 226(1):947–993, 2007.

[38] S. Mitarai, J.J. Riley, and G. Kosaly. Testing of mixing models for Monte Carlo probability density function simulations. Physics of Fluids, 17:047101–15, 2005.

[39] M. Muradoglu, K. Liu, and S.B. Pope. PDF modeling of a bluff-body stabilized turbulent flame. Combustion and Flame, 132:115–137, 2003.

[40] M. Muradoglu, S.B. Pope, and D.A. Caughey. The hybrid method for the PDF equations of turbulent reactive flows: consistency conditions and correction algorithms. Journal of Computational Physics, 172:841–878, 2001.

[41] S. Navarro-Martinez, A. Kronenburg, and F. Mare. Conditional moment closure for large eddy simulations. Flow, Turbulence and Combustion, 75:245–274, 2005.

[42] E.S. Oran and J.P. Boris. Detailed modelling of combustion systems. Progress in energy and combustion science, 7(1):1–72, 1981.

[43] M. Overholt and S.B. Pope. Direct numerical simulations of a passive scalar with imposed mean gradient in isotropic turbulence. Physics of Fluids, 8:3128–3148, 1996.

[44] N. Peters. Turbulent Combustion. Cambridge University Press, Cambridge, 2000.

[45] C.D. Pierce. Progress-Variable Approach for Large-Eddy Simulation of Turbulent Combustion. PhD thesis, Stanford University, 2001.

[46] C.D. Pierce and P. Moin. Progress-variable approach for large-eddy simulation of non-premixed turbulent combustion. Journal of Fluid Mechanics, 504:73–97, 2004.

[47] H. Pitsch. Large-eddy simulation of turbulent combustion. Annual Review of Fluid Mechanics, 38:453–482, 2006.

[48] T. Poinsot and D. Veynante. Theoretical and Numerical Combustion. R.T. Edwards, Inc., 2005.

[49] S.B. Pope. The relationship between the probability approach and particle models for reaction in homogeneous turbulence. Combustion and Flame, 35:41–45, 1979.

[50] S.B. Pope. Transport equation for the joint probability density function of velocity and scalars in turbulent flow. Physics of Fluids, 24:588–596, 1981.

[51] S.B. Pope. An improved turbulent mixing model. Combustion Science and Technology, 28:131–145, 1982.

[52] S.B. Pope. PDF methods for turbulent reactive flows. Progress in Energy and Combustion Science, 11:119–192, 1985.

[53] S.B. Pope. Computations of turbulent combustion: Progress and challenges. Proceedings of the Combustion Institute, 23:591–612, 1990.

[54] S.B. Pope. Application of the velocity dissipation probaility density function model to inhomogeneous turbulent flows. Physics of Fluids A, 3:1947–1957, 1991.

[55] S.B. Pope. Lagrangian PDF methods for turbulent flows. Annual Review of fluid Mechanics, 26:23–63, 1994.

[56] S.B. Pope. On the relationship between stochastic Lagrangian models of turbulence and second-moment closures. Physics of Fluids, 6:973–985, 1994.

[57] S.B. Pope. Computationally efficient implementation of combustion chemistry using in situ adaptive tabulation. Combustion Theory and Modeling, 1:41–63, 1997.

[58] S.B. Pope. The vanishing effect of molecular diffusivity on turbulent dispersion: Implications for turbulent mixing and the scalar flux. Journal of Fluid Mechanics, 359:299–312, 1998.

[59] S.B. Pope. Turbulent flows. Cambridge University Press, Cambridge, 2000.

[60] S.B. Pope. Self-conditioned fields for large-eddy simulations of turbulent flows. Journal of Fluid Mechanics, 652:139–169, 2010.

[61] S.B. Pope and Y.L. Chen. The velocity dissipation probability density function model for turbulent flows. Physics of Fluids A, 2:1437–1449, 1990.

[62] W.H. Press, S.A. Teukolsky, W.T. Vetterling, and B.P. Flannery. Numerical Recipes in Fortran. Cambridge University Press, New York, 1992.

[63] V. Raman and H. Pitsch. A consistent LES/filtered density function formulation for the simulation of turbulent flames with detailed chemistry. Proceedings of the Combustion Institute, 31:1711–1719, 2007.

[64] P.J. Roache. Code verication by the method of manufactured solutions. Journal of Fluids Engineering, 124(1):4–10, 2002.

[65] C.J. Roy. Review of code and solution verication procedures for computational simulation. Journal of Computational Physics, 205:131–156, 2005.

[66] C.J. Roy, C.C. Nelson, T.M. Smith, and C.C. Ober. Verication of Euler/Navier–Stokes codes using the method of manufactured solutions. International Journal for Numerical Methods in Fluids, 44:599–620, 2004.

[67] P. Sagaut. Large eddy simulation for incompressible flows. Springer, Berlin, 2006.

[68] R. Sankaran, E.R. Hawkes, J.H. Chen, T. Lu, and C.K. Law. Structure of a spatially developing turbulent lean methane–air bunsen flame. Proceedings of the Combustion Institute, 31(1):1291–1298, 2007.

[69] B.L. Sawford. Conditional scalar mixing statistics in homogeneous isotropic turbulence. New Journal of Physics, 6:1–31, 2004.

[70] B.L. Sawford. Micro mixing modeling of scalar fluctuations for plumes in

homogeneous turbulence. Flow,Turbulence and Combustion, 72:133–160, 2004.

[71] B.L. Sawford and J.C.R. Hunt. Effects of turbulence structure, molecular diffusion and source size on scalar fluctuations in homogeneous turbulence. Journal of Fluid Mechanics, 165:373–400, 1985.

[72] B.L. Sawford and C.M. Tivendale. Measurement of concentration statistics downstream of a line source in grid turbulence. In Proceedings of the 11th Australasian Fluid Mechanics Conference, pages 945–948, University of Tasmania, 1992.

[73] J. Smagorinsky. General circulation experiments with the primitive equations. Monthly Weather Review, 91(3):99–164, 1963.

[74] G.P. Smith, D.M. Golden, M. Frenklach, N.W. Moriarty, B. Eiteneer, M. Goldenberg, C. Thomas Bowman, R.K. Hanson, S. Song, W.C. Gardiner, V.V. Lissianski Jr., and Z. Qin. http://www.me.berkeley.edu/gri_mech/.

[75] J.C. Song. A velocity-biased turbulent mixing model for passive scalars in homogeneous turbulence. Physics of Fluids, 30:2046–2053, 1987.

[76] H. Stapountzis, B.L. Sawford, J.C.R. Hunt, and R.E Britter. Structure of the temperature field downwind of a line source in grid turbulence. Journal of Fluid Mechanics, 165:401–424, 1986.

[77] S. Subramaniam and S.B. Pope. A mixing model for turbulent reactive flows based on Euclidean minimum spanning trees. Combustion and Flame, 115:487–514, 1998.

[78] J.C. Sutherland, P.J. Smith, and J.H. Chen. Quantification of differential diffusion in nonpremixed systems. Combustion Theory and Modeling, 9(2):365–383, 2005.

[79] G.I. Taylor. Diffusion by continuous movements. Proceedings of the London Mathematical Society, 20:196–212, 1921.

[80] G.I. Taylor. Statistical theory of turbulence IV: Diffusion in a turbulent air stream. Proceedings of the Royal Society of London, 151:465–478, 1935.

[81] M.S. Uberoi and S. Corrsin. Diffusion of heat from a line source in isotropic turbulence. National Aeronautics and Space Administration Report, 1142, 1953.

[82] J. Villermaux and J.C. Devillon. Représentation de la coalescence et de la redispersion des domaines de ségrégation dans un fluide par un modèle d'interaction phénoménologique. In Proceedings of the 2nd International Symposium on Chemical Reaction Engineering, 26, pages 1–13, New York, 1972. Elsevier.

[83] S. Viswanathan and S.B. Pope. Numerical implementation of mixing and molecular transport in LES/PDF studies of turbulent reacting flows. (submitted), 2010.

[84] G. Wahba and S. Wold. A completely automatic french curve: fitting spline functions by cross validation. communications in statistics simulation and computation, 4:1 – 17, 1975.

[85] H. Wang and S.B. Pope. Time averaging strategies in the finite-volume/particle hybrid algorithm for the joint PDF equation of turbulent reactive flows. Combustion Theory and Modeling, 12(3):529–544, 2008.

[86] H. Wang and S.B. Pope. Large eddy simulation/probability density function modeling of a turbulent $CH_4/H_2/N_2$ jet flame. Proceedings of the Combustion Institute, 2010. (to be published).

[87] H. Wang, P.P. Popov, and S.B. Pope. Weak second order splitting schemes for Lagrangian Monte Carlo particle methods for the composition PDF/FDF transport equations. Journal of Computational Physics, 229:1852–1878, 2010.

[88] Z. Warhaft. The use of dual heat injection to infer scalar covariance decay in grid turbulence. Journal of Fluid Mechanics, 88:93–109, 1981.

[89] Z. Warhaft. The interference of thermal fields from line sources in grid turbulence. Journal of Fluid Mechanics, 144:363–387, 1984.

[90] Z. Warhaft and J.L. Lumley. An experimental study of the decay of temperature fluctuations in grid-generated turbulence. Journal of Fluid Mechanics, 88:659–684, 1978.

[91] J. Xu and S.B. Pope. Assessment of numerical accuracy of PDF/Monte Carlo methods for turbulent reactive flows. Journal of Computational Physics, 152:192–230, 1999.